Theoretical modelling of opto-electronic properties of monolayer TMDC materials

zur Erlangung des Doktorgrads
der Naturwissenschaften (Dr. rer. nat.)

dem

Fachbereich Physik
der Philipps-Universität Marburg
vorgelegt von

Josefine Neuhaus

aus
Marburg (Lahn)

Marburg, 2022

Vom Fachbereich Physik der
Philipps-Universität Marburg als
Dissertation angenommen am: 13.09.2022

Erstgutachter:	Prof. Dr. Stephan W. Koch
Erstprüfer mündliche Prüfung:	Prof. Dr. Torsten Meier
Zweitgutachterin:	Prof. Dr. Kerstin Volz

Tag der mündlichen Prüfung: 11.11.2022

Hochschulkennziffer: 1180

Kurzbeschreibung

Kleiner, flexibler, effizienter! In der Entwicklung elektronischer Bauteile ist dieser Trend klar erkennbar. Übergangsmetall-Dichalkogenide (TMDCs) werden hierbei als vielversprechende Kandidaten gehandelt, um dieses Ziel auf die Spitze zu treiben. Diese Materialien gehören zur Klasse der sogenannten van-der-Waals-Materialien. Diese Materialklasse zeichnet aus, dass die Materialien aus einzelnen Lagen aufgebaut sind, die nur schwach miteinander verbunden sind. Es ist daher möglich einzelne Lagen voneinander zu separieren. Diese Monolagen sind nur wenige Ångström dick, weisen aber eine starke Kopplung an Lichtfelder auf, wobei aufgrund der reduzierten Symmetrie des Systems eine polarisationsabhängige selektive Anregung von Elektronen unterschiedlicher Spins möglich ist. Durch die geringe Dicke sind die optischen Eigenschaften der Materialien darüber hinaus empfindlich gegenüber äußerer Einwirkungen, was einerseits das Spektrum potentieller Anwendungen, beispielsweise in der Sensorik, erweitert und andererseits eine gezielte Anpassung an die Anwendungsvoraussetzung erlaubt.

Im Rahmen dieser Dissertation wurden in mehreren Studien ausgewählte Aspekte der opto-elektronischen Eigenschaften halbleitender TMDC-Monolagen untersucht. Große Teile dieser Studien sind bereits veröffentlicht worden und werden in dieser Arbeit eingeleitet und zusammengefasst.

Die Materialien wurden mithilfe eines hybriden Ansatzes untersucht, der Methoden der Dichtefunktional-Theorie (DFT) mit Methoden der Dichtematrix-Theorie kombiniert, um ein effektives und präzises Werkzeug zur parameterfreien Beschreibung der untersuchten Systeme zu erhalten. Ergebnisse von DFT-Rechnungen wurden hierbei als Ausgangspunkt genommen, um eine modellhafte Beschreibung des nicht-wechselwirkenden Grundzustands des Systems zu entwickeln, auf dessen Basis die optischen und dynamischen Eigenschaften mit Hilfe eines Dirac-/Halbleiter-Bloch-Ansatzes (DBE/SBE) analysiert werden konnten. Hierbei bildete insbesondere die Modellbildung zur Beschreibung der Coulomb-Wechselwirkung ein fundamentales Bindeglied zwischen den beiden Ansätzen.

Den Schwerpunkt einer ersten Studie bildete folgerichtig die Erweiterung und Analyse eines Modells dieser Wechselwirkung, sowie weiterführende Untersuchungen der Modifikation der Wechselwirkung durch angeregte Ladungsträger und die dielektrische Umgebung, und schließlich deren Implikation für die elektronischen und optischen Energiespektren. Auf Basis des Coulombpotentials eines Schichtsystems und der aus DFT-

Rechnungen resultierenden Wellenfunktionen wurde ein isotropes Modell für die Coulombmatrixelemente in der Umgebung der direkten Bandlücken gefunden. Eine direkte experimentelle Beobachtung der Wechselwirkung ist nicht möglich, doch die gute Übereinstimmung der Ergebnisse für die ladungsträger- und umgebungsinduzierte Reduktion der Bandlücke und der Exzitonen-Bindungsenergien mit experimentellen Werten und etablierten theoretischen Modellen deuten darauf hin, dass das erarbeitete Modell eine sinnvolle und effiziente Näherung zur Beschreibung der Wechselwirkung darstellt. In allen nachfolgenden Untersuchungen wurde dieses Modell materialspezifisch angepasst und für die Wechselwirkungsbeschreibung im Bereich der Haupttäler (K/K') und der Nebentäler (Σ/Λ) verwendet.

In einer zweiten Studie wurde die Magnetfeldabhängigkeit des exzitonischen Spektrums untersucht. Die diamagnetische Verschiebung der s-artigen Zustände mit einem g-Faktor von $g_{ns} \gtrapprox 2$ wurde in Äquivalenz zu experimentellen Studien gesehen. Darüber hinaus wurde auch die nicht direkt optisch adressierbare – das heißt nicht über Ein-Photon-Prozesse anregbare – p-artige Exzitonenreihe untersucht, die aufgrund ihrer Drehmomentquantenzahl eine zusätzliche lineare magnetische Abhängigkeit aufweist, welche zu einer Zeeman-Aufspaltung der Zustände führt. Eine indirekte optische Untersuchung dieser p-artigen Zustände ist bei geeigneten Anregungsbedingungen möglich, da Übergänge zwischen s- und p-artigen Zuständen optisch induziert werden können. Aufgrund der energetischen Ordnung der Exzitonen ist insbesondere der Fall einer anfänglichen Besetzung des $2s$-Zustands interessant, da hier der Übergang zu den energetisch niedriger gelegenen $2p$-Zuständen eine Verstärkung des Signals im Terahertz-Bereich (THz) impliziert. Aufgrund der unterschiedlichen Magnetfeldabhängigkeit ist diese Verstärkung, die teilweise durch Absorption durch $2s$-$3p$-Übergänge abgeschwächt wird, darüber hinaus durch das magnetische Feld verstimmbar. Weiterhin kann die Lage des Gain-Maximums durch die Wahl der dielektrischen Umgebung verschoben werden.

Während exzitonische Eigenschaften im Regime niedriger Anregungsdichten die optische Antwort des Materials dominieren, führt eine starke Anregung zu einer starken Renormierung der Bandlücke, die die Bandlücke um mehrere $100\,\text{meV}$ verringert, zu einem Ausbleichen der exzitonischen Resonanzen, und schließlich zu einer Verstärkung des optischen Probe-Signals im Bereich unterhalb der niedrigsten Exziton-Resonanz. Unsere Analyse der Ladungsträgerdynamik am Beispiel von MoTe$_2$ hat gezeigt, dass die Ladungsträger nach einer optischen Anregung, bedingt durch die starke Coulombwechselwirkung, bereits auf Zeitskalen von wenigen Femtosekunden in heiße, Fermi-ähnliche Verteilungen relaxieren. In einer ersten Studie wurde der Fokus auf die Dynamik in der näheren Umgebung der direkten Bandlücke (Haupttals) gelegt, wobei eine Abschätzung des Beitrags der Seitentäler zeigte, dass dieser eine Zunahme der optischen Verstärkung bewirkt. Eine zweite Studie, in der die Analyse auf die gesamte Brillouin Zone (BZ) ausgedehnt wurde, zeigte, dass Streuzeiten in die Seitenminima (Nebentäler) sensibel

von den Anregungsbedingungen abhängen. Allerdings konnte hier für keines der untersuchten molybdänbasierten Materialien gezeigt werden, dass durch optische Anregung erzeugte Ladungsträger, die in das Seitental streuen, dazu führen, dass sich das Seitental energetisch unter das Haupttal schiebt – für alle untersuchten Konstellationen blieb die Bandlücke der Monolage direkt.

Abschließend wurde untersucht, wie sich die $1s$-Exzitonenresonanz im linearen optischen Spektrum verändert, wenn sich ein Elektron-Loch-Plasma im Material ausgebildet hat. Es wurde eine lineare Verbreiterung der Resonanz beobachtet, die sich in einem schnelleren Abfall des integrierten Vier-Wellen-Mischsignals, separiert von Beiträgen möglicher inhomogener Verbreiterungen, messen lässt. Außerdem wurde gezeigt, dass beide Relaxierungsprozesse, das heißt sowohl das Abkühlen der Ladungsträgerverteilung, als auch die Neugruppierung der Ladungsträger in den unterschiedlichen Tälern, zu einer Verschmälerung der Resonanz führen.

Abstract

Smaller, more flexible, more efficient! This trend is clearly visible in the development of electronic devices. Transition metal dichalcogenides (TMDCs) are considered promising candidates to push this goal to the extreme. These materials belong to the class of so-called van der Waals materials. This class of materials is characterised by the fact that the materials are made up of layers that are only weakly connected to each other. It is therefore possible to separate individual layers from each other. These monolayers are only a few Ångströms thick, but exhibit strong coupling to light fields, whereby polarisation-dependent selective excitation of electrons with different spins is possible due to the reduced symmetry of the system. Due to the small thickness, the optical properties of the materials are also sensitive to external influences, which on the one hand expands the spectrum of possible applications, for example in sensor technology, and on the other hand enables targeted adaptation to the application requirements.

In this dissertation, selected aspects of the opto-electronic properties of semiconducting TMDC monolayers were investigated in several studies. Large parts of these studies have already been published and are introduced and summarised in this thesis.

The materials were studied using a hybrid approach that combines density functional theory (DFT) methods with density matrix theory methods to produce an effective and accurate tool for a parameter-free description of the investigated systems. Results of DFT calculations were taken as a starting point to develop a model description of the non-interacting ground state of the system, on the basis of which the optical and dynamical properties could be analysed using a Dirac/semiconductor Bloch equation approach (DBE/SBE). Here, in particular, the modelling to describe the Coulomb interaction formed a fundamental link between the two approaches.

The focus of a first study was consequently the extension and analysis of a model of this interaction, as well as further investigations of the modification of the interaction by excited charge carriers and the dielectric environment, and finally its implication for the electronic and optical energy spectra. Based on the Coulomb potential of a layer system and the wave functions resulting from DFT calculations, an isotropic model was found for the Coulomb matrix elements in the vicinity of the direct band gap. Direct experimental observation of the interaction is not possible, but the good agreement of the results for the charge carrier- and environment-induced reduction of the band gap and exciton binding energies with experimental values and established theoretical models indicates

that the elaborated model is a reasonable and efficient approximation to describe the interaction. In all subsequent investigations, this model was adapted material-specifically and used for the interaction description in the area of the main valleys (K/K') and the side valleys (Σ/Λ).

In a second study, the magnetic field dependence of the excitonic spectrum was investigated. The predicted diamagnetic shift of the s-like states with a g-factor of $g_{ns} \gtrapprox 2$ was found to be equivalent to experimental studies. In addition, the p-like exciton series, which is not directly optically addressable – i.e. cannot be excited via one-photon-processes –, was investigated. Due to its angular momentum quantum number, this series exhibits an additional linear magnetic dependence, which leads to a Zeeman splitting of the states. An indirect optical investigation of these p-like states is possible under suitable excitation conditions, since transitions between s- and p-like excitonic states can be optically induced. Due to the energetic order of the excitons, the case of an initial occupation of the $2s$ state is particularly interesting, since here the transition to the energetically lower $2p$ states implies an amplification of the signal in the terahertz (THz) range. Due to the different magnetic field dependence, this amplification, which is partly superimposed by absorptive features of $2s$-$3p$-transitions, is tunable by a magnetic field. Furthermore, the position of the gain maximum can be shifted by the choice of the dielectric environment.

While excitonic properties dominate the optical response of the material in the regime of low excitation densities, strong excitation leads to a strong renormalisation of the band gap, reducing the band gap by several $100\,\text{meV}$, to a bleaching of the excitonic resonances, and finally to an amplification of the optical probe-signal in the region below the lowest exciton resonance. Our analysis of the charge carrier dynamics using the example of MoTe$_2$ has shown that in this material system the charge carriers relax into hot Fermi-like distributions after optical excitation due to the strong Coulomb interaction already on time scales of a few femtoseconds. In a first study, the focus was placed on the dynamics in the immediate vicinity of the direct band gap ($K/\,K'$), whereby an estimation of the contribution of the side valleys showed that this causes an increase in optical amplification. A second study, in which the analysis was extended to the entire Brillouin zone (BZ), showed that scattering times into the side minima (side valleys) depend sensitively on the excitation conditions. However, for none of the investigated molybdenum-based materials could be shown that the scattering of optically induced charge carriers into the side valley the side valley to push energetically under the main valley – for all constellations studied, the band gap of the monolayer remained direct.

Finally, it was investigated how the $1s$ exciton resonance in the linear optical spectrum changes when an electron-hole plasma has formed in the material. A linear broadening of the resonance was observed, which can be measured in a faster decay of the integrated four-wave mixed signal, separated from contributions of a possible inhomogeneous

broadening. Furthermore, it was shown that both relaxation processes, i.e. both the cooling of the charge distribution and the regrouping of the charge carriers in the different valleys, lead to a narrowing of the resonance.

Danksagung

Ohne die Hilfe und Unterstützung von vielen Menschen, wäre diese Arbeit wohl auch maximal ein quasi-zweidimensionales Objekt geblieben. Daher möchte mich bei den vielen Menschen bedanken, die ihr zur Ausbreitung in die dritte Dimension verholfen haben:

Ein großer Dank gilt Prof. Dr. Stephan W. Koch dafür, dass ich meine Forschung an diesem spannenden Themenkomplex fortführen durfte und er mich dabei mit seiner ruhigen, positiv bestärkenden Art unterstützt hat. Ein besonderer Dank gilt auch Dr. Tineke Stroucken. In zahlreichen Gesprächen und Diskussionen habe ich viel von Dir gelernt, über die Physik, die Mathematik und darüber hinaus. Bedanken möchte ich mich auch bei Lars Meckbach, der mich an seinem Wissen zu TMDC Materialien teilhaben ließ und somit einen wichtigen Teil des Fundaments dieser Arbeit legte.

Herzlich danken möchte ich auch Prof. Dr. Torsten Meier, der kurzfristig und unkompliziert eingesprungen ist als Prüfer bei der Disputation.

Ich möchte mich bei Prof. Dr. Kerstin Volz für die Übernahme des Zweitgutachtens bedanken, aber auch für die freundliche Aufnahme in den Räumen auf den Lahnbergen und die Bereitstellung von Möglichkeiten im Rahmen des SFB 1083 mit anderen Forscher*innen ins Gespräch zu kommen. Außerdem danke ich Prof. Dr. Peter Lenz für die Mitwirkung an meiner Prüfungskomommission.

Ich möchte mich bei Stephan und Prof. Dr. Jerry Moloney bedanken für die Möglichkeit einen Forschungsaufenthalt am College of Optical Sciences in Tucson zu machen. Trotz unzähliger Hindernisse in der Vorbereitung habt ihr beharrlich darauf hingearbeitet, dass wir diese Reise antreten und so unseren Horizont erweitern konnten. Die intensive Zusammenarbeit in der Gruppe und insbesondere auch mit Dr. Jörg Hader, sowie die ausgleichenden Ausflüge waren eine bereichernde Erfahrung.

Vielen herzlichen Dank auch den ehemaligen und aktuellen Mitgliedern der AG, für die digitalen und analogen Kaffeepausen, Mensaausflüge, Wanderungen, Motivationsgespräche,... , die mal mehr und mal weniger mit Arbeit verbunden waren, aber immer eine gute Abwechslung zur Computerarbeit bildeten.

Ein großes Dankeschön an Felix, Luise, Lotte, Nico und Ada, die sich mit Akribie und Ausdauer der Aufgabe gewidmet haben, meine Texte korrekturzulesen. Euren kritischen Anmerkungen und Kommentaren ist es zu verdanken, dass die Sätze nun kürzer, die Zusammenhänge klarer herausgearbeitet und manch sprachliche Ungenauigkeiten behoben sind ;-).

Author's contributions

This thesis aims to give a summarising introduction into selected aspects of the optical properties of semiconducting monolayer transition metal dichalcogenides that were studied in the course of my doctoral studies. Most of the results are already part of publications, where they are discussed in more detail. The interested reader is referred to these publications to delve deeper into the particular topics.

Publications

I **J. Neuhaus**, S. C. Liebscher, L. Meckbach, T. Stroucken, and S. W. Koch, "Microscopic Coulomb interaction in transition-metal dichalcogenides", J. Phys.: Condens. Matter **33** 035301 (2021)

II T. Stroucken, **J. Neuhaus**, and S. W. Koch, "Magnetic-field tuning of the intraexcitonic absorption and gain in transition metal dichalcogenides", Phys. Rev. B **104**, 075438 (2021)

III L. Meckbach, J. Hader, U. Huttner, **J. Neuhaus**, J. T. Steiner, T. Stroucken, J. V. Moloney, and S. W. Koch, "Ultrafast band-gap renormalization and build-up of optical gain in monolayer $MoTe_2$", Phys. Rev. B **101**, 076401 (2020)

IV J. Hader, **J. Neuhaus**, J. V. Moloney, and S. W. Koch, "On the importance of electron-electron and electron-phonon scatterings and energy renormalizations during carrier relaxation in monolayer transition-metal dichalcogenides", J. Phys.: Condens. Matter **34**, 285601 (2022)

V **J. Neuhaus**, T. Stroucken, and S. W. Koch, "Electron-hole plasma-induced dephasing in transition metal dichalcogenides", physica status solidi(RRL)-Rapid Research Letters **15**(11), 2100391 (2021)

Poster

- **J. Neuhaus**, T. Stroucken, S. W. Koch, *Electron-hole plasma-induced dephasing in transition metal dichalcogenides*, Poster presented at 'International conference on internal interfaces' in Rheinfels, Germany (2021)

Own contributions

All studies presented in the scope of this thesis are based on frequent and fruitful discussions within the group of *Theoretische Halbleiterphysik* and, in particular, with my supervisor Prof. Dr. Stephan W. Koch and my main former research colleague Dr. Tineke Stroucken. In these discussions, intermediate results were discussed and next steps were planned.

In a first project, the modelling of the Coulomb interaction was studied in more detail. Due to the finite thickness, a proper description of the Coulomb interaction in monolayer TMDC materials is crucial. First, this implies to examine in which way the Coulomb potential in these materials differs both from the exact two-dimensional as well as the three-dimensional formulation. Based on a first ansatz presented by S. C. Liebscher in his *Wissenschaftliche Hausarbeit*, I modified and extended the model to enable the investigation of the Coulomb matrix' dependencies e.g. on the spin, the material composition and the exact path in reciprocal space in more detail. I both performed the underlying density functional theory (DFT) calculations and the numerical evaluation of the Coulomb-matrix elements as well as planned and performed their analysis. Second, screening effects due to environmental and carrier-induced screening play a crucial role. Employing the numerical code developed by L. Meckbach as starting point and adapting it to the specific material system and question, I performed the numerical calculations and analysed the varying dependencies and their implications on the linear optical properties and the band gap. The results of these studies were published in Ref. [I], where I wrote the main part of the manuscript. Its main results are summarised in Ch. 3.

Driven by the idea of a tunable amplification of a terahertz-pulse (THz) due to intraexcitonic transitions, in a second project, we studied the magnetic field dependence of excitonic resonances and the THz response of a pre-excited sample. In order to numerically evaluate these settings, I extended the numerical code to capture the magnetic field contributions as well as to model the THz response. T. Stroucken and I frequently discussed and compared our results based on independent numerical implementations for different material systems and settings leading to publication [II]. In Ref. [II], the results of numerical simulations are exemplary analysed for an hexagonal boron nitride (hBN) encapsulated MoS_2 monolayer. I contributed to the writing and discussion of the manuscript. The main results are, extended by further analysis of the dependence on the chosen material system, summarised in Ch. 4.

In a third project consisting of two subprojects, we extended our studies beyond quasi-equilibrium investigations and concentrated on the carrier dynamics after optical excitation. All studies performed in this context were executed in close collaboration of our research group with Jörg Hader and Jerome V. Moloney (University of Arizona, Tucson, USA). The main results of the two subprojects are summarised in Ch. 5. In a first part of the project, leading to publication [III], the theoretical model was extended to

capture carrier- and phonon-scattering contributions in order to simulate and analyse a full pump-probe experiment in proximity to the K-point and analyse the optical spectra. Furthermore, the change in the gain spectra after relaxation of carriers to the side valleys was estimated. This study was performed exemplary for $MoTe_2$. I contributed in carrying out DFT calculations to gain insights on fundamental material parameters and to expand the model of the Coulomb interaction to the side valley. Furthermore, I contributed to the discussion of the manuscript.

While in this first part, the influence of the side valley was only estimated in the quasi-equilibrium limit, in the second part, we extended the model such that the relaxation dynamics through the whole Brillouin zone (BZ) could be evaluated. The results for the carrier dynamics for different excitation conditions led to Ref. [IV]. I contributed to these studies by performing the DFT calculations providing the two-dimensional band structure as well as fundamental material parameters and a model for the Coulomb potential. Furthermore, I contributed in writing and discussing the manuscript.

Finally, we analysed in more detail the optical response and the dependence of the broadening of the spectral resonances on the exact distribution of the carriers in the low-density regime. As a separation of homogeneous and inhomogeneous broadening effects is experimentally achieved for example by four-wave mixing (FWM) experiments, I derived a theoretical model for a degenerate FWM experiment including pre-pulse excited carriers, in consultation with T. Stroucken. I extended the numerical code, performed the calculations and analysed the results. The results of this study were published in Ref. [V], where I wrote the main manuscript. After publication, I presented the results at the 'International conference on internal interfaces', organised by the SFB 1083. Key insights of this study are summarised in Ch. 6.

List of abbreviations

BZ	Brillouin zone
CE	Cluster expansion
DBE	Dirac-Bloch equations
DF(P)T	Density functional (perturbation) theory
EID	Excitation-induced dephasing
eom	Equation of motion
FWHM	Full width at half maximum
hBN	Hexagonal boron nitride
IR	Infrared
LO	Longitudinal optical
MDFs	Massive Dirac fermions
OPTP	Optical pump terahertz probe
SBE	Semiconductor-Bloch equations
THz	Terahertz
TMDC	Transition metal dichalcogenide
WE	Wannier equation

Inhaltsverzeichnis

1. | Introduction

> THE BUMBLEBEE CAN'T ACTUALLY FLY.
> BUT SHE DOES NOT KNOW THAT AND JUST
> FLIES ANYWAY!

Sometimes it pays to try something, even if people are sceptical about what to expect, or even convinced of its failure. Sometimes only curiosity and trying even at the risk of failure gets one to see flying frogs or to lay the corner stone for a new branch of science. In fact, it was curious experimentation that led to the Nobel prize in physics, 2010, for "groundbreaking experiments regarding the two-dimensional material graphene" [1]. Theoretical studies on the differing physical properties between bulk materials and their corresponding monolayers[1] and the expectation of being able to study astonishing new physics reaches back to the 1940s. It was already 1947 that P. Wallace published one of the first studies in this context on 'graphite monolayers' – by now, we call them 'graphene' –, where he derived their surprising band structure on the basis of a tight-binding model. This band structure shows a vanishing band gap and linear dispersion around this gap, resulting in a resistance equally low or even lower as in copper [2]. Even though this early work demonstrated promising material features, consecutive experimental studies are hardly found. Even later on, the focus of most studies was on different graphene alloys such as fullerenes [3, 4] – balls formed out of different numbers of carbon atoms – or nanotubes [5]. One of the reasons for this lack of experimental research on planar monolayer materials was the prediction that these materials are, in contrast to their curved counterparts, thermodynamically unstable. Unimpressed by this forecast, A. Geim and K. Novoselov tried hard at the preparation of graphene and, finally, proved the doubters wrong – the bumblebee can fly indeed [6, 7]. Even more surprisingly, they demonstrated that the preparation of a monolayer from a van-der-Waals bound material – a class of materials where the atoms are covalently bound in a plane but interact only weakly, via van-der-Waals interaction, in the perpendicular direction – is fairly simple.

---

[1]In the context of this thesis the term "monolayer" is not only used for monoatomic planar layers but also for materials that intrinsically consist of few atomic layers.

It only requires a certain dexterity and adhesive tape to separate single layers from bulk material. This success of Geim and Novoselov set off an avalanche of new research on planar, low-dimensional materials – often called two-dimensional even though, as we will elucidate later on, all materials have a finite extension in all three spatial directions. Nowadays, the preparation methods are developed further, which is essential for possible large scale applications and allows to go beyond naturally occurring material and prepare artificial material compositions [8, 9, 10]. The zoo of quasi-two-dimensional materials is no longer limited to graphene alone but consists of a variety of materials, which only have their low dimensionality in common [11, 12, 13]. One species of this zoo are transition metal dichalcogenides (TMDCs), that are, as the name suggests, characterised by its composition; the materials are composed of transition metal and chalcogen atoms in a ration 1:2. The optical, magnetic and electronic properties of these materials are diverse, ranging from superconducting to isolating. There is one subspecies, where transition metals of the VIth group are incorporated – therefore they are called group-VI TMDCs –, that exhibits semiconducting behaviour. The bulk-parents of these group VI-TMDCs were already in the focus of researchers in the 1960s/70s, but as the reduction of dimensionality revealed new promising possibilities for their application, the monolayers received incomparably much more attention in the past decade [14, 15, 16, 17].

In 2010, a drastic increase of a resonance in the photoluminescence spectrum of MoS_2 by several orders of magnitude was reported when the sample thickness was reduced to a monolayer [18, 19]. A transition of the material from an indirect to a direct semiconductor was found responsible for this enhancement of the signal [18]. In the following years, comparable results were found for further materials. Nowadays, the typical representatives of the semiconducting TMDCs, that are also discussed, with different weighting, in the studies summarised in this thesis, are $Mo\{S/Se/Te\}_2$ and $W\{S/Se\}_2$[2] [22, 23]. Regarding the application in an opto-electronic device, a material with a direct band gap is advantageous, because the excitation or relaxation of an electron in the material, which is accompanied by an absorption or emission of light, respectively, can take place 'directly' without any momentum transfer. Therefore, no further quasiparticles, i.e. phonons, need to be involved in the process in order to fulfil conservation laws, which makes the transition more probable.

Interestingly, similar to graphene and unlike to many conventional semiconducting structures, the band gap in TMDC monolayers is not located at the center of the Brillouin zone (BZ), but at its corners. To comprehend the importance of this finding, let us take a step back and look more closely at the material structure as displayed in Fig. 1.1. Comparing the top view, TMDCs are – at least in their predominant phase – similar to

---

[2]There is an ongoing discussion regarding the directness of the band gap in WSe_2. Several studies indicate that the material remains indirect even in the monolayer, but no final conclusions were drawn other than the insight of a high sensitivity e.g. to strain and doping [20, 21].
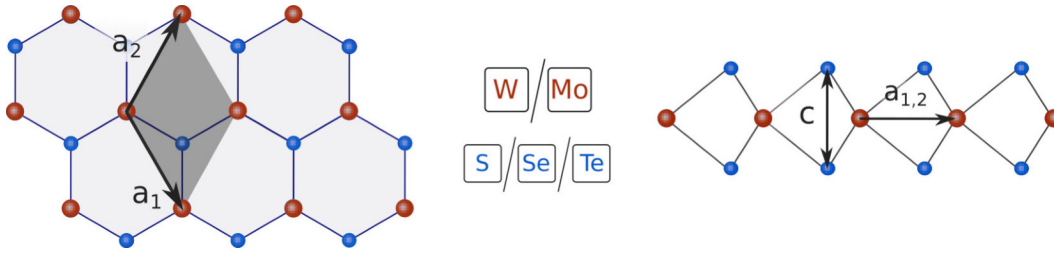
Abbildung 1.1: Lattice structure of the analysed TMDCs. Left: Top-view, right: Side-view.

graphene. Both structures are reminiscent of a honeycomb from the top, but in graphene carbon atoms build the honeycombs corners and in TMDCs neighboured corners are alternately occupied by atoms of different kinds. From the side view, the TMDC structure is three-layered, the metal layer is enclosed by two chalcogen layers. The structure is classified as trigonal prismatic.

This lattice structure of a monolayer is important for the energetic spectrum as it is not inversion symmetric. Since in the same way as the lattice structure is not inversion symmetric, the band structure is not inversion symmetric and the energetic states electrons of opposite spin may occupy are degenerate – at the same energy level – only at few special points of high symmetry. Especially at the corners of the BZ the lack of inversion symmetry leads to a splitting of the energetic states occupied by particles of opposite spin. Neighbouring corners of the BZ are consequently similar but unequal, therefore they are named K and K'. Whereas the splitting for the lowest unoccupied states ($\hat{=}$ conduction band) is only in the order of a few meV, the splitting is in the order of several hundred meV for the highest occupied states ($\hat{=}$ valence band). The exact energy splitting depends on the material and is approximately twice as large in tungsten- as in molybdenum-based materials, because of the larger mass of tungsten. Additionally, the ordering of the spin states differ in tungsten- and molybdenum-based materials: in tungsten-based materials, the states that are energetically closest have different spin character, in contrast, in molybdenum-based materials, they have the same spin character. Thus, in tungsten-based materials the energetically lowest transition is spin-forbidden. This difference between tungsten- and molybdenum-based materials has implications for the optical properties of these materials, to which we will refer again at a later point.

Furthermore, the states at the different corners of the BZ couple to differently circular polarised light. Thus, excitations can be induced separately at the different valleys at the K/K' point. This difference in coupling behaviour, in combination with the large spin-splitting of the bands, has the potential to use the spin or the valley index as a degree of freedom, e.g. to store and process information via the spin or the crystal momentum. These possible areas of application are traded under the terms spin- and valleytronics.

Moreover, the material thinness in combination with the large coupling to light in the visible to near-infrared (IR) regime is attractive for many different optical and opto-electronic applications. From a practical point of view, their thinness promises further miniaturisation and flexibility of possible devices. Furthermore, the thinness goes along with strong many-body interactions that are accompanied by a high sensitivity of the optical properties to internal and external conditions. On the one hand, this sensitivity yields the possibility to tune the devices in a certain range and tailor them for specific application purposes. On the other hand, it enables an application in the context of sensing. Indeed, several studies on the implementation of TMDC monolayers in different device applications like photovoltaic solar cells [24], LEDs [25], field effect transistors [26], lasers [27, 28], sensing devices for heavy-metals and biomolecules [29] showed the variety of application, but also its challenges. Despite this promising spectrum of potential applications and the immeasurable number of studies on TMDC materials, a lot of these challenges are still to be solved and there are still open questions that require further research.

In this thesis, selected aspects of the complex interrelationships and interdependencies of the linear and non-linear optical properties of group VI-TMDCs are investigated on the basis of a combined approach of density-functional theory (DFT) and a microscopic density matrix approach based on the massive Dirac fermion (MDF) model. In particular, we aim to understand the tunability of electronic and optical properties by external parameters like the dielectric environment or a magnetic field, and we aim for a description of the dynamics of excited carriers and their influence on the energetic and optical spectra. Different aspects of this large topic were focused on in different studies that led to the publications listed above. In the following, the structure of this thesis and the motivation for and connections between the different subprojects will be further explained.

Ch. 2 gives an introduction into the general theoretical framework of this thesis. Here, fundamental theoretical concepts are explained and their application to the material system is presented. Some of the concepts introduced in this chapter are further elaborated and adapted to specific settings in later chapters.

In the first subproject, summarised in **Ch. 3**, we took a closer look at the modelling of the Coulomb interaction in TMDC materials. As introduced above, due to the confinement of the carriers within the layer, the thinness of the material is accompanied by large Coulomb effects that manifest themselves in large exciton binding energies in the range of several hundred meV, fast electronic scattering processes on the femtosecond timescale and large renormalisations of the band gap [18, 30, 31]. When describing the Coulomb interaction theoretically, the finite thickness makes it necessary to consider two aspects in particular: First, even though the electrons are confined within the layers, the electromagnetic field which mediates their interaction reaches out of the layer.

Consequently, the material properties are sensitive to the environment, which shows the necessity to take the dielectric surrounding of the material into account in the theoretical description. Whereas the inclusion of further layers surrounding the target material is numerically challenging in standard DFT calculations, different analytical approaches have been formulated to effectively include environmental effects [32, 33, 34, 35]. Second, as mentioned above, even though these monolayer materials are often called 'two-dimensional materials', they are part of the three-dimensional world. Due to the confined but finite extension of the carrier wave functions, the Coulomb potential neither corresponds to the potential of a three-dimensional material nor to the potential of a strictly two-dimensional material, but is somewhere in between these two limits. We propose to include these finite thickness effects by introducing an effective form factor based on an approximation of the Coulomb-matrix elements which are calculated using the DFT wave functions. The analysis of the Coulomb interaction is rounded off by an investigation of the complex interplay of finite thickness and environment- and carrier-induced screening effects. In particular, we analyse their influence on the band gap and the excitonic resonance energies.

Because of the strong Coulomb interaction, the optical absorption spectrum in the low excitation regime is dominated by sharp peaks that can be traced back to bound electron-hole pairs – excitons – with binding energies in the order of several hundred meV. Besides the excitonic resonances that are seen in the linear optical spectrum there is a broad spectrum of excitonic states, comparable to the stationary states of a hydrogen atom. Due to the optical selection rules, only s-type excitonic states couple directly to light, but these states then couple to p-type excitonic states upon excitation by light in the mid-IR to terahertz (THz) range. In **Ch. 4**, we analyse this extended excitonic spectrum and its observability in the material linear response in the presence of excitonic occupations. Furthermore, we analyse the changes of the excitonic spectrum when applying a magnetic field perpendicular to the sample plane and the resulting tunability of intraexcitonic transitions. Again, the effects of the interplay of varying external parameters – namely dielectric surrounding and magnetic field – on the excitonic spectrum is investigated.

In the high-excitation regime, the formation of bound excitons is energetically unfavourable, but the excited charge carriers can be described as an electron-hole plasma. Upon exposing a TMDC monolayer to a high-intensity laser pulse with a suitable wavelength, electrons are excited and interact with one another and with phonons. Both processes lead to a relaxation of the carriers within the bands. To describe these processes of excitation and relaxation in more detail, we analyse the dynamics of carriers upon above band gap excitation in **Ch. 5**. In a first part, we focus on the dynamics in proximity to the direct band gap and analyse the build-up of optical gain. In a second part, we expand our model to describe the relaxation dynamics in the full BZ.

Finally, even in the low density regime, the presence of excited carriers has an influence

on the optical spectrum. Before gain becomes measurable, the interaction of carriers manifests in a broadening of the excitonic resonances in the linear absorption spectrum. The influence of excited carriers on the linewidth of the lowest excitonic resonance and its changes upon relaxation of the carriers within the bands is analysed in **Ch. 6**. The broadening of the excitonic resonances is a result of different contributions, which experimentally cannot be separated when analysing the linear absorption spectrum only. But higher-order non-linearities allow for some separation: the homogeneous broadening can explicitly be extracted from four-wave mixing (FWM) experiments. Thence, I conclude our study with a simulation of the impact of electron-hole plasma on the FWM signal. With these manifold insights into the opto-electronic properties of TMDC monolayers, I hope to help the mountain of knowledge grow by another one or two monolayers.

2. | Theory

Describing the physical properties of a solid on a microscopic scale is a non-trivial task, as the complexity increases exponentially with the number of particles that needs to be treated. Each particle interacts with all other particles, which makes the problem that complicated that only a system as small as two particles can be solved exactly. But, already a single molybdenum atom for example contains 42 electrons and protons, and we strive to gain insights on the material containing not only one but a multitude of these and further atoms. Thus, in order to investigate the electronic and optical properties of solid state materials, one is interested in a precise and versatile theoretical model that is as simple as possible but as complex as necessary in order to capture the main physical effects. Our approach to the systems complexity is twofold.

First, we employ a density functional theory (DFT) approach, for which in its basic formalism only ground state properties are accessible. Here, the interactions of the particles are treated implicitly by hiding all interaction contributions in an artificial background landscape that each particle feels individually. In this way, the many-body problem is transformed into many coupled effective single-particle problems. We employ this approach in particular to gain insight on fundamental material properties such as the single-particle dispersion or the materials macroscopic dielectric properties.

Second, our approach is based on an evaluation of the temporal evolution of a microscopic density matrix on the footing of a model Hamiltonian employing a Heisenberg equation of motion (eom) approach. The microscopic density matrix yields insights into both the underlying fundamental processes taking place and macroscopic observables. This approach enables us to explicitly study the influence of chosen settings on the macroscopic observables by selectively switching interaction paths in the system on or off. In the following, the basic concepts of this combined approach are elucidated and notes on their application on the investigated materials are given. Here, we start with an introduction into the basic concepts of DFT (Ch. 2.1). In the following subsections, the matrix density approach is explained, where the fundamental model Hamiltonian is sketched (Ch. 2.2), before the deduction of the microscopic dynamics based on this model is described (Ch. 2.3). Finally, the connection between the microscopic density matrix and the macroscopically observable optical response is outlined.

Further analysis and developments of theoretical concepts necessary for the adaptation to specific experimental settings are also contained in the following chapters.

2.1 Density Functional Theory

As stated above, the analytically oriented approach based on a model Hamiltonian requires some input information on material parameters, including for example the electronic band structure or the dielectric properties. One way of getting insights into these and many other basic material properties is given by the so-called density function theory (DFT). DFT is a so-called *ab initio* approach meaning that in principal no input parameters are required, but calculations can be executed from scratch – at least in theory, in practice it is common to employ, for example, information on the lattice structure from experiments.

While several approaches on dealing with the many-body Schrödinger equation have been made earlier, the cornerstone for modern DFT was laid by Hohenberg, Kohn and Sham in the 1970s by developing its basic theorems [36, 37]. Here, the fundamental idea consists of reducing the complexity of the problem by transforming the many-particle problem into an effective single-particle problem and expressing the most fundamental formulas in terms of the density – depending on three spatial coordinates – instead of the wave functions – depending on all particles three spatial coordinates. This basic concept was developed further in the following years and has become a fundamental and versatile tool for material scientific, chemistry and physics problems, and it is still today subject to further development and change.

In the following, only the basic foundations of this concept are elucidated, for in-depth explanations the reader is referred to more detailed reviews as e.g. [38, 39]. Furthermore, as most calculations summarised in the context of this thesis were performed using the *Vienna ab-initio simulation package* (VASP) [40, 41, 42, 43] the focus is on underlying concepts implemented in this code.

2.1.1 Hohenberg-Kohn theorems

In general, the ground state of a system containing N interacting electrons in an external potential V is fully described by its wave function $\Psi(\vec{r_1}, \vec{r_2}, ..., \vec{r_N})$, where $\vec{r_i}$ are the spatial coordinates. The wave function, in real space representation, in turn is defined as solution of the many-body Schrödinger equation

$$\mathcal{H}\,\Psi(\vec{r_1}, \vec{r_2}, ..., \vec{r_N}) \,=\, E\,\Psi(\vec{r_1}, \vec{r_2}, ..., \vec{r_N}), \qquad (2.1)$$

where H denotes the system Hamiltonian and E the total energy of the system. In particular, the system Hamiltonian is given in terms of

$$\mathcal{H} = \mathcal{T} + \mathcal{V} + \mathcal{U} \tag{2.2}$$

$$= -\frac{\hbar^2}{2m_0} \sum_i^{N} \nabla_i^2 + \sum_i^{N} v(\vec{r}) + \frac{e^2}{4\pi\epsilon_0} \sum_{i<j}^{N} \frac{1}{|\vec{r}_i - \vec{r}_j|}. \tag{2.3}$$

Here, $\mathcal{T}$ describes the kinetic energy of the particles, $\mathcal{V}$ the external potential and $\mathcal{U}$ the Coulomb interaction between the particles. It is interesting to note that the wave function intrinsically depends on the spatial coordinates of all particles, as the description of a single particle in the system is by means of the Coulomb interaction coupled to all other particles, which makes the problem numerically demanding already for small systems. Instead of solving the problem for the wave function, Hohenberg and Kohn proved 1964 [36] in two theorems, that the ground state problem can be reformulated in dependence of the electron density $n(\vec{r})$; this way, the complexity of the problem is drastically reduced as the later only depends on the three spatial coordinates instead of N times three as the wave function:

> **First theorem:** $v(\vec{r})$, *being an external potential, is a unique functional of* $n(\vec{r})$ *apart from a trivial additive constant.*

As a consequence, the expectation value of the full many-body Hamiltonian can be interpreted as a functional of the density, $E = \langle\Psi|\mathcal{H}|\Psi\rangle = \langle\Psi|\mathcal{T} + \mathcal{U} + \mathcal{V}|\Psi\rangle = E[n]$.

> **Second theorem:** *Under the constraint of* $N[n] = \int \mathrm{d}^3r\, n(\vec{r}) = N$ *for a system of N particles, the correct density* n_0 *minimises the energy yielding the systems ground state* $E[n_0] = E_0$

According to the second theorem, the task is to minimise the functional $E[n] = \langle\Psi|\mathcal{H}|\Psi\rangle$. However, while the external potential is easily rewritten in this way, as

$$V[n(\vec{r})] = \int \mathrm{d}^3r\, \mathcal{V}(\vec{r})\, n(\vec{r}), \tag{2.4}$$

this problem is non-trivial neither with respect to the kinetic energy nor the Coulomb interaction. Nevertheless, with their fundamental work on proving the existence of a general functional, Hohenberg and Kohn laid the foundation for further development of DFT.

2.1.2 Kohn-Sham equation

Even though it is practically impossible to reformulate the full Hamiltonian as an exact functional of the density, we can approach this quest on a formal level by separating the

parts we know how to rewrite from those which we do not. Let us start with the kinetic part of the Hamiltonian. This part can be separated into a single-particle (T_s) and a correlation (T_c) term

$$T[n(\vec{r})] = -\frac{\hbar^2}{2m_0} \sum_i^N \int \mathrm{d}^3r \, \phi_i^*(\vec{r}) \nabla^2 \phi_i(\vec{r}) + T_c[n], \qquad (2.5)$$

with the single-particle wave functions $\phi_i(\vec{r})$. In a similar way, the Coulomb interaction can be split into a Hartree (U_H) and an exchange (U_x) term

$$U[n(\vec{r})] = \frac{e^2}{8\pi\epsilon_0} \int \int \mathrm{d}^3r \, \mathrm{d}^3r' \, \frac{n(\vec{r}) \, n(\vec{r'})}{|\vec{r} - \vec{r'}|} + U_x[n]. \qquad (2.6)$$

This way, the terms that can be expressed explicitly are separated from the unknown remainder which in summary is called exchange correlation energy $E_{xc} = T_c + U_x$. Thus, the expression for the systems total energy

$$E[n] = T_S[n] + U_H[n] + V[n] + E_{xc}[n] \qquad (2.7)$$

remains formally exact.

Minimising the energy with respect to the density yields the condition

$$0 = \frac{\delta E[n]}{\delta n(\vec{r})} = \frac{\delta T_S[n]}{\delta n(\vec{r})} + \frac{\delta U_H[n]}{\delta n(\vec{r})} + \frac{\delta V[n]}{\delta n(\vec{r})} + \frac{\delta E_{xc}[n]}{\delta n(\vec{r})}$$

$$= \frac{\delta T_S[n]}{\delta n(\vec{r})} + v(\vec{r}) + u_H(\vec{r}) + v_{xc}(\vec{r}). \qquad (2.8)$$

If we compare this condition to the minimisation condition for a system of non-interacting particles in an external potential V_S,

$$0 = \frac{\delta E[n]}{\delta n(\vec{r})} = \frac{\delta T_S[n]}{\delta n(\vec{r})} + v_S(\vec{r}), \qquad (2.9)$$

it becomes evident that the above expressions are equivalent if we interpret $v_{eff} = v(\vec{r}) + u_H(\vec{r}) + v_{xc}(\vec{r})$ as an effective potential. Consequently, by introducing Lagrange multipliers ϵ_i to solve the minimisation problem, the full many-body problem is reformulated in N single-particle problems. Thus, as illustrated in Fig. 2.1, one has to solve N single-particle Schrödinger equations where all interactions are hidden in an effective potential v_{eff},

$$\left(-\frac{\hbar^2}{2m_0} \nabla^2 + v_{eff} \right) \psi_i(\vec{r}) = \epsilon_i \psi_i(\vec{r}). \qquad (2.10)$$

external potential   effective potential
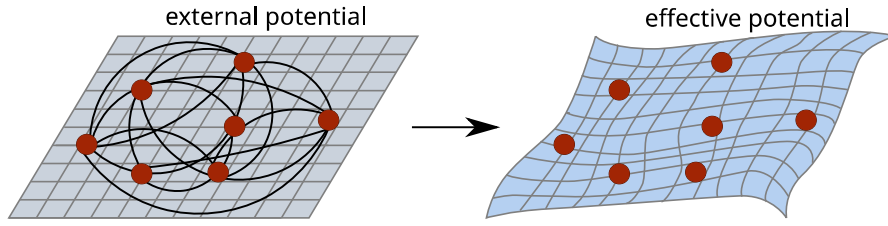
Abbildung 2.1: Illustration of the basic idea of DFT: Instead of calculating the full interactions between particles, one minimises the energy for N particles in an approximated effective potential to find the ground state.

This equation in turn yields the electron density

$$n(\vec{r}) \,=\, \sum_i f_i \,|\psi_i(\vec{r})|^2\,, \tag{2.11}$$

with the wave functions ψ_i and the occupation of the ith orbital f_i. This combination of equations is known as Kohn-Sham equations and its solutions ϵ_i are interpreted as approximation of the systems energy levels [37].

As the Kohn-Sham equations are interdependent, an iterative scheme is applied to solve them, starting from an initial approximation for $\psi_i(\vec{r})$ that is employed to calculate the electron density and the Hamiltonian. Subsequently solving the Kohn-Sham equations yields new wave functions as input for the Hamiltonian. This scheme is aborted after a pre-set condition for the energy convergence is met.

Computational details

While the Kohn-Sham equations are formally exact, approximations are inevitable as we simply concealed all unknown parts on a formal level. As a consequence, we can not give an exact expression for the effective exchange energy term. A lot of effort was put in searching appropriate formulations that approximate this term and a great variety of functionals were and are still proposed. Generally, the functionals are classified according to their degree of complexity and the interplay of physical constraints and experimental findings they are based on. The lowest order approximation is called *local density approach* (LDA) and sets the functional to the known expression of a constant electron gas where the respective local density is inserted. The next degree of approximation is called *general gradient approximations* in which additionally to the local density also its gradient is taken into account. Here, numerous parametrisations exist. In all publications that are included in this thesis, the parametrisation of Perdew-Burke-Erzerhof as implemented in VASP was applied [44].

Furthermore, different correction terms to include further effects were developed. In our calculations, we include correction terms for the van-der-Waals interactions as proposed

by Grimme *et al.* [45]. It was seen that the lattice constants are underestimated without this correction terms. As the Kohn-Sham energy dispersion of the TMDC monolayer structures sensitively depends on the exact lattice constants, these corrections were seen inevitable for a consistent calculation.

Furthermore, in VASP periodic boundary conditions are applied. This is advantageous for modelling bulk solid-state systems due to their – approximately infinite – translational invariance, but causes difficulties in systems with a finite extension in one or more directions. We treat the finite extension of monolayer materials by an artificial expansion of the real space unit cell, where we include a large area of vacuum to decouple the periodically repeated layers. An analysis of the lattice- and band structure-dependence revealed that an interlayer distances in the order of $15 - 20\,\text{Å}$ is sufficient for the materials investigated.

For more explicit details on the exact parameters used in the different calculation we refer to the respective publications.

2.2 Model Hamiltonian

In the interplay with the DFT calculations, we employ a many-particle density matrix approach based on a model Hamiltonian. In the remainder of this chapter, the model Hamiltonian and its connection to the DFT calculations is explained. First, the non-interacting part of the Hamiltonian is analysed, where it is explained in which way results from DFT calculations can be exploited to derive a model description of the ground state energetic structure. Thereafter, the different contributions arising from intrinsic interactions within the material and from interactions with external sources are reconsidered. The full model Hamiltonian is obtained as a sum of these contributions. In our studies not all contributions are included equally, as will be noted in the following, where appropriate.

2.2.1 Single-particle dispersion – Massive Dirac Fermion model

Our model of the materials energy dispersion is in several ways connected to findings obtained by DFT. Therefore, we start with a description and analysis of DFT calculations, before its implications on the model are worked out. The DFT results are introduced exemplary for MoS_2 and notes regarding deviations in the other materials are given where appropriate.

In the previous chapter, we introduced DFT as an efficient method to derive a materials ground state. Even though this method is treated as an *ab initio*-method, it is common to exploit experimental knowledge of the material lattice structure. As already expressed in the introduction, we only discuss the trigonal prismatic phase of the materials in our studies, where the atoms are covalently bound in the layer via s-p hybridisation.

As the sketch of the lattice structure in Fig. 1.1 shows, the atoms form a hexagonal

structure from the top view, where neighbouring corners are occupied by different species, and a three-layered structure from the side view, where two layers of chalcogen atoms (here: S/Se/Te) surround a layer of metal atoms (here: Mo/W). Based on this lattice structure, we compute the material band structure.

In the left panel of Fig. 2.2, the band structure along a straight path through the BZ is shown exemplary for MoS_2. Here, the most important features of the band structure are captured: In the monolayer, we see for all materials investigated direct band gaps at the K and K' points, which are located at the BZ corners.[1] The energetic structure at these two valley is equivalent but due to the lack of an inversion center, they are not equal but connected via time-reversal symmetry. This implies that the bands are of opposite spin character at the different valleys. Thus, spin and valley index are coupled. While the smallest gap is spin-allowed in molybdenum-based materials, it is spin forbidden in tungsten-based materials, which has noticeable consequences for the physical properties and in particular for dynamical properties in the different materials. Furthermore, spin-orbit coupling results in a splitting of both valence and conduction band. The splitting of the conduction band is relatively small, for molybdenum-based materials it is only in the range of few meV. But the valence band splitting is considerably larger, for molybdenum-based the splitting at the K/K' valley reaches about $150 - 200\,\mathrm{meV}$, the larger mass of tungsten causes an even larger splitting in the order of $400\,\mathrm{meV}$ in those materials. As is seen in Fig. 2.2, the conduction band has another local minimum along the $|K\Gamma|$-path, which is often referred to as Λ/Σ valley, where the valleys differ in the ordering of the spin.[2] Due to the hexagonal symmetry, each main valley (K-point) is surrounded by three side valleys. The energetic offset between side and main valley is often discussed, as it is not directly measurable for the ground state and theoretical predictions from DFT calculations are very sensitive e.g. on the exact choice of the lattice constant.

The opto-electronic properties in the regimes of interest in this thesis are dominated by the contributions of the highest valence and lowest conduction band. Furthermore, while the full DFT band structure is included when studying the relaxation dynamics through the whole BZ (Ref. [IV] and Ch. 5), most our studies focus on an analysis of processes that take place at the different band structure extrema. In the following, we therefore limit ourselves to a closer look at these specific bands and regions.

Let us start with the main valleys. DFT studies show that the bands at these valleys are mainly composed of the different transition metals d-orbitals. In Fig. 2.3, the contributions of the different orbitals is presented, where the overlap between wave function and the specific Mo d-orbitals is shown. Based on these observations, at the K/K' point and in their proximity the valence band wave function can be approximated as

---

[1] Concerning the material WSe_2, it is frequently discussed, whether the material exhibits a direct or indirect band gap [21, 20]. In our calculations, we only found an indirect band gap if the lattice constant was predicted to large compared to experimental values.

[2] There is no unified nomenclature for these valleys, one also finds e.g. the labels P or Q.
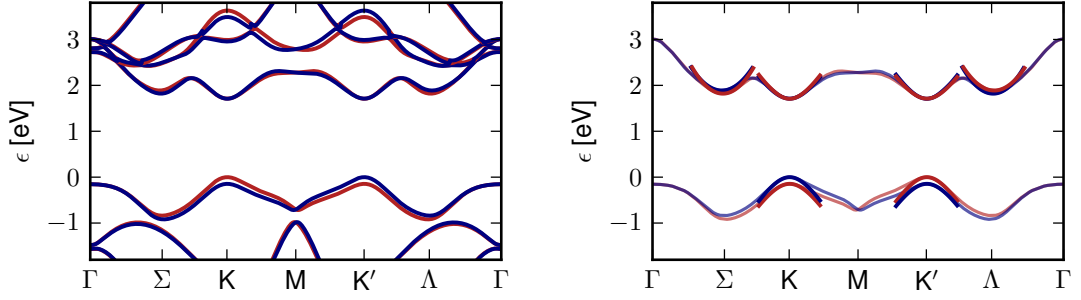
Abbildung 2.2: Left: Kohn-Sham eigenvalues for monolayer MoS₂ along a straight path through the BZ. Right: Valence and conduction band for monolayer MoS₂. The sorted DFT bands are shown together with the analytic fits of the band structure at the K/K'- and Σ/Λ-point. The different spin characters are reflected by color.
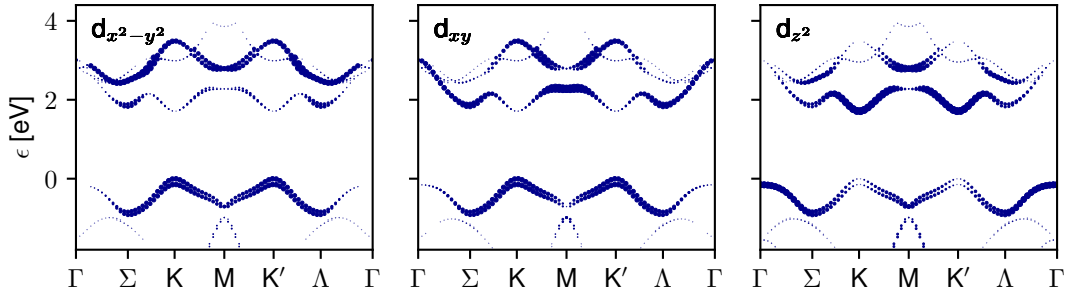
Abbildung 2.3: Atomic orbital weights of the energy band wave functions exemplary shown for the most relevant molybdenum d-orbitals in MoS₂. The marker size resembles the overlap of wave function and orbital.

$|\Phi_{vb}^\tau\rangle = \frac{1}{\sqrt{2}}\left(|d_{x^2-y^2}\rangle + i\tau|d_{xy}\rangle\right)$, with the valley index τ, and the conduction band wave function as $|\Phi_{cb}\rangle = |d_{z^2}\rangle$. These approximated wave functions at the K-point are eigenfunctions of the rotation operator C_3 with $C_3^n\Phi_{l,m} = \exp\left(i\tau m\frac{2\pi n}{3}\right)\Phi_{l,m}$ – with $m_v - m_c = \mp 2$, where the exact values m_v, m_c depend on the rotational center but their difference remains invariant. As the action of this symmetry operation on the momentum operators $\hat{p}_\pm$ is $C_3\hat{p}_\pm C_3^\dagger = \exp\left(\mp i\frac{2\pi}{3}\right)\hat{p}_\pm$ with momentum operators $\hat{p}_\pm$, the resulting Hamilton operator in proximity to the K/K'-point in first order $\mathbf{k}\cdot\mathbf{p}$ theory including spin-orbit coupling effects reads [46, 47, 48]

$$\hat{H}_{0,s\tau k}^{\mathbf{k}\cdot\mathbf{p}} = \gamma\left(\tau k_x\hat{\sigma}_x + k_y\hat{\sigma}_y\right) + \frac{\Delta}{2}\hat{\sigma}_z - \lambda\tau\frac{\hat{\sigma}_z - 1}{2}\hat{s}_z. \tag{2.12}$$

Here, τ is the valley index, $\hat{\sigma}_i$ are the Pauli matrices and $\hat{s}_z$ is the Pauli matrix for the

spin. Δ denotes the energy gap and 2λ the spin-orbit coupling-induced valence band splitting. Furthermore, in analogy to the description of gapped graphene, the parameter γ can be identified as $\gamma = \hbar v_F$ with the Fermi velocity v_F, and the model is called massive Dirac fermion (MDF) model. Summarizing the gap and the spin-splitting in a spin- and valley-dependent band gap $\Delta_{s\tau}$, diagonalisation yields eigenstates with the relativistic dispersion $\epsilon_{s\tau k}$ and the eigenfunctions $\psi_{\mathbf{k}}^{c/v}$

$$\epsilon_{s\tau k} = \sqrt{\left(\frac{\Delta_{s\tau}}{2}\right)^2 + (\hbar v_F k)^2} \tag{2.13}$$

$$\psi_{\mathbf{k}}^c = \begin{pmatrix} u_{\mathbf{k}} \\ v_{\mathbf{k}} \exp(-i\tau\theta_k) \end{pmatrix} \qquad \psi_{\mathbf{k}}^v = \begin{pmatrix} v_{\mathbf{k}} \exp(i\tau\theta_k) \\ -u_{\mathbf{k}} \end{pmatrix}, \tag{2.14}$$

with $u_{\mathbf{k}} = \frac{\epsilon_{s\tau k} + \Delta_{s\tau k}/2}{2\epsilon_{s\tau k}}$ and $v_{\mathbf{k}} = \frac{\epsilon_{s\tau k} - \Delta_{s\tau k}/2}{2\epsilon_{s\tau k}}$. This dispersion may be generalized to multilayer structures by additionally including a layer-dependent Fermi energy $E_{F,n}$ in order to display the correct energy alignment. In the remainder, the bands at K/K' are referred to as A bands if $s\tau = +1$ and B band, otherwise.

Furthermore, we estimate the influence of the side minima on different physical properties of the materials. Here, we use an effective mass approximation to describe the dispersion.

Finally, we again combine the model and the DFT calculations. In order to gain the material specific parameters such as non-interacting band gap, Fermi velocity and effective mass, we fit the model function for the dispersion to the DFT band structure, where we assumed a rotational symmetry of the dispersion in proximity to the points of interest. The DFT band structure and the resulting model dispersion are illustrated in the right panel of Fig. 2.2. It becomes evident that the approximation is valid in the close proximity of the extrema but differs further away.

2.2.2 Interactions

So far, we examined how to combine DFT results with group theory considerations and physical concepts to derive a model for the single-particle energies. But the charge carriers do not move independently through the materials background potential but are subject to interactions with one another, with quasiparticles like phonons and are influenced by external settings. In the following, we strive for formulations to include these interactions into our model Hamiltonian.

Coulomb interaction

As introduced previously, Coulomb interaction plays a crucial role in monolayer materials. The monolayer structure requires that two particular aspects need to be taken care of in a model description. Namely, the effect of the material finite thickness and the influence of the dielectric environment. But, let us start with the most general form of
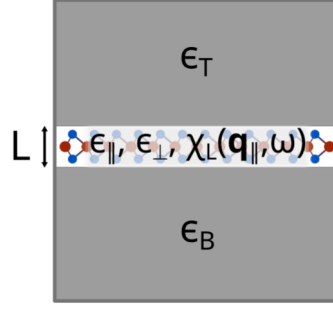
Abbildung 2.4: Sketch of the modelled sample geometry: TMDC monolayer embedded in a dielectric environment with dielectric constants ϵ_T (top) and ϵ_B (bottom).

the two-particle Coulomb interaction, which reads

$$\hat{H}_C = \frac{1}{2} \sum_{\mathbf{k},\mathbf{k}',\mathbf{q}} : \Psi^\dagger_{\mathbf{k}-\mathbf{q}} \Psi_{\mathbf{k}} V_{\mathbf{q}} \Psi^\dagger_{\mathbf{k}'+\mathbf{q}} \Psi'_{\mathbf{k}} :, \tag{2.15}$$

where $\Psi_{\mathbf{k}}$ denote pseudospinors and $V_{\mathbf{q}}$ the Coulomb potential. Expanding the pseudo-spinors in terms of the eigenstates of H_0 and explicitly reducing the expression to the in-plane crystal momenta $\hbar \mathbf{k}_\parallel$, the Coulomb interaction is represented by

$$\hat{H}_C = \frac{1}{2} \sum_{\alpha\alpha'\beta\beta'} \sum_{\mathbf{k}_\parallel \mathbf{k}'_\parallel \mathbf{q}_\parallel \neq 0} V^{\alpha\beta\beta'\alpha'}_{\mathbf{q}_\parallel;\mathbf{k}'_\parallel;\mathbf{k}_\parallel} a^\dagger_{\alpha\mathbf{k}_\parallel-\mathbf{q}_\parallel} a^\dagger_{\beta\mathbf{k}'_\parallel+\mathbf{q}_\parallel} a_{\beta'\mathbf{k}'_\parallel} a_{\alpha\mathbf{k}_\parallel} \tag{2.16}$$

with the Coulomb-matrix element $V^{\alpha\beta\beta'\alpha'}_{\mathbf{q}_\parallel;\mathbf{k}'_\parallel;\mathbf{k}_\parallel} = V_{\mathbf{q}_\parallel} \langle \alpha\mathbf{k}_\parallel - \mathbf{q}_\parallel | \alpha'\mathbf{k}_\parallel \rangle \langle \beta\mathbf{k}'_\parallel + \mathbf{q}_\parallel | \beta'\mathbf{k}'_\parallel \rangle$ and $\alpha^{(\prime)}, \beta^{(\prime)} \in \{c, v\}$. In order to include finite thickness as well as groundstate and environmental screening effects, a closer look at the potential $V_{\mathbf{q}_\parallel}$ is required.

Dielectric environment and stacking

In contrast to a bulk material, where the interaction between charges is screened by the material itself and the induced polarisation, in the monolayer the interaction becomes less weakened by the material itself and instead the interchangeable dielectric environment becomes more important. To obtain an expression for the Coulomb potential for a TMDC layer embedded in an environment characterized by the dielectric constants ϵ_T (top) and ϵ_B (bottom), as depicted in Fig. 2.4, we strive for a solution of the first Maxwell's equation $\nabla \cdot \mathbf{D} = 4\pi \rho_{ext}$ for this anisotropic system. To account for the anisotropy, following the derivation in Ref. [49], we explicitly split the dielectric displacement field into contributions perpendicular and parallel to the field:

$$\mathbf{D} = \epsilon_\parallel \mathbf{E}_\parallel + \epsilon_\perp E_z \hat{e}_z + 4\pi \mathbf{P}. \tag{2.17}$$

While $\mathbf{P}$ contains the non-local, time- and frequency-dependent resonant contributions, the non-resonant contributions are contained in the explicitly z-dependent background dielectric constants. Assuming a lateral homogeneity as well as a constant dielectric value within the layer, we approximate the dielectric structure as

$$\epsilon_\parallel(z) = \begin{cases} \epsilon_\parallel^T & z < -L/2, \\ \epsilon_\parallel & |z| < L/2, \\ \epsilon_\parallel^B & L/2 < z \end{cases} \qquad \epsilon_\perp(z) = \begin{cases} \epsilon_\perp^T & z < -L/2, \\ \epsilon_\perp & |z| < L/2, \\ \epsilon_\perp^B & L/2 < z. \end{cases} \qquad (2.18)$$

and assume the thickness of the layer, L, to equal the interlayer distance in a corresponding bulk structure. In the following, we express the electric field in terms of vector and scalar potentials, $\mathbf{A}$ and ϕ and apply the generalized Coulomb gauge $\epsilon_\parallel \nabla_\parallel \cdot \mathbf{A} + \epsilon_\perp \partial_z A_z = 0$. Exploiting the in-plane homogeneity, which allows for a Fourier transformation according to the in-plane components and consequently to express the potential in terms of the in-plane $\mathbf{q}_\parallel$-vector, the Poisson equation determining the anisotropic scalar potential reads

$$\left(-\epsilon_\perp \partial_z^2 + \epsilon_\parallel \mathbf{q}_\parallel^2\right)\phi(\mathbf{q}_\parallel, z, \omega) = 4\pi\left(\rho_{ext}(\mathbf{q}, z, \omega) - i\mathbf{q}\cdot\mathbf{P}_\parallel^L(\mathbf{q}, z, \omega) - \partial_z P_z\right). \qquad (2.19)$$

Let us first analyse the non-resonant part of this equation and neglect the resonant contributions ($\mathbf{P}_\parallel^L(\mathbf{q}, z, \omega)$ and P_z). For a charge localized at the center of the layer $\rho_{ext} = \delta(z)$, solving Eq. 2.19 under the constraint of the boundary conditions at $z = \pm L/2$ yields for the potential within the layer

$$\begin{aligned} \phi_\mathbf{q}(z, z') = \frac{2\pi}{\kappa q}\Big[&e^{-\tilde{q}|z-z'|} \\ &+ c^{+-}e^{-\tilde{q}(L+z+z')} + c^{-+}e^{-\tilde{q}(L-z-z')} \\ &+ c^{--}\left(e^{-\tilde{q}(2L-z+z')} + e^{-\tilde{q}(2L+z-z')}\right)\Big] \end{aligned} \qquad (2.20)$$

with $\tilde{q} = \sqrt{\frac{\epsilon_\parallel}{\epsilon_\perp}}q$,

$$c^{\eta\eta'} = \frac{(\kappa + \eta\kappa_T)(\kappa + \eta'\kappa_B)}{(\kappa + \kappa_T)(\kappa + \kappa_B) - (\kappa - \kappa_T)(\kappa - \kappa_B)e^{-2\tilde{q}L}} \qquad (2.21)$$

and $\kappa_i = \sqrt{\epsilon_{\parallel,i}\epsilon_{\perp,i}}$. While the first line in Eq. 2.20 can be understood as direct interaction between charges located at z and z' and is referred to as $\Phi_\mathbf{q}^{2D}$ in the following, the next lines describe interactions via image charges, $\Delta\Phi_\mathbf{q}$. This lengthy expression is often simplified in the limiting case of small momenta or in the two-dimensional case, $q\,d \to 0$, to the so-called Rytova-Keldysh potential $V_q^{RK} = \frac{2\pi}{q((\kappa_T+\kappa_B)/2+d(2\kappa^2-\kappa_T^2-\kappa_B^2)/4\epsilon_\perp)}$ [50, 51, 52]. Similar, but in details differing, approaches are derived in [35, 52].

The material parameters for the dielectric constants $\epsilon_\parallel$ and $\epsilon_\perp$ were taken from DFT

calculations. In DFT, the determination of the dielectric properties includes averaging over the whole unit cell. In numerical codes that are based on the assumption of periodic boundary conditions, where monolayer properties are calculated by artificially including large areas of vacuum, this implies an averaging over those. Consequently, the dielectric properties of monolayer structures are not directly accessible by these DFT codes. Nevertheless, they can be inferred from calculations of the corresponding bulk structures. While $\epsilon_\perp$ can be set equal to the bulk value, a comparison of the two-dimensional and three-dimensional solution of the Poisson equation suggests the identification

$$\epsilon_\| = \epsilon_\|^B - \lim_{\mathbf{q}_\| \to 0} 4\pi e^2 \chi_L(\mathbf{q}_\|, \omega)/d, \tag{2.22}$$

with the linear susceptibility $\chi_L(\mathbf{q}_\|, \omega)$ [49].

In the next step, the influence of resonant contributions is to be considered. As the studies summarised in this thesis are only concerned with in-plane interactions, we neglect the out-of-plane contributions P_z, which are studied in detail for example in [53]. The parallel resonant contributions can be treated approximately in linear response theory, thus, again assuming a charge localized at the layers center, we rewrite it as

$$\mathbf{P}_\|^L = -ie^2 \mathbf{q}_\| \chi_L(\mathbf{q}_\|, \omega) \phi(\mathbf{q}_\|, z_0, \omega) \delta(z - z_0) \tag{2.23}$$

with the longitudinal susceptibility $\chi_L(\mathbf{q}_\|, \omega)$. This approximation is easily generalized to a multilayer structure by considering charges at the individual layer centres and summing on the right hand side over the layer-dependent susceptibility and potential. Solving equation 2.19 in this linear approximation yields for the non-locally screened Coulomb potential in the layer

$$\phi_0(\mathbf{q}_\|, z, z', \omega) = \frac{\phi_0(\mathbf{q}_\|, z, z')}{1 + e^2 \mathbf{q}_\|^2 \chi_L(\mathbf{q}_\|, \omega) \phi_0(\mathbf{q}_\|, z, z')}. \tag{2.24}$$

Thus, the resonant contributions induced by point charges result in a screening of the Coulomb potential with $\epsilon_{res}(\mathbf{q}_\|, z, z', \omega) = 1 + e^2 \mathbf{q}_\|^2 \chi_L(\mathbf{q}_\|, \omega) \phi_0(\mathbf{q}_\|, z, z')$. In our calculations, we include the ground state polarisation function $\Pi(\mathbf{q}_\|, \omega) = e^2 \mathbf{q}_\|^2 \chi_L(\mathbf{q}_\|, \omega)$ in the long wavelength and static limit. It was derived in [54] that in this limit in random phase approximation, the ground state polarisation function is calculated as $\Pi(\mathbf{q}_\|, 0) = -\frac{1}{6\pi} \frac{q^2}{\Delta_{s\tau}}$ for the different spin and valley combinations. The full systems polarisation is gained by summing over all spin- and valley-indices.

Form factor

Besides the intrinsic and environmental screening effects, it is necessary to include effects due to the material finite thickness. The intrinsic three-layer structure and the finite extension of the carrier wave functions perpendicular to the plane causes that neither

the exact two-dimensional nor the exact three-dimensional Coulomb potential yields a proper description of the potential. To model this anisotropic structure, we start out with the real-space representation of the Coulomb Hamiltonian in second quantization

$$\hat{H}_C = \frac{1}{2} \int_{\mathcal{V}} \int_{\mathcal{V}} \mathrm{d}^3 r \, \mathrm{d}^3 r' \hat{\Psi}^\dagger(\mathbf{r}) \hat{\Psi}^\dagger(\mathbf{r}') \, V(\mathbf{r}, \mathbf{r}') \, \hat{\Psi}(\mathbf{r}') \hat{\Psi}(\mathbf{r}), \tag{2.25}$$

with the normalization volume $\mathcal{V}$. To achieve a description of this quasi-two-dimensional structure, we employ the in-plane periodicity and expand the field operators in the resulting Bloch states

$$\hat{\Psi}(\mathbf{r}) = \frac{1}{\mathcal{A}} \sum_{\alpha, \mathbf{k}_\parallel} \mathrm{e}^{i \mathbf{k}_\parallel \cdot \mathbf{r}} u_{\alpha, \mathbf{k}_\parallel} c_{\alpha, \mathbf{k}_\parallel} \tag{2.26}$$

that depend on the in-plane crystal momenta $\mathbf{k}_\parallel$, but 3D spatial coordinates. Here, $\mathcal{A}$ is the normalization area, α the band index and $u_{\alpha, \mathbf{k}_\parallel}$ a lattice periodic function. Fourier transforming the Coulomb potential according to the in-plane components, taking advantage of the periodicity again by rewriting the integration into a sum of integrals over a unit cell only, $\int \mathrm{d}^3 r \rightarrow \sum_i \int_{uc} \mathrm{d}^3 r$, and making use of the completeness relation $\frac{1}{N} \sum_i \mathrm{e}^{i(\mathbf{k}_\parallel - \mathbf{k}_\parallel')R_i} = \delta_{\mathbf{k}_\parallel, \mathbf{k}_\parallel'}$, the Coulomb potential can be rewritten as

$$\hat{H}_C = \frac{1}{2} \sum_{\alpha, \alpha', \beta, \beta'} \sum_{\mathbf{k}_\parallel, \mathbf{k}_\parallel', \mathbf{q}_\parallel} V^{\alpha, \beta, \beta', \alpha'} \, \hat{c}^\dagger_{\alpha, \mathbf{k}_\parallel - \mathbf{q}_\parallel} \hat{c}^\dagger_{\beta, \mathbf{k}_\parallel' + \mathbf{q}_\parallel} \hat{c}_{\beta', \mathbf{k}_\parallel'} \hat{c}_{\alpha', \mathbf{k}_\parallel} \tag{2.27}$$

with the matrix elements

$$V^{\alpha, \beta, \beta', \alpha'} = \int_{uc} \int_{uc} \mathrm{d}^3 r \, \mathrm{d}^3 r' \, u^*_{\alpha \mathbf{k}_\parallel - \mathbf{q}_\parallel}(\mathbf{r}) \, u^*_{\beta \mathbf{k}_\parallel' + \mathbf{q}_\parallel}(\mathbf{r}') \, V_{\mathbf{q}_\parallel}(z, z') \, u_{\beta' \mathbf{k}_\parallel'}(\mathbf{r}') \, u_{\alpha' \mathbf{k}_\parallel}(\mathbf{r}). \tag{2.28}$$

Inserting for the Coulomb potential the expression we derived above for a slab geometry, Eq. 2.20, we can separate the matrix elements as a product of the Coulomb potential and a form factor term

$$V^{\alpha, \beta, \beta', \alpha'} = V_{\mathbf{q}_\parallel}^{2D} \, F_{\mathbf{k}_\parallel, \mathbf{k}_\parallel'}^{\alpha, \beta, \beta', \alpha'}(\mathbf{q}_\parallel) - \Delta V_{\mathbf{q}_\parallel}^{2D} \, \Delta F_{\mathbf{k}_\parallel, \mathbf{k}_\parallel'}^{\alpha, \beta, \beta', \alpha'}(\mathbf{q}_\parallel). \tag{2.29}$$

Here, we introduced the form factor

$$F_{\mathbf{k}_\parallel, \mathbf{k}_\parallel'}^{\alpha, \beta, \beta', \alpha'}(\mathbf{q}_\parallel) = \int_{uc} \int_{uc} \mathrm{d}^3 r \, \mathrm{d}^3 r' \, u^*_{\alpha \mathbf{k}_\parallel - \mathbf{q}_\parallel}(\mathbf{r}) u^*_{\beta \mathbf{k}_\parallel' + \mathbf{q}_\parallel}(\mathbf{r}') \, \mathrm{e}^{-\tilde{q}|z - z'|} \, u_{\beta' \mathbf{k}_\parallel'}(\mathbf{r}') u_{\alpha' \mathbf{k}_\parallel}(\mathbf{r}).$$
$$\tag{2.30}$$

and its correlated part

$$\Delta F^{\alpha,\beta,\beta',\alpha'}_{\mathbf{k}_\parallel,\mathbf{k}'_\parallel}(\mathbf{q}_\parallel) = F^{\alpha,\beta,\beta',\alpha'}_{\mathbf{k}_\parallel,\mathbf{k}'_\parallel}(\mathbf{q}_\parallel) - f^{\alpha,\alpha'}_{\mathbf{k}_\parallel}(\mathbf{q}_\parallel)\, f^{\beta,\beta'}_{\mathbf{k}'_\parallel}(\mathbf{q}_\parallel) \tag{2.31}$$

$$f^{\alpha,\alpha'}_{\mathbf{k}_\parallel}(\mathbf{q}_\parallel) = \int_{uc} \mathrm{d}^3 r\, u^*_{\alpha\mathbf{k}_\parallel - \mathbf{q}_\parallel}(\mathbf{r})\, \mathrm{e}^{\tilde{q}z}\, u_{\alpha'\mathbf{k}_\parallel}(\mathbf{r}). \tag{2.32}$$

This shows that the Coulomb interaction in the quasi-two-dimensional structure can be described by a simple modification of the exact two-dimensional Coulomb interaction. Considering the limiting case of an exact two-dimensional material, the orthonormality of the wave functions and the vanishing argument in the exponential terms result in a recovery of the exact two-dimensional Coulomb potential. Further analysis of the expression shows that for no momentum interchange, $\mathbf{q}_\parallel = 0$, the form factor and correlated parts are $F^{\alpha,\beta,\beta',\alpha'}_{\mathbf{k}_\parallel,\mathbf{k}'_\parallel}(\mathbf{q}_\parallel = 0) = f^{\alpha,\alpha'}_{\mathbf{k}_\parallel}(\mathbf{q}_\parallel = 0) = f^{\beta,\beta'}_{\mathbf{k}_\parallel}(\mathbf{q}_\parallel = 0) = \delta_{\alpha,\alpha'}\delta_{\beta,\beta'}$. In the opposite limit of large scattering vectors, the form factor approaches 0.

The exact modelling of the interaction and of the form factor in particular formed an essential part of the studies that underlie this thesis. Therefore, a more extensive elaboration of these topics is contained in Ch. 3.

Light-matter interaction

The interaction between a material and an electromagnetic field can be described on the semiclassical level within the concept of minimal coupling by replacing the momentum operator $\mathbf{p} = \hbar\mathbf{k}$ by the canonical momentum $\mathbf{p} \to \mathbf{p} - \frac{e}{c}\mathbf{A}(t)$ with $\mathbf{A}(t)$ being the time-dependent classical vector potential. Employing this procedure for the above introduced MDF Hamiltonian, the resulting light-matter interaction Hamiltonian reads

$$\hat{H}_I = -\frac{e}{c}\sum_{\mathbf{k}} v_{F,s\tau}\hat{\Psi}^\dagger_{\mathbf{k}}(\tau A_x\hat{\sigma}_x + A_y\hat{\sigma}_y)\hat{\Psi}_{\mathbf{k}}. \tag{2.33}$$

Expanding the pseudospinors $\hat{\Psi}_{\mathbf{k}}$ in terms of the eigenfunctions of the single-particle Hamiltonian $\hat{H}_0$, $\hat{\Psi}_{\mathbf{k}_\parallel} = \sum_\alpha |\alpha\mathbf{k}_\parallel\rangle\hat{a}_{\alpha\mathbf{k}_\parallel}$, the Hamiltonian reads

$$\hat{H}_I = -\frac{e}{c}\sum_{\alpha,\beta,\mathbf{k}_\parallel} v_{F,s\tau}\langle\alpha\mathbf{k}_\parallel|\tau\mathbf{A}_x\hat{\sigma}_x + \mathbf{A}_y\hat{\sigma}_y|\beta\mathbf{k}_\parallel\rangle\hat{a}^\dagger_{\alpha\mathbf{k}_\parallel}\hat{a}_{\beta\mathbf{k}_\parallel} \tag{2.34}$$

$$= -\frac{e}{c}\sum_{\alpha,\beta,\mathbf{k}_\parallel} v_{F,s\tau}\langle\alpha\mathbf{k}_\parallel|\mathbf{A}(t)\cdot\hat{\sigma}_\tau|\beta\mathbf{k}_\parallel\rangle\hat{a}^\dagger_{\alpha\mathbf{k}_\parallel}\hat{a}_{\beta\mathbf{k}_\parallel} \tag{2.35}$$

with $\hat{\sigma}_\tau = (\tau\hat{\sigma}_x, \hat{\sigma}_y)$. Here, the so-called circular dichroism, which states that the different K/K'-valleys can be addressed by light with different circular polarisation, is implied.

A comparison to the more general formulation of the light-matter interaction – in Coulomb gauge ($\nabla \cdot \mathbf{A} = 0$) and neglecting contributions quadratic in $\mathbf{A}$ –, which is used in

publication [IV],

$$\hat{H}_I = -\frac{e}{m_0 c} \sum_{\alpha \neq \beta \mathbf{k}_\parallel} \mathbf{A}(t) \cdot \mathbf{p}_{\alpha\beta}\left(\mathbf{k}_\parallel\right) \hat{a}^\dagger_{\alpha \mathbf{k}_\parallel} \hat{a}_{\beta \mathbf{k}_\parallel}, \qquad (2.36)$$

with the momentum operator $\mathbf{p}_{\alpha\beta}\left(\mathbf{k}_\parallel\right)$, allows in the vicinity of the K/K'-point the identification

$$\mathbf{A} \cdot \mathbf{p}_{\alpha\beta}\left(\mathbf{k}_\parallel \approx K/K'\right) = m_0 v_F \left\langle \alpha \mathbf{k}_\parallel | \mathbf{A}(t) \cdot \hat{\sigma}_\tau | \beta \mathbf{k}_\parallel \right\rangle. \qquad (2.37)$$

Besides an interband transition, the coupling with an electromagnetic field may induce an intraband current as charge carriers in the bands get accelerated. The interaction can be described via

$$\hat{H}_{I,intra} = -\mathbf{A}(t) \cdot \sum_{\alpha, \mathbf{k}_\parallel} \mathbf{j}_\alpha(\mathbf{k}_\parallel) \hat{a}^\dagger_{\alpha \mathbf{k}_\parallel} \hat{a}_{\alpha \mathbf{k}_\parallel}, \qquad (2.38)$$

with the intraband current matrix elements $\mathbf{j}_\alpha(\mathbf{k}_\parallel) = \frac{|e|}{\hbar} \nabla_{\mathbf{k}_\parallel} \epsilon^\alpha_{\mathbf{k}_\parallel}$. While this contribution to the total induced current is negligible in scenarios with resonant and above-band gap excitations, it becomes dominant for the interaction with low-frequency fields. Therefore, we include this term when studying the interaction with a THz field and omit it otherwise.

Magnetic field interaction

As introduced in the previous chapter, the interaction of a material to an electromagnetic field can be dealt with employing the concept of minimal coupling. To study the influence of a magnetic field, we hereby start with H_0 in first quantization $H_0 = \sum_i \frac{\hbar^2}{2m_e} \mathbf{p}_i^2$. Substituting the momentum in this expression by the canonical momentum as stated above, applying the Coulomb gauge, $\nabla \cdot \mathbf{A} = 0$, and working in the symmetric gauge $\mathbf{A}(\mathbf{r}) = \frac{1}{2}\mathbf{B} \times \mathbf{r}$, we find for the interaction with a magnetic field

$$H = \sum_i \frac{e}{2m_e c} \mathbf{B} \cdot \mathbf{L}_i + \frac{e^2 \mathbf{B}^2}{8m_e c} r_i^2 \sin^2 \theta_i \qquad (2.39)$$

with $\mathbf{L} = \mathbf{r} \times \mathbf{p}$ being the orbital angular momentum and θ denoting the angle between $\mathbf{B}$ and $\mathbf{r}$ [55]. For a magnetic field perpendicular to the plane, $\mathbf{B} = B\hat{e}_\perp$, we find for the interaction in second quantization in effective mass approximation

$$\hat{H}_B = \sum_{\alpha \mathbf{k}} \left(\frac{eB}{2m_\alpha c} \hat{l}_z + \frac{e^2 B^2}{8m_\alpha c^2} \hat{r}^2 \right) \hat{a}^\dagger_{\alpha \mathbf{k}} \hat{a}_{\alpha \mathbf{k}}. \qquad (2.40)$$

This shows that the magnetic field contributes within two terms to the Hamiltonian. The first term induces a linear shift depending on the states angular momentum and is called Zeeman-shift. The second term gives rise to a diamagnetic shift that is quadratic in B.

Phonon interaction

The interaction of the particles with distortions and vibrations of the lattice structure is summarised as electron-phonon interaction. Considering the vibrations of the lattice as perturbation and introducing phonon operators $b_{\mathbf{q}_\parallel}^{(\dagger)}$, describing the absorption or emission of a phonon with momentum $\mathbf{q}_\parallel$, the intraband interaction of electrons and phonons is described in linear approximation by the so-called Fröhlich Hamiltonian

$$\hat{H}_{e-ph} = \sum_{\alpha,m} \sum_{\mathbf{k}_\parallel \mathbf{q}_\parallel \neq 0} g_{\mathbf{k}_\parallel;\mathbf{q}_\parallel}^m \hat{a}_{\alpha\mathbf{k}_\parallel+\mathbf{q}_\parallel}^\dagger \hat{a}_{\alpha\mathbf{k}_\parallel} \left(\hat{b}_{\mathbf{q}_\parallel} + \hat{b}_{-\mathbf{q}_\parallel}^\dagger \right). \tag{2.41}$$

Here, the phonon matrix element $g_{\mathbf{k}_\parallel;\mathbf{q}_\parallel}^m$ describes the probability amplitude that an electron of momentum $\mathbf{k}_\parallel + \mathbf{q}_\parallel$ is scattered into a state of momentum $\mathbf{k}_\parallel$ under absorption (emission) of a phonon with momentum $(-)\mathbf{q}_\parallel$ and branch index m. As the unit cell of a monolayer TMDC contains three atoms, there are nine phonon branches, three acoustic and six optical. In publication [III] we only include longitudinal optical (LO)-phonons that were shown to have the most important contributions at the K/K'-point [56]. Furthermore, we adapt the model Sohier *et al.* developed to describe the interaction matrix in vicinity to the high-symmetry point and in an anisotropic dielectric environment by $g_{\mathbf{k}_\parallel=K/K';\mathbf{q}_\parallel}^{LO} = \frac{\mathcal{C}_\mathcal{Z}}{\epsilon_{eff}(|\mathbf{q}_\parallel|)}$ with the bare interaction $\mathcal{C}_\mathcal{Z}$ and the effective screening approximated in first order Taylor expansion $\epsilon_{eff}(|\mathbf{q}_\parallel|) \approx \epsilon_{eff}^0 + r_{eff}|\mathbf{q}_\parallel|$ with the effective screening parameter r_{eff}. For both parameters, we employ *ab initio* based approximation as derived in [56].

For the analysis of the relaxation dynamics within the whole Brillouin zone (publication [IV]), in contrast, we include all nine phonon branches and the full $\mathbf{k}$- and $\mathbf{q}$-dependence of their matrix elements. Here, the phonon dispersions and coupling matrix elements were calculated by means of density function perturbation theory (DFPT) using the Quantum Espresso code [57, 58]. While the previous model only allowed to study the intervalley interaction in proximity of the main valleys at the high-symmetry points, this expansion additionally allows to study phenomena like intervalley-scattering.

2.2.3 Summary

In summary, against the background of DFT calculations, we have derived a model for the energetic ground state and introduced formalisms and approximations to model different intrinsic material interactions – between the carriers and with phonon – as well as with external parameters – such as electromagnetic fields and dielectric environments. With

these different components, we are able to describe the many-body system restricted to the valence and conduction band. Based on the full model Hamiltonian

$$
\begin{aligned}
\hat{H} &= \hat{H}_0 + \hat{H}_C + \hat{H}_I + \hat{H}_B + \hat{H}_{e-ph} \\
&= \sum_{\alpha \mathbf{k}_\parallel} \epsilon_{\mathbf{k}_\parallel} \hat{a}_{\alpha \mathbf{k}_\parallel}^\dagger \hat{a}_{\alpha \mathbf{k}_\parallel} + \frac{1}{2} \sum_{\alpha \alpha' \beta \beta'} \sum_{\mathbf{k}_\parallel \mathbf{k}_\parallel' \mathbf{q}_\parallel \neq 0} V_{\mathbf{q}_\parallel; \mathbf{k}_\parallel'; \mathbf{k}_\parallel}^{\alpha \beta \beta' \alpha'} a_{\alpha \mathbf{k}_\parallel - \mathbf{q}_\parallel}^\dagger a_{\beta \mathbf{k}_\parallel' + \mathbf{q}_\parallel}^\dagger a_{\beta' \mathbf{k}_\parallel'} a_{\alpha \mathbf{k}_\parallel} \\
&\quad - \frac{e}{m_0 c} \sum_{\alpha \neq \beta \mathbf{k}} \mathbf{A}(t) \cdot \mathbf{p}_{\alpha \beta}\left(\mathbf{k}_\parallel\right) \hat{a}_{\alpha \mathbf{k}_\parallel}^\dagger \hat{a}_{\beta \mathbf{k}_\parallel} - \mathbf{A}(t) \cdot \sum_{\alpha, \mathbf{k}_\parallel} \mathbf{j}_\alpha(\mathbf{k}_\parallel) \hat{a}_{\alpha \mathbf{k}_\parallel}^\dagger \hat{a}_{\alpha \mathbf{k}_\parallel} \\
&\quad + \sum_{\alpha \mathbf{k}_\parallel} \left(\frac{eB}{2 m_\alpha c} \hat{l}_z + \frac{e^2 B^2}{8 m_\alpha c^2} \hat{r}^2 \right) \hat{a}_{\alpha \mathbf{k}_\parallel}^\dagger \hat{a}_{\alpha \mathbf{k}_\parallel} \\
&\quad + \sum_{\alpha, m} \sum_{\mathbf{k}_\parallel \mathbf{q}_\parallel \neq 0} g_{\mathbf{k}_\parallel; \mathbf{q}_\parallel}^m \hat{a}_{\alpha \mathbf{k}_\parallel + \mathbf{q}_\parallel}^\dagger \hat{a}_{\alpha \mathbf{k}_\parallel} \left(\hat{b}_{\mathbf{q}_\parallel} + \hat{b}_{-\mathbf{q}_\parallel}^\dagger \right),
\end{aligned}
\tag{2.42}
$$

we now want to deduce the systems dynamical properties. As already stated in the different subsection, in our studies, we do not always include the full Hamiltonian, but focus on specific aspects and only include those parts that contribute in the chosen settings.

2.3 Equation of motion approach

To describe the dynamics of the many-body system determined by the previously introduced Hamiltonian, we employ the Heisenberg equation of motion approach (eom). Here, the observables are treated as time-dependent quantities, and their temporal evolution is derived by the expectation value of the commutation of the corresponding operator $\hat{\mathcal{O}} = \hat{\mathcal{O}}(t)$ with the system Hamiltonian

$$
-i\hbar \frac{\partial}{\partial t} \langle \hat{\mathcal{O}} \rangle = \left\langle \left[\hat{H}, \hat{\mathcal{O}} \right] \right\rangle.
\tag{2.43}
$$

Formally, this equation looks simple, but the interaction terms that are contained within the Hamiltonian induce an infinite series when the commutation is evaluated. We can picture the problem in the following way: If we select just one single particle, e.g. an electron, of the system, then we have to evaluate how this electron pairwise influences and is influenced by every other individual particle – holes, electrons and phonons – in the system. But, then the question arises how these pairs of particles interact with one another and with further particles. Any time we try to evaluate the interaction of a subsystem of N particles with the remaining particles in the system, we experience, that the subsets we have to take into account grows. Formally spoken, the interaction between charge carriers as well as with phonons and, if treated in a quantised way, with photons causes that the dynamics of an N-particle operator couples to the dynamics of an $(N + 1)$-particle operator. The latter in turn couples to the dynamics of an $(N + 2)$-

full correlation   singlets   doublets   triplets
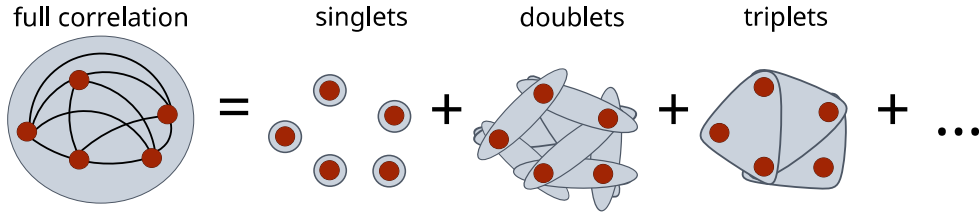
Abbildung 2.5: Illustration of the basic idea of the cluster expansion: The full correlated system of N interacting particles is systematically split up in correlated subsystems – called clusters.

particle operator. This pattern can be described by

$$\frac{\partial}{\partial t} \langle N \rangle = T\left[\langle N \rangle\right] + V\left[\langle N+1 \rangle\right],\tag{2.44}$$

where $\langle N \rangle$ symbolises an N-particle operator consisting of N creation and annihilation operators and in the functionals T and V the non-interacting and interacting parts of the equation are formally summarised. This pattern does not end but discloses an infinite series of dependencies.

This infinite hierarchy can not be treated exactly, but requires a reasonable truncation of the occuring series. An effective way of truncation is proposed by the concept of a cluster expansion (CE) that finally yields a closed set of equations [59, 60]. Its basic idea is sketched in Fig. 2.5. The idea is to systematically split up larger groups of particles into contributions of smaller groups of particles – called clusters. At the lowest level of approximation, which is equivalent to the so-called Hartree-Fock approximation (HF), one factorises all groups into its contributions of single particles, called singlets, according to the scheme

$$\langle N \rangle_S = \sum_{\pi}(-1)^{\pi}\prod_{i=1}^{N}\langle a^{\dagger}_{\mathbf{k}_i} a_{\mathbf{k}_{\pi}i}\rangle,\tag{2.45}$$

where π refers to the permutation of the $\mathbf{k}_i$. Regarding a single particle, we only have singlet contributions, but already for a two-particle state, in this approximation one neglects the correlated part $\Delta\langle 2 \rangle$. Formally, the full particle state can be written as

$$\langle 2 \rangle = \langle 2 \rangle_S + \Delta\langle 2 \rangle.\tag{2.46}$$

The cluster expansion approach now yields a recursive scheme describing the systematic

splitting of an N-particle state into its lower clusters and correlated parts:

$$\begin{aligned}
\langle 1 \rangle &= \langle 1 \rangle_S \\
\langle 2 \rangle &= \langle 2 \rangle_S + \Delta \langle 2 \rangle \\
\langle 3 \rangle &= \langle 1 \rangle_S + \langle 1 \rangle \Delta \langle 2 \rangle + \Delta \langle 3 \rangle \\
\langle N \rangle &= \langle N \rangle_S + \langle N - 2 \rangle \Delta \langle 2 \rangle + \langle N - 4 \rangle \Delta \langle 4 \rangle \\
&\quad + ... + \langle N - 3 \rangle \Delta \langle 3 \rangle + ... + \Delta \langle N \rangle .
\end{aligned} \tag{2.47}$$

Here, in analogy to the Hartree-Fock factorisation, the terms include sums over all permutations of the N coordinates with a corresponding sign.

This expansion is formally exact, but still only reformulates the problem. The advantage of this reformulation is that it allows for a systematic truncation of the scheme at a certain level of correlation. Often, higher order terms are then approximated as additional screening and by phenomenological approximations. The actual level of truncation needs to be chosen in accordance to the physical system and situation as for studying an effect that involves m particles, at least all terms up to Δm need to be included. In this way, the cluster expansion approach allows to find a closed set of equations that approximately describes the system.

Ground state renormalisation

In quasi-two-dimensional materials, the strong Coulomb interaction causes a difference between the non-interacting and the interacting ground state, as the interaction e.g. results in an unphysical finite expectation value for the interband polarisation in the ground state [61, 62, 63]. In [61] an expression for the interacting ground state is derived that is explained in detail in [62], in the following only the main concept is sketched. The starting point is a Hamiltonian including only the groundstate Hamiltonian and Coulomb interaction, $\hat{H} = \hat{H}_0 + \hat{H}_C$. For the ground state to be stationary, the variables $\Pi_{s\tau\mathbf{k}_\parallel} = \langle b_{s\tau\mathbf{k}_\parallel}^\dagger a_{s\tau\mathbf{k}_\parallel} \rangle$ and $\Gamma_{s\tau\mathbf{k}_\parallel} = f_{s\tau\mathbf{k}_\parallel}^b - f_{s\tau\mathbf{k}_\parallel}^a = \langle b_{s\tau\mathbf{k}_\parallel}^\dagger b_{s\tau\mathbf{k}_\parallel} \rangle - \langle a_{s\tau\mathbf{k}_\parallel}^\dagger a_{s\tau\mathbf{k}_\parallel} \rangle$, where $a_{s\tau\mathbf{k}_\parallel}^{(\dagger)}$ and $b_{s\tau\mathbf{k}_\parallel}^{(\dagger)}$ refer to operators that annihilate (create) a particle with pseudospin up (down), need to be stationary. The variable dynamics can be determined by the above introduced equation of motion and are in Hartree-Fock approximation given by

$$\begin{aligned}
i\hbar \frac{\partial}{\partial t} \Pi_{s\tau\mathbf{k}_\parallel} &= \left(\Delta_{s\tau\mathbf{k}_\parallel} + V[\Gamma_{s\tau\mathbf{k}_\parallel}] \right) \Pi_{s\tau\mathbf{k}_\parallel} + \left(\tau\hbar v_F k e^{-i\tau\theta_{\mathbf{k}_\parallel}} - V[\Pi_{s\tau\mathbf{k}_\parallel}] \right) \Gamma_{s\tau\mathbf{k}_\parallel} \\
i\hbar \frac{\partial}{\partial t} f_{s\tau\mathbf{k}_\parallel}^a &= -i\hbar \frac{\partial}{\partial t} f_{s\tau\mathbf{k}_\parallel}^b = 2\Im \left\{ \Pi_{s\tau\mathbf{k}_\parallel} \tau\hbar v_F k e^{-i\tau\theta_{\mathbf{k}_\parallel}} \right\},
\end{aligned} \tag{2.48}$$

where the abbreviation $V[f] = \sum_{\mathbf{k}_\parallel' \neq \mathbf{k}_\parallel} V_{|\mathbf{k}_\parallel - \mathbf{k}_\parallel'|} f_{\mathbf{k}_\parallel'}$ was introduced. Under the constraint $\Gamma_{s\tau\mathbf{k}_\parallel}^2 = 1 - 4|\Pi_{s\tau\mathbf{k}_\parallel}|^2$, which holds for any coherent state, the demand of stationary variables yields a closed set of integral equations for the renormalised band gap

and Fermi velocity. The so-called gap equations (GE) read

$$\tilde{\Delta}_{s\tau\mathbf{k}_\parallel} = \Delta_{s\tau} + \sideset{}{'}\sum_{\mathbf{k}_\parallel' \neq \mathbf{k}_\parallel} V_{|\mathbf{k}_\parallel - \mathbf{k}_\parallel'|} \frac{\tilde{\Delta}_{s\tau\mathbf{k}_\parallel'}}{2\epsilon_{s\tau\mathbf{k}_\parallel'}} \tag{2.49}$$

$$\tilde{v}_{F\mathbf{k}_\parallel} = v_{F,s\tau} + \sideset{}{'}\sum_{\mathbf{k}_\parallel' \neq \mathbf{k}_\parallel} V_{|\mathbf{k}_\parallel - \mathbf{k}_\parallel'|} \frac{k_\parallel'}{k_\parallel} \frac{\tilde{v}_{F,\mathbf{k}_\parallel'}}{2\epsilon_{s\tau\mathbf{k}_\parallel'}} \cos(\theta_{\mathbf{k}_\parallel} - \theta_{\mathbf{k}_\parallel'}), \tag{2.50}$$

where the abbreviation $\sideset{}{'}\sum_{\mathbf{k}_\parallel' \neq \mathbf{k}_\parallel} = \sum_{\mathbf{k}_\parallel' \neq \mathbf{k}_\parallel} \delta_{s,s'} \delta_{\tau,\tau'}$ was introduced. Furthermore, we introduced the renormalised gap and Fermi velocity as

$$\tilde{\Delta}_{s\tau\mathbf{k}_\parallel} = \Delta_{s\tau} + V[\Gamma_{s\tau\mathbf{k}_\parallel}]$$
$$\tau\hbar\tilde{v}_{F,s\tau\mathbf{k}_\parallel} k e^{-i\tau\theta_{\mathbf{k}_\parallel}} = \tau\hbar v_{F,s\tau} k e^{-i\tau\theta_{\mathbf{k}_\parallel}} - V[\Pi_{s\tau\mathbf{k}_\parallel}]. \tag{2.51}$$

This explicit determination of the renormalised ground state by solving the GE iteratively was applied when magnetic field contributions were included.

In the remaining publications, we account for the interacting ground state by including the so-called Coulomb-hole contribution, that enters the Dirac-Bloch equations discussed below upon traversing from the conduction-valence-band to the electron-hole picture. Here, the complete valence band was shifted by a constant shift $\Delta\epsilon_{vb,\mathbf{k}_\parallel} = -\sideset{}{'}\sum_{\mathbf{k}_\parallel' \neq \mathbf{k}_\parallel} \left(V^{vvvv}_{\mathbf{k}_\parallel - \mathbf{k}_\parallel';\mathbf{k}_\parallel';\mathbf{k}_\parallel} - V^{vcvc}_{\mathbf{k}_\parallel - \mathbf{k}_\parallel';\mathbf{k}_\parallel';\mathbf{k}_\parallel} \right)$. Thus, the interaction between the particles in the valence band results in an increase of the electronic band gap. The Fermi velocity was renormalised equivalently. These two formulations of renormalising the band structure were numerically verified to yield the same results.

The Hamiltonian correctly describing this interacting system is achieved by substituting the band gap $\Delta_{s\tau}$ and the Fermi velocity $v_{F,s\tau}$ by their renormalised correspondents in the above expressions $\tilde{\Delta}_{s\tau\mathbf{k}_\parallel}$ and $\tilde{v}_{F\mathbf{k}_\parallel}$.

Dirac-Bloch equation

Having found the systems interacting ground state, our aim is to describe the dynamics of electrons in a material on the microscopic level under varying external conditions. Precisely, we are interested in the dynamics of the carrier occupations in the different bands $f^\alpha_{\mathbf{k}_\parallel} = p^{\alpha\alpha}_{\mathbf{k}_\parallel} = \langle a^\dagger_{\alpha\mathbf{k}_\parallel} a^\dagger_{\alpha\mathbf{k}_\parallel} \rangle$ and the transition amplitudes between different bands, namely the microscopic polarisation, $p_{\mathbf{k}_\parallel} = \langle a^\dagger_{\alpha\mathbf{k}_\parallel} a^\dagger_{\alpha'\mathbf{k}_\parallel} \rangle$ with $\alpha \neq \alpha'$. The application of the eom approach reveals the temporal evolution of these quantities to be described by

the coupled set of integral equations [59]

$$i\hbar \frac{\mathrm{d}}{\mathrm{d}t} p_{\mathbf{k}_{\parallel}} = \left(\Sigma_{\mathbf{k}_{\parallel}}^{c} - \Sigma_{\mathbf{k}_{\parallel}}^{v} \right) p_{\mathbf{k}_{\parallel}} - \left(f_{\mathbf{k}_{\parallel}}^{v} - f_{\mathbf{k}_{\parallel}}^{c} \right) \Omega_{\mathbf{k}_{\parallel}} + i\hbar \frac{\mathrm{d}}{\mathrm{d}t} p_{\mathbf{k}_{\parallel}} \Big|_{corr} \tag{2.52}$$

$$\hbar \frac{\mathrm{d}}{\mathrm{d}t} f_{\mathbf{k}_{\parallel}}^{c/v} = \mp 2\Im \left\{ \Omega_{\mathbf{k}_{\parallel}} p_{\mathbf{k}_{\parallel}}^{*} \right\} + \hbar \frac{\mathrm{d}}{\mathrm{d}t} f_{\mathbf{k}_{\parallel}}^{c/v} \Big|_{corr} , \tag{2.53}$$

with $\mathbf{k}_{\parallel}$ and $\mathbf{k}_{\parallel}'$ summarising spin, valley index and crystal momentum. These equations are formally equivalent to the widely used semiconductor Bloch equations (SBE), but due to their derivation based on the MDF Hamiltonian, they are often named Dirac-Bloch equations (DBE). Here, the renormalised energies $\Sigma_{\mathbf{k}_{\parallel}}^{c/v}$ and the renormalised Rabi energy $\Omega_{\mathbf{k}_{\parallel}}$ contain the Hartree-Fock contributions and explicitly read

$$\Sigma_{\mathbf{k}_{\parallel}}^{c/v} = \epsilon_{\mathbf{k}_{\parallel}}^{c/v} - \sideset{}{'}\sum_{\mathbf{k}_{\parallel}' \neq \mathbf{k}_{\parallel}} \left(V_{\bar{\mathbf{k}}_{\parallel} - \bar{\mathbf{k}}_{\parallel}'; \bar{\mathbf{k}}_{\parallel}'; \bar{\mathbf{k}}_{\parallel}}^{cccc/vvvv} - V_{\bar{\mathbf{k}}_{\parallel} - \bar{\mathbf{k}}_{\parallel}'; \bar{\mathbf{k}}_{\parallel}'; \bar{\mathbf{k}}_{\parallel}}^{cvcv/vcvc} \right) f_{\mathbf{k}_{\parallel}'}^{c/v} \tag{2.54}$$

$$\Omega_{\mathbf{k}_{\parallel}} = \frac{e}{m_0 c} \mathbf{A} \cdot \mathbf{p}_{cv\mathbf{k}_{\parallel}} - \sideset{}{'}\sum_{\mathbf{k}_{\parallel}' \neq \mathbf{k}_{\parallel}} \left(V_{\bar{\mathbf{k}}_{\parallel} - \bar{\mathbf{k}}_{\parallel}'; \bar{\mathbf{k}}_{\parallel}'; \bar{\mathbf{k}}_{\parallel}}^{cvvc} p_{\mathbf{k}_{\parallel}'} + V_{\bar{\mathbf{k}}_{\parallel} - \bar{\mathbf{k}}_{\parallel}'; \bar{\mathbf{k}}_{\parallel}'; \bar{\mathbf{k}}_{\parallel}}^{ccvv} p_{\mathbf{k}_{\parallel}'}^{*} \right) . \tag{2.55}$$

Here, non-resonant Auger and pair-creation contributions are already neglected as they were shown to have minor impact on the renormalisation for wide gap materials [64]. In the renormalised Rabi frequency, the term $\propto p_{\mathbf{k}_{\parallel}'}^{*}$, which couples the temporal evolution of the microscopic polarisation to its complex conjugate, makes the problem non-trivial. As approaches of treating this term perturbatively have shown its negligible influence on the results, we drop this contribution in the following. Moreover, $\epsilon_{\mathbf{k}_{\parallel}}^{c/v}$ denote the unrenormalised single-particle energies, as the ground state renormalisation due to the Coulomb-hole introduced above is included implicitly and seen explicitly, when transforming into the electron-hole picture, where $f_{\mathbf{k}_{\parallel}}^{v} = 1 - f_{\mathbf{k}_{\parallel}}^{h} = 1$ holds. All contributions due to many-body correlations, thus contributions beyond the HF approximation, are subsumed in $i\hbar \frac{\mathrm{d}}{\mathrm{d}t} p_{\mathbf{k}_{\parallel}} \big|_{corr}$ and $\hbar \frac{\mathrm{d}}{\mathrm{d}t} f_{\mathbf{k}_{\parallel}}^{c/v} \big|_{corr}$.

Instead of expressing the DBE for electrons in valence and conduction band respectively, they are often transformed into the electron-hole picture, in which instead of analysing the behaviour of electrons in the valence band, the lack of electrons – named holes – are considered. The transformation between the two pictures is given via

$$\epsilon_{\mathbf{k}_{\parallel}}^{c} \to \epsilon_{\mathbf{k}_{\parallel}}^{e} \qquad \qquad \epsilon_{\mathbf{k}_{\parallel}}^{v} \to -\epsilon_{-\mathbf{k}_{\parallel}}^{h} \tag{2.56}$$

$$f_{\mathbf{k}_{\parallel}}^{c} \to f_{\mathbf{k}_{\parallel}}^{e} \qquad \qquad f_{\mathbf{k}_{\parallel}}^{v} \to (1 - f_{-\mathbf{k}_{\parallel}}^{h}). \tag{2.57}$$

Coulomb-induced particle interaction

In the DBE as written above, only singlet terms are included explicitly and all many-particle correlations arising from Coulomb- and phonon-mediated interactions are hidden

in the equations last terms. On the simplest level of approximation, namely the singlet or Hartree-Fock level, we assume that relaxation and dephasing processes are independent of exact excitation conditions and can be treated by constant decay/dephasing rates γ. Thus, we include correlation contributions by setting e.g.

$$i\hbar \frac{\mathrm{d}}{\mathrm{d}t} p_{\mathbf{k}_\parallel}^{\alpha\alpha'} \bigg|_{corr} = -i\hbar\gamma_{\alpha\alpha'} p_{\mathbf{k}_\parallel}^{\alpha\alpha'}.$$

At this level, the constant treatment of decay and dephasing conceals insights on relaxation processes due to scattering processes, density-dependent changes in the dephasing or plasma screening effects. In order to gain insights into these processes, we have to analyse the correlation term in more detail. The following elaboration follows the presentation in publication [III]. The Coulomb interaction couples the singlet terms $p_{\mathbf{k}_\parallel}^{\alpha\alpha'}$ to the doublet correlation $\Delta \langle a_{\alpha\mathbf{k}_\parallel}^\dagger a_{\gamma\mathbf{k}_\parallel'-\mathbf{q}_\parallel}^\dagger a_{\gamma'\mathbf{k}_\parallel'} a_{\beta\mathbf{k}_\parallel-\mathbf{q}_\parallel} \rangle \equiv \Delta C_{\mathbf{q}_\parallel\mathbf{k}_\parallel'\mathbf{k}_\parallel}^{\alpha\gamma\gamma'\beta}$ according to

$$i\hbar \frac{\mathrm{d}}{\mathrm{d}t} p_{\mathbf{k}_\parallel}^{\alpha\alpha'} \bigg|_{corr.}^{el.} = \sum_{\mathbf{q}_\parallel \mathbf{k}_\parallel'} \sum_{\beta\gamma\gamma'} \left\{ V_{-\mathbf{q}_\parallel;\mathbf{k}_\parallel';\mathbf{k}_\parallel-\mathbf{q}_\parallel}^{\alpha'\gamma\gamma'\beta} \Delta C_{\mathbf{q}_\parallel\mathbf{k}_\parallel'\mathbf{k}_\parallel}^{\alpha\gamma\gamma'\beta} - \left[V_{-\mathbf{q}_\parallel;\mathbf{k}_\parallel';\mathbf{k}_\parallel-\mathbf{q}_\parallel}^{\alpha\gamma\gamma'\beta} \Delta C_{\mathbf{q}_\parallel\mathbf{k}_\parallel'\mathbf{k}_\parallel}^{\alpha'\gamma\gamma'\beta} \right]^* \right\}.$$

$$(2.58)$$

Neglecting, again, Auger contributions ($\gamma \neq \gamma'$) and the orbital- as well as $\mathbf{k}_\parallel/\mathbf{k}_\parallel'$-dependence of the Coulomb potential, the eom resulting from the system Hamiltonian for the doublet correlations reads

$$i\hbar \frac{\mathrm{d}}{\mathrm{d}t} \Delta C_{\mathbf{q}_\parallel\mathbf{k}_\parallel'\mathbf{k}_\parallel}^{\alpha\beta\beta\alpha'} = \Delta\Sigma_{\mathbf{q}_\parallel\mathbf{k}_\parallel'\mathbf{k}_\parallel}^{\alpha\beta\beta\alpha'} \Delta C_{\mathbf{q}_\parallel\mathbf{k}_\parallel'\mathbf{k}_\parallel}^{\alpha\beta\beta\alpha'} + \left(f_{\mathbf{k}_\parallel'-\mathbf{q}_\parallel}^\beta - f_{\mathbf{k}_\parallel'}^\beta \right) I_{\mathbf{q}_\parallel\mathbf{k}_\parallel}^{\alpha\alpha'} + S_{\mathbf{q}_\parallel\mathbf{k}_\parallel'\mathbf{k}_\parallel}^{\alpha\beta\beta\alpha'}$$

$$+ \text{ remaining doublets} + i\hbar \frac{\mathrm{d}}{\mathrm{d}t} \Delta C_{\mathbf{q}_\parallel\mathbf{k}_\parallel'\mathbf{k}_\parallel}^{\alpha\beta\beta\alpha'} \bigg|_{tri}^{el.}, \qquad (2.59)$$

where $\Delta\Sigma_{\mathbf{q}_\parallel\mathbf{k}_\parallel'\mathbf{k}_\parallel}^{\alpha\beta\beta\alpha'} = \Sigma_{\mathbf{k}_\parallel-\mathbf{q}_\parallel}^{\alpha'} + \Sigma_{\mathbf{k}_\parallel'}^\beta - \Sigma_{\mathbf{k}_\parallel'-\mathbf{q}_\parallel}^\beta - \Sigma_{\mathbf{k}_\parallel}^\alpha$. Here, we factorised the triplet terms in its singlet and doublet contributions and kept the remaining fully correlated term [60]. In the following, we truncate the expansion at this level and approximate the triplet correlations by a constant dephasing $i\hbar\frac{\mathrm{d}}{\mathrm{d}t}\Delta C_{\mathbf{q}_\parallel\mathbf{k}_\parallel'\mathbf{k}_\parallel}^{\alpha\beta\beta\alpha'}\bigg|_{tri}^{el.} = -i\hbar\gamma_T \Delta C_{\mathbf{q}_\parallel\mathbf{k}_\parallel'\mathbf{k}_\parallel}^{\alpha\beta\beta\alpha'}$, marking the singlet-doublet approximation. Furthermore, we separated the plasma screening contributions summarised in $I_{\mathbf{q}_\parallel\mathbf{k}_\parallel}^{\alpha\alpha'} = V_{\mathbf{q}_\parallel} \sum_{\beta\mathbf{k}_\parallel'} C_{\mathbf{q}_\parallel\mathbf{k}_\parallel'\mathbf{k}_\parallel}^{\alpha\beta\beta\alpha'}$ from the remaining contributions. In $S_{\mathbf{q}_\parallel\mathbf{k}_\parallel'\mathbf{k}_\parallel}^{\alpha\beta\beta\alpha'}$, the terms resulting from the singlet factorisation are subsumed, that explicitly

read

$$S_{\mathbf{q}_{\parallel}\mathbf{k}'_{\parallel}\mathbf{k}_{\parallel}}^{\alpha\beta\beta\alpha'} = V_{\mathbf{q}_{\parallel}}\left(p_{\mathbf{k}_{\parallel}}^{\alpha\alpha'}f_{\mathbf{k}'_{\parallel}-\mathbf{q}_{\parallel}}^{\beta}\bar{f}_{\mathbf{k}'_{\parallel}}^{\beta} - p_{\mathbf{k}_{\parallel}-\mathbf{q}_{\parallel}}^{\alpha\alpha'}\bar{f}_{\mathbf{k}'_{\parallel}-\mathbf{q}_{\parallel}}^{\beta}f_{\mathbf{k}'_{\parallel}}^{\beta}\right)$$
$$+ V_{\mathbf{k}_{\parallel}-\mathbf{k}'_{\parallel}}p_{\mathbf{k}_{\parallel}}^{\alpha\beta}\sum_{\gamma}p_{\mathbf{k}'_{\parallel}-\mathbf{q}_{\parallel}}^{\beta\gamma}\left(p_{\mathbf{k}_{\parallel}-\mathbf{q}_{\parallel}}^{\gamma\alpha'} - \delta_{\gamma\alpha'}\right)$$
$$- V_{\mathbf{k}_{\parallel}-\mathbf{k}'_{\parallel}}p_{\mathbf{k}'_{\parallel}}^{\alpha\beta}\sum_{\gamma}p_{\mathbf{k}_{\parallel}-\mathbf{q}_{\parallel}}^{\gamma\alpha'}\left(p_{\mathbf{k}'_{\parallel}-\mathbf{q}_{\parallel}}^{\beta\gamma} - \delta_{\gamma\beta}\right)$$
$$+ V_{\mathbf{k}_{\parallel}-\mathbf{k}'_{\parallel}}\left(p_{\mathbf{k}'_{\parallel}-\mathbf{q}_{\parallel}}^{\beta\alpha'} - p_{\mathbf{k}_{\parallel}-\mathbf{q}_{\parallel}}^{\beta\alpha'}\right)\sum_{\gamma}p_{\mathbf{k}_{\parallel}}^{\alpha\gamma}p_{\mathbf{k}'_{\parallel}}^{\gamma\beta}. \tag{2.60}$$

Assuming plasma screening to be the dominant correlation effect and the single-particle distributions to be quasistatic, we neglect the remaining doublet contributions, which makes it possible to solve the dynamics of the doublet correlations by Fourier transformation. Finally, within these approximations, we find a frequency-dependent expression for the Coulomb-mediated transition/occupation probabilities, including the full doublet contributions $C_{\mathbf{q}_{\parallel}\mathbf{k}'_{\parallel}\mathbf{k}_{\parallel}}^{\alpha\beta\beta\alpha'}$

$$I_{\mathbf{q}_{\parallel}\mathbf{k}'_{\parallel}\mathbf{k}_{\parallel}}^{\alpha\alpha'}(\omega) = \left. I_{\mathbf{q}_{\parallel}\mathbf{k}'_{\parallel}\mathbf{k}_{\parallel}}^{\alpha\alpha'}(\omega)\right|_{S} + V_{\mathbf{q}_{\parallel}}\sum_{\beta\mathbf{k}'_{\parallel}}\frac{f_{\mathbf{k}'_{\parallel}-\mathbf{q}_{\parallel}}^{\beta} - f_{\mathbf{k}'_{\parallel}}^{\beta}}{\hbar\omega - \Sigma_{\mathbf{q}_{\parallel}\mathbf{k}'_{\parallel}\mathbf{k}_{\parallel}}^{\alpha\beta\beta\alpha'} + i\hbar\gamma_{T}}I_{\mathbf{q}_{\parallel}\mathbf{k}'_{\parallel}\mathbf{k}_{\parallel}}^{\alpha\alpha'}(\omega)$$
$$+ V_{\mathbf{q}_{\parallel}}\sum_{\beta\mathbf{k}_{\parallel}}\frac{S_{\mathbf{q}_{\parallel}\mathbf{k}'_{\parallel}\mathbf{k}_{\parallel}}^{\alpha\beta\beta\alpha'}}{\hbar\omega - \Sigma_{\mathbf{q}_{\parallel}\mathbf{k}'_{\parallel}\mathbf{k}_{\parallel}}^{\alpha\beta\beta\alpha'} + i\hbar\gamma_{T}}$$
$$= W_{\mathbf{q}_{\parallel}\mathbf{k}_{\parallel}}^{\alpha\alpha'}(\omega + i\hbar\gamma_{T})\sum_{\beta\mathbf{k}'_{\parallel}}\left. C_{\mathbf{q}_{\parallel}\mathbf{k}'_{\parallel}\mathbf{k}_{\parallel}}^{\alpha\beta\beta\alpha'}\right|_{S}$$
$$+ W_{\mathbf{q}_{\parallel}\mathbf{k}_{\parallel}}^{\alpha\alpha'}(\omega + i\hbar\gamma_{T})\sum_{\beta\mathbf{k}_{\parallel}}\frac{S_{\mathbf{q}_{\parallel}\mathbf{k}'_{\parallel}\mathbf{k}_{\parallel}}^{\alpha\beta\beta\alpha'}}{\hbar\omega - \Sigma_{\mathbf{q}_{\parallel}\mathbf{k}'_{\parallel}\mathbf{k}_{\parallel}}^{\alpha\beta\beta\alpha'} + i\hbar\gamma_{T}}. \tag{2.61}$$

Here, the screened Coulomb-matrix element including the Lindhard polarisation function, $\Pi_{\mathbf{q}_{\parallel}}(\omega)$,

$$W_{\mathbf{q}_{\parallel}\mathbf{k}_{\parallel}}^{\alpha\alpha'}(\omega) = \frac{V_{\mathbf{q}_{\parallel}}}{1 - V_{\mathbf{q}_{\parallel}}\Pi_{\mathbf{q}_{\parallel}\mathbf{k}_{\parallel}}^{\alpha\alpha'}(\omega)}$$
$$\Pi_{\mathbf{q}_{\parallel}\mathbf{k}_{\parallel}}^{\alpha\alpha'}(\omega) = \Pi_{\mathbf{q}_{\parallel}}\left(\omega + \left(\Sigma_{\mathbf{k}_{\parallel}}^{\alpha} - \Sigma_{\mathbf{k}_{\parallel}-\mathbf{q}_{\parallel}}^{\alpha'}\right)\right)$$
$$\Pi_{\mathbf{q}_{\parallel}}(\omega) = \sum_{\beta\mathbf{k}_{\parallel}}\frac{f_{\mathbf{k}_{\parallel}-\mathbf{q}_{\parallel}}^{\beta} - f_{\mathbf{k}_{\parallel}}^{\beta}}{\hbar\omega + \Sigma_{\mathbf{k}_{\parallel}-\mathbf{q}_{\parallel}}^{\beta} - \Sigma_{\mathbf{k}_{\parallel}}^{\beta}} \tag{2.62}$$

was introduced. The first term of the second line of Eq. 2.61, which describes the renormalisation of the single-particle and Rabi energies, shows that one consequence of the doublet correlations is the screening of the Coulomb interaction at the singlet level. Consequently, this advises to replace the Coulomb-matrix even in the Hartree-Fock approximation by its screened counterpart to include an important part of the doublet correlations. Taking the CE approach further, it can be seen, that next order correlations among others result in a screening of the energies entering the denominator of the Lindhard polarisation function and the scattering integral [60]. Hence, these contributions should be included by replacing these energies by their screened counterparts.

Phonon scattering

To determine phonon-mediated scattering processes, we analyse the eom resulting from the electron-phonon Hamiltonian (Eq. 2.41), following the description in [59],

$$
i\hbar p^{\alpha\alpha'}_{\mathbf{k}_\parallel}\Big|_{ph} = \sum_{\mathbf{q}_\parallel m\zeta} g^m_{\mathbf{k}_\parallel\mathbf{q}_\parallel} \left(G^{\alpha\alpha'm\zeta}_{\mathbf{q}_\parallel\mathbf{k}_\parallel} - G^{\alpha\alpha'm\zeta}_{\mathbf{q}_\parallel,\mathbf{k}_\parallel-\mathbf{q}_\parallel} \right), \tag{2.63}
$$

where $\zeta = \pm 1$ and $G^{\alpha\alpha'm+}_{\mathbf{q}_\parallel\mathbf{k}_\parallel} = \langle a^\dagger_{\alpha'\mathbf{k}_\parallel+\mathbf{q}_\parallel} a_{\alpha\mathbf{k}_\parallel} b^m_{\mathbf{q}_\parallel}\rangle$ and $G^{\alpha\alpha'm-}_{\mathbf{q}_\parallel\mathbf{k}_\parallel} = \langle a^\dagger_{\alpha'\mathbf{k}_\parallel+\mathbf{q}_\parallel} a_{\alpha\mathbf{k}_\parallel} b^{m\dagger}_{-\mathbf{q}_\parallel}\rangle$ are the phonon-mediated density matrices describing the in- and out-scattering into/from state $p^{\alpha\alpha'}_{\mathbf{k}_\parallel}$ under absorption $(-)$ respectively emission $(+)$ of a photon. As the factorisation of these matrices would vanish at this level of approximation, an analysis of their dynamics is mandatory to gain insights into phonon-induced scattering and dephasing processes. As the matrices describing emission and absorption can be deduced from each other by reversing the momentum and phonon frequency, it is sufficient to evaluate the dynamics for one of them. Similar to the Coulomb-induced scattering, we truncate the infinite hierarchy and factorise the occurring expectation values into its singlet contributions, where we approximate the phonon number $\langle b^\dagger_{\mathbf{q}_\parallel} b_{\mathbf{q}'_\parallel}\rangle \approx n_{\mathbf{q}_\parallel}\delta_{\mathbf{q}_\parallel,\mathbf{q}'_\parallel}$ to follow a Bose-Einstein distribution. The resulting eom, neglecting corrections to the energy spectrum and approximating higher order correlations by a constant phenomenological damping η, reads

$$
\begin{aligned}
i\hbar\frac{\mathrm{d}}{\mathrm{d}t} G^{\alpha\alpha'm+}_{\mathbf{q}_\parallel\mathbf{k}_\parallel} = {}& -\left(\Sigma^{\alpha'}_{\mathbf{k}_\parallel+\mathbf{q}_\parallel} - \Sigma^{\alpha}_{\mathbf{k}_\parallel} - \hbar\omega^m_{\mathbf{q}_\parallel} + i\hbar\eta \right) G^{\alpha\alpha'm+}_{\mathbf{q}_\parallel\mathbf{k}_\parallel} \\
& + g^m_{\mathbf{q}_\parallel} \sum_\gamma \left\{ n_{\mathbf{q}_\parallel} p^{\alpha\gamma}_{\mathbf{k}_\parallel} \left(\delta_{\gamma\alpha'} - p^{\gamma\alpha'}_{\mathbf{k}_\parallel+\mathbf{q}_\parallel} \right) - (n_{\mathbf{q}_\parallel}+1) p^{\alpha\gamma}_{\mathbf{k}_\parallel+\mathbf{q}_\parallel} \left(\delta_{\gamma\alpha'} - p^{\gamma\alpha'}_{\mathbf{k}_\parallel} \right) \right\}.
\end{aligned}
$$
$$\tag{2.64}$$

Proceeding with these scattering terms in a comparable way as for the electronic scattering terms, thus, assuming quasistatic single-particle occupations, this equation can be

solved by Fourier transformation, which yields the frequency-dependent expression

$$
G^{\alpha\alpha'm+}_{\mathbf{q}_\parallel \mathbf{k}_\parallel}(\omega) = \frac{g^m_{\mathbf{q}_\parallel} \sum_\gamma \left\{ n_{\mathbf{q}_\parallel} p^{\alpha\gamma}_{\mathbf{k}_\parallel} \left(\delta_{\gamma\alpha'} - p^{\gamma\alpha'}_{\mathbf{k}_\parallel+\mathbf{q}_\parallel} \right) - (n_{\mathbf{q}_\parallel} + 1) p^{\alpha\gamma}_{\mathbf{k}_\parallel+\mathbf{q}_\parallel} \left(\delta_{\gamma\alpha'} - p^{\gamma\alpha'}_{\mathbf{k}_\parallel} \right) \right\}}{\hbar\omega + \Sigma^{\alpha'}_{\mathbf{k}_\parallel+\mathbf{q}_\parallel} - \Sigma^{\alpha}_{\mathbf{k}_\parallel} - \hbar\omega^m_{\mathbf{q}_\parallel} + i\hbar\eta}.
$$

$$(2.65)$$

Again, on this level of approximation, the unrenormalised energies and interaction matrix elements enter the equation. In order to treat Coulomb- and phonon-induced scattering terms on the same level of approximation, we replace the unscreened quantities by their screened counterparts.

2.4 Macroscopic optical response

In the previous sections, the fundamental microscopic approach that was applied within this thesis was elucidated, but the question how the described relationships are expressed on a macroscopically measurable level has not yet been addressed. Macroscopically, optical phenomena are captured with the Maxwell equations that determine the wave equation for the optical vector potential $\mathbf{A}(\mathbf{r}, t) = -\frac{\mathrm{d}}{\mathrm{d}t}\mathbf{E}(\mathbf{r}, t)$

$$
\left(\nabla^2 - \frac{n^2}{c^2}\frac{\partial}{\partial t} \right) \mathbf{A}(\mathbf{r}, t) = -\frac{4\pi}{c}\mathbf{j} \tag{2.66}
$$

linking the incoming field $\mathbf{E}(\mathbf{r}, t)$ and the induced current $\mathbf{j}$. The induced current in turn can be related to the microscopic quantities. In terms of the microscopic polarisation and occupations, it is given by

$$
\mathbf{j} = -c\langle \frac{\delta H}{\delta \mathbf{A}} \rangle = -\frac{e}{m_0} \sum_{\alpha\alpha'\mathbf{k}_\parallel} \mathbf{p}_{\alpha\alpha'\mathbf{k}_\parallel} \langle a^\dagger_{\alpha\mathbf{k}_\parallel} a_{\alpha'\mathbf{k}_\parallel} \rangle. \tag{2.67}
$$

Here, the off-diagonal parts result from interband contributions, while the diagonal parts result from intraband contributions. The relative weight between these two contributions depends on the intensity and frequency of the incoming fields. The intraband contributions vanish for equilibrium occupations due to the different parity of density distribution and intraband current. Consequently, they mainly contribute for low-frequency fields, which induce an oscillation of carriers in the bands, and can be neglected for near-resonant and above-band gap excitation.

Important physical insights on a materials optical properties are gained by probing their linear response to an external field. For low-intensity fields, the response can be modelled in its linear approximation: $\mathbf{j}(\omega) = \epsilon_0\omega^2\chi(\omega)\mathbf{A}(\omega)$, where we introduced the linear optical susceptibility $\chi(\omega)$. It can be shown that its imaginary part is directly connected to the damping through the sample of the field and thus yields first insights on the qua-

litative features of monolayer absorption. Further evaluation of the above wave equation and an evaluation of reflected and transmitted signal for an incoming field perpendicular to the plane yields, that the true absorption coefficient of a monolayer, embedded in an environment with refractive index of $n_{T/B}$, is given by

$$\alpha(\omega) = \frac{4\pi n_T \frac{\omega}{c} \Im\{\chi(\omega)\}}{\left| \frac{n_T + n_B}{2} - 2\pi i \frac{\omega}{c} \chi(\omega) \right|^2}. \tag{2.68}$$

In the low density regime, the optical response is, due to the large Coulomb interaction in TMDC monolayers, even at room temperature dominated by excitonic features. To gain further insights on this behaviour, we take one step back and take again the microscopic equation into account. For (quasi-)static density distributions, the coupled set of equations simplifies to a single equation for the microscopic polarisation:

$$i\hbar \frac{\mathrm{d}}{\mathrm{d}t} p_{\mathbf{k}_\parallel} = \left(\Sigma^c_{\mathbf{k}_\parallel} - \Sigma^v_{\mathbf{k}_\parallel} - i\hbar\gamma \right) p_{\mathbf{k}_\parallel}$$
$$- \left(1 - f^e_{\mathbf{k}_\parallel} - f^h_{\mathbf{k}_\parallel} \right) \left(\frac{e}{m_0 c} \mathbf{A} \cdot \mathbf{p}_{cv\mathbf{k}_\parallel} - \sum_{\mathbf{k}'_\parallel} \left(V^{cvvc}_{\mathbf{k}_\parallel - \bar{\mathbf{k}}'_\parallel; \bar{\mathbf{k}}'_\parallel; \bar{\mathbf{k}}_\parallel} p_{\mathbf{k}'_\parallel} \right) \right). \tag{2.69}$$

Here, a phenomenological dephasing γ was introduced, that summarises phononic, electronic, radiative and intrinsic dephasing contributions. Its electronic dependence on the amount and distribution of excited carriers in the material is discussed in Ch. 6. Furthermore, the Auger term was neglected. In order to gain further insights, we first analyse the homogeneous part of the equation, the so-called (Dirac-) Wannier equation (WE)

$$\left(\Sigma^c_{\mathbf{k}_\parallel} - \Sigma^v_{\mathbf{k}_\parallel} \right) \Phi^R_\lambda(\mathbf{k}_\parallel) - \left(1 - f^e_{\mathbf{k}_\parallel} - f^h_{\mathbf{k}_\parallel} \right) \sum_{\mathbf{k}'_\parallel} \left(V^{cvvc}_{\mathbf{k}_\parallel - \bar{\mathbf{k}}'_\parallel; \bar{\mathbf{k}}'_\parallel; \bar{\mathbf{k}}_\parallel} \Phi^R_\lambda(\mathbf{k}'_\parallel) \right) = \epsilon_\lambda \Phi^R_\lambda(\mathbf{k}_\parallel),$$

$$\tag{2.70}$$

which can be solved numerically by matrix inversion.[3] This equation is similar to the two-particle Schrödinger equation, and its eigenstates and -energies define excitons: quasiparticles that are formed due to the Coulomb-mediated attraction between oppositely charged carriers. Upon expanding the polarisation in terms of these eigenstates, $p_{\mathbf{k}_\parallel} = \sum_\lambda p_\lambda \Phi^R_\lambda(\mathbf{k}_\parallel)$, the DBE can be solved in frequency space yielding

$$p_\lambda(\omega) = \frac{Q_\lambda}{\hbar\omega - \epsilon_\lambda + i\hbar\gamma}, \tag{2.71}$$

---

[3]In this formulation, we find different right- and left-handed eigenfunctions, which are connected via $\Phi^L_\lambda(\mathbf{k}_\parallel) = \frac{\Phi^R_\lambda(\mathbf{k}_\parallel)}{1 - f^e_{\mathbf{k}_\parallel} - f^h_{\mathbf{k}_\parallel}}$. The equation may be symmetrised by division through $\sqrt{1 - f^e_{\mathbf{k}_\parallel} - f^h_{\mathbf{k}_\parallel}}$, yielding equivalent right- and left-handed eigenfunctions.

where $Q_\lambda = \frac{e}{m_0 c} \mathbf{A} \cdot \mathbf{p}_{cv\mathbf{k}_\parallel}$ is the linear source term. Based on this result, the susceptibility is given in the exciton basis by the so-called Elliott formula [65]

$$\chi(\omega) = -\frac{e^2}{m_0^2 \omega^2} \sum_\lambda \frac{\left| \sum_{\mathbf{k}_\parallel} \mathbf{p}_{cv\mathbf{k}_\parallel} \Phi_\lambda^R(\mathbf{k}_\parallel) \right|^2}{\hbar\omega - \epsilon_\lambda + i\hbar\gamma}. \tag{2.72}$$

As the system absorption depends on the susceptibilities imaginary part, several features of the linear optical spectrum can be directly deduced from this expression. First of all, this shows that resonances occur at frequencies, that equal the excitonic eigenstate frequencies, whereat the resonances width is determined by the dephasing constant γ. Furthermore, the nominator correlates to the oscillator strength of the transition.

3. | Interaction in low dimensions – Coulomb interaction revisited

Coulomb interaction plays an important role in monolayer TMDC materials. This can for example be seen in their linear absorption spectra that exhibit clear resonances below the continuum absorption indicating excitons – bound electron-hole pairs – with large binding energies. Analyses of the differences between optical and electronic band gap show that the strong Coulomb interactions in these materials causes these excitons to have binding energies in the order of few hundred meV [18, 66, 67]. From this, the necessity of a proper description of the Coulomb interaction to model the opto-electronic properties of monolayer materials becomes evident. As introduced in section 2.2.2, two challenges arise due to density distributions that are confined within the layer on the one hand, but have a finite out-of-plane extension on the other hand. Different ansatzes have been pursued to address these challenges. Regarding the treatment of the material finite thickness the ansatzes reach from neglecting the finite extension in close proximity to the K-point and assuming point charges to introducing an effective finite thickness, e.g. via the Ohno potential, or approximating the density distribution by a step function of the layers thickness, thus, assuming line charges [32, 49]. We developed an ansatz that explicitly takes into account finite extension of the wave functions: Our ansatz is based on a derivation of the Coulomb potential of a layered structure – including environmental effects – by solving the Poisson equation for point charges, as sketched in section 2.2.2. In a next step, we consider the full three-dimensionality and $\mathbf{q}_{\parallel}$-dependence of the wave functions when calculating the Coulomb-matrix elements using the Kohn-Sham eigenfunctions. Finally, an analytical approximation is established by formulating a form factor that captures the main features of the DFT based results and successfully yields an effective approximation which can easily be included in further calculations. This ansatz is outlined in the first section of this chapter. Here, the results are elaborated for the example of MoS_2 and deviations for other material systems are pointed out where appropriate.

Thereafter, different aspects of screening effects on the Coulomb interaction, namely the influence of the dielectric environment and excited carriers and their interplay, are

discussed.

As an extensive analysis of the importance of the Coulomb interaction, its modelling and consequences for the opto-electronic properties, are already contained in our publication *"Microscopic Coulomb interaction in transition-metal dichalcogenides"* (Ref. [I]), here, I focus on a summary of key insights on a more qualitative level. For further explanations and more quantitative descriptions, the reader is referred to the original publication.
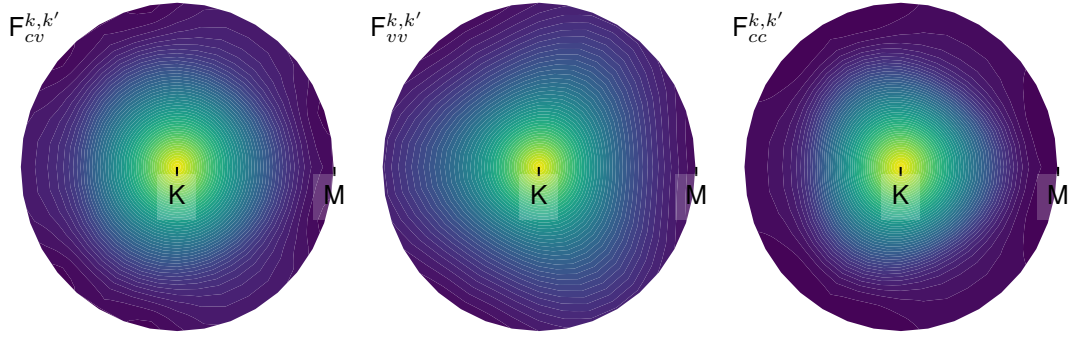
3.1 Finite thickness effects

As Fig. 2.3 illustrates, the global extrema of valence and conduction band are mainly formed by the transition metals d-orbitals and only very small contributions arise from the chalcogen atoms. Consequently, the probability density distribution is mainly localised around the transition metal atoms which includes that it is mainly localised within the monolayer, in between the chalcogen layers surrounding the transition metal sheet. As a result, even in a multilayer structure, the density distributions forming the relevant bands are only marginally affected by neighbouring layers, resulting in a relatively large independence of the band gap at the K-point. Still, the d-orbitals are not planar but the resulting wave functions have a finite extension perpendicular to the layer. To account for this finite extension, we strive for an approximation of the Coulomb-matrix elements, Eq. 2.29, on basis of the DFT wave functions in the limit of $|\mathbf{k}_\parallel - \mathbf{k}_\parallel'| = |\mathbf{q}_\parallel|$, that is most relevant for optical excitations. The matrix elements are

$$V^{\alpha,\beta,\beta',\alpha'} = V_{\mathbf{q}_\parallel}^{2D} F_{\mathbf{k}_\parallel,\mathbf{k}_\parallel'}^{\alpha,\beta,\beta',\alpha'}(\mathbf{q}_\parallel) - \Delta V_{\mathbf{q}_\parallel}^{2D} \Delta F_{\mathbf{k}_\parallel,\mathbf{k}_\parallel'}^{\alpha,\beta,\beta',\alpha'}(\mathbf{q}_\parallel), \qquad (3.1)$$

where we introduced $F_{\mathbf{k}_\parallel,\mathbf{k}_\parallel'}^{\alpha,\beta,\beta',\alpha'}(\mathbf{q}_\parallel)$ as a form factor and $\Delta F_{\mathbf{k}_\parallel,\mathbf{k}_\parallel'}^{\alpha,\beta,\beta',\alpha'}(\mathbf{q}_\parallel)$ subsuming its correlated parts. Whereas the correlated part $\Delta F_{\mathbf{k}_\parallel,\mathbf{k}_\parallel'}^{\alpha,\beta,\beta',\alpha'}(\mathbf{q}_\parallel)$ becomes zero due to the wave functions orthonormality in the long wavelength limit, the contribution due to image charges $\Delta V_{\mathbf{q}_\parallel}^{2D}$ is especially relevant in this limit. In the different limits always one of the factors of the second term in the equation is negligible, which results in an overall small contribution of their product. Thus, the overall contribution of the second term is small in comparison to the first term and the Coulomb-matrix elements of the quasi-two-dimensional structures are captured in good approximation by the exact two-dimensional term modified with the form factor $F_{\mathbf{k}_\parallel,\mathbf{k}_\parallel'}^{\alpha,\beta,\beta',\alpha'}(\mathbf{q}_\parallel)$.

Let us first take a look on an approximate calculation, where we evaluate this term on the basis of the MDF Hamiltonians eigenfunctions and assume that the wave functions k-dependence is fully captured by the MDF prefactors. We find that the inter- and intraband matrix elements in proximity to the K-point can be equally approximated by

$$F_{inter/intra}^{MDF}(\mathbf{q}_\parallel) \approx u_q^2 \int_{uc} \int_{uc} \mathrm{d}^3 r \, \mathrm{d}^3 r' \, u_{\alpha\mathbf{K}}^*(\mathbf{r}) u_{\beta\mathbf{K}}^*(\mathbf{r}') \mathrm{e}^{-\tilde{q}|z-z'|} u_{\beta'\mathbf{K}}^*(\mathbf{r}') u_{\alpha'\mathbf{K}}^*(\mathbf{r}), \qquad (3.2)$$

Abbildung 3.1: Form factor matrix elements around the K-point shown exemplary for MoS$_2$, with the K point at the center. One of the M points – $0.66\,\text{Å}^{-1}$ apart – is given for orientation.

as $\langle v\mathbf{k}'_\parallel|v\mathbf{k}_\parallel\rangle\,\langle v\mathbf{k}_\parallel|v\mathbf{k}'_\parallel\rangle = \langle c\mathbf{k}'_\parallel|c\mathbf{k}_\parallel\rangle\,\langle c\mathbf{k}_\parallel|c\mathbf{k}'_\parallel\rangle = u_k^2 u_{k'}^2 + 2u_k u_{k'} v_k v_{k'}\cos(\theta_{k-k'}) + v_k^2 v_{k'}^2 \approx u_q^2$ for $|\mathbf{k}_\parallel-\mathbf{k}'_\parallel| = |\mathbf{q}_\parallel|$ and similarly for the interband matrix, where we used that $u_K = 1$ and $v_K = 0$. The resulting graph for MoS$_2$ is shown in grey in Fig. 3.2 together with the exact calculations, where the full $\mathbf{k}_\parallel$-dependence of the wave functions is taken into account, that are shown in blueish colors and discussed later on. This MDF based approximation correctly captures the limiting case $F^{\alpha,\beta,\beta',\alpha'}_{\mathbf{k}_\parallel,\mathbf{k}'_\parallel}(\mathbf{q}_\parallel = 0) = \delta_{\alpha,\alpha'}\delta_{\beta,\beta'}$ and the decrease with larger momenta, as we would expect from theoretical considerations, but a comparison to the blueish graphs – more exact calculations – shows that the decrease is underestimated. Thus, this MDF model based approximation shows to overestimate the Coulomb interaction for larger scattering vectors and indicated the necessity of an inclusion of the full wave functions q-dependence.

The exact calculation of the form factor depends on the path in reciprocal space along which we move away from the direct band gap. In order to analyse this path-dependency, we calculated the form factor matrix elements along different paths through the BZ starting at the K point. These results for the inter- and the two intraband-matrix elements are depicted in Fig. 3.1 exemplary for MoS$_2$, where a circular area with a radius of $|\mathbf{k}_\parallel - \mathbf{k}'_\parallel| \approx 0.66\,\text{Å}^{-1}$ around the K point is shown. Similar results were obtained for all investigated materials. For the intraband contributions, the form factor shows to be isotropic up to a range of $|\mathbf{k}_\parallel - \mathbf{k}'_\parallel| \approx 0.15\,\text{Å}^{-1}$, for the interband contributions, this holds up to a range of $|\mathbf{k}_\parallel - \mathbf{k}'_\parallel| \approx 0.45\,\text{Å}^{-1}$ for molybdenum- and $|\mathbf{k}_\parallel - \mathbf{k}'_\parallel| \approx 0.30\,\text{Å}^{-1}$ for tungsten-based materials. But even for larger scattering vectors, the angular dependence is small. This observation legitimises to employ an isotropic approximation of the form factor. As a consequence, we have used a weighted average of the calculations for different paths for further analysis.

Averaged results for the inter- and intraband matrix elements are illustrated in blueish colors in Fig. 3.2. In proximity to the high symmetry point and up to $|\mathbf{k}_\parallel-\mathbf{k}'_\parallel| \approx 0.22\,\text{Å}^{-1}$,

these matrix elements are of comparable slope. For larger distances the intraconduction band form factor decreases faster than the inter- and intravalence band terms. This behaviour holds for all material systems investigated in the course of this thesis, but the general slope of the form factor steepens with the mass of the incorporated atoms. Thus, the slope is slightly steeper for tungsten- than for molybdenum-based materials and steepens for materials containing tellurium in comparison to those containing selenium. As the form factor was introduced as a measure of the deviation of the exact two-dimensional Coulomb potential, this trend resembles the expectation as larger incorporated atoms lead to larger deviations – the material is for larger atoms 'less two-dimensional'.

In order to describe the slope of the decrease properly and to simplify the expressions for consecutive calculations it is useful to find an analytical formulation to approximate the form factor. Here, we started with the approach of including a finite thickness (d) by means of the so-called Ohno potential, $F(\mathbf{q}) \approx e^{-q_\parallel d}$, that was established in the description of molecules and nanotubes but also successfully applied in the description of graphene [61, 68, 69]. As we found that the Ohno potential can not be fitted properly to the form factor, we extended the formula and described the form factor by $F(\mathbf{q}) \approx e^{-(\sigma^2 q_\parallel^2/2 + q_\parallel d)}$. Furthermore, we additionally included the prefactors arising from the overlap matrix elements in the MDF model in this fit function in the cases where we applied the MDF model in subsequent calculations.

Further insights on the physical interpretation of this form factor can be gained by taking a look at its real space representation that is given by $V(\mathbf{r}_\parallel) = \sum_{\mathbf{q}_\parallel} e^{i\mathbf{q}_\parallel \cdot \mathbf{r}_\parallel} F(\mathbf{q}_\parallel) V_{\mathbf{q}_\parallel}^{2D}$ $= \frac{1}{2\pi\sigma^2} \int d^2 r_\parallel' \, e^{-|\mathbf{r}_\parallel - \mathbf{r}_\parallel'|/2\sigma^2} \frac{1}{\sqrt{r_\parallel'^2 + d^2}}$ and illustrated in Fig. 3.2. While the exact two-dimensional potential and the quasi-two-dimensional potential are equal for distances $|\mathbf{r}_\parallel \geq 7\text{Å}|$, for small distances the exact potential diverges whereas the modified one reaches a finite value. The comparison shows that the exponent linear in $\mathbf{q}_\parallel$ results in a regularisation of the Coulomb potential for $\mathbf{r}_\parallel = 0\,\text{Å}$ by introducing an effective thickness d and thereby suppressing the divergence. Due to the effective thickness term, the denominator $\sqrt{r_\parallel'^2 + d^2}$ that enters the Coulomb potential and that is responsible for the divergence does not approximate $0\,\text{Å}$ any more but approximates this finite thickness, $0\,\text{Å}+d$, through which the potential remains finite even at the origin. This linear expression resembles the previously mentioned Ohno potential. Additionally, the exponent quadratic in $\mathbf{q}_\parallel$ leads to a convolution of this linear expression with a Gaussian of width σ.

In conclusion, we found that the modifications of the Coulomb interaction resulting from finite extension of the wave functions perpendicular to the sample can be captured in good approximation by an isotropic model. This modification can be analytically modelled and taken into account in subsequent calculations by means of a form factor.
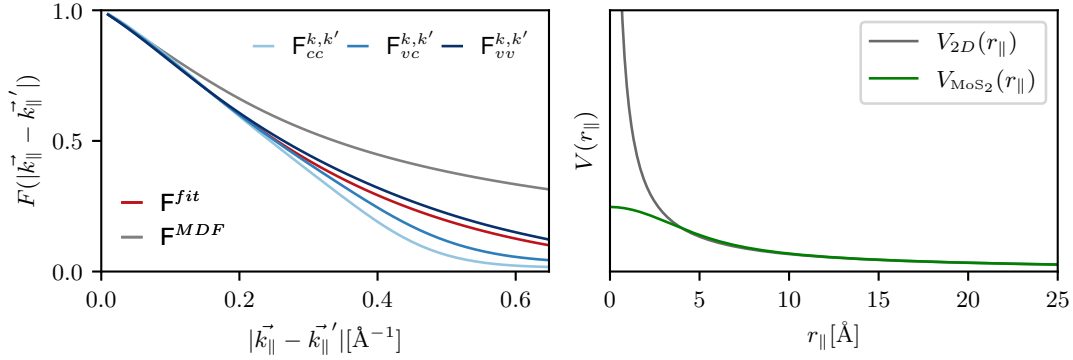
Abbildung 3.2: Form factor and resulting real-space Coulomb potential. Left panel: Form factor for inter- and intraband Coulomb-matrix elements for MoS$_2$ (blueish) as calculated based on full wave functions and comparison to quasi-MDF approximation, where q-dependencies are only included in the exponential and the main contribution of the MDF prefactor (grey). In red, the analytic approximation of the form factor is shown. Right panel: Comparison of two-dimensional real-space Coulomb potential with (green) and without (grey) including a form factor.

3.2 Screening of the Coulomb interaction – Influence of surrounding and increased carrier density

Besides the regularisation of the Coulomb potential for small distances due to the material finite extension perpendicular to the layer, this also causes high sensitivity to screening effects i.e. due to the environment or carrier populations. Here, we study how these environment- and carrier-induced effects on the screening reveal themselves in a renormalisation of the band gap and changes of the excitonic resonance energies. Here, we discuss the dependencies only with respect to the A-bands, similar results can be obtained for the B-bands.

The renormalised band gap in presence of excited carriers is given by

$$\tilde{\Delta} = \Delta_{s\tau} + \sum_{\mathbf{k}'_\parallel \neq \mathbf{k}_\parallel} \left(W^{eeee}_{\bar{\mathbf{k}}_\parallel - \bar{\mathbf{k}}'_\parallel; \bar{\mathbf{k}}'_\parallel; \bar{\mathbf{k}}_\parallel} - W^{hehe}_{\bar{\mathbf{k}}_\parallel - \bar{\mathbf{k}}'_\parallel; \bar{\mathbf{k}}'_\parallel; \bar{\mathbf{k}}_\parallel} \right) \left(1 - f^h_{\mathbf{k}_\parallel} - f^e_{\mathbf{k}_\parallel} \right). \tag{3.3}$$

This shows that the band gap is influenced by two contributions. On the one hand, there is the Coulomb interaction that is changed depending on the dielectric environment and screened by excited charge carriers – as included in the interaction with image charges ΔW and through the Lindhard polarisation function respectively. Comparing the excitation-induced band gap shrinkage (see publication [I] for a detailed comparison) to experimental data we found that treating the Lindhard polarisation in the static limit $\hbar\omega \to 0$, successfully applied for many semiconducting systems, overestimates the scree-
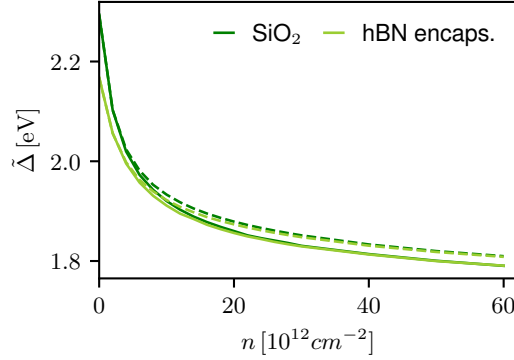
Abbildung 3.3: Influences of dielectric environment and excited carriers on the screening of the Coulomb energy as it indirectly manifests in the changes of band gap. The excitation-induced band gap renormalisation is shown for MoS_2 in two different dielectric environments and for different processes of carrier creation: Solid lines resemble optical excitation with equal number of electrons and hole, dashed lines resemble electron doping. In the dynamical screening a triplet dephasing of $\gamma_T = 150\,\mathrm{meV}$ is included.

ning for small carrier densities. Similarly, in another project the simulation of a probe experiment showed that calculating the dynamics of the microscopic polarisation in this static limit results in unphysical absorption behaviour (see publication [III]). These two observations emphasise the necessity to reconsider the application of this static limit and the treatment of the frequency-dependence. While the band gap properties are captured to a good approximation assuming the dominant time contribution being proportional to $e^{i(\Sigma_{\mathbf{k}_\parallel}^e - \Sigma_{\mathbf{k}_\parallel}^h)t}$, for the description of the systems optical behaviour the full frequency-dependence of the Lindhard polarisation had to be taken into account. Additionally, a large triplet dephasing in the order of few 100 meV had to be included to match experimental observations on the excitation-induced band gap shrinkage. The role and impact of the triplet dephasing will be discussed in more detail in Ch. 6.

Furthermore, phase space filling effects contribute to the shrinkage of the band gap with increasing carrier density via $\left(1 - f_{\mathbf{k}_\parallel}^h - f_{\mathbf{k}_\parallel}^e\right)$. Whereas screening can be seen as a global phenomenon in the sense that excited carriers with certain crystal momenta affect the Coulomb interaction for all carriers, phase space filling effects can be considered to act more locally as they only affect the bands and valleys, the carriers are located at.

To analyse the complex interplay of these different contributions, in Fig. 3.3 we compare the carrier density-dependent band gap shrinkage for MoS_2 in different dielectric environments. Furthermore, we analyse how the distribution of the carriers in the different bands affects the band gap renormalisation. Therefore, we compare a scenario of optically excited carriers, where equal amounts of carriers occupy the electron and hole

band, and a scenario of electron doping. In both scenarios, we assume that the carriers are Fermi distributed at a temperature of 300 K and occupations of the A and B band are equal. Thus,

$$f_{i\mathbf{k}_\parallel}^{e/h}\left(\mu_i^{e/h}, T = 300\,\mathrm{K}\right) = \left(\mathrm{e}^{\beta\left(\Sigma_{i\mathbf{k}_\parallel}e/h - \mu_i^{e/h}\right)} + 1\right)^{-1}, \qquad \text{with } \beta = k_\mathrm{B}T,$$

with temperature T and $\mu_i^{e/h}$ denoting the band-dependent chemical potential – with $i = \sigma, \tau$ summarising band and valley index. The chemical potentials are assumed to be decoupled and determined by the condition that the total number of carriers equals the k-space integration of the distribution.

For the unexcited samples, we find band gaps (A-band) of 2.279 eV and 2.16 eV for MoS$_2$ on a SiO$_2$ substrate and encapsulated in hBN, respectively. Thus, through the increase of the dielectric screening by changing the substrate, band gap changes in the range of more than 100 meV can be expected. Both values are in good agreement with experimental findings deduced from photoluminescence (PL) and scanning tunnelling spectroscopy (STS) measurements [70, 71]. Similar good agreements both concerning absolute energy values and relative band gap changes due to the environment-induced changes in screening were found for all material systems including molybdenum-based materials. A detailed table comparing our results to experimental and theoretical findings can be found in publication [I]. For tungsten-based material systems, the relative changes were captured in good agreement with experimental deductions. Concerning the absolute values our calculations predict values that are about $100 - 200$ meV below experimentally predicted values – even though these experimental values spread over a wide range of up to 600 meV demonstrating the sensitivity of the deduction of the quasiparticle band gap from experiments on the underlying theoretical model and the sample quality. As it is well known that DFT underestimates the band gap, we assume that these discrepancies between our results and the experimental findings may be a consequence from this uncertainty. Despite the discrepancies in absolute values, our model for the Coulomb interaction can successfully describe the influence of the dielectric environment on the band gap. Thus, in contrast to standard DFT and GW calculations, where the dielectric environment needs to be included explicitly, which results in numerically very costly calculation, our model of the Coulomb interaction enables us to predict the influence of any dielectric environment in a computationally efficient and parameter-free way.

Besides the environmental screening, screening due to an enhancement of the carrier densities induces a reduction of the band gap. While for small carrier densities screening effects dominate the band gap behaviour, where contributions of environment- and density-induced screening contribute, the increased splitting between the dashed and the solid line in Fig. 3.3 manifest the complex interplay of screening and phase space filling effects for larger carrier densities. For medium to large carrier densities, the envi-
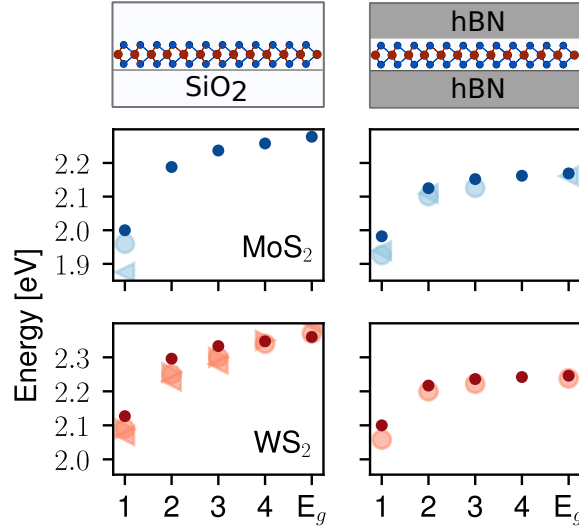
Abbildung 3.4: Influence of dielectric environment on the excitonic spectrum. In the top row, the structure of the different environmental settings is sketched. Calculated exciton resonance energies and band gap together with experimental findings (light colors) for MoS_2 (middle) and WS_2 (bottom) for different environmental setting. For a better comparability, the band gap is shifted by $149\,meV$ for WS_2-based systems, as discussed in the text. Experimental findings are taken from [30, 31, 66, 70, 72, 73, 74, 75, 76]. (According to publication [I].)

ronmental screening fade into the background. Here, the effects occurring from different distributions of the carriers dominate the effects of the dielectric environments. For a symmetric excitation of electrons and holes – as by optical excitation –, phase space filling contributes both to valence and conduction band renormalisation. In contrast, in the case of electron doping, phase space filling only contributes to a conduction band renormalisation and the valence band is shifted only due to screening of the Coulomb-hole contribution. The former leads to a steeper slope for the band gap renormalisation than the latter. For larger densities, the overall slope of the band gap reduction becomes flatter and the environmental contributions get negligible in comparison to the differences in density distribution.

The comparably large Coulomb interaction in quasi-two-dimensional materials does not only result in large band gap renormalisation effects as described above, but also in large excitonic binding energies in the range of several hundred meV. To analyse the effects of dielectric screening on the excitonic resonance and binding energies, we analyse the excitonic spectra for different materials. In Fig. 3.4 the resonance energies and band gap calculated by solving the Dirac-Wannier equation, Eq. 2.70, for four different material

systems are depicted. With the applied model for the Coulomb interaction, the known non-hydrogenic exciton series can be reproduced and is in good agreement with experimental findings marked by differently shaped light coloured symbols. Note that due to the previously discussed systematic underestimation of the non-interacting band gap for tungsten-based materials, we shifted the gap by $149\,$meV prior to renormalisation and calculation of the excitonic resonances. Furthermore, it can be seen in Fig. 3.4 that for all material systems, the influence of the dielectric environment mainly affects higher excitonic resonances and the band gap, whereas the lowest exciton resonance is more or less unaffected by a change of the dielectric environment. Both, the higher resonance energies and the band gap experience a pronounced red shift with an increase of the dielectric screening. In contrast, for the lowest exciton resonance, the renormalisation of the band gap and of the binding energy nearly cancel out resulting in a very small red shift of the resonance. Consequently, comparing the samples embedded on a SiO_2 substrate and encapsulated in hBN, the 1s exciton binding energy reduces, for both TMDC samples, by $90-100\,$meV, whereas the binding energy of the higher states is reduced only by about a third of this amount.

4. Excitons in a magnetic field – tunable gain and absorption spectra

As discussed in the previous chapter, the strong Coulomb interaction causes large exciton binding energies. So far, we only analysed the s-type excitonic resonances. Due to the optical selection rules, only these excitonic states can be formed upon single-photon processes and are therefore referred to as 'bright' excitons. But, comparable to atomic states, there are further excitonic states which are called optically 'dark' as they can not be addressed by single-photon processes. Nevertheless, for example p-type excitonic states are accessible via two-photon processes processes or can be addressed in properly pre-excited samples, by inducing transitions between optically bright s- to optically dark p-type excitonic states by means of a second light pulse. In TMDC materials, these intraexcitonic transitions take place energetically in the mid-IR- to THz-range, thus, they can be studied by optical pump-THz probe-experiments (OPTP) [77, 78, 79]. Here, s-type excitonic populations build up after excitation by an optical pulse and intraexcitonic transitions are mediated by a second pulse in the THz-regime. Depending on the initial conditions after excitation, intraexcitonic transitions can lead to an absorption or amplification of the probing THz light.

Additionally, the energetic spectra of a material can be manipulated by external modifications of the setup, for example by changing the samples dielectric environment or applying an external magnetic field.

In our publication *"Magnetic-field tuning of the intraexcitonic absorption and gain in transition metal dichalcogenides"* (Ref. [II]), we investigated the influences of a magnetic field – applied perpendicular to the sample – on the energetic spectrum of the excitons and its manifestation in absorption spectra when an initial occupation of s-type excitonic states is assumed. Here, main insights of this study are summarised. Note, that in contrast to the published data, the encapsulating hBN was modelled by an effective dielectric screening of $\kappa = 4.5$ to be consistent within the scope of this thesis. The consequences of the exact choice of the effective dielectric constant will be discussed in Sec.

4.2.3. Moreover, in addition to the published data, the interplay of the magnetic field-induced and the screening induced energetic shifts as well as the material-dependence of the observed tunability of the intraexcitonic spectra will be discussed.

4.1 Influence of a magnetic field on the excitonic spectrum

The application of a magnetic field perpendicular to the sample results in a change of its electronic structure. As introduced in Sec. 2.2.2, the magnetic field induces a Zeeman shift linear to the angular momentum as well as a diamagnetic shift. Concerning a materials optical properties, both the influence on the ground state band structure and on the excitonic energy states needs to be considered. In the following, the different contributions resulting from a Zeeman and diamagnetic shift are separated and analysed independently.

For TMDC materials, the optically interesting bands at the main valleys are primarily composed of the transition metals d-orbitals. While the d_{z^2}-orbitals forming the conduction bands display an angular momentum quantum number of $m_z = 0$, the angular momentum of the orbitals forming the valence band is $m_z = \pm 2$. Due to the different character of the valence bands at the different valleys, the difference in their angular momentum quantum number $|\Delta m_z| = 4$ induces a Zeeman splitting between the different main valleys non-interacting groundstate which is further increased by the gap renormalisation. Theoretical results show g-factors slightly larger than 4 and are in good agreement with experimental findings [76, 80, 81]. At each valley, the Zeeman shift influences the excitonic states. The optically bright s-type excitons have an angular momentum quantum number of zero and therefore no Zeeman shift would be expected for these states. Nevertheless, a small linear shift in the range of few meV is seen that can be referred to the magnetic field dependent modification of the ground state. Thus, the s-type states experience an indirect Zeeman shift. For the optically dark p-states on the other hand, the term $\propto \hat{l}_z$ results in a splitting of the excitons with positive and negative angular momentum and an enhancement, respective reduction, of the magnetic g-factor proportional to the inverse reduced mass, as can be expected from the Wannier equation.

The diamagnetic shift, in contrast, directly leads to a shift for all excitonic states. Numerically, we employ the relation $\hat{r} = i\nabla_{\mathbf{k}}$ and approximate the resulting second derivative by a first order central finite difference method – at the boundaries of our grid, we employ the forward/ backward finite difference method – to include this diamagnetic contribution in the Wannier equation. The diamagnetic shift increases with the radial extension of the eigenstate that in turn increases with its main quantum number. Consequently, the shift is more pronounced for higher excitonic states. Furthermore, we find that the diamagnetic shift is more pronounced for the s- than for the corresponding p-states which again can be referred to the radial extension and is in correspondence with the larger
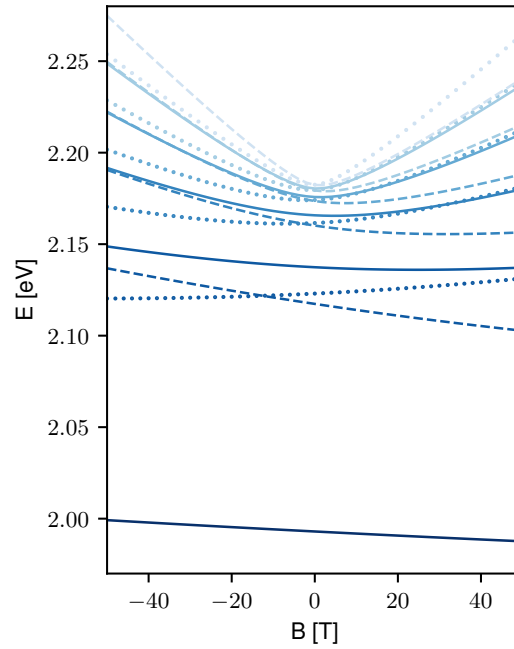
Abbildung 4.1: Magnetic field-dependent exciton spectrum at the K-valley for s-(solid lines) and $p^{\pm}$-excitons (dashed, dotted lines) in hBN encapsulated MoS_2. p-type excitons are below s excitons of equal quantum number n.

binding energy.

The resulting magnetic field dependent excitonic resonances are shown in Fig. 4.1, both for the s- and p-type excitons at the K valley. The corresponding spectrum at the K' valley is obtained by reversing the sign of the magnetic field and, concerning the p-states, interchanging p^+ and p^-. Here, the differing influence of the magnetic field on the various excitonic states as described above can be seen. The s-state resonances lie energetically below the p-state resonances of equal main quantum number, but due to the different behaviour under application of a magnetic field, these differences are strongly field-dependent. This tunability opens up possibilities for optical applications, as intraexcitonic transitions are in the technologically interesting mid-IR to THz range.

4.2 Optical Pump – Terahertz Probe Experiments

4.2.1 Terahertz-Elliott Formula

To gain further insights into the consequences of the above described intraexcitonic transitions on the interaction with an optical field, we want to analyse the systems linear absorption spectrum. As introduced above, interesting intraexcitonic transition are energetically in the range below 150 meV. Consequently, they can be probed by low

intensity radiation in the mid-IR to THz regime. In this regime, the electromagnetic field primarily induces an intraband current and the induced interband current contributions are negligible. In effective mass approximation, the intraband current, Eq. 2.38, can be written as

$$\mathbf{j}_{intra} = -e \sum_{\alpha \mathbf{k}_\parallel} \hbar \mathbf{k}_\parallel \left(\frac{1}{m_\alpha} f^\alpha_{\mathbf{k}_\parallel} \right).$$ (4.1)

Taking its derivative, we can insert the equations of motion for the density distributions yielding

$$
\frac{\mathrm{d}}{\mathrm{d}t}\mathbf{j}_{intra} = \frac{2e}{\hbar m_r} \Im \left\{ \sum_{\mathbf{k}_\parallel, \mathbf{Q}_\parallel, \mathbf{q}_\parallel} \hbar \mathbf{k}_\parallel V^{cvvc}_{\mathbf{q}_\parallel, \mathbf{k}_\parallel + \mathbf{q}_\parallel, \mathbf{k}_\parallel} \langle a^\dagger_{c,\mathbf{k}_\parallel + \mathbf{Q}^e_\parallel} a_{v,\mathbf{k}_\parallel - \mathbf{Q}^h_\parallel} a^\dagger_{v,\mathbf{k}_\parallel - \mathbf{q}_\parallel - \mathbf{Q}^h_\parallel} a_{c,\mathbf{k}_\parallel - \mathbf{q}_\parallel + \mathbf{Q}^e_\parallel} \rangle \right\}
$$
$$
+ \frac{2e^2}{m_r \hbar c} \Im \left\{ \sum_{\mathbf{k}_\parallel} \hbar \mathbf{k}_\parallel \mathbf{A} \cdot \mathbf{p}_{cv\mathbf{k}_\parallel} \right\},
$$

with the reduced mass m_r and momenta $\mathbf{Q}^{e/h}_\parallel = \frac{m_{e/h}}{m_e + m_h} \mathbf{Q}_\parallel$. In the following, we omit the term proportional to the interband dipole matrix as this term has insignificant contributions for low-frequency fields and is thus negligible even in an OPTP scenario, if the different pulses are temporally separated.

As we are interested in intra-excitonic absorption, it is intuitive to make a basis transformation and express the intraband current in terms of excitonic creation and annihilation operators. For the symmetrised WE, the operator annihilating an exciton in state λ reads

$$B^\dagger_\lambda(\mathbf{Q}_\parallel) = \sum_{\mathbf{k}_\parallel} \frac{\psi^*_\lambda(\mathbf{k}_\parallel)}{\sqrt{1 - f^e_{\mathbf{k}_\parallel} - f^h_{\mathbf{k}_\parallel}}} a^\dagger_{v,\mathbf{k}_\parallel - \mathbf{Q}^h_\parallel} a_{c,\mathbf{k}_\parallel + \mathbf{Q}^e_\parallel}.$$ (4.2)

Inserting this expression in the equation of motion for the intraband current and using that $\psi_\lambda(\mathbf{k}_\parallel)$ are eigenstates of the DWE with eigenvalues ϵ_λ, we find for the intraband current in the exciton basis

$$i\hbar \frac{\mathrm{d}}{\mathrm{d}t} \mathbf{j}_{intra} = \sum_{\lambda \lambda'} \mathbf{j}_{\lambda \lambda'} (\epsilon_{\lambda'} - \epsilon^*_\lambda) n_{\lambda \lambda'} - i\hbar \Gamma \mathbf{j}_{intra}.$$ (4.3)

Here, we introduced the excitonic current matrix $\mathbf{j}_{\lambda \lambda'} = \frac{e}{m_r} \sum_{\mathbf{k}_\parallel} \psi^*_\lambda(\mathbf{k}_\parallel) \hbar \mathbf{k}_\parallel \psi_{\lambda'}(\mathbf{k}_\parallel)$ and the excitonic density operator $n_{\lambda \lambda'} = \sum_{\mathbf{Q}_\parallel} \langle B^\dagger_\lambda(\mathbf{Q}_\parallel) B_{\lambda'}(\mathbf{Q}_\parallel) \rangle$, where the diagonal elements describe populations of true excitons and off-diagonal elements a correlated electron-hole plasma. Additionally, a phenomenological dephasing rate Γ for the macroscopic THz-induced intraband current is included. Note, that the well known optical selection rules for intraexcitonic transitions follow directly from the formulation of the

excitonic current matrix. Based on symmetry, an excitonic current matrix element is non-zero only for excitonic states of opposite parity. In particular, it vanishes for transitions between excitons of equal angular momentum, but has a finite contribution for transitions between s- and $p^{\pm}$-states. The optical selection rules are thus comparable to the atomic dipole transition rules. The excitonic density operator is determined by its equation of motion reading

$$
i\hbar \frac{\mathrm{d}}{\mathrm{d}t} n_{\lambda\lambda'}(\mathbf{Q}_{\parallel}) = (\epsilon_{\lambda'} - \epsilon_{\lambda}) \, n_{\lambda\lambda'}(\mathbf{Q}_{\parallel}) + \frac{1}{c} \sum_{\lambda''} (\mathbf{j}_{\lambda\lambda''} n_{\lambda''\lambda'} - n_{\lambda\lambda''} \mathbf{j}_{\lambda''\lambda'}) \cdot \mathbf{A}_{THz}
$$
$$
+ \, i\hbar \frac{\mathrm{d}}{\mathrm{d}t} n_{\lambda\lambda'}(\mathbf{Q}_{\parallel}) \Big|_{corr}. \quad (4.4)
$$

Treating the scattering contributions by a phenomenological dephasing, $\frac{\mathrm{d}}{\mathrm{d}t} n_{\lambda\lambda'}(\mathbf{Q}_{\parallel})\big|_{corr} = -\gamma n_{\lambda\lambda'}(\mathbf{Q}_{\parallel})$, the above equations of motion can be solved by Fourier transformation. This results in the THz-Elliott formula for the susceptibility [60]:

$$
\chi_{THz}(\omega) = \frac{c}{\omega^2} \frac{\delta \mathbf{j}_{intra}}{\delta \mathbf{A}_{THz}}
$$
$$
= \frac{1}{\omega^2} \sum_{\lambda\lambda'\lambda''} \frac{1}{\hbar\omega - i\hbar\Gamma} \frac{\epsilon_{\lambda'} - \epsilon_{\lambda}^*}{\hbar\omega - \epsilon_{\lambda'} + \epsilon_{\lambda}^* + i\hbar\gamma} \mathbf{j}_{\lambda\lambda'} (\mathbf{j}_{\lambda\lambda''} n_{\lambda''\lambda'} - n_{\lambda\lambda''} \mathbf{j}_{\lambda'\lambda''}). \quad (4.5)
$$

The optical absorption is proportional to the susceptibilities imaginary part. Consequently, resonances in the absorption spectra arise for optical frequencies matching energetic differences between excitonic states, $\hbar\omega = \Re\{\epsilon_{\lambda'} - \epsilon_{\lambda}^*\}$. Their amplitude depends on the initial excitation state of the sample as well as the energy difference between the states. Furthermore, in contrast to optical absorption arising from interband currents, the amplitude may involve all and not only initial and final state. In the following, the optical absorption spectra for specific initial conditions and their tunability by application of a magnetic field and changes in the dielectric environment are discussed. Finally, the material-dependence of the optical spectra is analysed.

4.2.2 Tuning the absorption via a magnetic field

To analyse varying dependencies of the absorption spectrum, we restrict ourselves to two particular scenarios, namely an initial occupation of the $1s$- and $2s$- excitonic states, respectively, without microscopically studying the exciton formation processes [79]. In these cases, the susceptibility is linear proportional to the initial exciton density. Furthermore, we restrict our analyses to the K valley, as the respective spectra at the K' can be deduced from these.

In Fig. 4.2, the upper row shows the absorption spectra for an initial occupation of the $1s$ state and circular polarised light. Here, the dominant contribution arises from the $1s \rightarrow 2p^{\pm}$ transition, where the absorption of $\sigma^{\pm}$ photons induces transitions to $2p^{\pm}$,
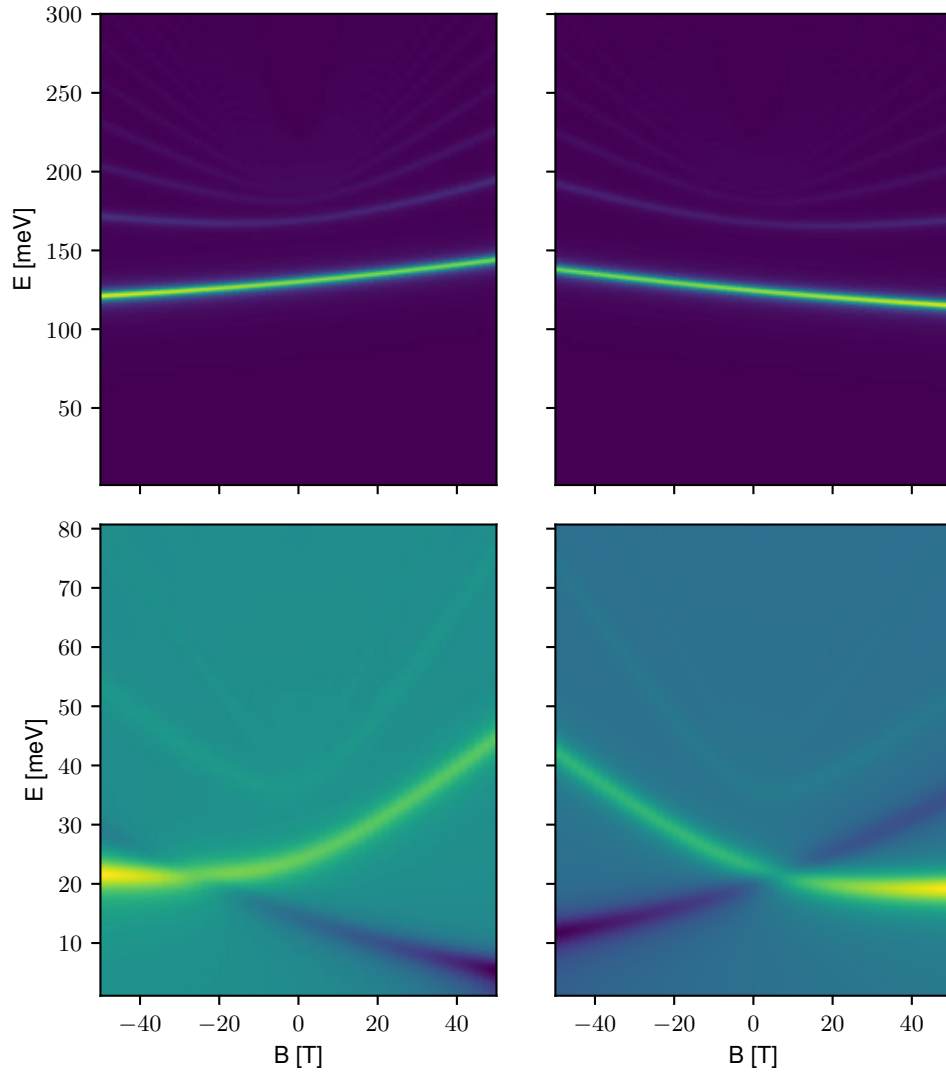
Abbildung 4.2: Magnetic field dependent absorption spectra for different initial exciton populations and polarisation sequences. Upper row: Initial $1s$-population. Absorption due to transition from $1s$ to np states. Lower row: Initial $2s$-population. Positive and negative absorption separate upon application of magnetic field. Left panels: Co-polarised light, Right panels: Cross-polarised light. Phenomenological decay rates of $\gamma = 10\,\mathrm{meV}/\hbar$ and $\Gamma = 2.5\,\mathrm{meV}/\hbar$ are assumed.

respectively. It can be seen, that the transition oscillator strength increases with increasing field strength, making transitions to higher excitonic states visible at higher field strengths.

When assuming that not the ground state but an excited state is populated initially, absorptive and gain features compete, as transitions to lower $p^{\pm}$ states correspond to an emission of photons, while the transition to higher states occurs upon the absorption of photons. In the lower row of Fig. 4.2, the absorption spectra for an initial occupation of the $2s$ state is shown. At low magnetic fields, the competing processes result in a partly superposition of absorptive and gain features resulting in a low net gain, but by applying a magnetic field these features can be shifted with respect to each other resulting in more pronounced gain.

As discussed in the previous section, the $p^{\pm}$ states behave differently under application of a magnetic field as the Zeeman shift explicitly depends on the angular momentum quantum number. As a consequence, the absorptive and gain features separate in opposite directions depending on the polarisation direction of the light.

4.2.3 Tuning the gain via the dielectric surrounding

As discussed in Sec. 3.2, the energetic position of the excitonic states can additionally be changed by the dielectric environment. Here, we want to examine, how this additional screening influences the intraexcitonic absorption, when an external magnetic field is applied.

The excitonic binding energies reduce for enhanced screening, which only partly compensates with the decrease of the band gap but overall results in a red-shift of the resonances. The spectral shift is not equivalent for all excitonic states but it is more pronounced for higher excitonic states, thus, for states that are extended further in real space, the changes in screening are more influential. In particular, this affects the energetic separation between the $2s$- and the p-states and allows a tuning of the THz-probe spectra by changing the dielectric environment. In Fig. 4.3, the spectra of a MoS_2 sample encapsulated in materials with dielectricity – modelled by changing the effective dielectric constant $\kappa = \sqrt{\epsilon_{\parallel}\epsilon_{\perp}}$ – is shown for a magnetic field with $B = 20\,\mathrm{T}$ and co-polarised pulses. Both the gain-region ($2s \rightarrow 2p^{+}$ transition) and the absorption-region ($2s \rightarrow 3p^{+}$ transition) are red-shifted upon increasing the dielectric constant and their energetic separation decreases. Hereby, the relative shift with enhanced screening decreases with increasing dielectric screening and the energetic difference between the $2s \rightarrow 2p$ and $2s \rightarrow 3p$ transition reduces. While the total shift of the peaks is in the order of $40\,\mathrm{meV}$, their difference energy reduces by $5\,\mathrm{meV}$ only. Furthermore, the intensity of the signals varies, namely, the peak gain and absorption are reduced with increasing dielectric screening.
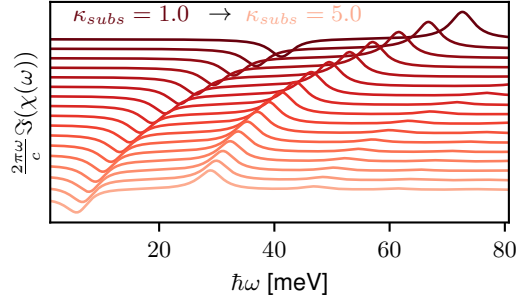
Abbildung 4.3: Absorption spectrum for MoS_2 in dependence on the environmental screening (encapsulated sample) for an initial $2s$-exciton population. The magnetic field is kept fixed with $B = 20\,T$ and the pump and probe pulse are co-polarised.

4.2.4 Material-dependence

All previous analyses were executed exemplary for the widely studied material MoS_2. Naturally, the question arises, in which way the observations alter when interchanging not the dielectric surrounding but the basic material itself. Therefore, in Fig. 4.4, we exemplary compare the magnetic field dependent absorption spectra for MoS_2 and its tungsten-based correspondent WS_2, both encapsulated by hBN layers, for an initial occupation of the $n_{\lambda\lambda'} = n_{2s}$ at the K point for σ^+-polarised light.

Besides the smaller absolute intraexcitonic transition energies, in this juxtaposition, two aspects stand out. First, the oscillator strength for the optical transitions in the tungsten-based material is larger than in the molybdenum base material such that even transition to the $5p^+$-state are clearly visible, especially when a magnetic field is applied. Second, also the magnetic field induced changes are more pronounced in the tungsten- than in the molybdenum-based material. While the absorption and gain peak shift about $25\,meV$ for MoS_2, the shifts are $10/15\,meV$ larger for WS_2.

Both observations are in accordance with the smaller reduced mass in WS_2 ($m_r(WS_2) = 0.161m_e$) than in MoS_2 ($m_r(MoS_2) = 0.161m_e$), as both the current matrix element $j_{\lambda\lambda'}$ determining the oscillator strength and the magnetic field-induced changes in the Wannier equation depend on the inverse of the reduced mass.

Consequently, a smaller reduced mass results in an enhancement of oscillator strength and magnetic field-induced changes.
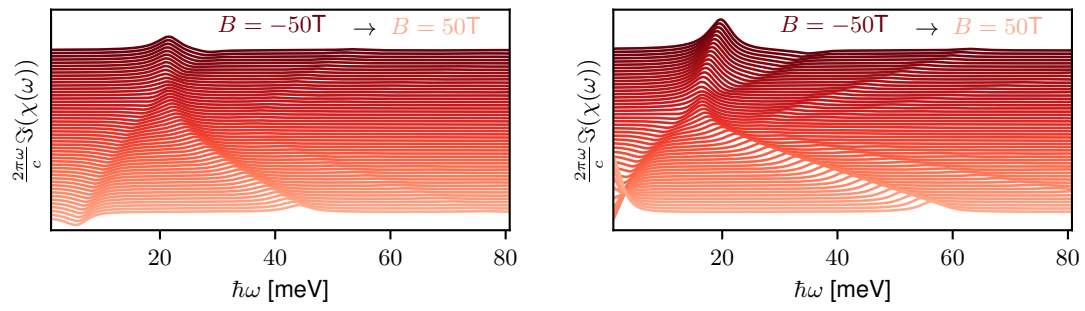
Abbildung 4.4: Magnetic field dependent absorption spectrum for initial 2s-exciton population and different materials embedded in hBN. Left panel: MoS_2; Right panel: WS_2.

5. | Relaxation on a higher level – scattering through the full Brillouin zone

In order to analyse the carrier dynamics in TMDC materials, we investigated the temporal evolution of the material properties upon optical excitation above the quasiparticle band gap. When exciting the sample close to the direct quasiparticle band gap, it is legitimate to assume that the interaction with the optical pump pulse mainly results in the creation of carriers close to the main gap. Thereafter, different scattering processes cause a reordering of the carriers within the bands. In bulk materials, intervalley scattering processes were seen to take place on $10^1 - 10^2$ fs timescales [82, 83], but in contrast to bulk materials, monolayers exhibit a direct band gap and $MoTe_2$ exhibits a large offset between global and local conduction band minimum. Both of these aspects reinforce the assumption of larger intervalley scattering times in monolayer materials. Hence, in a first study, that led to publication "*Ultrafast band-gap renormalization and build-up of optical gain in monolayer* $MoTe_2$" (Ref. [III]), we focused on this area in reciprocal space and employed the MDF model that only captures the behaviour in this area. Nevertheless, to gain first insights on the changes due to carrier relaxations into the side valley, in a next step, we analysed the linear response upon an ultrashort, low-intensity pulse and changes in the gain spectra when comparing the scenario before and after intervalley relaxation processes and an equilibration of the carriers in the bands took place. In a consecutive study, summarised in "*On the importance of electron-electron and electron-phonon scatterings and energy renormalizations during carrier relaxation in monolayer transition-metal dichalcogenides*" (Ref. [IV]), we extended our model and explicitly took into account the full two-dimensional band structure enabling the detailed analysis of different relaxation processes including intra- as well as intervalley scattering.
The carrier dynamics were analysed exemplary for $MoTe_2$.

<h3>5.0.1   Analysis of excitation and relaxation dynamics at the K-point</h3>

To analyse the carrier dynamics in proximity to the K-point, we simulate the interaction of $MoTe_2$ with a pump pulse of central frequency slightly above the interacting B-band gap ($\hbar\omega \gtrsim \tilde{\Delta}_B$) with aid of the DBE, Eq. 2.52. Considering the excitation and relaxation dynamics it was seen that the exact dephasing of the microscopic polarisation is of minor importance such that it is sufficient to include higher order scattering contributions on the screened Hartree-Fock level. Thus, we replaced in Eq. 2.52 the Coulomb-matrix elements by their respective screened counterparts, including plasma screening in the static limit. The carrier scattering terms were treated within Markov approximation and the explicit quantum-Boltzmann-like scattering rates due to carrier-carrier and carrier-phonon interaction read

$$
\begin{aligned}
\left.\frac{\mathrm{d}}{\mathrm{d}t} f^{\alpha}_{i\mathbf{k}_{\parallel}}\right|_{el} &= \frac{2\pi}{\hbar} \sum_{\mathbf{q}_{\parallel}\neq 0} \; W_{\mathbf{q}_{\parallel}} \sum_{j,\mathbf{p}_{\parallel}} \left(V_{\mathbf{q}_{\parallel}} - V_{\mathbf{k}_{\parallel}-\mathbf{p}_{\parallel}}\delta_{ij}\right) \mathcal{D}\left(\tilde{\Sigma}^{\alpha}_{i\mathbf{k}_{\parallel}} - \tilde{\Sigma}^{\alpha}_{i\mathbf{k}_{\parallel}-\mathbf{q}_{\parallel}} - \tilde{\Sigma}^{\alpha}_{j\mathbf{p}_{\parallel}} + \tilde{\Sigma}^{\alpha}_{j\mathbf{p}_{\parallel}-\mathbf{q}_{\parallel}}\right) \\
&\quad \times \left[f^{\alpha}_{i\mathbf{k}_{\parallel}} \bar{f}^{\alpha}_{i\mathbf{k}_{\parallel}-\mathbf{q}_{\parallel}} f^{\alpha}_{j\mathbf{p}_{\parallel}-\mathbf{q}_{\parallel}} \bar{f}^{\alpha}_{j\mathbf{p}_{\parallel}} - \bar{f}^{\alpha}_{i\mathbf{k}_{\parallel}} f^{\alpha}_{i\mathbf{k}_{\parallel}-\mathbf{q}_{\parallel}} \bar{f}^{\alpha}_{j\mathbf{p}_{\parallel}-\mathbf{q}_{\parallel}} f^{\alpha}_{j\mathbf{p}_{\parallel}} \right] \\
&\quad + \frac{2\pi}{\hbar} \sum_{\mathbf{q}_{\parallel}\neq 0,\bar{\alpha}} W_{\mathbf{q}_{\parallel}} \sum_{j,\mathbf{p}_{\parallel}} \left(V_{\mathbf{q}_{\parallel}} - V_{\mathbf{k}_{\parallel}-\mathbf{p}_{\parallel}}\delta_{ij}\right) \mathcal{D}\left(\tilde{\Sigma}^{\alpha}_{i\mathbf{k}_{\parallel}+\mathbf{q}_{\parallel}} - \tilde{\Sigma}^{\alpha}_{i\mathbf{k}_{\parallel}} - \tilde{\Sigma}^{\bar{\alpha}}_{j\mathbf{p}_{\parallel}} + \tilde{\Sigma}^{\bar{\alpha}}_{j\mathbf{p}_{\parallel}-\mathbf{q}_{\parallel}}\right) \\
&\quad \times \left[f^{\alpha}_{i\mathbf{k}_{\parallel}} \bar{f}^{\alpha}_{i\mathbf{k}_{\parallel}+\mathbf{q}_{\parallel}} f^{\bar{\alpha}}_{j\mathbf{p}_{\parallel}} \bar{f}^{\bar{\alpha}}_{j\mathbf{p}_{\parallel}-\mathbf{q}_{\parallel}} - \bar{f}^{\alpha}_{i\mathbf{k}_{\parallel}} f^{\alpha}_{i\mathbf{k}_{\parallel}+\mathbf{q}_{\parallel}} \bar{f}^{\bar{\alpha}}_{j\mathbf{p}_{\parallel}} f^{\bar{\alpha}}_{j\mathbf{p}_{\parallel}-\mathbf{q}_{\parallel}} \right], \quad (5.1)
\end{aligned}
$$

$$
\begin{aligned}
\left.\frac{\mathrm{d}}{\mathrm{d}t} f^{\alpha}_{i\mathbf{k}_{\parallel}}\right|_{ph} &= \frac{2\pi}{\hbar} \sum_{\mathbf{q}_{\parallel}\neq 0,m} g^{\alpha,m}_{\mathbf{k}_{\parallel};\mathbf{q}_{\parallel}} \tilde{g}^{\alpha,m}_{\mathbf{k}_{\parallel};\mathbf{q}_{\parallel};\mathbf{k}_{\parallel}+\mathbf{q}_{\parallel}} \mathcal{D}\left(\tilde{\Sigma}^{\alpha}_{i\mathbf{k}_{\parallel}+\mathbf{q}_{\parallel}} - \tilde{\Sigma}^{\alpha}_{i\mathbf{k}_{\parallel}} - \hbar\omega^{m}_{\mathbf{q}_{\parallel}}\right) \\
&\quad \times \left[(n^{m}_{\mathbf{q}_{\parallel}}+1) f^{\alpha}_{i\mathbf{k}_{\parallel}+\mathbf{q}_{\parallel}} \bar{f}^{\alpha}_{i\mathbf{k}_{\parallel}} - n^{m}_{\mathbf{q}_{\parallel}} f^{\alpha}_{i\mathbf{k}_{\parallel}} \bar{f}^{\alpha}_{i\mathbf{k}_{\parallel}+\mathbf{q}_{\parallel}} \right] \\
&\quad + \frac{2\pi}{\hbar} \sum_{\mathbf{q}_{\parallel}\neq 0,m} g^{\alpha,m}_{\mathbf{k}_{\parallel};\mathbf{q}_{\parallel}} \tilde{g}^{\alpha,m}_{\mathbf{k}_{\parallel};\mathbf{q}_{\parallel};\mathbf{k}_{\parallel}} \mathcal{D}\left(\tilde{\Sigma}^{\alpha}_{i\mathbf{k}_{\parallel}-\mathbf{q}_{\parallel}} - \tilde{\Sigma}^{\alpha}_{i\mathbf{k}_{\parallel}} - \hbar\omega^{m}_{\mathbf{q}_{\parallel}}\right) \\
&\quad \times \left[n^{m}_{\mathbf{q}_{\parallel}} f^{\alpha}_{i\mathbf{k}_{\parallel}-\mathbf{q}_{\parallel}} \bar{f}^{\alpha}_{i\mathbf{k}_{\parallel}} - (n^{m}_{\mathbf{q}_{\parallel}}+1) f^{\alpha}_{i\mathbf{k}_{\parallel}} \bar{f}^{\alpha}_{i\mathbf{k}_{\parallel}-\mathbf{q}_{\parallel}} \right]. \quad (5.2)
\end{aligned}
$$

Here, $\alpha \neq \bar{\alpha}$ denote the band indices and m the phonon branch. When concentrating on the intravalley scattering processes, we only included LO-phonons, that were reported to have major contributions, with an approximately constant energy of $\hbar\omega^{LO}_{\mathbf{q}_{\parallel}} = 27.72\,\mathrm{meV}$ [56]. In this case, the sum over m vanishes in the above equation. The energy conservation was treated numerically via $\pi\mathcal{D}(x) = \frac{\eta}{x^2+\eta^2}$, where a phenomenological broadening η was included. It was numerically tested that the exact value η was of minor influence for the final results. Furthermore, in these energy conservation terms, energy conservation is required with respect to the renormalised energies. But, as all these energy difference terms pairwise belong to energies of the same band, thus, they are of the form $\tilde{\Sigma}^{\alpha}_{\mathbf{k}_{\parallel}} - \tilde{\Sigma}^{\alpha}_{\mathbf{k}_{\parallel}-\mathbf{q}_{\parallel}}$, and as excitation-induced renormalisation mainly yield constant shifts of the bands, it is a reasonable approximation to replace the renormalised energies by their unrenormalised equivalents.
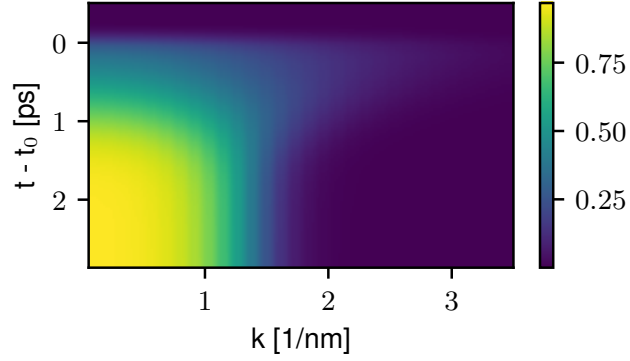
Regarding the carrier-carrier scattering processes, the first two lines of the equation describe scattering of particles in the same band, whereas scattering processes between electrons and holes are contained in the last two lines. For all processes, the initial state has to be occupied with a probability $f_{\mathbf{k}_{\|}}^{\alpha} > 0$, whereas the final state needs to be empty $\bar{f}_{\mathbf{k}_{\|}'}^{\alpha} = 1 - f_{\mathbf{k}_{\|}'}^{\alpha} > 1$. Concerning the phonon scattering, in- and out-scattering processes due to phonon absorption ($\propto n_{\mathbf{q}_{\|}}^{m}$) and emission ($\propto (1 + n_{\mathbf{q}_{\|}}^{m})$) are described.

The coupled set of equations was solved applying a forth-order Runge-Kutta method [84]. The resulting carrier dynamics for excitation with a high-intensity Gaussian shaped pulse ($E_0 = 1.25 \frac{\text{MV}}{\text{cm}}$, $\sigma = 300\,\text{ps}$) is depicted exemplary for the electron distribution in the A band in Fig. 5.1. The dynamics of the corresponding hole distribution is equivalent and the carrier dynamics in the B band is similar but even more efficient as the excitation energy was chosen nearly resonant with this band. Further details on the numerical implementation are provided in [85].

During excitation, no accumulation of carriers at the excitation energy is seen. It was seen that ultrafast carrier-carrier scattering relaxations in combination with the renormalisation of the states – both processes enhanced by the strong Coulomb interactions – drives the carriers away from the excitation energy and enables an efficient absorption of incoming photons. Already within a few femtoseconds the carriers have relaxed into a hot quasi-equilibrium distribution due to carrier-carrier relaxation. The efficient absorption is accompanied by a large renormalisation of the band gap in the order of $390\,\text{meV}$, when the maximum of optically induced charge carriers is reached. Thereafter, carrier-phonon interaction results in a thermalisation of the distributions, as is seen in a narrowing of the distribution in Fig. 5.1. The hot carriers are predicted to have relaxed into room temperature Fermi-like distributions, and thus reached the phonon bath temperature, within $2.5\,\text{ps}$. As the screening wave vector is approximately given by the value of the carrier distributions at $\mathbf{k}_{\|} = \text{K}$, which increases through cooling of the carriers, this thermalisation leads to further screening of the Coulomb interaction and consequently in a further reduction of the band gap in the order of $20\,\text{meV}$.

Experimentally, the carrier dynamics is not observable directly, but changes in the material response upon an additional second low-intensity pulse can be seen. To model this scenario, we assume that the pump and probe pulse can be decoupled in the simulation and the density distributions obtained by evaluating the carrier dynamics can be treated as quasistatic with respect to the ultrashort probe pulse. In this limit, the equation determining the microscopic polarisation can be solved in frequency space

$$\left[\hbar(\omega + i\gamma) - \left(\Sigma_{\mathbf{k}_{\|}}^{h} + \Sigma_{\mathbf{k}_{\|}}^{e} \right) \right] p_{\mathbf{k}_{\|}}(\omega) + (1 - f_{\mathbf{k}_{\|}}^{h} - f_{\mathbf{k}_{\|}}^{e}) \sum_{\mathbf{k}_{\|}' \neq \mathbf{k}_{\|}} V_{\mathbf{k}_{\|} - \bar{\mathbf{k}}_{\|}'; \bar{\mathbf{k}}_{\|}'; \bar{\mathbf{k}}_{\|}}^{cvvc} p_{\mathbf{k}_{\|}} - \Gamma_{\mathbf{k}_{\|}}^{he}(\omega)$$

$$= -(1 - f_{\mathbf{k}_{\|}}^{h} - f_{\mathbf{k}_{\|}}^{e}) \frac{e}{m_0 c} \mathbf{p}_{cv}(\mathbf{k}_{\|}) \cdot \mathbf{A}(\omega). \tag{5.3}$$

Abbildung 5.1: Dynamics of the electron distribution in the A-band after excitation with a linear polarised Gaussian shaped pulse with $E_0 \propto 1.25\,\mathrm{MV/cm}$, FWHM of $\sigma = 300\,\mathrm{ps}$ slightly above $\tilde{\Delta}_B$.

Here, the plasma screening effects are fully contained in the dephasing parameter $\Gamma_{\mathbf{k}_\parallel}^{he}(\omega)$, in which carrier- and phonon-induced scattering contributions are subsumed. Thus, the unscreened Coulomb interaction needs to be included in the remaining parts of the equation. Formally the dephasing can be separated into carrier- and phonon-contributions

$$\Gamma_{\mathbf{k}_\parallel}^{he}(\omega) = \sum_{\mathbf{k}_\parallel' \neq \mathbf{k}_\parallel} \left[\Delta I_{\mathbf{k}_\parallel - \mathbf{k}_\parallel', \mathbf{k}_\parallel}^{he}(\omega) + G_{\mathbf{k}_\parallel - \mathbf{k}_\parallel', \mathbf{k}_\parallel}^{he,+}(\omega) + G_{\mathbf{k}_\parallel - \mathbf{k}_\parallel', \mathbf{k}_\parallel}^{he,-}(\omega) - (\mathbf{k}_\parallel \leftrightarrow \mathbf{k}_\parallel') \right] \quad (5.4)$$

Neglecting exchange contributions and only considering contributions that are linear in the microscopic polarisation, based on Eq. 2.61 and 2.65, the different contributions can be explicitly written as

$$\Delta I_{\mathbf{k}_\parallel - \mathbf{k}_\parallel', \mathbf{k}_\parallel}^{he}(\omega) = W_{\mathbf{k}_\parallel - \mathbf{k}_\parallel', \mathbf{k}_\parallel}^{he}(\omega) V_{\mathbf{k}_\parallel - \mathbf{k}_\parallel'} \left[\Lambda_{\mathbf{k}_\parallel - \mathbf{k}_\parallel', \mathbf{k}_\parallel}^{he}(\omega) - \Pi_{\mathbf{k}_\parallel - \mathbf{k}_\parallel'}^{he}(\omega) f_{\mathbf{k}_\parallel}^{h} \right] p_{\mathbf{k}_\parallel'}(\omega)$$
$$- W_{\mathbf{k}_\parallel - \mathbf{k}_\parallel', \mathbf{k}_\parallel}^{he}(\omega) V_{\mathbf{k}_\parallel - \mathbf{k}_\parallel'} \left[\Lambda_{\mathbf{k}_\parallel - \mathbf{k}_\parallel', \mathbf{k}_\parallel}^{he}(\omega) - \Pi_{\mathbf{k}_\parallel - \mathbf{k}_\parallel'}^{he}(\omega) f_{\mathbf{k}_\parallel'}^{e} \right] p_{\mathbf{k}_\parallel}(\omega) \quad (5.5)$$

$$G_{\mathbf{k}_\parallel - \mathbf{k}_\parallel', \mathbf{k}_\parallel}^{he,+}(\omega) = g_{\mathbf{k}_\parallel - \mathbf{k}_\parallel', \mathbf{k}_\parallel}^{he}(\omega) g_{\mathbf{k}_\parallel - \mathbf{k}_\parallel'}^{0} \frac{\left\{ \bar{f}_{\mathbf{k}_\parallel}^{e} n_{\mathbf{k}_\parallel - \mathbf{k}_\parallel'} \right\}_\Sigma p_{\mathbf{k}_\parallel}(\omega) - \left\{ \bar{f}_{\mathbf{k}_\parallel}^{h} n_{\mathbf{k}_\parallel - \mathbf{k}_\parallel'} \right\}_\Sigma p_{\mathbf{k}_\parallel'}(\omega)}{\Delta \tilde{\Sigma}_{\mathbf{k}_\parallel - \mathbf{k}_\parallel', \mathbf{k}_\parallel}^{he}(\omega) + \hbar \omega_{\mathbf{k}_\parallel - \mathbf{k}_\parallel'} + i\hbar\eta}$$

$$(5.6)$$

$$G_{\mathbf{k}_\parallel - \mathbf{k}_\parallel', \mathbf{k}_\parallel}^{he,-}(\omega) = g_{\mathbf{k}_\parallel - \mathbf{k}_\parallel', \mathbf{k}_\parallel}^{he}(\omega) g_{\mathbf{k}_\parallel - \mathbf{k}_\parallel'}^{0} \frac{\left\{ f_{\mathbf{k}_\parallel}^{e} n_{\mathbf{k}_\parallel - \mathbf{k}_\parallel'} \right\}_\Sigma p_{\mathbf{k}_\parallel}(\omega) - \left\{ f_{\mathbf{k}_\parallel}^{h} n_{\mathbf{k}_\parallel - \mathbf{k}_\parallel'} \right\}_\Sigma p_{\mathbf{k}_\parallel'}(\omega)}{\Delta \tilde{\Sigma}_{\mathbf{k}_\parallel - \mathbf{k}_\parallel', \mathbf{k}_\parallel}^{he}(\omega) + \hbar \omega_{\mathbf{k}_\parallel - \mathbf{k}_\parallel'} + i\hbar\eta},$$

$$(5.7)$$

Abbildung 5.2: Absorption spectra for various time differences in the thermalisation re-
gime after exciting a MoTe$_2$ sample. The inset depicts the corresponding
carrier distribution of the electrons in the A-band. (According to publi-
cation [III].)

where the shorthand notations

$$\left\{ \bar{f}_{\mathbf{k}}^{\alpha} n_{\mathbf{q}} \right\}_{\Sigma} \equiv f_{\mathbf{k}}^{\alpha} n_{\mathbf{q}} + \bar{f}_{\mathbf{k}}^{\alpha} (1 + n_{\mathbf{q}}),$$

$$\Delta \tilde{\Sigma}_{\mathbf{k}_{\|} - \mathbf{k}_{\|}', \mathbf{k}_{\|}}^{he} \equiv \hbar\omega - \tilde{\Sigma}_{\mathbf{k}_{\|}}^{h} - \tilde{\Sigma}_{\mathbf{k}_{\|}'}^{e},$$

$$\mathcal{O}_{\mathbf{k}_{\|} - \mathbf{k}_{\|}', \mathbf{k}_{\|}}^{he}(\omega) \equiv \mathcal{O}_{\mathbf{k}_{\|} - \mathbf{k}_{\|}'} \left(\Delta \tilde{\Sigma}_{\mathbf{k}_{\|} - \mathbf{k}_{\|}', \mathbf{k}_{\|}}^{he} / \omega + i\gamma_T \right)$$

were introduced. Furthermore, we introduced the function

$$\Lambda_{\mathbf{q}_{\|}}(\omega) = \sum_{\alpha \mathbf{k}_{\|}} \frac{f_{\mathbf{k}_{\|} - \mathbf{q}_{\|}}^{\alpha} \bar{f}_{\mathbf{k}_{\|}}^{\alpha}}{\hbar\omega + \tilde{\Sigma}_{\mathbf{k}_{\|} - \mathbf{q}_{\|}}^{\alpha} - \tilde{\Sigma}_{\mathbf{k}_{\|}}^{\alpha}}. \tag{5.8}$$

To reduce the numerical complexity, both this function and the Lindhard polarisation
function were pre-calculated on a dense frequency grid and in subsequent calculations
the desired energy value is mapped to the closest grid point. In this approximation, the
microscopic polarisation can be calculated numerically efficient via matrix inversion.

In Fig. 5.2 the changes in the absorption spectra during the thermalisation process are
depicted together with the corresponding electron distribution in the A-band. Due to
the narrowing of the carrier distribution, the phase space filling factor decreases and
results after 0.5 ps in inversion $(1 - f_{\mathbf{k}_{\|}}^{e} - f_{\mathbf{k}_{\|}}^{h} < 0)$ and optical gain slightly below the
resonance of the lowest A-exciton in the low density regime. Our calculations predict
that the continuum absorption of the A band overcompensates the negative absorption
of the B band and no netto gain is expected in this energy region.

To gain first insight on the impact of the intervalley scattering processes, we estimate
their influence by comparing the absorption spectra for different carrier densities before

and after equilibration within the bands. In particular, we compare the cases of an equal distribution of carriers in the different bands and valleys to the case where the carriers in different valleys have an equal chemical potential. In the latter, the distribution of the carriers is determined by solving

$$0 = n^e - \frac{1}{\mathcal{A}} \sum_{s,\mathbf{k}_\parallel,\zeta_s} \mathrm{dgn}(\zeta_s) f^e_{\tau_s \mathbf{k}_\parallel}(\mu^e, T)$$

$$0 = n^h - \frac{1}{\mathcal{A}} \sum_{s,\mathbf{k}_\parallel,\zeta_s} \mathrm{dgn}(\zeta_s) f^h_{\zeta_s \mathbf{k}_\parallel}(\mu^h, T),$$

for a given temperature T and carrier density $n^{e/h}$. Due to the hexagonal symmetry, the degeneracy of the side valleys is $\mathrm{dgn}(\zeta_s = \Lambda/\Sigma) = 3$. Regarding the holes, only the two main valleys K and K' are included. Due to the large spin-splitting of the valence bands at the K- and K'-valley of about $230\,\mathrm{meV}$, less than 1% of the holes is located at the energetically unfavourable valley, even in the high density regime of $n = 10^{14}\,\mathrm{cm}^{-2}$. Regarding the excited electrons, both the main and the side valleys need to be considered. Even though the side valley is energetically above the main minimum, up to 25% of the electrons occupy the different side valleys in this high density regime. These two aspects of carrier equilibration have counteracting effects on the gain spectrum. While the decrease in electron population at the main valley reduces the amount of carriers that can recombine optically, the hole drain to the A band increases the inversion. In Fig. 5.3, the spectra before and after equilibration of the carriers in the bands are depicted. Here, it is seen that the mentioned counteracting processes lead to an overall increase in peak optical gain. Normalised to the layer thickness, the peak optical gain reaches $10^5\,\mathrm{cm}^{-1}$ for the largest carrier density analysed here. According to our simulations, the optical gain per material thickness in $MoTe_2$ is an order of magnitude larger than in typical III/V semiconductors, where the optical gain is in the order of $5000\,\mathrm{cm}^{-1}$.

5.0.2 Analysis of a pump scenario in two dimensions

This first estimation of the contribution of the side valleys already showed their considerable influence on the optical properties of $MoTe_2$ for the examined high carrier densities. Additionally to this observed influence on the optical spectra, it is frequently discussed whether TMDCs become indirect semiconductors upon optical excitation, as the side gap renormalisation overruns the renormalisation of the main valley [86, 87]. To address this question on the renormalisation dynamics and get deepened insights on the relaxation dynamics of the carriers in the full BZ, we expanded our model beyond the MDF approach. Instead of approximating the band structure and absolute dipole matrix elements, the full $\mathbf{k}_\parallel$-dependent energy dispersion and dipole matrix elements for the conduction and valence bands, as well as all nine phonon branches were taken
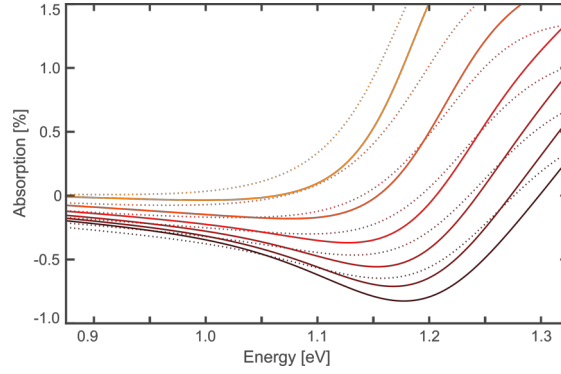
Abbildung 5.3: Comparison of absorption spectra for different amounts of excited carriers from $2 \times 10^{13} \, \mathrm{cm}^{-2}$ (yellow) to $12 \times 10^{13} \, \mathrm{cm}^{-2}$ (black) with (solid lines) and without (dotted lines) inclusion of carrier drain to side valley and between K-valleys. Equilibration results in an enhancement of peak optical gain. (According to publication [III].)

into account as derived by DF(P)T calculations. Here, the eigenvalue problem determining the energetic states is solved independently for every k-point and the eigenvalues are sorted according to their energetic value only, neglecting any correlation of the values of neighbouring points. Thus, a post-processing of the data in which the data is sorted according to their energetic bands is needed prior to consecutive calculations. Unfortunately, an automated sorting according to the overlap and the gradient between neighbouring k-points did not work out, and this sorting was executed manually. Both DFT and SBE calculations were performed on the irreducible BZ, thus, the basis points for the numerical evaluations where distributed equidistantly on an equilateral triangle. To include scattering processes through the whole BZ, the symmetries of the system were made use of.

Regarding the various interactions, we applied similar approximations as before. Namely, we treated the microscopic polarisation on the screened HF level and included the Boltzmann-like scattering terms concerning the carrier occupation probabilities (Eq. 5.1), where screening was included in the static limit. The Coulomb interaction was modelled on the basis of the previously introduced form factor. The form factor was calculated explicitly only with respect to the main and side valley and was approximated for all other points with the form factor of the closest valley respectively.

To study the influence of the different relaxation processes and their respective time scales separately from the excitation processes, we set an artificial initial carrier distri-

bution

$$f_{\mathbf{k}_\parallel}^\alpha \;=\; \frac{f_0 \mathbf{p}_{\mathbf{k}_\parallel \alpha}^2}{|\mathbf{p}_{max}|^2}\, e^{-\frac{1}{2}\left(\frac{\epsilon_{\mathbf{k}_\parallel}^e - \epsilon_{\mathbf{k}_\parallel}^h - \hbar\omega_L}{\Delta}\right)^2}$$

approximating the excitation by a laser pulse at energy $\hbar\omega_L$ and of width $\Delta = 66\,\mathrm{meV}$. In order to analyse the relaxation dynamics of carriers excited high above the band gap, the central frequency of the pulses was chosen to be $800\,\mathrm{meV}$ above the non-interacting band gap. Furthermore, the occupation probabilities is weighted by the dipole matrix elements, $\mathbf{p}_{\mathbf{k}_\parallel \alpha}$, that are normalised by the maximum dipole matrix element between any states, $\mathbf{p}_{max}$.

In Fig. 5.4, the relaxation dynamics after such an artificial excitation is shown for the excited electrons ($f_0 = 1.28$) in the A band at different times after excitation. The contributions to the electron dynamics arising from carrier-carrier and carrier-phonon interaction are shown separately. In accordance with the observations in our first study, it is seen that the dynamics is dominated by carrier-scattering during the first few fs. These carrier-scatterings result in an initial broadening of the distribution. Here, it is seen that these contributions are up to two orders of magnitude larger than contributions arising due to phonon-scattering. To analyse the carrier dynamics even more closely, in Fig. 5.5 the contributions arising from the different phonon branches are compared by depicting the full phononic contributions and the contributions arising from optical phonons side by side. Here, a lower excitation density ($f_0 = 0.16$) was used in the simulation, as the relative importance of phononic contributions is larger decreases with increasing carrier density. It can be seen that both optical and acoustic phonons are of equal importance in the first few femtoseconds but affect the distribution in different ways. Changes due to optical phonons are found in the proximity of the regions of initial excitation, in contrast, acoustic phonons induce changes that are spread larger in momentum space. This shows, as expected, that optical phonons are efficient for small scattering vectors, while acoustic phonons are of importance for larger scattering vectors, and thus are of key importance to model intervalley scattering processes.

Similar to previous observations in the isotropic model, already within the first few femtoseconds, the carriers have relaxed into hot Fermi like distributions. This undermines the previously seen ultrafast relaxation times resulting from efficient carrier-carrier scattering due to the enhanced Coulomb interaction. Thereafter, the scattering dynamics slow down by 2-3 orders of magnitude and contributions due to phonons and electrons become of equal importance (see Fig. 5.4). The closer look on the different phonon branch contributions (Fig. 5.5) reveals, that in this time domain, where mainly a process of cooling takes place, the phonon contributions are mostly due to optical phonons. $0.5\,\mathrm{ps}$ after excitation, the carrier dynamics further slow down by an order of magnitude, but the

carriers still have a temperature of about 1900 K. Nevertheless, the in- and out-scattering contributions due to phononic and electronic interaction respectively become more alike demonstrating the evolution of the carrier distribution towards a quasi-equilibrium situation.

As these analyses show, under conditions of an artificial distribution approximating the scenario of excitation high in the band, scattering takes place over the whole BZ with a non-negligible amount of carriers being scattered into the side valley already within a few femtoseconds. In contrast, when assuming resonant excitation conditions, as analysed in more depth in publication [IV], the intervalley transfer was seen to be strongly slowed down and takes place on a picosecond time scale. This justifies our previous assumption regarding the different time scales of intra- and intervalley scattering processes for nearly resonant excitation conditions.

Finally, the strong Coulomb interaction in TMDC materials gives rise to large excitation-induced band gap renormalisations. The exact renormalisation of the bands depends on their occupation as well as the Coulomb-matrix elements and their screening. The Coulomb-matrix elements depend on the overlap of the respective wave functions of the states. As the orbital contributions to the wave functions differ, slight differences of the matrix elements at the main and side valley are experienced. Furthermore, the screening depends both on plasma screening and phase space filling effects. Plasma screening is a global effect in the sense that the screening equally affects electronic interactions all over the BZ. In contrast, phase space filling can be seen as a more local effect in reciprocal space. It depends on the local occupation that in turn is connected to the local dispersion, as the excitation-dependent occupation changes are enhanced in valleys with lower effective mass. Thus, resulting from the local dispersion, the excitation-induced band gap renormalisation at the side valley is stronger than at the main valley. But, despite the larger renormalisation per occupation effects, the initial energy offset between the valleys results in a higher occupation of the main valley. Even if we assume that the carriers are in a global thermal equilibrium, the difference in occupation of the different valleys is so large that we do not observe a transition from a direct to an indirect band gap. Our study thus indicates that the question whether such a transition takes place in TMDC structures highly depends on the ground-state band structure that in turn is highly sensitive e.g. to the exact lattice structure. As has been shown in different studies – both experimentally and theoretically–, the energy offset between the valleys is in particular sensitive to strain. Theoretical studies e.g. indicate that changes of the lattice constant below 1% lead to a shift of the conduction band side valley below the main valley [88, 89, 90]. Consequently, the carrier dynamics in the bands and the material lattice structure are interrelated and the energetic structure of monolayer materials are highly sensitive to changes in both parameters. Clarifying this interplay of
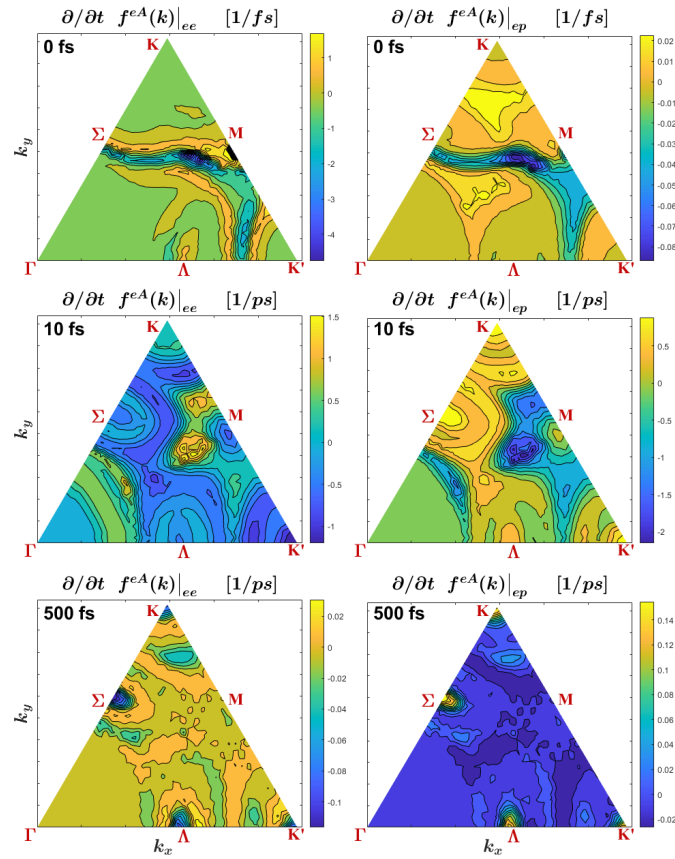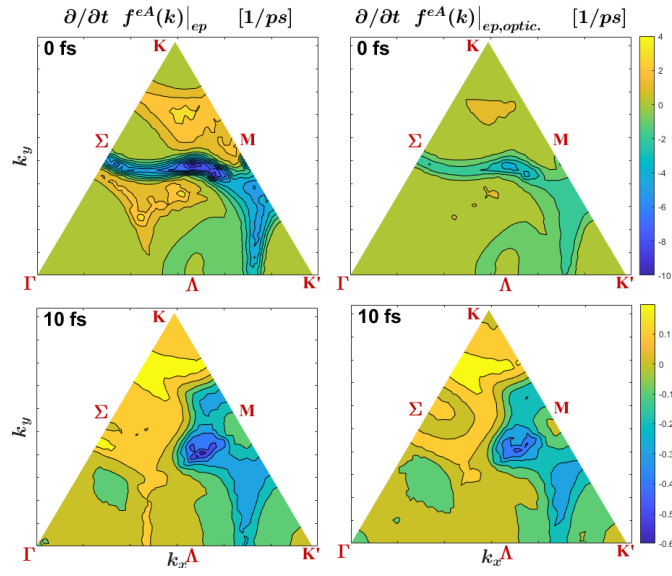
Abbildung 5.4: Comparison of the influence of different scattering contributions on the dynamics of the electron distributions in the A-band at different times. Left panel: Contributions from electron-electron scattering. Right panel: Contributions from electron-phonon scattering. Mind that changes are shown for different time scales for topmost ([1/fs]) and bottom ([1/ps]). (According to publication [IV].)

Abbildung 5.5: Comparison of the influence of different phonon scattering contributions on the dynamics of the electron distribution in the A-band at different times. Left panel: Scattering contributions from all phonon branches. Right panel: Scattering contributions from optical phonon branches only. (According to publication [IV].)

lattice structure, carrier dynamics and excitation-induced renormalisation effects would be an interesting extension of our study.

6. | Increase destructive interference – Electron-hole plasma induced dephasing

The absorption spectra of TMDC monolayers are in the low excitation regime, even at room temperature, dominated by excitonic resonances. The exact shape of the resonances is influenced by many different aspects that were partially discussed in previous studies [91]. For example, it was observed that the dielectric environment goes along with a change of the pulse shape. Experimentally it was seen that an encapsulation with hBN dramatically reduces the linewidth, yielding linewidths of down to 2 meV in the low energy regime, compared to the fivefold value for samples on quartz substrates. This narrowing is usually attributed to a higher stability of and a suppression of impurities in the sample. Due to the narrowing, the encapsulation with hBN enables further discrimination of the signals and the observation of higher excitonic states [92, 93, 94]. Furthermore, due to the temperature-dependence of exciton-phonon-interactions, the linewidth was shown to increase superlinear with temperature, whereas different excitonic contributions dominate the increase for tungsten- and molybdenum-based materials [95, 96]. Additionally, the dephasing increases when excited carriers are generated in the material. Here, previous studies focused on changes due to enhanced occupations of excitonic states. In particular, the different contributions of inter- and intravalley excitons to the homogeneous linewidth were analysed. Here, different relative contributions were observed for molybdenum- and tungsten-based materials. While intervalley excitonic contributions are marginal in molybdenum-based materials, they contribute significantly in tungsten-based materials. This different behaviour can be attributed to the different energetic ordering in these materials, as the intervalley excitons were seen to be energetically favourable in these materials [95, 97, 98, 99, 100, 101]. Because optical excitation high in the bands leads to an electron-hole plasma prior to the population of bound excitonic states, we extended these studies by focussing on the excitation-induced dephasing due to an electron-hole plasma. In our study, which led to publication "*Electron-hole plasma-induced dephasing in transition metal dichalcogenides*" (Ref. [V]), we neglected
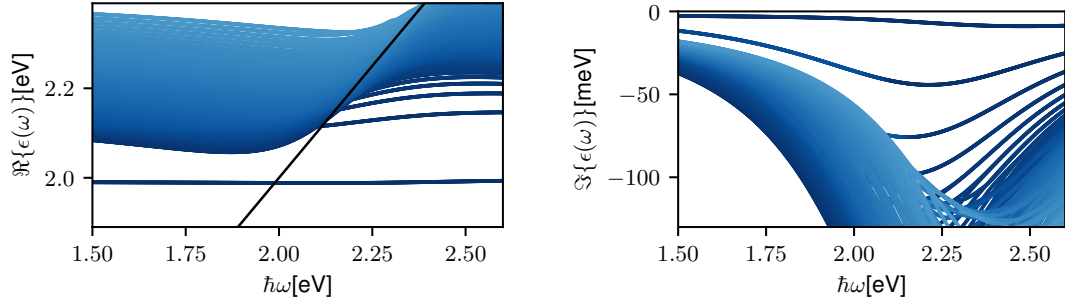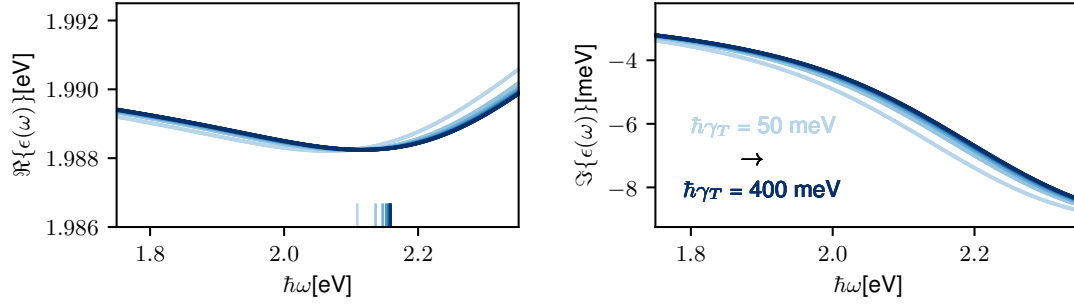
Abbildung 6.1: Frequency-dependent eigenvalues of $\mathcal{H}_{\mathbf{k}_\parallel \mathbf{k}'_\parallel}(\omega)$ for a Fermi distributed carrier density located around the K point of $n_A = n_B = 1.5 \times 10^{12}\,\mathrm{cm}^{-2}$. In the representation of the real values (left) the black line indicates where $\mathcal{R}(\epsilon) = \hbar\omega$, which allows to identify the resonance positions. The imaginary part correlates to the linewidth. An additional intrinsic dephasing of $\hbar\gamma = 2\,\mathrm{meV}$ and a triplet dephasing of $\hbar\gamma_T = 300\,\mathrm{meV}$ are included.

phononic contributions – which would only yield a lattice-temperature-dependent constant shift – but focused on the influence of electronic interactions.

Let us first examine the results of the homogeneous part of the polarisation equation, Eq. 2.52, including the dephasing in form of the previously deduced excitation- and frequency-dependent carrier-scattering contributions, Eq. 5.4. The right hand side of the equation can be reformulated in a matrix representation, where upon substituting $\tilde{p}_{\mathbf{k}_\parallel} = \sqrt{\frac{k}{1 - f^e_{\mathbf{k}_\parallel} - f^h_{\mathbf{k}_\parallel}}} p_{\mathbf{k}_\parallel}$ the matrix excluding scattering contributions becomes hermitian, yielding

$$i\hbar \frac{\mathrm{d}}{\mathrm{d}t} \tilde{p}_{\mathbf{k}_\parallel} = \sum_{\mathbf{k}'_\parallel} \mathcal{H}_{\mathbf{k}_\parallel, \mathbf{k}'_\parallel} \tilde{p}_{\mathbf{k}'_\parallel}, \text{ with}$$

$$\mathcal{H}_{\mathbf{k}_\parallel, \mathbf{k}'_\parallel} = \left(\Sigma^c_{\mathbf{k}'_\parallel} - \Sigma^v_{\mathbf{k}'_\parallel} \right) \delta_{\mathbf{k}_\parallel \mathbf{k}'_\parallel} \bar{V}^{ccvv}_{\mathbf{k}_\parallel \mathbf{k}'_\parallel} + i\hbar \sqrt{\frac{k \left(1 - f^e_{\mathbf{k}_\parallel} - f^h_{\mathbf{k}_\parallel} \right)}{k'(1 - f^e_{\mathbf{k}'_\parallel} - f^h_{\mathbf{k}'_\parallel})}} \Gamma^{he}_{\mathbf{k}_\parallel \mathbf{k}'_\parallel},$$

$$\bar{V}^{ccvv}_{\mathbf{k}_\parallel \mathbf{k}'_\parallel} = \sqrt{\frac{k}{1 - f^e_{\mathbf{k}_\parallel} - f^h_{\mathbf{k}_\parallel}}} V^{ccvv}_{\mathbf{k}_\parallel \mathbf{k}'_\parallel} \sqrt{\frac{k'}{1 - f^e_{\mathbf{k}'_\parallel} - f^h_{\mathbf{k}'_\parallel}}} \qquad (6.1)$$

In Fig. 6.1, the frequency-dependent matrix eigenvalue spectrum for a MoS_2 monolayer embedded in hBN is shown exemplary for a carrier density of $n_A = n_B = 1.5 \times 10^{12}\,\mathrm{cm}^{-2}$ following a Fermi distribution at room temperature. Real and imaginary part are shown separately. Here, an intrinsic dephasing of $\gamma = 2\,\mathrm{meV}$ and a triplet dephasing of $\gamma_T = 300\,\mathrm{meV}$ were inserted. In the real part of the eigenvalue spectrum the lowest eigenvalue is clearly recognisable, whereas the higher eigenvalues are overshadowed in the

Abbildung 6.2: Frequency-dependent lowest eigenvalue of $\mathcal{H}_{\mathbf{k}_\parallel \mathbf{k}'_\parallel}(\omega)$ for a Fermi distributed carrier density located around the K point of $n_A = n_B = 1.5 \times 10^{12}\,\mathrm{cm}^{-2}$ for different triplet dephasings γ_T. Furthermore, the respective band gap is indicated along the x-axis.

lower frequency range by continuum states, which shift spectrally below them, and are visible as distinct states in the high frequency range only. Thus, instead of sorting the eigenvalues according to their real part eigenvalue, it proves to be more appropriate to sort them according to their oscillator strength. This insight becomes even more obvious when taking into account the imaginary part of the eigenvalue spectrum expressing the frequency-dependent dephasing of the states. Here, the continuum states show immense dephasing constants of more than $25\,\mathrm{meV}$ in the whole analysed frequency range. Concerning the linear absorption spectrum, according to the Elliott formula, which implies that $\chi(\omega) \propto (\hbar\omega - \epsilon_\lambda + i\hbar\gamma)^{-1}$, resonances are observed when $\hbar\omega = \mathcal{R}\{\epsilon_\lambda(\omega)\}$, which in the figure corresponds to a crossing with the black curve. Thus, in the relevant regime, the dephasing of the continuum states reaches values exceeding $100\,\mathrm{meV}$. In general, it is seen that the frequency-dependence of the states increases with its resonance energy ($\hbar\omega = \mathcal{R}\{\epsilon_\lambda(\omega)\}$). Consequently, for the higher states, the electron-hole plasma-induced dephasing is more pronounced than for the lowest state indicating a bleaching out of these states already for lower excitation densities.

In our model, in the unexcited case, both real and imaginary part would be frequency-independent, whereby the imaginary part only reflects intrinsic dephasing. The above analysis reveals a significant frequency-dependence of the resonances and, even more pronounced, of their dephasing for an excited sample. This observation highlights the importance of including screening effects dynamically when evaluating the polarisation dynamics and consecutive absorption spectra.

In the applied treatment of the carrier-polarisation scattering, we explicitly include terms up to the doublet level only and include higher order correlations by means of screening. We summarise further contributions in a constant dephasing γ_T. In general, this term is density- and frequency-dependent. To determine the influence of the size of γ_T on
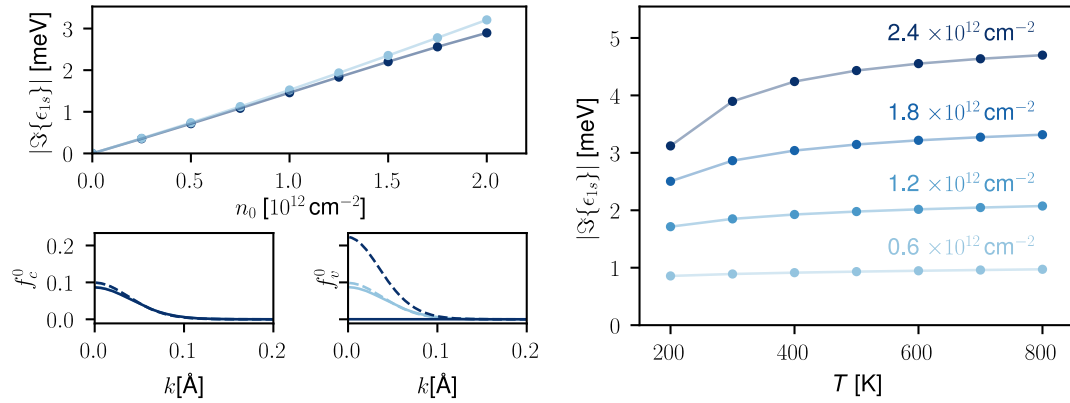
Abbildung 6.3: Dependence of EID on carrier distribution and carrier temperature. Upper left: EID before and after equilibration of carriers in the different valleys. Carriers are either distributed equally in the different bands and valleys (light blue) or assumed to have relaxed towards a common chemical potential (dark blue). Exemplary, the carrier distributions for $n_0 = 2.0 \times 10^{12} \, \text{cm}^{-2}$ in the conduction (lower left) and valence (lower right) band are shown. Right: Temperature-dependence of the excitation-induced dephasing for various fixed carrier densities distributed equally in the bands and valleys. (Adapted from publication [V].)

the EID of the lowest exciton resonance, the real and imaginary part of the lowest eigenvalue of $\mathcal{H}$ is shown in Fig. 6.2 for various triplet dephasings. Additionally, the respective quasiparticle band gap is indicated. As already discussed in Sec. 3.2, the density-dependent band gap is underestimated for small triplet dephasings but depends only little on its exact value, if the triplet dephasing is chosen to be large enough. In contrast, the real part of the eigenvalue is affected only marginally already for small triplet dephasings. In particular, in the relevant frequency range – in proximity to the resonance energy –, changes are in the sub-meV range. Regarding the imaginary part of the eigenvalues, the differences for increasing triplet dephasings become smaller and are moderate for $\hbar\gamma_T > 100\,\text{meV}$. In conclusion it is seen that an exact treatment of higher correlation contributions would be desirable to gain further insights in the relaxation dynamics and to justify more profoundly the short dephasing times. But, for the present analysis that is focused on the EID of the lowest exciton resonance, the approximation of the dephasing by a constant value seems to be appropriate to gain first insights. The value ($\hbar\gamma_T = 300\,\text{meV}$) is chosen to yield density-dependent band gap changes that are consistent with experimental observations.

The relaxation studies in the previous chapters revealed, that the excitation of carriers is followed by their ultrafast relaxation towards hot Fermi like distributions and a consecutive redistribution of the carriers in the BZ. Therefore, we analysed the influence

of these two effects on the homogeneous linewidth of the lowest exciton resonance and found that both processes result in a sharpening of the resonance as displayed in Fig. 6.3. Here, only the imaginary part of the eigenvalues of $\mathcal{H}$ are shown excluding further phenomenological dephasing to illustrate the different dependencies. In (a) we depict the influence of hole drain to the energetically favourable valence band for a constant carrier temperature of $300\,\mathrm{K}$. The large conduction band offset between side and main valley of $133\,\mathrm{meV}$ causes that for the analysed low carrier densities only a small amount of electrons moves to the side valley. Unlike to observations in tungsten-based materials, where the smaller energetic distances between the valleys and the different spin ordering at the main valley was shown to result in large contributions of the side valley, those contributions are negligible in the MoS_2 [95, 100]. In contrast, the large valence band offset between the main valleys leads to a more pronounced reorganisation of carriers. After the reorganisation of carriers in the materials, nearly all holes occupy the energetically favourable valley. Even though this reorganisation is similar for all investigated carrier densities, it has only marginal influence for low densities, but becomes somewhat more pronounced with increasing densities.

The cooling results in a reorganisation of the carriers within the valleys and bands as with decreasing temperature the distribution becomes narrower in k-space. This in turn results in an enhanced screening of the Coulomb interaction – that is approximately proportional to the occupation at $k = K$ – and an increase of phase space filling effects. For small carrier densities, the occupation is below $0.5 \times 10^{-2}\,\mathrm{cm}^{-2}$ for all temperatures and thus the influence on the EID is small. In contrast, for the largest density analysed, the occupation at K decreases from 0.22 at $200\,\mathrm{K}$ to 0.04 at $800\,\mathrm{K}$ and consequently the influence of the cooling process is much larger resulting in an additional temperature-dependent broadening of $1.6\,\mathrm{meV}$. For high temperatures the broadening of the distribution results in the analysed excitation regime in low occupations all over the whole BZ. Therefore, the EID does not increase further but reaches for high temperatures a density-dependent plateau.

Experimentally, in the linear spectrum, the linewidth of a resonance is determined by a combination of homogeneous and inhomogeneous broadening effects. A possibility to separate these two contributions are e.g. four-wave mixing (FWM) experiments, where the response of a sample upon interaction with two (degenerate FWM) or three low intensity ,temporally sharp pulses for which the temporal delay is varied is investigated. The homogeneous linewidth can be deduced from the delay-dependent integrated signal. Explicitly, in a DFWM experiment, we are interested in the signal resulting from the interaction of the second pulse with the grating induced by the interaction of the polarisation of the first and the second pulse, that can be detected in direction $2\mathbf{k}_2 - \mathbf{k}_1$, where $\mathbf{k}_i$ denote the respective wave vectors. To gain insight on the electron-hole plasma-induced dephasing, the sample additionally needs to be excited by a prior high intensity
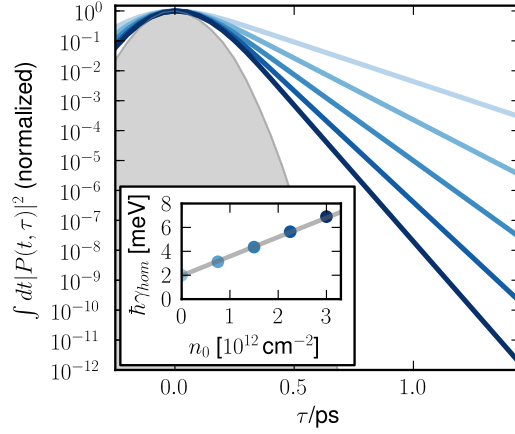
Abbildung 6.4: Excitation-induced dephasing as observed in DFWM spectra. The blu-
eish lines show the integrated DFWM signal for different carrier den-
sities that are assumed to be Fermi distribute equally in the different
bands/valleys. The corresponding densities are indicated in the inset.
The gray area marks the self-correlated signal of the pulses of temporal
width $t_{width} = 150\,\text{fs}$ and central frequency $\omega_1 = \omega_2 = \omega_{1s}$. (Adapted
from publication [V].)

pulse. To model such a scenario, we separate the polarisation ($p_{\mathbf{k}_\parallel}$) and occupations
($f_{\mathbf{k}_\parallel}^{e/h}$) into contributions arising from a pre-pulse (x^0) and those arising from further
pulses (Δx):

$$
\begin{aligned}
p_{\mathbf{k}_\parallel} &= p_{\mathbf{k}_\parallel}^0 + \Delta p_{\mathbf{k}_\parallel} \\
f_{\mathbf{k}_\parallel}^{e/h} &= f_{\mathbf{k}_\parallel}^{e/h,0} + \Delta f_{\mathbf{k}_\parallel}^{e/h}.
\end{aligned}
\tag{6.2}
$$

Inserting these expressions in the DBE, Eq. 2.52, one can derive, for the case of tem-
porally separated pulses, where the pre-pulse induced polarisation already has decayed
before further pulses arrive, the relation

$$
\Delta f_{\mathbf{k}_\parallel}^{e/h} = \frac{1}{2}\left(1 - f_{\mathbf{k}_\parallel}^{e,0} - f_{\mathbf{k}_\parallel}^{h,0}\right) \pm \frac{1}{2}\sqrt{\left(1 - f_{\mathbf{k}_\parallel}^{e,0} - f_{\mathbf{k}_\parallel}^{h,0}\right)^2 - 4|\Delta p_{\mathbf{k}_\parallel}|^2} \approx \frac{|\Delta p_{\mathbf{k}_\parallel}|^2}{\left(1 - f_{\mathbf{k}_\parallel}^{e,0} - f_{\mathbf{k}_\parallel}^{h,0}\right)},
\tag{6.3}
$$

where the approximation is valid if the polarisation induced by further pulses is small
compared to $\left(1 - f_{\mathbf{k}_\parallel}^{e,0} - f_{\mathbf{k}_\parallel}^{h,0}\right)$.

Making the ansatz $p_{\mathbf{k}_\parallel} = \sum_n p_{\mathbf{k}_\parallel}^{[n]}$, where n denotes the order in the optical field, and
expanding the polarisation in terms of the eigenfunctions $\phi_\lambda^R(\mathbf{k}_\parallel)$ of $\mathcal{H}^0$ including pre-
pulse generated carrier distributions, $p_{\mathbf{k}_\parallel}^{[n]} = \sum_\lambda p_\lambda^{[n]} \phi_\lambda^R(\mathbf{k}_\parallel)$, we can solve the problem

iteratively, as the temporal evolution of $p_\lambda^{[n]}$ is given by

$$p_\lambda^{[n]}(t) = -\frac{i}{\hbar} \int_\infty^t \mathrm{d}t' \, \mathrm{e}^{-i(\epsilon_\lambda/\hbar - i\gamma)(t-t')} Q_\lambda^{[n]}(t').$$ (6.4)

Here, $Q_\lambda^{[n]}(t)$ denotes the source term in n^{th} order of the optical field. As discussed above, in general, the eigenvalues and -functions are frequency-dependent, but as we are interested in the homogeneous dephasing of the lowest excitonic state and the system response upon pulses resonant to this state, we reduce our calculations in the following to the dominant frequency $\omega = \omega_{1s} = \frac{\epsilon_{1s}}{\hbar}$. Furthermore, for the numerical calculations, the eigenvalues were sorted according to their oscillator strength and it was tested to be sufficient to include the 50 lowest states. The linear source term hereby reads

$$Q_\lambda^{[1]}(t) = \frac{e}{m_0 c} \sum_{\mathbf{k}_\parallel} \sqrt{\left(1 - f_{\mathbf{k}_\parallel}^{e,0} - f_{\mathbf{k}_\parallel}^{h,0}\right) k} \, \mathbf{p}_{cv} \cdot \mathbf{A}(t) \, [\phi_\lambda^L(\mathbf{k}_\parallel)]^*.$$ (6.5)

While experimentally, the signal need to be measured in the correct scattering direction, mathematically, we are able to separate the relevant and irrelevant contributions to the cubic source term. Keeping only terms proportional to $\propto A_1^* A_1^2$, the relevant cubic source term reads

$$\begin{aligned}
Q^{[3],DFWM}/2 = \; & \frac{e}{m_0 c} \sum_{\mathbf{k}_\parallel} \sum_{\lambda_1, \lambda_2} \frac{\mathbf{p}_{cv} \cdot \mathbf{A}_2}{\sqrt{1 - f_{\mathbf{k}_\parallel}^{e,0} - f_{\mathbf{k}_\parallel}^{h,0}}} [\phi_\lambda^L(\mathbf{k}_\parallel)]^* [\phi_{\lambda_1}^R(\mathbf{k}_\parallel)]^* \phi_{\lambda_2}^R(\mathbf{k}_\parallel) p_{\lambda_1}^{[1]*} p_{\lambda_2}^{[2]} \\
& + \sum_{\mathbf{k}_\parallel, \mathbf{k}_\parallel'} \sum_{\lambda_1, \lambda_2, \lambda_3} [\phi_\lambda^L(\mathbf{k}_\parallel)]^* \phi_{\lambda_2}^R(\mathbf{k}_\parallel) \phi_{\lambda_3}^R(\mathbf{k}_\parallel') p_{\lambda_1}^{[1]*} p_{\lambda_2}^{[2]} p_{\lambda_3}^{[2]} \\
& \left([\phi_{\lambda_1}^R(\mathbf{k}_\parallel)]^* W_{\mathbf{k}_\parallel, \mathbf{k}_\parallel'}^{ccvv} \frac{\sqrt{\left(1 - f_{\mathbf{k}_\parallel'}^{e,0} - f_{\mathbf{k}_\parallel'}^{h,0}\right) k'}}{\sqrt{\left(1 - f_{\mathbf{k}_\parallel}^{e,0} - f_{\mathbf{k}_\parallel}^{h,0}\right) k}} - [\phi_{\lambda_1}^R(\mathbf{k}_\parallel')]^* (W_{\mathbf{k}_\parallel, \mathbf{k}_\parallel'}^{vvvv} - W_{\mathbf{k}_\parallel, \mathbf{k}_\parallel'}^{cvvc}) \frac{1}{k'} \right),
\end{aligned}$$

with the left-/righthanded eigenstates $\phi_\lambda^{L/R}(\mathbf{k}_\parallel)$, that are unequal due to the non-Hermitian scattering contributions. The resulting time-integrated signal for pulses of width $t_{width} = 150\,\mathrm{fs}$ and central frequency $\omega_1 = \omega_2 = \omega_{1s}$ is shown in Fig. 6.4 for different pre-pulse generated Fermi distributed ($T = 300\,\mathrm{K}$) carrier densities. In the inset, the respective carrier density and the corresponding homogeneous linewidth γ_{hom} are depicted. The integrated signal decreases for positive delay times exponentially with an exponent proportional to $2\gamma_{hom}$. Due to the electron-hole plasma-induced dephasing, the slope steepens with increasing carrier density approaching the self-correlated signal, that is illustrated as gray area.

7. Summary and outlook

The physical properties of TMDC materials are promising, their potential applications in opto-electronic devices are versatile. To further advance the understanding of these materials, in this thesis we aimed to elaborate computational efficient and comprehensible but precise theoretical models to describe monolayer TMDC materials, namely MoS_2, $MoSe_2$, $MoTe_2$, WS_2, WSe_2, under varying external conditions and utilize these models to investigate the impact of the varying conditions on the material response to external optical fields. Here, the complex interplay of initial excitation, dielectric environment and magnetic field and its influence on the interaction of electrons and phonons and the energetic spectrum was analysed. In the different studies summarised in this thesis, different physical phenomena were focused on and the theoretical models were adapted to the respective research question.

In general, we applied a combined approach based on DFT and SBE/DBE formalisms to model the material systems. Here, DFT was employed to find fundamental material properties like the single-particle band structure, dielectric properties and phononic dispersions. These findings were then used to set up a model Hamiltonian to describe the energetic structure and interactions of electrons, phonons and electromagnetic fields. Different models regarding the interactions were applied to describe the behaviour in proximity to the K/K'-points (MDF model) and the remaining BZ. The dynamics of the density matrix, as described by their equation of motion based on the model Hamiltonian, was evaluated in different approximations and yielded, with the time-dependent microscopic density matrix, all informations to derive the macroscopic optical properties. The material thinness causes enhanced many-body interactions and a high sensitivity on environmental conditions resulting in large exciton binding energies, large renormalisation effects, versatile tools to tune the opto-electronic properties and ultrafast dynamics within the sample. Hence, a proper model for describing the Coulomb interaction in these materials is essential for further investigations. In our model, we explicitly included finite thickness and environmental screening effects by deriving an expression for the Coulomb potential based on a solution of the Poisson equation for a slab geometry and by deriving an analytical approximation of the Coulomb-matrix elements which were evaluated based on the DFT wave functions. Here, the Coulomb potential differs from both the exact

two-dimensional and the exact three-dimensional case. Our study has shown that the effective thickness of a material increases with the size of the incorporated atoms, in line with the expectation. The precise incorporation of the Coulomb interaction into the SBE enables the prediction of the electronic and optical energy spectrum. Comparisons to experimental studies have shown that our model is able to successfully describe the ground state optical and electronic band gap and its dependence on the dielectric environment. The Coulomb interaction is screened by the dielectric environment and consequently, the electronic band gap and the exciton binding energy are reduced for materials with enhanced dielectric constants. Furthermore, the Coulomb interaction is screened by the presence of excited carriers due to higher order correlations. Here, two aspects were observed in different studies: First, it was seen that a static approximation of the screening results in an overestimation of screening effects for small carrier densities. In contrast, for larger densities, differences between a static and a dynamical treatment become smaller and are in the range of $10\,\mathrm{meV}$ only. This legitimises this static approximation when studying relaxation dynamics after excitation with high-intensity laser pulses. Second, further analyses of the frequency-dependence have shown that approximations are justified when restricting to the analysis of particular properties. Here, it is sufficient to take into account only the dominant frequency. But, in contrast, this does not hold for an analysis of the density-dependent linear optical response. It was seen that regarding the optical response, the full frequency-dependence needs to be considered. Moreover, we included higher order correlations exceeding the singlet-doublet approximation by a phenomenological dephasing that also enter the equations via the plasma screening. Our studies have shown that a large triplet dephasing constant of several hundred meV needs to be assumed to achieve proper descriptions of the density-dependent band gap shrinkage and optical spectra. Here, a deepened understanding of the dephasing processes due to higher correlations is desirable – to test the assumption of this large triplet dephasing and to investigate e.g. its density-dependence. To analyse the dephasing processes in more detail requires the explicit treatment of next order correlations and is thus a challenging task. Nevertheless, the present model is already effective and its predictions for the excitonic spectrum and the density-dependent band gap renormalisation are in good agreement with experimental data.

Based on this efficient description of the Coulombic interactions between carriers, in further studies, we investigated the carrier dynamics in the materials after strong above-band gap excitation. Here, we focused on molybdenum-based materials that display an optically bright (spin-allowed) direct band gap. The strong Coulomb interaction was shown to lead to large renormalisations of the band gap in the order of several $100\,\mathrm{meV}$ already during the first femtoseconds and ultrafast carrier-relaxation dynamics. In a first study, the numerical analysis of a pump-probe scenario showed an efficient absorption of the incident light as the carriers were effectively driven away from the excitation

energy due to carrier-carrier-scattering and large renormalisation effects. Thereafter, the phonon-mediated thermalisation of the carriers led to the build-up of optical gain below the lowest A-exciton which was predicted to be enhanced due to equilibration of the carriers in the different valleys of the BZ.

Because the model applied in this first study was restricted to the dynamics at the main valley, and the equilibration of the carriers was shown to have an impact on the material optical response, we expanded and modified our model for a consecutive study. Here, we took into account the full DFT band structure and absolute dipole matrix elements of conduction and valence bands, as well as all phonons. Again, it was seen that excited carriers were driven into hot, Fermi-like distributions on a femtosecond timescale, where carrier-carrier scattering processes were seen to dominate the dynamics. Furthermore, the timescales for intravalley scattering processes mediated by acoustic phonons were shown to depend crucially on the initial excitation conditions – we experienced intravalley-scattering on the femtosecond timescale for excitation high in the bands and on picosecond timescales for resonant excitation. After the first few femtoseconds, phononic contributions of optical phonons dominate the dynamics and result in a cooling of the hot distributions. In contrast to previous theoretical predictions, we did not find a transition of the material to an indirect semiconductor upon optical excitation for any of the investigated molybdenum-based materials [86, 87].

Furthermore, in the low-density regime, the strong Coulomb interaction gives rise to pronounced excitonic resonances. In two studies, we investigated different aspects of these quasiparticles under varying initial conditions. First, we focused on the influence of the interplay of material properties, magnetic field and dielectric environment on the excitonic spectrum and changes in the optical spectrum upon occupations of the different excitonic states. Within our model we could predict the magnetic field-induced shifts for the excitonic resonance energies. Our findings regarding the magnetic field-induced shift of the s-exciton series are in good agreement with experimental findings [76]. Furthermore, our studies predict an optical gain in the THz-regime upon proper excitation conditions, namely in the presence of a $2s$-excitonic occupation. This gain is tunable by applying a magnetic field – due to the different dependencies of s- and p-type excitonic states on the magnetic field – and by changing the dielectric environment. This tunability was seen to be even more pronounced in tungsten than in molybdenum-based materials. Second, we analysed the homogeneous broadening of the lowest excitonic resonance in the presence on an electron-hole plasma. We have seen a density-dependent linear increase of the broadening, which in a simulation of a FWM measurement results in a faster decay of the signal for higher densities, as the signal decreases exponentially with twice the dephasing constant. Additionally, both processes taking place after an initial excitation – the cooling and the redistribution of carriers in the different valleys due to equilibration – result in a sharpening of the exciton resonance.

In these two case studies, we assumed idealised density distributions: Whereas we assumed excitonic occupations in the former, we assumed an electron-hole plasma in the latter. In a realistic scenario, a conglomeration of bound and unbound states is present after excitation, and their ratio depends on the excitation conditions [78, 79, 102]. Hence, in an experimental study slightly different results can be expected. To include more realistic density distributions, expansions of our model in two ways would be interesting. First, a combination of the numerical simulation of the relaxation dynamics in the full BZ and their influence on the optical spectra. Second, a detailed analysis of the exciton formation processes and its dependence on the excitation conditions. However, this possibility of choosing the initial conditions enables the theoretical study to discriminate influences of different contributions on the optical spectrum. Thus, in first approximations, the influence of excitonic occupations on the dephasing of the exciton resonances and an estimation of the OPTP-spectrum upon mixed occupation conditions of bound and unbound states could be investigated.

In the course of this thesis, we blazed a trail from the linear optical properties in the low-density regime to the high-density regime and took a step back again to the low-density regime where we analysed the non-linear FWM signal. Continuing on this path, a next intermediate goal shows up: the study of the highly non-linear high-harmonic generation (HHG). In conventional semiconducting structures, the research on high-harmonic generation is well advanced, but the origin of even order harmonics in particular has been questioned again in the last years. A discussion arose around the importance of the wave functions phase, which is expressed in phase-dependent dipole- and Coulomb-matrix elements [103, 104, 105]. In previous studies, the phase-dependency was neglected in favour of an exclusive consideration of absolute values. In contrast, in recent studies of the HHG signals parallel and perpendicular to the incident field, differing importances of even and odd order harmonics in these spectra were explicitly explained in a semiclassical approach by a finite Berry curvature [106]. Regarding the microscopic evaluation of the dynamics, several difficulties occur when one aims to include the phase. In general, the derivation of the ground state by diagonalising the system Hamiltonian, is executed independently for the different crystal momenta. Therefore, a random k-point-dependent phase of the wave functions is introduced, whereas the microscopic analysis requires a continuous phase. Thus, a post-processing of the DFT output data, regarding the wave functions and dipole-matrix elements, is needed in order to smooth the phase along the chosen path in reciprocal space. Different procedures based on parallel-transport theory and executed using either the real or the momentum space representation of the wave functions have been established [103, 107, 108]. Here, especially if a Berry phase is accumulated along a path which results in a finite Berry connection ($\equiv$ 'intraband dipole'), and if a periodicity of the dipoles is desired, a reconsideration of the assignment of different HHG contributions to inter- and intraband terms is required [108]. Additio-

nally to these challenges arising with a proper treatment of the complex dipole matrix elements, in TMDC materials the Coulomb interaction is important, other than in conventional semiconductors, where the Coulomb interactions are of minor importance and consequently neglected in many theoretical studies [109, 110]. In previous experimental studies, enhanced HHG signals per layer for a monolayer compared to the bulk material were attributed to Coulomb interactions [106]. Despite the slightly increasing number of experimental studies that were mostly interpreted on a semiclassical basis, a model describing the observations on a microscopic level is lacking [111, 112, 113]. Such a model would require to go beyond the MDF and the effective two-band model as well as an inclusion of phase information. Studying the interplay of quantum interference, geometric phase and Coulombic contributions as observed in HHG spectra of TMDC monolayers promises to be an interesting new task in the context of low-dimensional materials.

Literaturverzeichnis

[1] https://www.nobelprize.org/prizes/physics/2010/press-release/ (06/07/2022).

[2] P. R. Wallace. „The Band Theory of Graphite". *Phys. Rev.*, 71(9):622–634, May 1947.

[3] H. W. Kroto, J. R. Heath, S. C. O'Brien, R. F. Curl, and R. E. Smalley. „C60: Buckminsterfullerene". *Nature*, 318(6042):162–163, November 1985.

[4] https://www.nobelprize.org/prizes/chemistry/1996/summary/ (06/07/2022).

[5] A. Krishnan, E. Dujardin, M. M. J. Treacy, J. Hugdahl, S. Lynum, and T. W. Ebbesen. „Graphitic cones and the nucleation of curved carbon surfaces". *Nature*, 388(6641):451–454, July 1997.

[6] K. S. Novoselov, A. K. Geim, S. V. Morozov, D. Jiang, Y. Zhang, S. V. Dubonos, I. V. Grigorieva, and A. A. Firsov. „Electric Field Effect in Atomically Thin Carbon Films". *Science*, 306(5696):666–669, October 2004.

[7] J. Young, S. M. Walker, R. J. Bomphrey, G. K. Taylor, and A. L. R. Thomas. „Details of Insect Wing Design and Deformation Enhance Aerodynamic Function and Flight Efficiency". *Science*, 325(5947):1549–1552, September 2009.

[8] A. L. Elías, N. Perea-López, A. Castro-Beltrán, A. Berkdemir, R. Lv, S. Feng, A. D. Long, T. Hayashi, Y. A. Kim, M. Endo, H. R. Gutiérrez, N. R. Pradhan, L. Balicas, T. E. Mallouk, F. López-Urías, H. Terrones, and M. Terrones. „Controlled Synthesis and Transfer of Large-Area WS$_2$ Sheets: From Single Layer to Few Layers". *ACS Nano*, 7(6):5235–5242, June 2013.

[9] J.-K. Huang, J. Pu, C.-L. Hsu, M.-H. Chiu, Z.-Y. Juang, Y.-H. Chang, W.-H. Chang, Y. Iwasa, T. Takenobu, and L.-J. Li. „Large-Area Synthesis of Highly Crystalline WSe$_2$ Monolayers and Device Applications". *ACS Nano*, 8(1):923–930, January 2014.

[10] S. M. Eichfeld, L. Hossain, Y.-C. Lin, A. F. Piasecki, B. Kupp, A. G. Birdwell, R. A. Burke, N. Lu, X. Peng, J. Li, A. Azcatl, S. McDonnell, R. M. Wallace, M. J. Kim, T. S. Mayer, J. M. Redwing, and J. A. Robinson. „Highly Scalable,

Atomically Thin WSe$_2$ Grown via Metal-Organic Chemical Vapor Deposition". *ACS Nano*, 9(2):2080–2087, February 2015.

[11] S. Z. Butler, S. M. Hollen, L. Cao, Y. Cui, J. A. Gupta, H. R. Gutiérrez, T. F. Heinz, S. S. Hong, J. Huang, A. F. Ismach, E. Johnston-Halperin, M. Kuno, V. V. Plashnitsa, R. D. Robinson, R. S. Ruoff, S.Salahuddin, J. Shan, L. S., M. G. Spencer, M. Terrones, W. Windl, and J E. Goldberger. „Progress, Challenges, and Opportunities in Two-Dimensional Materials Beyond Graphene". *ACS Nano*, 7(4):2898–2926, April 2013.

[12] M. Xu, T. Liang, M. Shi, and H. Chen. „Graphene-Like Two-Dimensional Materials". *Chem. Rev.*, 113(5):3766–3798, May 2013.

[13] P. Miro, M. Audiffred, and T. Heine. „An atlas of two-dimensional materials". *Chem. Soc. Rev.*, 43(18):6537–6554, 2014.

[14] J. A. Wilson and A. D. Yoffe. „The transition metal dichalcogenides discussion and interpretation of the observed optical, electrical and structural properties". *Advances in Physics*, 18(73):193–335, May 1969.

[15] A. J. Grant, J. A. Wilson, and A. D. Yoffe. „Optical studies of transition metal dichalcogenide layer crystals at high pressures". *The Philosophical Magazine: A Journal of Theoretical Experimental and Applied Physics*, 25(3):625–636, March 1972.

[16] A. R. Beal, J. C. Knights, and W. Y. Liang. „Transmission spectra of some transition metal dichalcogenides. II. Group VIA: trigonal prismatic coordination". *J. Phys. C: Solid State Phys.*, 5(24):3540–3551, December 1972.

[17] C. N. R. Rao and K. P. R. Pisharody. „Transition metal sulfides". *Progress in Solid State Chemistry*, 10:207–270, January 1976.

[18] K. F. Mak, C. Lee, J. Hone, J. Shan, and T. F. Heinz. „Atomically Thin MoS$_2$: A New Direct-Gap Semiconductor". *Phys. Rev. Lett.*, 105(13):136805, September 2010.

[19] A. Splendiani, L. Sun, Y. Zhang, T. Li, J. Kim, C.-Y. Chim, G. Galli, and F. Wang. „Emerging Photoluminescence in Monolayer MoS$_2$". *Nano Letters*, 10(4):1271–1275, 2010.

[20] W.-T. Hsu, L.-S. Lu, D. Wang, J.-K. Huang, M.-Y. Li, T.-R. Chang, Y.-C. Chou, Z.-Y. Juang, H.-T. Jeng, L.-J. Li, and W.-H. Chang. „Evidence of indirect gap in monolayer WSe$_2$". *Nat Commun*, 8(1):929, October 2017.

[21] C. Zhang, Y. Chen, A. Johnson, M.-Y. Li, L.-J. Li, P. C. Mende, R. M. Feenstra, and C.-K. Shih. „Probing Critical Point Energies of Transition Metal Dichalcogenides: Surprising Indirect Gap of Single Layer WSe$_2$“. *Nano Lett.*, 15(10):6494–6500, October 2015.

[22] K. S. Novoselov, A. Mishchenko, A. Carvalho, and A. H. Castro Neto. „2D materials and van der Waals heterostructures“. *Science*, 353(6298):aac9439, July 2016.

[23] C. Zhang, H. Wang, W. Chan, C. Manolatou, and F. Rana. „Absorption of light by excitons and trions in monolayers of metal dichalcogenide MoS$_2$: Experiments and theory“. *Phys. Rev. B*, 89(20):205436, May 2014.

[24] D. Jariwala, A. R. Davoyan, J. Wong, and H. A. Atwater. „Van der Waals Materials for Atomically-Thin Photovoltaics: Promise and Outlook“. *ACS Photonics*, 4(12):2962–2970, December 2017.

[25] O. Lopez-Sanchez, E. Alarcon Llado, V. Koman, A. F. i Morral, A. Radenovic, and A. Kis. „Light Generation and Harvesting in a van der Waals Heterostructure“. *ACS Nano*, 8(3):3042–3048, March 2014.

[26] B. Radisavljevic, M. B. Whitwick, and A. Kis. „Integrated Circuits and Logic Operations Based on Single-Layer MoS$_2$“. *ACS Nano*, 5(12):9934–9938, December 2011.

[27] B. Radisavljevic, M. B. Whitwick, and A. Kis. „Small-signal amplifier based on single-layer MoS2“. *Appl. Phys. Lett.*, 101(4):043103, July 2012.

[28] Y. Ye, Z. J. Wong, X. Lu, X. Ni, H. Zhu, X. Chen, Y. Wang, and X. Zhang. „Monolayer excitonic laser“. *Nature Photon*, 9(11):733–737, November 2015.

[29] Md T. Rahman, R. Kumar, M. Kumar, and Q. Qiao. „Two-dimensional transition metal dichalcogenides and their composites for lab-based sensing applications: Recent progress and future outlook“. *Sensors and Actuators A: Physical*, 318:112517, February 2021.

[30] F. Liu, M. E. Ziffer, K. R. Hansen, J. Wang, and X. Zhu. „Direct Determination of Band-Gap Renormalization in the Photoexcited Monolayer MoS$_2$“. *Phys. Rev. Lett.*, 122(24):246803, June 2019.

[31] M. M. Ugeda, A. J.Bradley, S.-F. Shi, H. Felipe, Y. Zhang, D. Y. Qiu, W. Ruan, S.-K. Mo, Z. Hussain, Z.-X. Shen, and others. „Giant bandgap renormalization and excitonic effects in a monolayer transition metal dichalcogenide semiconductor“. *Nature materials*, 13(12):1091–1095, 2014.

[32] S. Latini, T. Olsen, and K. S. Thygesen. „Excitons in van der Waals heterostructures: The important role of dielectric screening". *Phys. Rev. B*, 92(24):245123, December 2015.

[33] M. Drüppel, T. Deilmann, P. Krüger, and M. Rohlfing. „Diversity of trion states and substrate effects in the optical properties of an MoS_2 monolayer". *Nat Commun*, 8(1):2117, December 2017.

[34] M. Florian, M. Hartmann, A. Steinhoff, J. Klein, A. W. Holleitner, J. J. Finley, T. O. Wehling, M. Kaniber, and C. Gies. „The Dielectric Impact of Layer Distances on Exciton and Trion Binding Energies in van der Waals Heterostructures". *Nano Lett.*, 18(4):2725–2732, April 2018.

[35] D. Van Tuan, M. Yang, and H. Dery. „Coulomb interaction in monolayer transition-metal dichalcogenides". *Phys. Rev. B*, 98(12):125308, September 2018.

[36] P. Hohenberg and W. Kohn. „Inhomogeneous Electron Gas". *Phys. Rev.*, 136(3B):B864–B871, November 1964.

[37] W. Kohn and L. J. Sham. „Self-Consistent Equations Including Exchange and Correlation Effects". *Phys. Rev.*, 140(4A):A1133–A1138, November 1965.

[38] D. S. Sholl and J. A. Steckel. *Density Functional Theory: A Practical Introduction.* John Wiley & Sons, September 2011.

[39] Rb. O. Jones. „Density functional theory: Its origins, rise to prominence, and future". *Rev. Mod. Phys.*, 87(3):897–923, August 2015.

[40] G. Kresse and J. Hafner. „Ab initio molecular dynamics for liquid metals". *Phys. Rev. B*, 47(1):558–561, January 1993.

[41] G. Kresse and J. Hafner. „Ab initio molecular-dynamics simulation of the liquid-metal–amorphous-semiconductor transition in germanium". *Phys. Rev. B*, 49(20):14251–14269, May 1994.

[42] G. Kresse and J. Furthmüller. „Efficiency of ab-initio total energy calculations for metals and semiconductors using a plane-wave basis set". *Computational Materials Science*, 6(1):15–50, July 1996.

[43] G. Kresse and J. Furthmüller. „Efficient iterative schemes for ab initio total-energy calculations using a plane-wave basis set". *Phys. Rev. B*, 54(16):11169–11186, October 1996.

[44] J. P. Perdew, K. Burke, and M. Ernzerhof. „Generalized Gradient Approximation Made Simple". *Phys. Rev. Lett.*, 77(18):3865–3868, October 1996.

[45] S. Grimme, J. Antony, S. Ehrlich, and H. Krieg. „A consistent and accurate ab initio parametrization of density functional dispersion correction (DFT-D) for the 94 elements H-Pu". *The Journal of Chemical Physics*, 132(15):154104, April 2010.

[46] D. Xiao, G.-B. Liu, W. Feng, X. Xu, and W. Yao. „Coupled Spin and Valley Physics in Monolayers of MoS_2 and Other Group-VI Dichalcogenides". *Phys. Rev. Lett.*, 108(19):196802, May 2012.

[47] G.-B. Liu, Di Xiao, Y. Yao, X. Xu, and W. Yao. „Electronic structures and theoretical modelling of two-dimensional group-VIB transition metal dichalcogenides". *Chem. Soc. Rev.*, 44(9):2643–2663, April 2015.

[48] A. Kormányos, G. Burkard, M. Gmitra, J. Fabian, V. Zólyomi, N. D. Drummond, and V. Fal'ko. „k·p theory for two-dimensional transition metal dichalcogenide semiconductors". *2D Materials*, 2(2):022001, April 2015.

[49] L. Meckbach, T. Stroucken, and S. W. Koch. „Influence of the effective layer thickness on the ground-state and excitonic properties of transition-metal dichalcogenide systems". *Phys. Rev. B*, 97(3):035425, January 2018.

[50] L. V. Keldysh. „Coulomb interaction in thin semiconductor and semimetal films". *Soviet Journal of Experimental and Theoretical Physics Letters*, 29:658, June 1979. ADS Bibcode: 1979JETPL..29..658K.

[51] S. Schmitt-Rink and C. Ell. „Excitons and electron-hole plasma in quasi-two-dimensional systems". *Journal of Luminescence*, 30(1):585–596, February 1985.

[52] P. Cudazzo, I. V. Tokatly, and A. Rubio. „Dielectric screening in two-dimensional insulators: Implications for excitonic and impurity states in graphane". *Phys. Rev. B*, 84(8):085406, August 2011.

[53] C. E. Stevens, T. Stroucken, A. V. Stier, J. Paul, H. Zhang, P. Dey, S. A. Crooker, S. W. Koch, and D. Karaiskaj. „Superradiant coupling effects in transition-metal dichalcogenides". *Optica*, 5(6):749, June 2018.

[54] A. S. Rodin and A. H. Castro Neto. „Excitonic collapse in semiconducting transition-metal dichalcogenides". *Phys. Rev. B*, 88(19):195437, November 2013.

[55] W. Nolting. *Grundkurs Theoretische Physik 5/2*. Springer-Lehrbuch. Springer, Berlin, Heidelberg, 2015.

[56] T. Sohier, M. Calandra, and F. Mauri. „Two-dimensional Fröhlich interaction in transition-metal dichalcogenide monolayers: Theoretical modeling and first-principles calculations". *Phys. Rev. B*, 94(8):085415, August 2016.

[57] P. Giannozzi, S. Baroni, N. Bonini, M. Calandra, R. Car, C. Cavazzoni, D. Ceresoli, G. L. Chiarotti, M. Cococcioni, I. Dabo, A. Dal Corso, S. de Gironcoli, S. Fabris, G. Fratesi, R. Gebauer, U. Gerstmann, C. Gougoussis, A. Kokalj, M. Lazzeri, L. Martin-Samos, N. Marzari, F. Mauri, R. Mazzarello, S. Paolini, A. Pasquarello, L. Paulatto, C. Sbraccia, S. Scandolo, G. Sclauzero, A. P. Seitsonen, A. Smogunov, P. Umari, and R. M. Wentzcovitch. „QUANTUM ESPRESSO: a modular and open-source software project for quantum simulations of materials". *J. Phys.: Condens. Matter*, 21(39):395502, September 2009.

[58] P. Giannozzi, O. Andreussi, T. Brumme, O. Bunau, M. Buongiorno Nardelli, M. Calandra, R. Car, C. Cavazzoni, D. Ceresoli, M. Cococcioni, N. Colonna, I. Carnimeo, A. Dal Corso, S. de Gironcoli, P. Delugas, R. A. DiStasio, A. Ferretti, A. Floris, G. Fratesi, G. Fugallo, R. Gebauer, U. Gerstmann, F. Giustino, T. Gorni, J. Jia, M. Kawamura, H.-Y. Ko, A. Kokalj, E. Küçükbenli, M. Lazzeri, M. Marsili, N. Marzari, F. Mauri, N. L. Nguyen, H.-V. Nguyen, A. Otero-de-la Roza, L. Paulatto, S. Ponc'e, D. Rocca, R. Sabatini, B. Santra, M. Schlipf, A. P. Seitsonen, A. Smogunov, I. Timrov, T. Thonhauser, P. Umari, N. Vast, X. Wu, and S. Baroni. „Advanced capabilities for materials modelling with Quantum ESPRESSO". *J. Phys.: Condens. Matter*, 29(46):465901, October 2017.

[59] H. Haug and S. W. Koch. *Quantum Theory Of The Optical And Electronic Properties Of Semiconductors (5th Edition)*. World Scientific Publishing Company, January 2009.

[60] M. Kira and S. Koch. „Many-body correlations and excitonic effects in semiconductor spectroscopy". *Prog. Quantum. Electron.*, 30, 2006.

[61] T. Stroucken, J. H. Grönqvist, and S. W. Koch. „Optical response and ground state of graphene". *Phys. Rev. B*, 84(20):205445, November 2011.

[62] T. Stroucken and S. W Koch. „Microscopic Theory for the Groundstate and Linear Optical Response of Novel Two-Dimensional Materials with Hexagonal Symmetry". In Rolf Binder, editor, *Optical Properties of Graphene*, pages 43 – 84. World Scientific Publishing, Singapur, 2017. Section: 2.

[63] J. Sabio, F. Sols, and F. Guinea. „Variational approach to the excitonic phase transition in graphene". *Phys. Rev. B*, 82(12):121413, September 2010.

[64] L. Meckbach. „Exzitonische Eigenschaften von TMDCs", 2017. Master thesis (Fachbereich Physik, Philipps-Universität Marburg).

[65] C. G. Kuper and G. D. Whitfield, editors. *Polarons and excitons*. Plenum Press, New York, 1963. Meeting Name: Scottish Universities Summer School in Physics.

[66] A. Chernikov, T. C. Berkelbach, H. M. Hill, A. Rigosi, Y. Li, O. B. Aslan, D. R. Reichman, M. S. Hybertsen, and T. F. Heinz. „Exciton Binding Energy and Non-hydrogenic Rydberg Series in Monolayer WS$_2$". *Phys. Rev. Lett.*, 113(7):076802, August 2014.

[67] A. Chernikov, A. M. van der Zande, H. M. Hill, A. F. Rigosi, A. Velauthapillai, J. Hone, and T. F. Heinz. „Electrical Tuning of Exciton Binding Energies in Monolayer WS$_2$". *Phys. Rev. Lett.*, 115(12):126802, September 2015.

[68] W. Barford, I. Boczarow, and T. Wharram. „Ultrafast Dynamical Localization of Photoexcited States in Conformationally Disordered Poly(p-phenylenevinylene)". *The Journal of Physical Chemistry A*, 115(33):9111–9119, 2011.

[69] S. K. Ignatov, A. G. Razuvaev, V. N. Kokorev, and Yu. A. Aleksandrov. „Semiempirical calculation of two-electron integrals using bipolar expansion of the Ohno potential". *Journal of Structural Chemistry*, 36(4):538–543, July 1995.

[70] A. F. Rigosi, H. M. Hill, K. T. Rim, G. W. Flynn, and T. F. Heinz. „Electronic band gaps and exciton binding energies in monolayer Mo$_x$W$_{1-x}$S$_2$ transition metal dichalcogenide alloys probed by scanning tunneling and optical spectroscopy". *Phys. Rev. B*, 94(7):075440, August 2016.

[71] M. Goryca, J. Li, A. V. Stier, T. Taniguchi, K. Watanabe, E. Courtade, S. Shree, C. Robert, B. Urbaszek, X. Marie, and others. „Revealing exciton masses and dielectric properties of monolayer semiconductors with high magnetic fields". *Nature communications*, 10(1):1–12, 2019.

[72] K. S. Thygesen. „Calculating excitons, plasmons, and quasiparticles in 2D materials and van der Waals heterostructures". *2D Materials*, 4(2):022004, June 2017.

[73] I. C. Gerber and X. Marie. „Dependence of band structure and exciton properties of encapsulated WSe$_2$ monolayers on the hBN-layer thickness". *Phys. Rev. B*, 98(24):245126, December 2018.

[74] G. Wang, X. Marie, I. Gerber, T. Amand, D. Lagarde, L. Bouet, M. Vidal, A. Balocchi, and B. Urbaszek. „Giant Enhancement of the Optical Second-Harmonic Emission of WSe$_2$ Monolayers by Laser Excitation at Exciton Resonances". *Phys. Rev. Lett.*, 114(9):097403, March 2015.

[75] E. Liu, J. van Baren, T. Taniguchi, K. Watanabe, Y.-C. Chang, and C. H. Lui. „Magnetophotoluminescence of exciton Rydberg states in monolayer WSe$_2$". *Phys. Rev. B*, 99(20):205420, May 2019.

[76] A. V. Stier, N. P. Wilson, K. A. Velizhanin, J. Kono, X. Xu, and S. A. Crooker. „Magnetooptics of Exciton Rydberg States in a Monolayer Semiconductor". *Phys. Rev. Lett.*, page 6, 2018.

[77] C. Poellmann, P. Steinleitner, U. Leierseder, P. Nagler, G. Plechinger, M. Porer, R. Bratschitsch, C. Schüller, T. Korn, and R. Huber. „Resonant internal quantum transitions and femtosecond radiative decay of excitons in monolayer WSe$_2$". *Nature Mater*, 14(9):889–893, September 2015.

[78] P. Steinleitner, P. Merkl, P. Nagler, J. Mornhinweg, C. SchÃ¼ller, T. Korn, A. Chernikov, and R. Huber. „Direct Observation of Ultrafast Exciton Formation in a Monolayer of WSe$_2$". *Nano Lett.*, 17(3):1455–1460, March 2017.

[79] S. Brem, M. Selig, G. Berghaeuser, and E. Malic. „Exciton Relaxation Cascade in two-dimensional Transition Metal Dichalcogenides". *Sci Rep*, 8(1):8238, December 2018.

[80] J. Zipfel, J. Holler, A. A. Mitioglu, M. V. Ballottin, P. Nagler, A. V. Stier, T. Taniguchi, K. Watanabe, S. A. Crooker, P. C. M. Christianen, T. Korn, and A. Chernikov. „Spatial extent of the excited exciton states in WS$_2$ monolayers from diamagnetic shifts". *Phys. Rev. B*, 98(7):075438, August 2018.

[81] Y. Li, J. Ludwig, T. Low, A. Chernikov, X. Cui, G. Arefe, Y. D. Kim, A. M. van der Zande, A. Rigosi, H. M. Hill, S. H. Kim, J. Hone, Z. Li, D. Smirnov, and T. F. Heinz. „Valley Splitting and Polarization by the Zeeman Effect in Monolayer MoSe$_2$". *Phys. Rev. Lett.*, 113(26):266804, December 2014.

[82] R. Wallauer, J. Reimann, N. Armbrust, J. Güdde, and U. Höfer. „Intervalley scattering in MoS$_2$ imaged by two-photon photoemission with a high-harmonic probe". *Appl. Phys. Lett.*, 109(16):162102, October 2016.

[83] R. Bertoni, C. W. Nicholson, L. Waldecker, H. Hübener, C. Monney, U. De Giovannini, M. Puppin, M. Hoesch, E. Springate, R. T. Chapman, C. Cacho, M. Wolf, A. Rubio, and R. Ernstorfer. „Generation and Evolution of Spin-, Valley-, and Layer-Polarized Excited Carriers in Inversion-Symmetric WSe$_2$". *Phys. Rev. Lett.*, 117(27):277201, December 2016.

[84] W. H. Press, S. A. Teukolsky, W. T. Vetterling, and B. P. Flannery. *Numerical Recipes 3rd Edition: The Art of Scientific Computing*. Cambridge University Press, September 2007.

[85] L. Meckbach. „Microscopic theory of the linear and nonlinear optical properties of TMDCs", 2020. Philipps-Universität Marburg.

[86] F. Lohof, A. Steinhoff, M. Florian, M. Lorke, D. Erben, F. Jahnke, and C. Gies. „Prospects and Limitations of Transition Metal Dichalcogenide Laser Gain Materials". *Nano Lett.*, 19(1):210–217, January 2019.

[87] D. Erben, A. Steinhoff, C. Gies, G. Schönhoff, T. O. Wehling, and F. Jahnke. „Excitation-induced transition to indirect band gaps in atomically thin transition-metal dichalcogenide semiconductors". *Phys. Rev. B*, 98(3):035434, July 2018.

[88] F. A. Rasmussen and K. S. Thygesen. „Computational 2D Materials Database: Electronic Structure of Transition-Metal Dichalcogenides and Oxides". *J. Phys. Chem. C*, 119(23):13169–13183, June 2015.

[89] E. Blundo, M. Felici, T. Yildirim, G. Pettinari, D. Tedeschi, A. Miriametro, B. Liu, W. Ma, Y. Lu, and A. Polimeni. „Evidence of the direct-to-indirect band gap transition in strained two-dimensional WS_2, MoS_2, and WSe_2". *Phys. Rev. Research*, 2(1):012024, January 2020.

[90] Y. Aksu Korkmaz, C. Bulutay, and C. Sevik. „$k \cdot p$ Parametrization and Linear and Circular Dichroism in Strained Monolayer (Janus) Transition Metal Dichalcogenides from First-Principles". *J. Phys. Chem. C*, 125(13):7439–7450, April 2021.

[91] L. Ren, C. Robert, B. Urbaszek, X. Marie, M. Semina, and M. M. Glazov. „Tuning absorption and emission in monolayer semiconductors: a brief survey". *Comptes Rendus. Physique*, 22(S4):43–52, 2021.

[92] F. Cadiz, E. Courtade, C. Robert, G. Wang, Y. Shen, H. Cai, T. Taniguchi, K. Watanabe, H. Carrere, D. Lagarde, M. Manca, T. Amand, P. Renucci, S. Tongay, X. Marie, and B. Urbaszek. „Excitonic Linewidth Approaching the Homogeneous Limit in MoS_2 -Based van der Waals Heterostructures". *Phys. Rev. X*, 7(2):021026, May 2017.

[93] C. Robert, M. A. Semina, F. Cadiz, M. Manca, E. Courtade, T. Taniguchi, K. Watanabe, H. Cai, S. Tongay, B. Lassagne, P. Renucci, T. Amand, X. Marie, M. M. Glazov, and B. Urbaszek. „Optical spectroscopy of excited exciton states in MoS_2 monolayers in van der Waals heterostructures". *Phys. Rev. Materials*, 2(1):011001, January 2018.

[94] E. W. Martin, J. Horng, H. G. Ruth, E. Paik, M.-H. Wentzel, H. Deng, and S. T. Cundiff. „Encapsulation Narrows and Preserves the Excitonic Homogeneous Linewidth of Exfoliated Monolayer $MoSe_2$". *Phys. Rev. Applied*, 14(2):021002, August 2020.

[95] M. Selig, G. Berghäuser, A. Raja, P. Nagler, C. Schüller, T. F. Heinz, T. Korn, A. Chernikov, E. Malic, and A. Knorr. „Excitonic linewidth and coherence lifetime in

monolayer transition metal dichalcogenides". *Nat Commun*, 7(1):13279, November 2016.

[96] J. C. G. Henriques, N. A. Mortensen, and N. M. R. Peres. „Analytical description of the 1 s exciton linewidth temperature dependence in transition metal dichalcogenides". *Phys. Rev. B*, 103(23):235402, June 2021.

[97] T. Jakubczyk, M. Bartos, L. Scarpelli, K. Nogajewski, W. Langbein, M. Potemski, and J. Kasprzak. „Coherent dynamics of resonantly excited excitons in monolayers of transition metal dichalcogenides". In *Ultrafast Phenomena and Nanophotonics XXIV*, volume 11278, page 112781C. International Society for Optics and Photonics, February 2020.

[98] T. Jakubczyk, G. Nayak, L. Scarpelli, W.-L. Liu, S. Dubey, N. Bendiab, L. Marty, T. Taniguchi, K. Watanabe, F. Masia, G. Nogues, J. Coraux, W. Langbein, J. Renard, V. Bouchiat, and J. Kasprzak. „Coherence and Density Dynamics of Excitons in a Single-Layer MoS2 Reaching the Homogeneous Limit". *ACS Nano*, 13(3):3500–3511, March 2019.

[99] G. Moody, C. K. Dass, K. Hao, C.-H. Chen, L.-J. Li, A. Singh, K. Tran, G. Clark, X. Xu, G. Berghäuser, E. Malic, A. Knorr, and X. Li. „Intrinsic homogeneous linewidth and broadening mechanisms of excitons in monolayer transition metal dichalcogenides". *Nat Commun*, 6(1):8315, November 2015.

[100] D. Erkensten, S. Brem, and E. Malic. „Exciton-exciton interaction in transition metal dichalcogenide monolayers and van der Waals heterostructures". *Phys. Rev. B*, 103(4):045426, January 2021.

[101] M. R. Carbone, M. Z. Mayers, and D. R. Reichman. „Microscopic model of the doping dependence of linewidths in monolayer transition metal dichalcogenides". *J. Chem. Phys.*, 152(19):194705, May 2020.

[102] F. Katsch, M. Selig, and A. Knorr. „Exciton-Scattering-Induced Dephasing in Two-Dimensional Semiconductors". *Phys. Rev. Lett.*, 124(25):257402, June 2020.

[103] L. H. Thong, C. Ngo, H. T. Duc, X. Song, and T. Meier. „Microscopic analysis of high harmonic generation in semiconductors with degenerate bands". *Phys. Rev. B*, 103(8):085201, February 2021.

[104] R. E. F. Silva, F. Martín, and M. Ivanov. „High harmonic generation in crystals using maximally localized Wannier functions". *Phys. Rev. B*, 100(19):195201, November 2019.

[105] J. Li, X. Zhang, S. Fu, Y. Feng, B. Hu, and H. Du. „Phase invariance of the semiconductor Bloch equations". *Phys. Rev. A*, 100(4):043404, October 2019.

[106] H. Liu, Y. Li, Y. S. You, S. Ghimire, T. F. Heinz, and D. A. Reis. „High-harmonic generation from an atomically thin semiconductor". *Nature Phys*, 13(3):262–265, March 2017.

[107] D. Vanderbilt. *Berry Phases in Electronic Structure Theory: Electric Polarization, Orbital Magnetization and Topological Insulators*. Cambridge University Press, Cambridge, 2018.

[108] L. Yue and M. B. Gaarde. „Introduction to theory of high-harmonic generation in solids: tutorial". *J. Opt. Soc. Am. B*, 39(2):535, 2022.

[109] D. Golde, T. Meier, and S. W. Koch. „High harmonics generated in semiconductor nanostructures by the coupled dynamics of optical inter- and intraband excitations". *Phys. Rev. B*, 77(7):075330, February 2008.

[110] U. Huttner, M. Kira, and S. W. Koch. „Ultrahigh Off-Resonant Field Effects in Semiconductors". *Laser & Photonics Reviews*, 11(4):1700049, 2017.

[111] N. Yoshikawa, K. Nagai, K. Uchida, Y. Takaguchi, S. Sasaki, Y. Miyata, and K. Tanaka. „Interband resonant high-harmonic generation by valley polarized electron-bhole pairs". *Nat Commun*, 10(1):3709, August 2019.

[112] H. K. Avetissian and G. F. Mkrtchian. „High laser harmonics induced by the Berry curvature in time-reversal invariant materials". *Phys. Rev. B*, 102(24):245422, December 2020.

[113] J. M. Iglesias, E. Pascual, M. J. Martín, and R. Rengel. „High-order harmonic generation in 2D transition metal disulphides". *Appl. Phys. Lett.*, 119(1):012101, July 2021.

Publications

Paper I

J. Neuhaus, S. C. Liebscher, L. Meckbach, T. Stroucken, and S. W. Koch:

Microscopic Coulomb interaction in transition-metal dichalcogenides

Abstract: The quasi-two dimensional Coulomb interaction potential in transition metal dichalcogenides is determined using the Kohn-Sham wave functions obtained from *ab initio* calculations. An effective form factor is derived that accounts for the finite extension of the wave function in the direction perpendicular to the material layer. The resulting Coulomb matrix elements are used in microscopic calculations based on the Dirac Bloch equations yielding an efficient method to calculate the band gap and the opto-electronic material properties in different environments and under various excitation conditions.

Microscopic Coulomb interaction in transition-metal dichalcogenides

J Neuhaus, S C Liebscher, L Meckbach, T Stroucken[*] **and S W Koch**

Department of Physics and Material Sciences Center, Philipps University Marburg, Renthof 5, D-35032 Marburg, Germany

E-mail: tineke.stroucken@t-online.de

Abstract

The quasi-two dimensional Coulomb interaction potential in transition metal dichalcogenides is determined using the Kohn–Sham wave functions obtained from *ab initio* calculations. An effective form factor is derived that accounts for the finite extension of the wave functions in the direction perpendicular to the material layer. The resulting Coulomb matrix elements are used in microscopic calculations based on the Dirac Bloch equations yielding an efficient method to calculate the band gap and the opto-electronic material properties in different environments and under various excitation conditions.

(Some figures may appear in colour only in the online journal)

1. Introduction

With a thickness of just one unit cell, TMDC (transition metal dichalcogenide) monolayer materials can be viewed as the realization of effectively two-dimensional (2D) system. As revealed by density functional theory (DFT) calculations, the resulting 2D quasi-particle dispersions differ not only quantitatively, but also qualitatively from the three dimensional (3D) bandstructure of the corresponding bulk materials, making these systems interesting both for fundamental material science as well as technological applications. In particular, monolayers of TMDCs and TMDC-based heterostructures are currently investigated with regards to their application potential in opto-electronic devices. Unlike the bulk TMDC materials, the monolayers display a direct gap in the visible range with strong light matter interaction and many-body effects due to carrier confinement and weak intrinsic screening of the Coulomb interaction [1–5].

A central challenge for the predictive modeling of the TMDC opto-electronic properties is the analysis of the many-body effects and their influence on the optical spectra. Although state of the art, full *ab initio* GW–BSE calculations have been employed to calculate the linear optical spectra of

freely suspended TMDC monolayers, these are numerically extremely challenging and practically intractable for the general nonlinear response. Furthermore, numerical implementations of GW–BSE calculations for quasi-2D TMDCs are artificially 3D and require the insertion of large vacuum regions or truncations of the Coulomb interaction to avoid spurious inter-layer interactions. This not only increases the numerical effort despite decreasing the material's dimensionality, but also limits the applicability to situations where a monolayer is embedded into a more complex heterostucture or photonic crystal cavity. Hence, there is a need for *ab initio* based theoretical descriptions that are both accurate and flexible to describe the linear and nonlinear optical response under various excitation conditions and different geometries, and at the same allow for the identification and intuitive interpretation of the relevant physical processes.

A powerful tool to compute the optical response of semiconductors for a wide variety of excitation conditions is provided by the semiconductor Bloch equations (SBE), respectively the Dirac Bloch equations (DBE) for TMDCs. Based on the observation that only few bands contribute to the optical response, one derives the equation of motion (eom) for the relevant material parameters from an effective system Hamiltonian including only the relevant valence and

[*] Author to whom any correspondence should be addressed.

conduction bands, thus reducing the numerical complexity enormously. Due to its non-perturbative nature, this approach is particularly well suited to describe the linear and nonlinear optical response in the presence of strong many-body interactions.

As an essential input, the SBE/DBE approach needs the single-particle band structure and the interaction matrix elements. Whereas band dispersions and dipole matrix elements can be either accessed directly from *ab initio* DFT calculations or from a DFT based model Hamiltonian, the determination of the quasi-2D Coulomb potential and its matrix elements is a nontrivial task. For this purpose, we develop in this paper a parameter-free approach that allows us to efficiently determine the Coulombic input for the SBE from the Kohn–Sham wavefunctions without the need of additional approximations.

The paper is organized as follows: in the following section 2, we briefly summarize the microscopic SBE/DBE approach and introduce an orbital dependent form factor that accounts for the quasi-2D nature of Coulomb interaction potential in TMDCs. We show how this form factor can be computed from the Kohn–Sham wave functions. In section 3, we then provide details of the needed DFT calculations and present a detailed analysis of the form factor. In section 5, we develop an analytic approximation for the form factors that allows us to efficiently calculate the density dependent band-gap renormalization and exciton resonances for different material systems. We discuss and compare our results to available experimental and GW–BSE based *ab initio* results in section 5.1.

2. Preliminaries

2.1. 2D semiconductor Bloch equations

For a strictly 2D semiconductor, the basic system Hamiltonian is given by

$$H = H_0 + H_I + H_C$$

where

$$H_0 = \sum_{\alpha \mathbf{k}_\parallel} \epsilon_{\alpha \mathbf{k}_\parallel} c^\dagger_{\alpha \mathbf{k}_\parallel} c_{\alpha \mathbf{k}_\parallel}$$

describes the single-particle part,

$$H_I = \frac{e}{m_0 c} \sum_{\alpha \alpha' \mathbf{k}_\parallel} \mathbf{A} \cdot \mathbf{p}_{\alpha \alpha' \mathbf{k}_\parallel} c^\dagger_{\alpha \mathbf{k}_\parallel} c_{\alpha' \mathbf{k}_\parallel},$$

contains the light–matter interaction, and

$$H_C = \frac{1}{2} \sum_{\substack{\alpha \alpha' \beta \beta' \\ \mathbf{k}_\parallel \mathbf{k}_\parallel' \mathbf{q}_\parallel \neq 0}} V^{\alpha \beta \beta' \alpha'}_{\mathbf{q}_\parallel ; \mathbf{k}_\parallel' ; \mathbf{k}_\parallel} c^\dagger_{\alpha \mathbf{k}_\parallel - \mathbf{q}_\parallel} c^\dagger_{\beta \mathbf{k}_\parallel' + \mathbf{q}_\parallel} c_{\beta' \mathbf{k}_\parallel'} c_{\alpha' \mathbf{k}_\parallel}.$$

represents the Coulomb interaction, respectively. Here, $\hbar \mathbf{k}_\parallel$ is the in-plane crystal momentum, α combines spin and band index, $\epsilon_{\alpha \mathbf{k}_\parallel}$ contains the effective single-particle band dispersion, and $\mathbf{p}_{\alpha \alpha' \mathbf{k}_\parallel}$ and $V^{\alpha \beta \beta' \alpha'}_{\mathbf{q}_\parallel ; \mathbf{k}_\parallel' ; \mathbf{k}_\parallel} = V_{\mathbf{q}_\parallel} \langle \alpha \mathbf{k}_\parallel -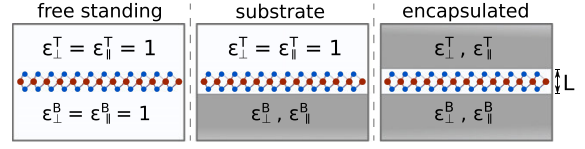 \mathbf{q}_\parallel | \alpha' \mathbf{k}_\parallel \rangle \langle \beta \mathbf{k}_\parallel' + \mathbf{q}_\parallel | \beta' \mathbf{k}_\parallel' \rangle$ denote the momentum and Coulomb matrix ele-

ments, respectively. Furthermore, $V_{\mathbf{q}_\parallel}$ is the Fourier transform of the 2D Coulomb potential. In the presence of a dielectric environment, the environmental screening of the Coulomb potential can be included into the definition of the 'bare' Coulomb potential.

The optical response is then given by $\mathbf{j} = -\frac{e}{m_0} \sum_{\alpha \alpha' \mathbf{k}_\parallel} \mathbf{p}_{\alpha \alpha' \mathbf{k}_\parallel} \langle c^\dagger_{\alpha \mathbf{k}_\parallel} c_{\alpha' \mathbf{k}_\parallel} \rangle$ and can be computed from the Heisenberg equations of motion for the transition amplitudes $P^{\alpha \alpha'}_{\mathbf{k}_\parallel} = \langle c^\dagger_{\alpha \mathbf{k}_\parallel} c_{\alpha' \mathbf{k}_\parallel} \rangle$:

$$i\hbar \frac{d}{dt} P^{\alpha \alpha'}_{\mathbf{k}_\parallel} = \left(\epsilon_{\alpha' \mathbf{k}_\parallel} - \epsilon_{\alpha \mathbf{k}_\parallel} - i\gamma \right) P^{\alpha \alpha'}_{\mathbf{k}_\parallel} + \tilde{Q}^{\alpha \alpha'}_{\mathbf{k}_\parallel} - \left(\tilde{Q}^{\alpha' \alpha}_{\mathbf{k}_\parallel} \right)^*$$
$$+ i\hbar \frac{d}{dt} P^{\alpha \alpha'}_{\mathbf{k}_\parallel} \bigg|_{\text{corr}}. \tag{1}$$

Here,

$$\tilde{Q}^{\alpha \alpha'}_{\mathbf{k}_\parallel} = \sum_\beta P^{\alpha \beta}_{\mathbf{k}_\parallel} \tilde{\Omega}^{\beta \alpha'}_{\mathbf{k}_\parallel} \tag{2}$$

$$\tilde{\Omega}^{\beta \alpha'}_{\mathbf{k}_\parallel} = \frac{e}{m_0 c} \mathbf{A} \cdot \mathbf{p}_{\alpha' \beta \mathbf{k}_\parallel} - \sum_{\substack{\gamma \gamma' \\ \mathbf{k}_\parallel' \neq \mathbf{k}_\parallel}} V^{\alpha' \beta \gamma \gamma'}_{\mathbf{k}_\parallel - \mathbf{k}_\parallel' ; \mathbf{k}_\parallel ; \mathbf{k}_\parallel'} P^{\gamma \gamma'}_{\mathbf{k}_\parallel'} \tag{3}$$

contains the sources and the renormalizations of the single particle energies and internal field. For the interband polarization $P^{\nu c}_{\mathbf{k}_\parallel}$, we explicitly have

$$\tilde{Q}^{\nu c}_{\mathbf{k}_\parallel} - \left(\tilde{Q}^{c \nu}_{\mathbf{k}_\parallel} \right)^* = \left(\tilde{\Omega}^{cc}_{\mathbf{k}_\parallel} - \tilde{\Omega}^{\nu \nu}_{\mathbf{k}_\parallel} \right) P^{\nu c}_{\mathbf{k}_\parallel} + \left(f^\nu_{\mathbf{k}_\parallel} - f^c_{\mathbf{k}_\parallel} \right) \tilde{\Omega}^{\nu c}_{\mathbf{k}_\parallel},$$

$$\tilde{\Omega}^{cc}_{\mathbf{k}_\parallel} = \frac{e}{m_0 c} \mathbf{p}_{cc \mathbf{k}_\parallel} \cdot \mathbf{A} - \sum_{\mathbf{k}_\parallel' \neq \mathbf{k}_\parallel}$$

$$\times \left(V^{cccc}_{\mathbf{k}_\parallel - \mathbf{k}_\parallel' ; \mathbf{k}_\parallel ; \mathbf{k}_\parallel'} f^c_{\mathbf{k}_\parallel'} + V^{cc \nu \nu}_{\mathbf{k}_\parallel - \mathbf{k}_\parallel' ; \mathbf{k}_\parallel ; \mathbf{k}_\parallel'} f^\nu_{\mathbf{k}_\parallel'} \right) + \text{NR},$$

$$\tilde{\Omega}^{\nu c}_{\mathbf{k}_\parallel} = \frac{e}{m_0 c} \mathbf{p}_{\nu c \mathbf{k}_\parallel} \cdot \mathbf{A}$$

$$- \sum_{\mathbf{k}_\parallel' \neq \mathbf{k}_\parallel} V^{c \nu \nu c}_{\mathbf{k}_\parallel - \mathbf{k}_\parallel' ; \mathbf{k}_\parallel ; \mathbf{k}_\parallel'} P^{\nu c}_{\mathbf{k}_\parallel'} + \text{NR},$$

and a similar expression for $\tilde{\Omega}^{\nu \nu}_{\mathbf{k}_\parallel}$. Here, NR refers to non-resonant Auger and pair-creation contributions. As can be recognized, Coulomb renormalizations of the single particle energies are contained in $\tilde{\Omega}^{cc}_{\mathbf{k}_\parallel}$ and $\tilde{\Omega}^{\nu \nu}_{\mathbf{k}_\parallel}$ whereas the attractive electron–hole interaction responsible for the formation of bound excitons is contained in $\tilde{\Omega}^{\nu c}_{\mathbf{k}_\parallel}$. Correlation effects beyond the mean field approximation are contained in

$$i\hbar \frac{d}{dt} P^{\alpha \alpha'}_{\mathbf{k}_\parallel} \bigg|_{\text{corr}}. \tag{4}$$

It can be shown that the dominant correlation effect is the replacement of the 'bare' Coulomb potential in equation (3) by its dynamically screened counterpart, yielding the screened Hartree–Fock approximation [6], whereas if correlation effects are neglected, the renormalizations of

the single particle energies correspond to the Hartree–Fock approximation.

If the system is excited with an optical pulse of central frequency ω_L, the induced optical current is dominated by transition amplitudes $P_{\mathbf{k}_\parallel}^{\alpha\alpha'}$ corresponding to dipole allowed transitions with transition energies $\epsilon_{\alpha'\mathbf{k}_\parallel} - \epsilon_{\alpha\mathbf{k}_\parallel} \approx \hbar\omega_L$ that are resonant or nearly resonant with the optical frequency. If the relevant bands are sufficiently isolated, one can restrict the microscopic analysis to the resonant transition amplitudes and occupation numbers $f_{\mathbf{k}_\parallel}^\alpha = P_{\mathbf{k}_\parallel}^{\alpha\alpha}$ of those bands and the only coupling to remote bands is via screening of the Coulomb potential. Treating screening within the RPA approximation, we can make the separation

$$\Pi_{\mathbf{q}_\parallel}(\omega) = \Pi_{\mathbf{q}_\parallel}^{\mathrm{GS}}(\omega) + \Delta\Pi_{\mathbf{q}_\parallel}(\omega) \tag{5}$$

$$W_{\mathbf{q}_\parallel}(\omega) = \frac{V_{\mathbf{q}_\parallel}}{1 - V_{\mathbf{q}_\parallel}\Pi_{\mathbf{q}_\parallel}(\omega)} = \frac{W_{\mathbf{q}_\parallel}^{\mathrm{GS}}}{1 - W_{\mathbf{q}_\parallel}^{\mathrm{GS}}\Delta\Pi_{\mathbf{q}_\parallel}(\omega)}. \tag{6}$$

Here, $W_{\mathbf{q}_\parallel}^{\mathrm{GS}}$ includes all ground state and environmental screening contributions,

$$\Delta\Pi_{\mathbf{q}_\parallel}(\omega) = \sum_{\alpha\alpha'\mathbf{k}_\parallel} \frac{\Delta f_{\mathbf{k}_\parallel - \mathbf{q}_\parallel}^\alpha - \Delta f_{\mathbf{k}_\parallel}^{\alpha'}}{\hbar\omega + \mathrm{i}\gamma_{\mathrm{T}} + \epsilon_{\alpha\mathbf{k}_\parallel - \mathbf{q}_\parallel} - \epsilon_{\alpha'\mathbf{k}_\parallel}}$$
$$\times \left|\langle\alpha\mathbf{k}_\parallel - \mathbf{q}_\parallel|\alpha'\mathbf{k}_\parallel\rangle\right|^2,$$

contains the optically induced deviations from the ground state polarization function only, and γ_{T} is the triplet dephasing rate, respectively. Hence, if the single particle dispersions, optical dipole and Coulomb matrix elements as well as the ground state screening of the Coulomb potential are known from *ab initio* calculations, the SBE provide a very efficient scheme to compute the optical response since they only need to be solved for a few bands and that part of $\mathbf{k}_\parallel$ space in which populations and/or polarizations are optically induced.

Specifically, for TMDCs it is often sufficient to include the two spin−split valence and conduction bands near the K-points where the single particle dispersion displays a direct gap. Here, the single particle dispersion can be approximated by the relativistic dispersion

$$\epsilon_{i\mathbf{K}+\mathbf{k}}^{c/v} = E_{\mathrm{F},i} \pm \frac{1}{2}\sqrt{\Delta_i^2 + (2\hbar v_{\mathrm{F},i}k)^2}, \tag{7}$$

that results from the widely used massive Dirac–Fermion (MDF) model Hamiltonian[?]. Here, $i = s\tau$ combines the spin and valley index, Δ_i, $v_{\mathrm{F},i}$ and $E_{\mathrm{F},i}$ are the spin and valley dependent gap, Fermi velocity and Fermi level, respectively. The occurring parameters can be adjusted to reproduce the DFT bandstructure near the K-points. The overlap matrix elements resulting from the MDF Hamiltonian are

$$\langle c\mathbf{K}+\mathbf{k}_\parallel|c\mathbf{K}+\mathbf{k}_\parallel'\rangle = \langle \nu\mathbf{K}+\mathbf{k}_\parallel'|\nu\mathbf{K}+\mathbf{k}_\parallel\rangle$$
$$= u_{\mathbf{k}_\parallel}u_{\mathbf{k}_\parallel'} + v_{\mathbf{k}_\parallel}v_{\mathbf{k}_\parallel'}\,\mathrm{e}^{-\mathrm{i}\theta_{\mathbf{k}_\parallel - \mathbf{k}_\parallel'}}$$

$$\langle c\mathbf{K}+\mathbf{k}_\parallel|\nu\mathbf{K}+\mathbf{k}_\parallel'\rangle = \left(u_{\mathbf{k}_\parallel}v_{\mathbf{k}_\parallel'}\,\mathrm{e}^{-\mathrm{i}\theta_{\mathbf{k}_\parallel'}} - v_{\mathbf{k}_\parallel}u_{\mathbf{k}_\parallel'}\,\mathrm{e}^{-\mathrm{i}\theta_{\mathbf{k}_\parallel}}\right)$$

Figure 1. Illustration of the different dielectric settings considered in the calculations presented in this paper.

with $u_{\mathbf{k}_\parallel}^2 = 1 - v_{\mathbf{k}_\parallel}^2 = \frac{\sqrt{\Delta_i^2 + (2\hbar v_{\mathrm{F},i}k)^2} + \Delta_i}{2\sqrt{\Delta_i^2 + (2\hbar v_{\mathrm{F},i}k)^2}}$.

2.2. Coulomb potential and screening in quasi-2D materials

Although the material excitations in quasi-2D materials are confined to a region $|z| \lesssim d/2 \leqslant L/2$, the Coulomb potential is long ranged and the interaction among particles confined in the layer is sensitive to the dielectric environment. Furthermore, for the evaluation of the opto-electronic system response, one needs the screened Coulomb potential that not only contains screening contributions from the dielectric environment but also all ground state contributions from the material itself.

Within DFT, the macroscopic (3D) dielectric constant is obtained as

$$\epsilon_{\mathrm{M}}^{-1}(\mathbf{q}) = \frac{\langle\tilde{V}_{\mathbf{q}}(\mathbf{r})\rangle_\Omega}{V_0} = \epsilon_{00}^{-1}(\mathbf{q}),$$

where $\tilde{V}_{\mathbf{q}}(\mathbf{r})$ is a lattice periodic function and $\langle\ldots\rangle_\Omega$ denotes a spatial average over the elementary unit cell. If applied to an artificial 3D crystal consisting of parallel monolayers separated by large vacuum regions, the averaging over a region much larger than the extension of the electron density yields a dielectric function that decreases with the size of the artificial unit cell and hence, cannot be used to construct the screened 2D Coulomb potential [7]. To avoid this complication, we developed in a previous publication [6] an electrostatic model that is based on the bulk dielectric functions which can be directly computed from 3D DFT calculations, thus avoiding any difficulties related to the artificial insertion of large vacuum layers.

Whereas we refer to reference [6] for a detailed derivation of our electrostatic model, we briefly summarize the most important steps with respect to the screened interaction for further use in this paper (figure 1). As visualized in figure 1, we considered TMDCs embedded in different dielectric surroundings, such as in vacuum, on a substrate and embedded in two different dielectric media.

To account for the environmental and ground state screening, we consider a slab geometry with

$$\epsilon_\parallel(z) = \begin{cases} \epsilon_\parallel^{\mathrm{T}} & z < -L/2, \\ \epsilon_\parallel & |z| < L/2, \\ \epsilon_\parallel^{\mathrm{B}} & L/2 < z \end{cases} \quad \epsilon_\perp(z) = \begin{cases} \epsilon_\perp^{\mathrm{T}} & z < -L/2, \\ \epsilon_\perp & |z| < L/2, \\ \epsilon_\perp^{\mathrm{B}} & L/2 < z. \end{cases}$$

and determine the interaction potential as solution of Poisson's equation. The resulting interaction potential within the slab is given by

a) conduction band
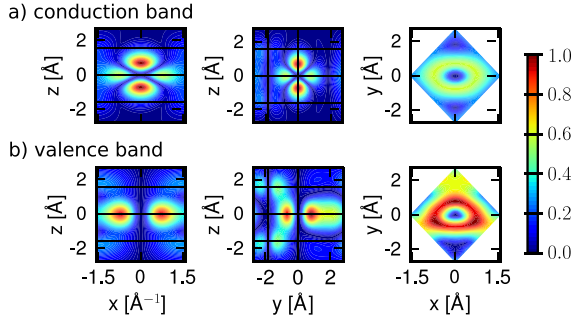
b) valence band

Figure 2. Probability density $\rho = |\psi(\mathbf{r})|^2$ for (a) the conduction and (b) the valence band of MoS_2 at the K-point plotted for cuts through the unit cell along the x-, y- and z-axis centered around the molybdenum atom. The black lines indicate the atomic z-position and illustrate the wave function localization in between the chalcogen layers.

$$\phi_{\mathbf{q}_\|}(z, z') = \frac{2\pi}{\kappa q} \left(e^{-\tilde{q}|z - z'|} \right.$$
$$+ c^{+-} e^{-\tilde{q}(L + z + z')} + c^{-+} e^{-\tilde{q}(L - z - z')}$$
$$\left. + c^{--} e^{-\tilde{q}(2L - z + z')} + c^{--} e^{-\tilde{q}(2L + z - z')} \right)$$
$$= \frac{2\pi}{\kappa q} e^{-\tilde{q}|z - z'|} + \Delta\phi_{\mathbf{q}_\|}(z, z') \tag{8}$$

with $\tilde{q} = \sqrt{\frac{\epsilon_\|}{\epsilon_\perp}} q$, $\kappa = \sqrt{\epsilon_\| \epsilon_\perp}$ and similar for $\kappa_{\mathrm{T/B}}$ and

$$c^{\eta\eta'} = \frac{(\kappa + \eta\kappa_{\mathrm{T}})(\kappa + \eta'\kappa_{\mathrm{B}})}{(\kappa + \kappa_{\mathrm{T}})(\kappa + \kappa_{\mathrm{B}}) - (\kappa - \kappa_{\mathrm{T}})(\kappa - \kappa_{\mathrm{B}}) e^{-2\tilde{q}_\| L}},$$

from which the 2D Coulomb potential is obtained as $\phi_{\mathbf{q}_\|}^{2\mathrm{D}} = \phi_{\mathbf{q}_\|}(0, 0)$. In the last line of equation (8), the first term describes the direct interaction of two electrons located at z and z' whereas the second term describes the interaction with image charges. From equation (8), the 'bare' Coulomb interaction $V_{\mathbf{q}_\|}(z, z')$, containing environmental screening only, is obtained by setting $\epsilon_\| = \epsilon_\perp = 1$ within the slab, whereas the true vacuum Coulomb interaction $V_{\mathbf{q}_\|}^{\mathrm{vac}}(z, z')$ is obtained by additionally setting $\kappa_{\mathrm{T}} = \kappa_{\mathrm{B}} = 1$. Hence, equation (8) suggests that the Coulomb potential without intrinsic screening can be expressed as $V_{\mathbf{q}_\|}(z, z') = V_{\mathbf{q}_\|}^{\mathrm{vac}}(z, z') + \Delta V_{\mathbf{q}_\|}(z, z')$, where the last term describes the interaction via image charges. Similarly, one obtains the screened Coulomb interaction in bulk, $W_{\mathbf{q}_\|}^{\mathrm{bulk}}(z, z')$, by inserting the bulk parameters for the in- and out-of-plane dielectric constants $\epsilon_\|^{\mathrm{B}}$ and $\epsilon_\perp^{\mathrm{B}}$ both within the slab and for the top and bottom environment.

Whereas both $V_{\mathbf{q}_\|}^{\mathrm{vac}}(z, z')$ and $W_{\mathbf{q}_\|}^{\mathrm{bulk}}(z, z')$ are independent of the slab thickness L, the interaction with image charges in the presence of environmental screening introduces a dependence on the slab thickness L both for the 'bare' and screened monolayer interaction potential. To model the monolayer potential, we shall assume a slab thickness $L = D$ where $D = c/2$ is the natural layer-to-layer distance in the naturally stacked bulk crystal. In the long wavelength limit

$q_\| D \to 0$ one obtains $W_{\mathbf{q}_\|}^{\mathrm{GS,2D}} = \frac{2\pi}{q((\kappa_{\mathrm{T}} + \kappa_{\mathrm{B}})/2 + r_0 q)}$, corresponding to the widely used Rytova–Keldysh potential with a screening length $r_0 = D(2\kappa^2 - \kappa_{\mathrm{T}}^2 - \kappa_{\mathrm{B}}^2)/4\epsilon_\perp$ that depends on the dielectric contrast between the TMDC material and dielectric environment. In particular, if the dielectric environment is the bulk TMDC crystal itself, the screening length vanishes. For the short wavelengths $q_\| L/2 \to \infty$, the screened potential approaches $2\pi/\kappa q\, e^{-\tilde{q}|z - z'|}$, independently of the dielectric environment. Comparison with the bulk Coulomb potential allows us to identify $\epsilon_\| = \epsilon_\|^{\mathrm{B}}$ and $\epsilon_\perp = \epsilon_\perp^{\mathrm{B}}$ for the ground state screening even in the case of a monolayer. Hence, we can write for the Coulomb potential including environmental and ground state screening

$$W_{\mathbf{q}_\|}^{\mathrm{GS}}(z, z') = W_{\mathbf{q}_\|}^{\mathrm{bulk}}(z, z') + \Delta W_{\mathbf{q}_\|}(z, z'), \tag{9}$$

where $\Delta W_{\mathbf{q}_\|}(z, z')$ describes the screened interaction via image charges. Equation (9) should be compared with the division $W = W^{\mathrm{ML}} + \Delta W$ that has been used in the $G\Delta W$ approach where ΔW contains the changes in the screened potential as compared to the suspended monolayer [7].

2.3. Form factor to quantify the impact of three-dimensionality

Even monolayer TMDCs have an intrinsic thickness since they consist of three atomic layers and their atomic orbitals have a finite extension perpendicular to the layer plane. Consequently, the Coulomb interaction in these materials differs both from the exact 2D and the three-dimensional cases. Taking the in-plane periodicity and the finite out-of-plane extension into account, a 2D ansatz gives the Bloch states,

$$\phi_{\alpha\mathbf{k}_\|}(\mathbf{r}) = \frac{1}{\sqrt{A}} e^{i\mathbf{k}_\| \cdot \mathbf{r}} u_{\alpha\mathbf{k}_\|}(\mathbf{r}) \tag{10}$$

with strictly 2D crystal momenta but 3D spatial coordinates $\mathbf{r}$. Hence, the Coulomb Hamiltonian contains the quasi-2D matrix elements

$$V_{\mathbf{q}_\|; \mathbf{k}_\|'; \mathbf{k}_\|}^{\alpha\beta\beta'\alpha'} = \int_{ec} \mathrm{d}^3 r \int_{ec} \mathrm{d}^3 r'\, u_{\alpha\mathbf{k}_\| - \mathbf{q}_\|}^*(\mathbf{r}) u_{\beta\mathbf{k}_\|' + \mathbf{q}_\|}^*(\mathbf{r}')$$
$$\times V_{\mathbf{q}_\|}(z, z') u_{\beta'\mathbf{k}_\|'}(\mathbf{r}') u_{\alpha'\mathbf{k}_\|}(\mathbf{r}),$$

and a similar expression holds for the matrix elements of the screened Coulomb potential.

According to equation (8), the Coulomb interaction differs from the exact two-dimensional potential only in the exponential terms. Hence, we can write for the screened Coulomb potential

$$W_{\mathbf{q}_\|; \mathbf{k}_\|'; \mathbf{k}_\|}^{\alpha\beta\beta'\alpha'} = W_{\mathbf{q}_\|}^{2\mathrm{D}} F_{\mathbf{k}_\|'; \mathbf{k}_\|}^{\alpha\beta\beta'\alpha'}(\mathbf{q}_\|) \tag{11}$$

$$- \Delta W_{\mathbf{q}_\|}^{2\mathrm{D}} \Delta F_{\mathbf{k}_\|'; \mathbf{k}_\|}^{\alpha\beta\beta'\alpha'}(\mathbf{q}_\|). \tag{12}$$

Here,

$$F_{\mathbf{k}_\|'; \mathbf{k}_\|}^{\alpha\beta\beta'\alpha'}(\mathbf{q}_\|) = \int_{ec} \mathrm{d}^3 r \int_{ec} \mathrm{d}^3 r'\, u_{\alpha\mathbf{k}_\| - \mathbf{q}_\|}^*(\mathbf{r}) u_{\beta\mathbf{k}_\|' + \mathbf{q}_\|}^*(\mathbf{r}')$$
$$\times e^{-\tilde{q}_\||z - z'|} u_{\beta'\mathbf{k}_\|'}(\mathbf{r}') u_{\alpha'\mathbf{k}_\|}(\mathbf{r}) \tag{13}$$

is a form factor and

$$\Delta F_{\mathbf{k}_\parallel';\mathbf{k}_\parallel}^{\alpha\beta\beta'\alpha'}(\mathbf{q}_\parallel) = F_{\mathbf{k}_\parallel';\mathbf{k}_\parallel}^{\alpha\beta\beta'\alpha'}(\mathbf{q}_\parallel) - f_{\mathbf{k}_\parallel}^{\alpha\alpha'}(\mathbf{q}_\parallel)f_{\mathbf{k}_\parallel'}^{\beta\beta'}(\mathbf{q}_\parallel) \quad (14)$$

$$f_{\mathbf{k}_\parallel}^{\alpha\alpha'}(\mathbf{q}_\parallel) = \int_{ec} \mathrm{d}^3 r\, u_{\alpha\mathbf{k}_\parallel-\mathbf{q}_\parallel}^*(\mathbf{r})\mathrm{e}^{-\bar{q}_\parallel z}u_{\alpha'\mathbf{k}_\parallel}(\mathbf{r}) \quad (15)$$

is its correlated part, respectively. In the 2D limit, the exponential term in the form factor approaches unity and the 2D Coulomb matrix element is recovered due to the wavefunctions orthonormality. Furthermore, $F_{\mathbf{k}_\parallel';\mathbf{k}_\parallel}^{\alpha\beta\beta'\alpha'}(\mathbf{q}_\parallel = 0) = \delta_{\alpha\alpha'}\delta_{\beta\beta'} = f_{\mathbf{k}_\parallel}^{\alpha\alpha'}(\mathbf{q}_\parallel = 0)f_{\mathbf{k}_\parallel'}^{\beta\beta'}(\mathbf{q}_\parallel = 0)$, while for large scattering vectors $\mathbf{q}_\parallel \to \infty$ the form factor approaches 0. Since the potential of the image charges is particularly important in the long wavelength limit where the correlated part of the form factor is negligible, the Coulomb matrix elements of the quasi-2D TMDC structures can be expressed in a good approximation by the exact 2D term modified by the form factor.

2.4. Combined SBE/DFT approach

In the following, we will assume that the single-particle band dispersion and wave functions can reliably be computed from DFT and use the DFT parameters as input for the SBE/DBE evaluations. From a fundamental point, this is in fact a non-trivial assumption. As is well known, DFT is based on the assumption that the two-particle interaction in any given system is a *universal* functional of the electron density while all system specific contributions to the many-body Hamiltonian are contained in the external potential. Using the dielectric model presented in section 2.2, it becomes clear that the substrate not only changes the screened Coulomb potential but also modifies the 'vacuum' potential that now contains interactions with image charges. Thus, in the presence of external screening, all particles (electrons and ions) interact via a modified Coulomb potential and hence, the electron–electron interaction can no longer be considered as universal.

However, analytical estimates based on the expression for the 'bare' Coulomb potential presented in section 2.2 show that the influence of the dielectric screening on the DFT single particle energies should be small for particles confined to a region $|z| \lesssim d/2 < D/2$. Indeed, rigorous treatments of monolayer TMDCs embedded in different dielectric environments have shown that the single-particle bandstructure in the proximity of the direct band gap at the K point remains unchanged for different environments [10]. Therefore, the single-particle bandstructure near the K-point can be obtained from an artificial 3D supercell calculation even in the presence of external screening.

3. Details of DFT computations

For our DFT calculations, we use the plane-wave based code Vienna *ab intio* Simulation Package (VASP) [11–14] including the core electrons contribution by precalculated projector augmented-wave pseudopotentials [15]. All calculations were performed using the non-empirical generalized gradient Perdew–Burke–Ernzerhof (PBE) functional [16], with
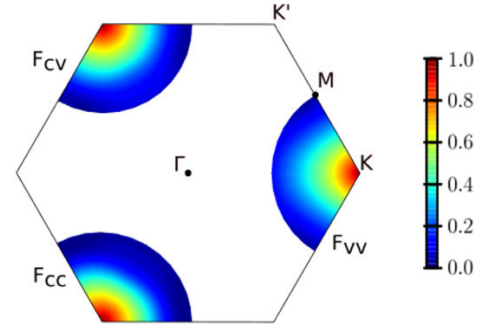
Figure 3. Form factor for inter- and intraband interaction of MoS$_2$ in a range of $|\overline{KM}| = |\mathbf{k}_\parallel - \mathbf{k}_\parallel'| \approx 0.62$ Å^{-1} around the K-point. As path dependent changes of the form factor are only small, they are approximated as isotropic around the K-point and subsequent calculations are performed using path-averaged form factors.

additionally including spin–orbit coupling and van-der-Waals interactions by the dispersion correction as proposed by Grimme (DFT-D3) [17].

In a first step, the materials structure was relaxed until remaining forces acting on the atoms were less than 1 meV Å^{-1}. The number of plane waves was hereby restricted by a cutoff energy of 750 eV and convergence was checked with respect to the discretization of the Brillouin zone and the vacuum region that was added in *z*-direction to prevent interactions between the monolayers despite periodic boundary conditions. For further calculations of electronic properties, the Brillouin zone was discretized by a $12 \times 12 \times 1$, Γ centered *k*-point Monkhorst–Pack [18] grid and the energy cutoff was set consistently with the precalculated pseudopotentials. In practice, approximately 15 Å of vacuum were included in *z*-direction.

Using the relaxed structures, the electronic properties were calculated for different paths in the Brillouin zone originating in one of the K points where the direct TMDC band gap is found. The paths were chosen along $\overline{KM}$ in addition to paths of the same length but rotated by 30° and 60° which, due to the hexagonal symmetry, is sufficient to describe the behavior around each K point in steps of 30°.

As the Kohn–Sham wave functions are determined up to an arbitrary phase that can be chosen at each $\mathbf{k}_\parallel$-point independently, we pick the phases such that the intra- and interband matrix elements are given by $\mathbf{p}_{\alpha\alpha\mathbf{k}_\parallel} = \frac{m_0}{\hbar}\vec{\nabla}_{\mathbf{k}_\parallel}\epsilon_{\alpha\mathbf{k}_\parallel}$ and $\mathbf{p}_{\alpha\alpha'\mathbf{k}_\parallel} = \frac{m_0}{\hbar}(\epsilon_{\alpha'\mathbf{k}_\parallel} - \epsilon_{\alpha\mathbf{k}_\parallel})\langle\alpha\mathbf{k}_\parallel|\vec{\nabla}_{\mathbf{k}_\parallel}|\alpha'\mathbf{k}_\parallel\rangle$ respectively, corresponding to the $\mathbf{p} \cdot \mathbf{A}$ gauge. The remaining free global phase is chosen such that bright excitons are predominantly *s*-type.

3.1. Ab initio wave functions

The finite extension of the electron density in the direction perpendicular to the TMDC plane is illustrated in figure 2(a) for the example of MoS$_2$. Here, the normalized density distribution for both valence and conduction band at the K-point is plotted for different cuts through the unit cell.

For MoS$_2$, the wave functions are linear combinations of the transition metal's *d*-orbitals that are strongly localized in between the chalcogenite layers. While the conduction-band

wave function is dominated by the d_z-orbital, the wave function of the valence band is a linear combination of the in-plane d_{xy}- and $d_{x^2y^2}$-orbitals [19]. This is different in tungsten based materials where the transition metal's s-orbital and the chalcogen atom's p_z-orbital both have a finite contribution to the conduction or valence band respectively. These features result in a relatively higher density distribution in the tungsten layer for the conduction band whereas for the valence band the density distribution extends farther in the direction towards the chalcogen atoms, respectively.

4. Analysis of the form factor

4.1. Path-dependency

For the optical response, the properties of the form factor are of interest especially close to the direct band. Therefore, we compute the form factor for scattering vectors $|\mathbf{k}_\parallel - \mathbf{k}'_\parallel|$ with $\mathbf{k}_\parallel$ fixed at the K-point and $\mathbf{k}'_\parallel$ modified along different paths through the first Brillouin zone. The band structure is similar for all paths close to the K-point but changes significantly farther away, particularly for the conduction band where in the $K + 60°$ direction a secondary minimum can be seen that forms the indirect band gap in the reference bulk structure.

In Figure 3, we show a density plot of the form factor for inter- and intraband interaction in the region around the K-points for the example of MoS$_2$. Despite the anisotropy of the band structure, the MoS$_2$ form factor of the interband interactions F_{cv} decreases isotropically around the K-point up to a range of $|\mathbf{k}_\parallel - \mathbf{k}'_\parallel| \approx 0.45$ Å^{-1}. The same is true for tungsten based materials, but only up to $|\mathbf{k}_\parallel - \mathbf{k}'_\parallel| \approx 0.30$ Å^{-1}. Thereafter, the gradient in K-direction is smaller than in Γ-direction, whereby the absolute differences are less than 0.06. Path dependent differences are larger with regard to the intraband interactions. Here, the gradient is smaller in the direction towards the Γ-point for the valence and towards the M-points for the conduction band, respectively. However, but even here, the form factor is isotropic in a range of $|\mathbf{k}_\parallel - \mathbf{k}'_\parallel| \approx 0.15$ Å^{-1} and absolute differences are always less than 0.12. Thus, the differences occurring for the intraband form factor depending on different orbital compositions of the states seem to balance out in the integration over both valence and conduction band states in the interband form factor. In the following, averages over calculations along different paths are shown and used in subsequent calculations.

4.2. Supercell dependency

In order to be useful, the introduced form factor should be insensitive to the periodic boundary conditions applied in the DFT code and it should be applicable not only to model the Coulomb interaction in monolayers but also in bulk structures. To check these properties, we calculated the form factor for different extensions of the vacuum region included in the supercell.

Our results show that as long as we properly relax the structure before calculating the form factor we obtain similar results independent of the used super cell size. The same is true even if we consider the transition to a quasi-bulk structure differing
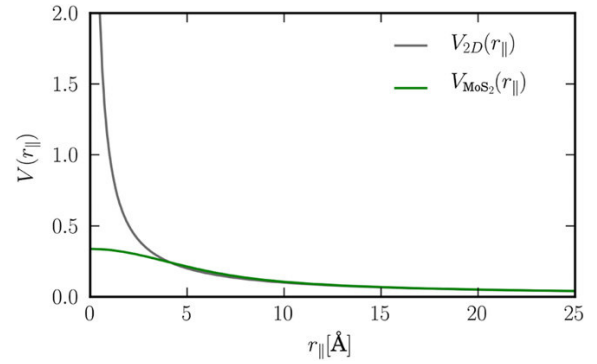
Figure 4. Comparison of the exact 2D Coulomb potential and the quasi-2D Coulomb potential in real space for the example of MoS$_2$.
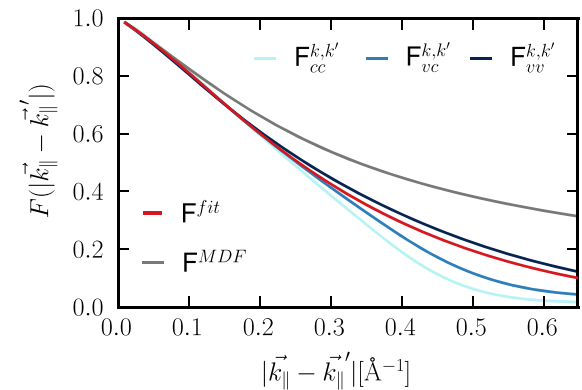
Figure 5. Comparison of the interband (subscript vc) and intraband (subscripts cc and vv) form factors together with the analytical approximation (red curve). The grey curve shows $F^{\mathrm{MDF}} = u^2_{\mathbf{k}_\parallel} \int_{ec} \mathrm{d}^3 r \int_{ec} \mathrm{d}^3 r' \, u^*_{\alpha\mathbf{K}}(\mathbf{r}) u^*_{\beta\mathbf{K}}(\mathbf{r}') \mathrm{e}^{-\tilde{q}_\parallel |z-z'|} u_{\beta'\mathbf{K}}(\mathbf{r}') u_{\alpha'\mathbf{K}}(\mathbf{r}).$

from the common crystalline structure of MoS$_2$ in stacking order (usually 2H-/3R-phases) and in the interlayer distance by about 0.6 Å. On this basis, we conclude that we can use the determined form factors to model a wide range of mono- and multi-layer systems in different dielectric environments.

4.3. Analytical description

To illustrate the effect of the form factor in real space, we compare in figure 4 the exact 2D and the quasi-2D Coulomb potentials for MoS$_2$. As we can see, the form factor effectively removes the Coulomb singularity at the origin but leaves the potential unchanged for larger distances, i.e., for $r_\parallel \gtrsim 7$ Å. the slope of the quasi-2D potential approaches that of the original 2D potential.

In figure 5, we show examples of the momentum dependent form factors for inter- and intraband transitions that were numerically evaluated using the full wavefunctions. To simplify detailed calculations on the SBE/DBE level, it is useful to develop analytical approximations for the form factor. For this purpose, we replace the full wavefunctions by their respective values at the K-point and incorporate the orbital dependent overlap matrix elements that occur within the MDF model.

As shown by the green curve in figure 5, this procedure captures the main features of the full form factors for small scattering vectors. However, for scattering vectors larger than 0.1 Å^{-1} or 0.2 Å^{-1} clear deviations are seen such that additional corrections are needed.

In some of our previous works (see e.g. references [6, 20]), we adopted a semi-empirical Ohno potential to account for the finite thickness of the TMDC layers. This approximation has also been used to describe the Coulomb potential of molecules and nanotubes (see references [21, 22]) and was successfully applied in calculations of optical properties of graphene and monolayer TMDCs.

By using the Ohno potential, one regularizes the singularity of the Coulomb potential by introducing an effective thickness parameter d, which in reciprocal space occurs in an additional prefactor $e^{-\mathbf{q}_{\parallel} d}$ of the Coulomb potential. Even though this ansatz reduces the Coulomb scattering for larger scattering vectors, the detailed analysis shows that it underestimates the form factor for small scattering vectors. Therefore, we additionally introduce an orbital independent exponential function of the form $F(\mathbf{q}_{\parallel}) = e^{-(\sigma^2 q_{\parallel}^2/2 + q_{\parallel} d)}$, while the orbital dependency is given by the MDF overlap matrix elements. With help of this function, the form factor can be described properly and physically correctly as it approximates 0 for large scattering vectors. Since the orbital dependence is contained in the MDF overlap matrix elements, the orbital independent part can be combined with the strictly 2D Coulomb potential to define the quasi-2D Coulomb potential $V_{\mathbf{q}_{\parallel}} = F(\mathbf{q}_{\parallel}) V_{\mathbf{q}_{\parallel}}^{2D}$.

A physical interpretation of the quadratic contribution can be obtained by considering the real space representation of the quasi-2D Coulomb potential:

$$V(\mathbf{r}_{\parallel}) = \sum_{\mathbf{q}_{\parallel}} e^{i\mathbf{q}_{\parallel} \cdot \mathbf{r}_{\parallel}} F(\mathbf{q}_{\parallel}) V_{\mathbf{q}_{\parallel}}^{2D}$$
$$= \frac{1}{2\pi\sigma^2} \int d^2 r_{\parallel}' \, e^{-|\mathbf{r}_{\parallel} - \mathbf{r}_{\parallel}'|^2/2\sigma^2} \frac{1}{\sqrt{r_{\parallel}'^2 + d^2}}. \quad (16)$$

Hence, the linear term in the exponent of the form factor changes the pure 2D Coulomb potential into the Ohno potential with thickness d, whereas the quadratic term lead to an additional convolution with a Gaussian of with σ.

4.4. Material dependence of the form factor

In figure 6, we show a comparison of the interband form factor for five commonly discussed examples of semiconducting TMDCs. We notice that for tungsten based materials the form factor decreases slightly faster than for molybdenum based materials. Even more significant modifications occur for different chalcogen atoms. The comparison in figure 6 reveals a more rapid form factor decay when changing from S to Se to Te demonstrating that the gradient becomes steeper with increasing atom size. Since the microscopic distance between the chalcogenide sheets increases with the size of the involved atoms, the systems become slightly more 3D which is reflected in the form factor being a measure for the influence of the finite thickness.
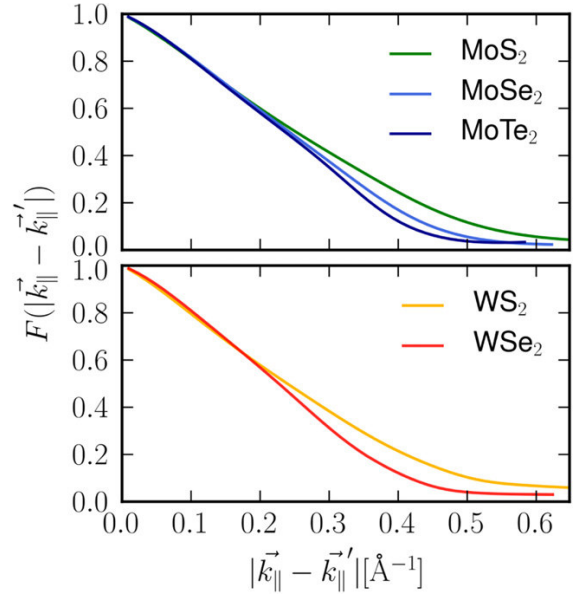
Figure 6. Interband form factors for different (a) Mo based and (b) We based TMDC monolayers. While the general slope is similar for all materials, the decay steepens with increasing size of the respective chalcogenide atoms.

5. Applications

5.1. Environmental dependent band gap renormalization

As a first application, we calculate the renormalization of the direct K point band gap for different dielectric environments. For the unexcited monolayer, the renormalized band gap is given by

$$\Delta_{\mathbf{K}} = \Delta^{\text{DFT}} + \sum_{\mathbf{q}_{\parallel}} \left(W_{\mathbf{q}_{\parallel};\mathbf{K};\mathbf{K}+\mathbf{q}_{\parallel}}^{\nu\nu\nu\nu} - W_{\mathbf{q}_{\parallel};\mathbf{K};\mathbf{K}+\mathbf{q}_{\parallel}}^{cc\nu\nu} \right) \quad (17)$$

In figure 7, we show the dependency of the gap on the environmental screening for five widely studied semiconducting monolayers (upper part). Since we plot the gap against the inverse value of the substrate dielectric constant, the figure covers the whole range of $\{1, \infty\}$ and $\{-\infty, -10\}$. For all materials investigated, we find a similar gap reduction for increased environmental screening. In the lower part of figure 7, we compare the gap shift of the different materials relative to the respective suspended monolayer with and without the form factor included. We note that the shift is almost independent of the form factor. To understand this behavior, we write the equation for the renormalized gap as

$$E_{\text{G}} = \Delta^{\text{DFT}} + \left(W_{\mathbf{K};\mathbf{K}}^{\nu\nu\nu\nu}(\mathbf{r}_{\parallel} = 0) - W_{\mathbf{K};\mathbf{K}}^{cc\nu\nu}(\mathbf{r}_{\parallel} = 0) \right) \quad (18)$$

and make use of equation (16).

Thus, for a strictly 2D system, the gap renormalization is determined by the screened Coulomb matrix elements at $\mathbf{r}_{\parallel} = 0$ and $z = z' = 0$. However, the form factor replaces $z = z' = d$ in the value of the screened Coulomb potential and additionally averages the Coulomb potential over a region
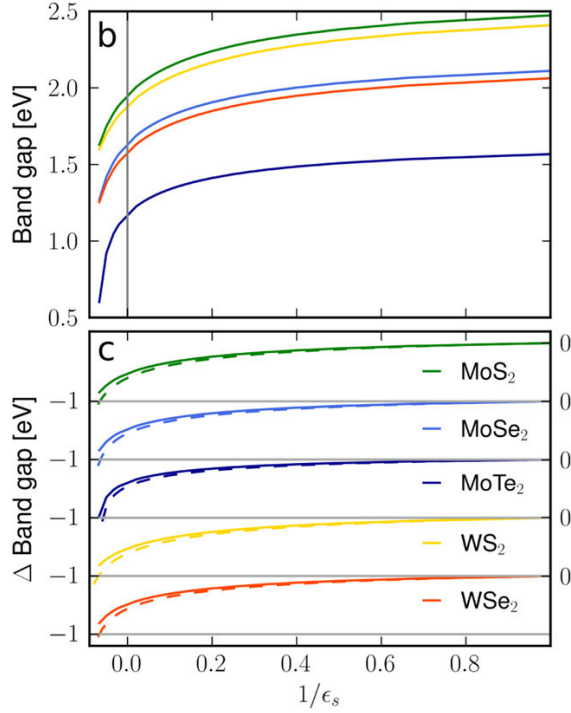
Figure 7. Dependence of the band gap on dielectric substrate screening of the five canonical TMDCs. Here, the limit $\epsilon_S \to -\infty$ represents the case of a conducting metallic substrate. The upper part (a) shows the absolute value of the gap, the lower part (b) the shift of the gap relative to the gap of a suspended monolayer with (full lines) and without (dashed lines) inclusion of the form factor.

around the origin using a Gaussian weight function. Both effects have a significant impact on the direct interaction contained in $W^{2Dbulk}(r_\parallel) = 1/\kappa r_\parallel$ that varies strongly in the region around the origin. In contrast, changes contained in $\Delta W \propto 1/\sqrt{r_\parallel^2 + L^2}$ vary only weakly within the region around the origin and hence are less affected by the form factor.

Furthermore, a comparison of the relative changes for the different materials in the regime of positive dielectric constants shows that these are slightly smaller for Mo rather than for W based materials with maximum differences in the range of few meV. Again, the influence of the incorporated chalcogenide atoms is more significant. Here, the maximum relative differences increase from Te to Se to S based compounds by approximately 80 meV and 45 meV, respectively.

In table 1, we give an overview of the computed band gaps for a variety of TMDCs and different dielectric environments. Comparison with available experimental data shows excellent agreement for all three Mo-based material systems. E.g. for MoS_2 we find $E_G = 2.025$ eV for the direct gap at the K-points in bulk, whereas we find $E_G = 2.473$ eV for the freely suspended, $E_G = 2.279$ eV on top of a fused silicon substrate, and $E_G = 2.160$ eV for an hBN encapsulated monolayer. The gap on a metal substrate (e.g. gold) can be estimated from the limit $1/\epsilon_S \to 0^-$, yielding $E_G = 1.944$ eV. These values are in excellent agreement with available experimental data, listed also in table 1. In contrast, the gaps for the W-based

materials appear to be 130–150 meV below reported experimental values. Comparison with the MoX_2 systems shows that the predicted gaps for the corresponding WX_2 and MoX_2 are very similar, whereas the experimentally reported WX_2 gaps are always above those of the corresponding MoX_2 systems under comparable conditions. Since the environmentally induced band gap changes are captured very well by our analysis, we speculate that the origin for the systematic underestimation of the gap in the W-based systems is most likely at the DFT level.

For the suspended monolayers, we can also compare our results with other *ab initio* methods. Reported quasi-particle gaps based on the GW/GdW approach vary over a wide range of up to 400 meV and we find our results at the lower end of this spectrum. Regarding the relative differences in the gaps of the W- and Mo-based monolayers, the LDA and PBE based GW results show the same trend as our results, namely almost equal gaps for the sulfides and the selenides, thus supporting the assumption that the systematic discrepancy for the WX_2 originates at the DFT level. Regarding the shifts of the band gap with increased dielectric screening, our results agree well with the available GW-based predictions.

5.2. Density dependent band gap renormalization

As a second application, we calculate the band gap renormalization resulting from finite carrier densities in different TMDCs. In the presence of excited carriers, the renormalized band gap

$$\Delta_{\mathbf{K}} = \Delta^{DFT} + \sum_{\mathbf{q}_\parallel} \left(W^{vvvv}_{\mathbf{q}_\parallel;\mathbf{K};\mathbf{K}+\mathbf{q}_\parallel} - W^{ccvv}_{\mathbf{q}_\parallel;\mathbf{K};\mathbf{K}+\mathbf{q}_\parallel} \right)$$
$$\times \left(f^{\nu}_{\mathbf{k}_\parallel-\mathbf{q}_\parallel} - f^{c}_{\mathbf{k}_\parallel-\mathbf{q}_\parallel} \right). \tag{19}$$

contains the dynamically screened Coulomb matrix elements $W_{\mathbf{q}_\parallel}(\hbar\omega - \tilde{\epsilon}_{c\mathbf{K}+\mathbf{k}_\parallel-\mathbf{q}_\parallel} + \tilde{\epsilon}_{\nu\mathbf{K}+\mathbf{k}_\parallel})$, that, in turn, contain the renormalized single particle dispersions $\tilde{\epsilon}_{c/\nu\mathbf{k}_\parallel}$. These equations are solved self consistently together with equation (6), assuming thermal carrier distributions at 300 K within the renormalized bands. Here, we distinguish between optically excited carrier densities (equal numbers of electrons and holes) and carrier densities due to doping, where we restrict the analysis to electron doping only. In the presence of excited carriers, both, screening of the Coulomb potential by the excited carriers and phase space filling contribute to the conduction and valence band renormalization. In contrast, for the case of electron doping, the valence band renormalization is solely due to screening effects corresponding to the Coulomb hole, whereas the phase space filling effects additionally contribute to the conduction band renormalization.

The interplay between phase space filling and screening contributions sensitively depends on the employed screening model. In particular, the approximation of static screening leads to an overestimation of screening effects. To show the importance of dynamical screening, we compare the band gap of a SiO_2 supported MoS_2 monolayer in figure 8 for different carrier excitation conditions. Using the static approximation for the screened Coulomb interaction, the gap decreases

Table 1. Substrate dependent quasiparticle band gap of five semiconducting TMDC systems. The band gap is given for freely suspended, a substrate supported (fused silicon and metal), and hBN encapsulated monolayers. Additionally, literature values based on experimental and/or theoretical investigations are listed for comparison. Here, we distinguish between theoretical GW/GdW calculations building on DFT calculations employing different functionals, namely a local density approach (LDA), the generalized gradient approximation parametrized as by PBE or the hybrid functional Heyd–Scuseria–Ernzerhof (HSE). Additionally, results based on the GVJ-2e approach are summarized. Furthermore, concerning experimental results, we distinguish between photoluminescence (excitation) [PL(E)] measurements yielding the optical band gap from which the quasiparticle gap is extrapolated on the basis of a model for the exciton resonance energies, and scanning tunneling spectroscopy (STS) and angle-resolved photoemission spectroscopy (ARPES) measurements.

Material	Substrate	E_g (eV)	Theor.			Exp.	
			LDA + GW/GdW	PBE/HSE + GW/GdW	GVJ-2e	PL/PLE + model	STS/ARPES
MoS$_2$		2.473	2.8 [10], 2.9 [23],	2.55 (@300 K), 2.63 (@0 K) [24], 2.53 [26], 2.62 [27], 2.54/2.65 [28]	2.38 [25]		
	SiO$_2$	2.279					2.17(4) [29]
	hBN encaps.	2.16				2.16 [30], 2.146 [29]	
	Au	1.945	2.3 [10]				1.95(5) [32], 1.90 [33]
MoSe$_2$		2.111	2.6 [23], 2.26 [34],	2.12 [26], 2.24 [35]	2.03 [25]		
	SiO$_2$	1.941					
	hBN encaps.	1.835				1.874 [30]	
	Au	1.628					
MoTe$_2$		1.57		1.72 [35], 1.72 [36]			
	SiO$_2$	1.444					
	hBN encaps.	1.356				1.352 [30]	
	Au	1.166					
WS$_2$		2.41	2.81 [23]	2.53 [26], 2.83 [35]	2.51 [25]		
	SiO$_2$	2.206				2.73 [37], 3.01 [38], 2.37 [3], 2.40 [39]	
	hBN encaps.	2.084				2.238 [30]	
	Au	1.877					
WSe$_2$		2.063	2.4 [23]	2.35 [40]	2.11 [25]		
	SiO$_2$	1.885				2.63 [38], 2.35(20) [41], 2.02 [5]	2.38(6) [29]
	hBN encaps.	1.777		2.22 [40]		1.884 [42], 1.890 [43]	
	Au	1.573					1.75 [33]

very rapidly with increasing carrier density. Here, the decrease depends only little on the fact whether the carriers are generated by optical excitation or doping, indicating that the gap renormalization is completely dominated by the Coulomb hole. In contrast, for the case of dynamic screening, the gap decreases more slowly with increasing carrier density and is larger for the symmetrical, optically induced electron–hole densities than for electron densities alone.

Using the dynamical screening calculations, we compare in figure 9 the density dependent gap for the five investigated monolayer materials assuming optically induced electron–hole densities (solid lines) and electron densities only (dashed lines). Whereas the overall behavior is similar in all materials, the effects are somewhat more pronounced in Mo than in based systems, also increasing from S to Te. Furthermore, the renormalization depends on the distribution of carrier densities, thus the band gap changes are weaker due to doping densities than due to optically excited carriers. This effect is more pronounced in than in Mo based materials.

Finally, we compare the influence of excited carriers on the band gap of MoS$_2$ for different dielectric environments in

figure 10. As we can see, the environmentally induced band gap offset vanishes rapidly with increasing carrier density, showing that density dependent screening effects dominate the band gap over dielectric screening effects for moderate to large carrier densities.

### 5.3. Exciton resonances and binding energies

As third and final application, we calculate the resonance energies of the A exciton series for different TMDCs in various dielectric environments. Similar to the band gap renormalization, we find that the exciton binding energy decreases due to enhanced screening of the Coulomb interaction in media with increased dielectric constant. For the 1s exciton, the decrease in the band gap renormalization and binding energy nearly cancel. As a net result, the 1s exciton shows only a small red shift with increased dielectric screening. In contrast, for the higher exciton states, the band gap renormalization dominates over the decreased binding, yielding a pronounced red shift of the excited states with enhanced dielectric screening.

As representative examples, we show in figure 11 the excitonic resonances generated by solving the Dirac–Wannier
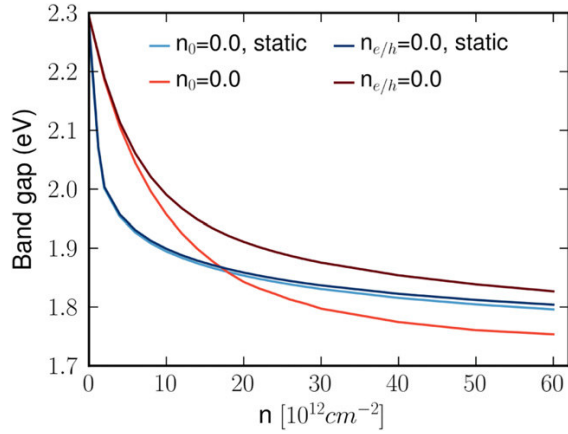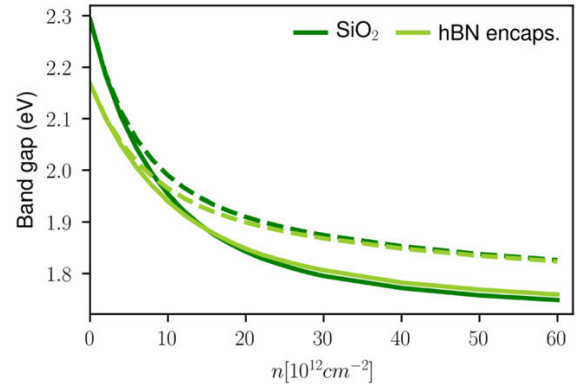
Figure 8. Comparison of the band gap renormalization in dependence of the carrier density n for static and dynamic screening for the example of a quartz supported MoS_2 monolayer. Here, $n_0 = 0$ indicates the absence of doping and $n_{e/h} = 0$ denotes the absence of optically excited carriers, respectively.
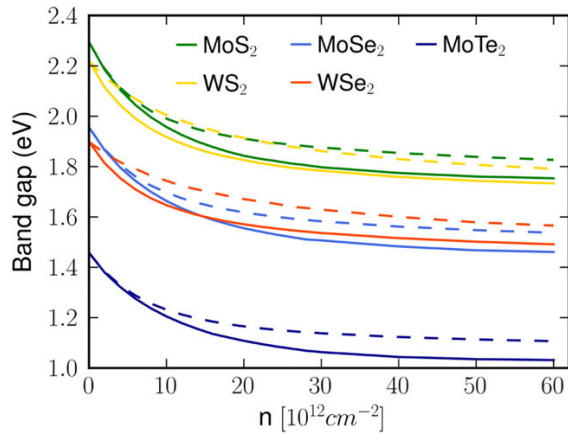

Figure 9. Dependence of the band gap renormalization on the carrier density for dynamical screening with $\gamma_T = 100$ meV for different transition metal dichalcogenides. Solid lines mark calculations with $n_0 = 0 \, \text{cm}^{-2}$, dashed lines belong to calculations with $n_{e/h} = 0 \, \text{cm}^{-2}$.

Figure 10. Dependence of the band gap renormalization on the carrier density for dynamical screening with $\gamma_T = 100$ meV for different MoS_2 in different dielectric environment, namely SiO_2 supported or hBN encapsulated.
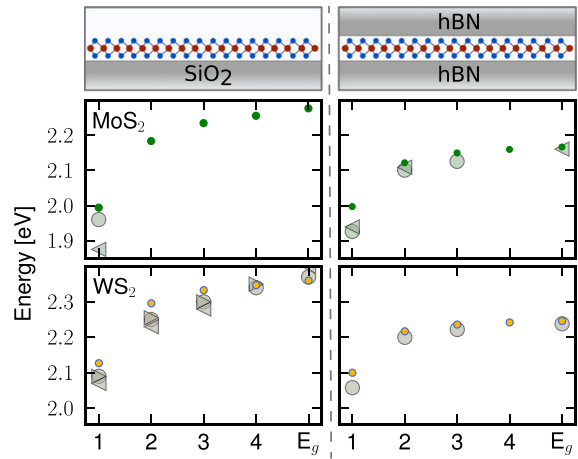
Figure 11. Resonance energies of the A exciton series and quasiparticle band gap for MoS_2 and WSe_2 at a SiO_2 substrate (left) and hBN encapsulated (right) as illustrated in the above sketch. Colored symbols mark our results. Experimental values were taken from 28, 29, 34, 39–44 and are shown for comparison (grey symbols). As for WS_2 the band gap is underestimated in DFT calculations, we shifted the DFT gap for WS_2 by 149 meV while keeping the dipole matrix elements constant. For both materials, the exciton resonances are in acceptable agreement with experimentally derived values.

equation for MoS_2 and WS_2 on a quartz substrate and for an hBN encapsulated configuration. Here, the four energetically lowest resonances are shown together with the quasiparticle band gap. As mentioned earlier, the gap of the W-based systems is systematically underestimated such that we have to shift the DFT gap by 149 meV for WS_2 while keeping the dipole matrix elements constant BEFORE we compute the renormalizations and exciton binding energies. While the band gap decreases from the SiO_2 to the hBN encapsulated sample by about 110 meV, the $1s$ resonance energy decreases only by less than a fourth of this amount. Thus, the binding energy is reduced by about 90–100 meV for WS_2 and MoS_2 respectively. In contrast, the binding energies of the $2s$, $3s$, $4s$ excitons are reduced by $40 - 20$ meV only.

6. Summary and conclusions

In summary, we investigated the effectively quasi-2D nature of the Coulomb interaction potential in TMDC monolayers. We compute the matrix elements at the K-points of the Brillouin zone and introduce a form factor that effectively captures the deviations from the corresponding ideally 2D case. We apply this concept to efficiently compute fundamental properties such as excitonic resonances and density-dependent band gap renormalizations for a range of TMDC monolayers in different dielectric environments and under various excitation conditions.

Table 2. MDF model parameters for different TMDCs based on DFT calculations using the PBE functional, namely the spin- and valley dependent band gap $\Delta_{s\tau}$, the spin splitting $2\lambda_v$, the dielectric constants for bulk materials $\epsilon_\parallel^B$, $\epsilon_\perp$ and the bulk interlayer distance d resulting directly from the calculations. Fermi velocity $\hbar v_F$ and in-plane dielectric constants $\epsilon_\parallel$ are derived from the band structure and the bulk value, respectively.

Material	$s \cdot \tau$	$\Delta_{s\tau}$ (eV)	$\hbar v_F$ (eV Å)	λ_v (eV)	$\epsilon_\parallel^B$	$\epsilon_\parallel$	$\epsilon_\perp$	d (Å)
MoS_2	+	1.682	3.532	0.146	15.19	11.65	6.38	6.18
	−	1.831	3.467					
$MoSe_2$	+	1.41	3.027	0.183	16.72	12.81	7.81	6.52
	−	1.614	3.001					
$MoTe_2$	+	1.017	2.526	0.214	20.30	15.43	10.9	6.99
	−	1.266	2.574					
WS_2	+	1.626	4.433	0.428	13.98	10.56	5.93	6.22
	−	2.022	4.208					
WSe_2	+	1.385	3.941	0.46	15.58	11.81	7.65	6.51
	−	1.801	3.757					

Comparing our results both to current experimental data and theoretical approaches based on GW/GdW–BSE calculations, we obtain good quantitative agreement as summarized in table 1. In particular, our computed dependence of the band gap dependence on the dielectric surrounding is qualitatively in good agreement with the GdW based study of Riis-Jensen *et al* [47]. Also the comparison with experimental data yields excellent agreement for the quasiparticle band gap of all Mo based materials.

For the W based systems, the experimentally obtained values vary in a wide range with differences up to 600 meV. Using the DFT results as an input, our computed band gaps are about 100–200 meV below most experimental values. Interestingly, it can be observed that results based on the PBE functional tend to be below results using an LDA functional. Thus, the choice of the XC-functional has an impact on the absolute band gap value and absolute differences may result from an underestimation of the band gap in the DFT calculations. Fitting the underestimated DFT gap for subsequent calculations for WS_2-systems but maintaining the gap unchanged for MoS_2-systems, we find an acceptable agreement of the A exciton series with experimental data, see figure 11. Furthermore, our approach reproduces the experimentally observed influence of the dielectric environment.

To illustrate the usefulness of our approach for the excitation dependent system properties, we compute the modifications induced by charge carriers on the dynamic band gap renormalization. In experimental studies, this effect has been analyzed by employing electrical gating, examining the influence of doping to the band gap [39, 48], or by pump-probe experiments, using laser pulses to modify the excited electron–hole density in the material [44, 49]. In agreement with experimental observations, our analysis shows that smaller band-gap modifications are obtained in the configuration where additional electrons are introduced by doping relative to the case where symmetrical electron–hole populations are generated by optical excitation.

Acknowledgments

Appendix. Material parameters

In table 2 we summarize the DFT based parameters used to model the dielectric and optical material properties near the respective K-points. While the bulk dielectric constants $\epsilon_\perp$, $\epsilon_\parallel^B$ and interlayer distance are direct results of DFT calculations, the band gap $\Delta_{s\tau}$, the valence band splitting $2\lambda_v$, and der Fermi velocity $\hbar v_F$ are determined by fitting the DFT band structure. The back ground dielectric constant $\epsilon_\parallel$ is derived in dependence of the bulk value as $\epsilon_\parallel^B = \epsilon_\parallel + \lim_{\mathbf{q}_\parallel \to 0} 4\pi e^2 \chi_L(\mathbf{q}_\parallel, \omega)/D$ [6] where $\chi_L(\mathbf{q}_\parallel, \omega)$ is the contribution of upper spin–split valence and lowest conduction bands to the total longitudinal susceptibility.

ORCID iDs

T Stroucken ⓘ https://orcid.org/0000-0002-0546-7289

References

[1] Mak K F, Lee C, Hone J, Shan J and Heinz T F 2010 *Phys. Rev. Lett.* **105** 136805
[2] Splendiani A, Sun L, Zhang Y, Li T, Kim J, Chim C Y, Galli G and Wang F 2010 *Nano Lett.* **10** 1271–5
[3] Chernikov A, Berkelbach T C, Hill H M, Rigosi A, Li Y, Aslan O B, Reichman D R, Hybertsen M S and Heinz T F 2014 *Phys. Rev. Lett.* **113** 076802
[4] Ross J S *et al* 2013 *Nat. Commun.* **4** 1–6
[5] He K, Kumar N, Zhao L, Wang Z, Mak K F, Zhao H and Shan J 2014 *Phys. Rev. Lett.* **113** 026803
[6] Meckbach L, Hader J, Huttner U, Neuhaus J, Steiner J T, Stroucken T, Moloney J V and Koch S W 2020 *Phys. Rev. B* **101** 075401

[7] Latini S, Olsen T and Thygesen K S 2015 *Phys. Rev.* B **92** 245123

[8] Meckbach L, Stroucken T and Koch S W 2018 *Phys. Rev.* B **97** 035425

[9] Winther K T and Thygesen K S 2017 *2D Mater.* **4** 025059

[10] Ryou J, Kim Y S, Santosh K and Cho K 2016 *Sci. Rep.* **6** 1–8

[11] Kresse G and Hafner J 1994 *Phys. Rev.* B **49** 14251–69

[12] Kresse G and Hafner J 1993 *Phys. Rev.* B **47** 558–61

[13] Kresse G and Furthmüller J 1996 *Phys. Rev.* B **54** 11169–86

[14] Kresse G and Furthmüller J 1996 *Comput. Mater. Sci.* **6** 15–50

[15] Kresse G and Joubert D 1999 *Phys. Rev.* B **59** 1758–75

[16] Perdew J P, Burke K and Ernzerhof M 1996 *Phys. Rev. Lett.* **77** 3865–8

[17] Grimme S, Antony J, Ehrlich S and Krieg H 2010 *J. Chem. Phys.* **132** 154104

[18] Monkhorst H J and Pack J D 1976 *Phys. Rev.* B **13** 5188–92

[19] Kormányos A, Burkard G, Gmitra M, Fabian J, Zólyomi V, Drummond N D and Fal'ko V 2015 *2D Mater.* **2** 022001

[20] Stroucken T, Grönqvist J H and Koch S W 2011 *Phys. Rev.* B **84** 205445

[21] Barford W, Boczarow I and Wharram T 2011 *J. Phys. Chem.* A **115** 9111–9

[22] Ignatov S K, Razuvaev A G, Kokorev V N and Aleksandrov Y A 1995 *J. Struct. Chem.* **36** 538–43

[23] Drüppel M, Deilmann T, Noky J, Marauhn P, Krüger P and Rohlfing M 2018 *Phys. Rev.* B **98** 155433

[24] Soklaski R, Liang Y and Yang L 2014 *Appl. Phys. Lett.* **104** 193110

[25] Gusakova J, Wang X, Shiau L L, Krivosheeva A, Shaposhnikov V, Borisenko V, Gusakov V and Tay B K 2017 *Phys. Status Solidi* A **214** 1700218

[26] Haastrup S *et al* 2018 *2D Mater.* **5** 042002

[27] Gerber I C *et al* 2019 *Phys. Rev.* B **99** 035443

[28] Thygesen K S 2017 *2D Mater.* **4** 022004

[29] Rigosi A F, Hill H M, Rim K T, Flynn G W and Heinz T F 2016 *Phys. Rev.* B **94** 075440

[30] Goryca M *et al* 2019 *Nat. Commun.* **10** 1–12

[31] Robert C *et al* 2018 *Phys. Rev. Mater.* **2** 011001

[32] Bruix A *et al* 2016 *Phys. Rev.* B **93** 165422

[33] Park S *et al* 2018 *2D Mater.* **5** 025003

[34] Ugeda M M *et al* 2014 *Nat. Mater.* **13** 1091–5

[35] Echeverry J P, Urbaszek B, Amand T, Marie X and Gerber I C 2016 *Phys. Rev.* B **93** 121107

[36] Robert C *et al* 2016 *Phys. Rev.* B **94** 155425

[37] Zhu B, Chen X and Cui X 2015 *Sci. Rep.* **5** 9218

[38] Hanbicki A, Currie M, Kioseoglou G, Friedman A and Jonker B 2015 *Solid State Commun.* **203** 16–20

[39] Chernikov A, van der Zande A M, Hill H M, Rigosi A F, Velauthapillai A, Hone J and Heinz T F 2015 *Phys. Rev. Lett.* **115** 126802

[40] Gerber I C and Marie X 2018 *Phys. Rev.* B **98** 245126

[41] Wang G, Marie X, Gerber I, Amand T, Lagarde D, Bouet L, Vidal M, Balocchi A and Urbaszek B 2015 *Phys. Rev. Lett.* **114** 097403

[42] Liu E, van Baren J, Taniguchi T, Watanabe K, Chang Y C and Lui C H 2019 *Phys. Rev.* B **99** 205420

[43] Stier A V, Wilson N P, Velizhanin K A, Kono J, Xu X and Crooker S A 2018 *Phys. Rev. Lett.* **120** 057405

[44] Liu F, Ziffer M E, Hansen K R, Wang J and Zhu X 2019 *Phys. Rev. Lett.* **122** 246803

[45] Cadiz F *et al* 2016 *2D Mater.* **3** 045008

[46] Molas M R *et al* 2019 *Phys. Rev. Lett.* **123** 096803

[47] Riis-Jensen A C, Lu J and Thygesen K S 2020 *Phys. Rev.* B **101** 121110

[48] Yao K *et al* 2017 *Phys. Rev. Lett.* **119** 087401

[49] Ulstrup S *et al* 2016 *ACS Nano* **10** 6315–22

Paper II

T. Stroucken, J. Neuhaus, and S. W. Koch:

Magnetic-field tuning of the intraexcitonic absorption and gain in transition metal dichalcogenides

Abstract: A systematic microscopic approach combining ab-initio density functional theory with the Dirac-Bloch equations is applied to investigate the intra-excitonic transitions of magneto-excitons in TMDC monolayers. For the example of hBN-encapsulated MoS_2, the linear optical response and mid-infrared spectra of the pre-excited system are numerically evaluated. It is shown that the transition probability between a subset of the magneto-excitons can be inverted under suitable conditions to display negative absorption, i.e. gain. With the help of an applied magnetic field, the absorption and gain spectra can be tuned over a wide spectral range. Evaluating the Zeeman shift of the excitonic states, effective g-factors are deduced that depend on the dielectric environment of the sample under consideration.

Magnetic-field tuning of the intraexcitonic absorption and gain in transition metal dichalcogenides

T. Stroucken ⬤,[*] J. Neuhaus ⬤, and S. W. Koch ⬤

Department of Physics and Material Sciences Center, Philipps University Marburg, Renthof 5, D-35032 Marburg, Germany

A systematic microscopic approach combining *ab-initio* density functional theory with the Dirac-Bloch equations is applied to investigate the intra-excitonic transitions of magneto-excitons in transition metal dichalcogenide monolayers. For the example of hBN-encapsulated MoS_2, the linear optical response and mid-infrared spectra of the pre-excited system are numerically evaluated. It is shown that the transition probability between a subset of the magneto-excitons can be inverted under suitable conditions to display negative absorption, i.e., gain. With the help of an applied magnetic field, the absorption and gain spectra can be tuned over a wide spectral range. Evaluating the Zeeman shift of the excitonic states, effective *g* factors are deduced that depend on the dielectric environment of the sample under consideration.

Monolayers of transition metal dichalcogenides (TMDCs) have attracted considerable interest in the past decade. The systematic thickness reduction leads to physical properties that differ qualitatively and quantitatively from the respective bulk counterparts and opens new perspectives regarding the study of fundamental physical processes as well as innovative technological applications. As has been demonstrated both experimentally and theoretically, the fundamental gap changes from indirect to direct [1–7] and the lack of an inversion center in the monolayer crystal lead to valley-selective optical selection rules [8–10]. Due to their reduced dimensionality and weak intrinsic screening, the optical spectra of TMDC monolayers are dominated by strong many-body effects, manifesting themselves as a huge renormalization of the single-particle band gap [11–16] and the existence of strongly bound excitons with binding energies of hundreds of meV [17–20]. Many of the unusual TMDC exciton properties have been vividly discussed in the literature [17–22] and optical spectroscopy under various excitation conditions in conjunction with sophisticated microscopic many-body theory has provided key insights into their energetic spectra, ultrafast dynamics, and many-body interactions [22–27]. In a properly pre-excited system, it is possible to study intra-excitonic transitions that couple optically bright *s* excitons to dark *p*-type excitons. These transitions require the absorption or emission of light with much lower energy, ranging from the THz to the mid-infrared frequency range, depending on the material system under investigation. For the typical semiconducting TMDCs, the transition energies from the 1*s*-exciton ground state to the *np*-excited exciton states range between 100 and 500 meV and are thus in the mid-infrared regime, whereas transitions between excited *ns*- and *n′p*-exciton states with $n, n' > 1$ are typically in the THz range [26,28–30]. Hence, intra-excitonic transitions can be studied by means of optical pump-THz-probe (OPTP) spectroscopy, where the exciton is created by an optical pump-pulse and subsequently probed by a THz probe-

pulse. In conventional semiconductors, OPTP spectroscopy has been proven to be the method of choice to study the formation dynamics of incoherent excitons after nonresonant excitation above the fundamental gap [31–34]. Similar studies have been performed for TMDC monolayers yielding exciton formation times on the picosecond time scale [26,28–30].

In this article, we theoretically investigate the possibility to magnetically control intra-excitonic transitions and their fingerprints in THz and mid-infrared optical spectra, for the example of hBN-encapsulated MoS_2. Under the influence of a perpendicular magnetic field, magneto-excitons exhibit a state-dependent Zeeman and diamagnetic shift. For the optically bright *s* excitons, these have been investigated both experimentally and theoretically [35–49]. Here we compute the field-induced shifts not only for the *s*-type states but also for the *p*-type states. We show that the peculiar level alignment in TMDCs with the *p*-type excitons energetically below the *s*-type excitons of equal main quantum number not only leads to THz absorption, but also, for proper initial conditions, enables THz amplification. Furthermore, we show that both the strength and the resonance energy of the THz absorption and gain can be tuned by an external perpendicular magnetic field, covering the technological interesting range from 1 to 10 THz.

The paper is organized as follows: In Sec. I, we briefly review the microscopic theory to describe the optical and THz response of magneto-excitons in TMDCs. In Sec. II, we present results for the linear optical response for the magneto-excitons for the example of hBN-encapsulated MoS_2 and we extract effective *g* factors for the different excitonic states. The THz response of an optically excited sample is evaluated in Sec. III and we discuss the magnetic field-induced tuning properties of the absorption and gain spectra. A short summary and conclusions are presented in Sec. IV.

I. THEORY

The wave equation for the vector potential

$$\vec{\nabla} \times \vec{\nabla} \times \mathbf{A} + \frac{\underline{\underline{\epsilon}}(\mathbf{r})}{c^2} \cdot \frac{\partial}{\partial t^2}\mathbf{A} = \frac{4\pi}{c}\mathbf{j}$$

---
[*]tineke.stroucken@physik.uni-marburg.de

couples to the optically induced material current

$$\mathbf{j} = -c \left\langle \frac{\delta H}{\delta \mathbf{A}} \right\rangle = -\frac{e}{m_0} \sum_{\alpha\alpha'\mathbf{k}} \mathbf{p}_{\alpha\alpha'\mathbf{k}} \langle c_{\alpha\mathbf{k}}^{\dagger} c_{\alpha'\mathbf{k}} \rangle . \tag{1}$$

Here, $\underline{\underline{\epsilon}}(\mathbf{r})$ is the anisotropic dielectric tensor, including screening contributions from the dielectric environment, as well as nonresonant static background contributions from the TMDC monolayer; $\alpha \equiv \{s, \tau, c/v\}$ combines the spin, valley, and band index, and $\mathbf{k}$ is a two-dimensional (2D) wave number; and $\mathbf{p}_{\alpha\alpha'\mathbf{k}} = \langle \alpha\mathbf{k}|\mathbf{p}|\alpha'\mathbf{k}\rangle$ is the matrix element of the momentum operator between the Bloch states.

The material current induced by the externally applied vector potential can be divided into its inter- and intraband contributions according to

$$\mathbf{j} = \mathbf{j}_{\text{intra}} + \mathbf{j}_{\text{inter}}, \tag{2}$$

with

$$\mathbf{j}_{\text{intra}} = -\frac{e}{m_0} \sum_{\mathbf{k}} \left(\mathbf{p}_{cc\mathbf{k}} f_{\mathbf{k}}^c + \mathbf{p}_{vv\mathbf{k}} f_{\mathbf{k}}^v \right)$$
$$= -e \sum_{\mathbf{k}} \hbar\mathbf{k} \left(\frac{1}{m_c} f_{\mathbf{k}}^c + \frac{1}{m_v} f_{\mathbf{k}}^v \right) \tag{3}$$

and

$$\mathbf{j}_{\text{inter}} = -\frac{e}{m_0} \sum_{\mathbf{k}} (\mathbf{p}_{vc\mathbf{k}} P_{\mathbf{k}} + \text{H.c.}). \tag{4}$$

Here, $f_{\mathbf{k}}^{\alpha} = \langle c_{\alpha\mathbf{k}}^{\dagger} c_{\alpha\mathbf{k}} \rangle$ denote the populations in the respective bands and $P_{\mathbf{k}} = \langle c_{v\mathbf{k}}^{\dagger} c_{c\mathbf{k}} \rangle$ is the coherent interband polarization. The populations and interband polarization are computed from their respective equations of motion, which, in the presence of a perpendicular static magnetic field $\mathbf{B} = B\mathbf{e}_z$, are given by

$$i\hbar \frac{d}{dt} P_{\mathbf{k}} = \left(\epsilon_{c\mathbf{k}} - \epsilon_{v\mathbf{k}} + \frac{e}{m_r c}\hbar\mathbf{k} \cdot \mathbf{A} + \frac{eB}{2m_r c}\hat{l}_z + \frac{e^2 B^2}{8m_r c^2}\hat{\mathbf{r}}^2 \right) P_{\mathbf{k}}$$
$$+ \sum_{\mathbf{q}\neq 0} V_{\mathbf{q}} \left[I_{\mathbf{q};\mathbf{k}}^{vc} - (I_{\mathbf{q};\mathbf{k}}^{cv})^{\dagger} \right] + \frac{e}{m_0 c}\mathbf{A} \cdot \mathbf{p}_{cv}(f_{\mathbf{k}}^v - f_{\mathbf{k}}^c), \tag{5}$$

$$\hbar \frac{d}{dt} f_{\mathbf{k}}^c = 2\text{Im} \left[\sum_{\mathbf{q}\neq 0} V_{\mathbf{q}} I_{\mathbf{q};\mathbf{k}}^{cc} + \frac{e}{m_0 c}\mathbf{A} \cdot \mathbf{p}_{cv} P_{\mathbf{k}}^* \right], \tag{6}$$

$$\hbar \frac{d}{dt} f_{\mathbf{k}}^v = 2\text{Im} \left[\sum_{\mathbf{q}\neq 0} V_{\mathbf{q}} I_{\mathbf{q};\mathbf{k}}^{vv} - \frac{e}{m_0 c}\mathbf{A} \cdot \mathbf{p}_{cv} P_{\mathbf{k}}^* \right]. \tag{7}$$

Here, m_r is the reduced mass of the electron-hole pair, $\hat{l}_z$ is the angular momentum operator, $\hat{\mathbf{r}} = i\nabla_{\mathbf{k}}$ is the position operator, $V_{\mathbf{q}}$ is the quasi-two-dimensional Coulomb interaction that contains screening from the dielectric environment and

background contributions of the remote bands,

$$I_{\mathbf{q};\mathbf{k}}^{\alpha\alpha'} = \langle c_{\alpha\mathbf{k}}^{\dagger} \hat{\rho}_{\mathbf{q}} c_{\alpha'\mathbf{k}-\mathbf{q}} \rangle \tag{8}$$

are two-particle correlations, and

$$\hat{\rho}_{\mathbf{q}} = \sum_{\alpha\mathbf{k}} c_{\alpha\mathbf{k}-\mathbf{q}}^{\dagger} c_{\alpha\mathbf{k}}$$

is the density operator, respectively. For an optical pump-THz-probe scenario with

$$\mathbf{A} = \mathbf{A}_{\text{opt}} + \mathbf{A}_{\text{THz}},$$

the optical field resonantly excites a coherent interband polarization, whereas the THz-field couples resonantly to the intraband current.

In the following, the TMDC monolayer is treated within the massive Dirac-Fermion (MDF) model [8] with a noninteracting single-particle dispersion $\epsilon_{s\tau\mathbf{k}}^{c/v} = \pm\frac{1}{2}\sqrt{\Delta_{s\tau}^2 + 4\hbar^2 v_F^2 k^2}$ with a spin- and valley-dependent gap $\Delta_{s\tau}$, the effective mass $m_c = -m_v = \Delta_{s\tau}/2v_F^2$, and a valley-dependent interband momentum matrix element $\mathbf{p}_{cv\mathbf{K}^{\pm}} = \sqrt{2}m_0 v_F \mathbf{e}^{\pm}$. The valley dependence of the dipole matrix elements leads to the well-known valley-specific optical selection rules, addressing the $\mathbf{K}^{\pm}$ valley with $\sigma^{\pm}$ circular polarized light. As all physical properties at the $\mathbf{K}^{\pm}$ valleys are related by parity or time-reversal symmetry, we will restrict the analysis to the $\mathbf{K}^+$ valley. Furthermore, we refer to the spin-valley combination $s\tau = \pm 1$ as A and B bands.

The necessary input material parameters for the Dirac-Bloch equations $(5 - 7)$ are obtained from density functional theory (DFT) [50] calculations utilizing the *Vienna ab initio simulation package* (VASP) [51–53]. In our calculations, we used the Perdew-Burke-Ernzerhof functional [54] including spin-orbit interaction [55]. The noninteracting gap and Fermi velocity are subsequently extracted by fitting the DFT band structure in proximity of the K points by the MDF dispersion. Coulomb-related properties are inferred by employing additional analytical approaches that combine the dielectric properties of the parent bulk material with Poisson's equation to calculate the screening under various environmental conditions as described in Ref. [21], and the DFT wave functions are exploited to obtain expressions for the Coulomb matrix elements [56]. Altogether, this provides a fully *ab-initio* description for the optical response of the monolayer/environment material system.

II. LINEAR OPTICAL RESPONSE

In the linear optical regime, the two-particle correlations $I_{\mathbf{q};\mathbf{k}}^{vc}$ can be treated on the screened Hartree-Fock level [16] where the Coulomb interaction leads to a renormalization of the free-particle dispersion and the emergence of bound exciton resonances. In the presence of a magnetic field $\mathbf{B} = B\mathbf{e}_z$, the linearly induced optical interband polarization displays resonances at the eigenvalues of the exciton equation [37],

$$\left(\mathcal{E}_{\mathbf{k}}^e[B] + \mathcal{E}_{\mathbf{k}}^h[B] + \frac{eB}{2m_r c}\hat{l}_z + \frac{e^2 B^2}{8m_r c^2}\hat{\mathbf{r}}^2 \right) \psi_{\mu}(\mathbf{k}) - \sum_{\mathbf{k}'} \overline{W}_{|\mathbf{k}-\mathbf{k}'|}^{cvvc}[f] \psi_{\mu}(\mathbf{k}') = \epsilon_{\mu} \psi_{\mu}(\mathbf{k}). \tag{9}$$

Here, $\overline{W}_{\mathbf{k}-\mathbf{k}'}^{cvvc}[f] = \sqrt{f_{\mathbf{k}}^v - f_{\mathbf{k}}^c}\, W_{\mathbf{k}-\mathbf{k}'}^{cvvc} \sqrt{f_{\mathbf{k}'}^v - f_{\mathbf{k}'}^c}$ with $W_{\mathbf{k}-\mathbf{k}'}^{cvvc}$ denote the quasi-two-dimensional screened electron-hole Coulomb matrix element and $f_{\mathbf{k}}^{c/v}$ describe static incoherent populations that may be induced, e.g., by doping or pumping by an optical prepulse. Furthermore, $\mathcal{E}_{\mathbf{k}}^{e/h}[B]$ is the Coulomb-renormalized single-particle dispersion that can be computed with the aid of the gap equations [21,57],

$$\tilde{\Delta}_{\mathbf{k}} = \Delta[B] + \frac{1}{2}\sum_{\mathbf{k}'} W_{|\mathbf{k}-\mathbf{k}'|} \frac{\tilde{\Delta}_{\mathbf{k}'}}{\mathcal{E}_{\mathbf{k}'}}\left(f_{\mathbf{k}'}^v - f_{\mathbf{k}'}^c\right), \qquad (10)$$

$$\tilde{v}_{\mathbf{k}} = v_F + \frac{1}{2}\sum_{\mathbf{k}'} W_{|\mathbf{k}-\mathbf{k}'|} \frac{k'}{k} \frac{\tilde{v}_{\mathbf{k}'}}{\mathcal{E}_{\mathbf{k}'}} \cos(\theta_{\mathbf{k}} - \theta_{\mathbf{k}'})$$
$$\times \left(f_{\mathbf{k}'}^v - f_{\mathbf{k}'}^c\right), \qquad (11)$$

$$\mathcal{E}_{\mathbf{k}} = \sqrt{\tilde{\Delta}_{\mathbf{k}}^2 + 4\hbar^2 \tilde{v}_{\mathbf{k}}^2 k^2}. \qquad (12)$$

As a consequence of the magnetic field, the unrenormalized single-particle dispersion contains a Zeeman shift of the atomic orbitals contributing to the valence and conduction band. As the valence band of TMDCs in proximity to the K points is composed of d-type orbitals exhibiting an orbital angular momentum of $m_z = \pm 2$, the application of a perpendicular magnetic field leads to a Zeeman shift of $\pm 2\mu_B B$ of the valence band maxima, where $\mu_B = e\hbar/2m_0 c$ is the Bohr magneton. Hence, the Zeeman shifts in the different valleys are related by $\Delta_{K^+}[B] = \Delta_{K^-}[-B]$. The respective shifts result in a splitting $\Delta_{K^+}[B] - \Delta_{K^-}[B] = -4\mu_B B$ between the $\mathbf{K}^{\pm}$ valleys [40,42,43]. Due to the gap renormalization, the Zeeman shift is slightly enhanced, without changing the symmetry relation between the distinct valleys under a change in the sign of B. This leads to g factors for the splitting with an absolute value slightly larger than 4, in good agreement with experimental findings [36,37,40,42,58] on similar material systems. Additionally, the term $\propto \hat{l}_z$ in Eq. (9) leads to a Zeeman shift of the exciton states. Although this term does not contribute to optically bright s-type resonances in the linear optical spectra, it does affect p-type excitons that can be addressed by a subsequent THz-field. For free particles, i.e., if Coulombic effects are neglected, the term $\propto B^2$ leads to the formation of Landau levels. Within the effective mass approximation, these are given by $E_n = \hbar\omega_c(n + 1/2)$ with a cyclotron frequency $\hbar\omega_c = e\hbar B/2m_r c$. If Coulombic effects dominate, i.e., the exciton binding is large compared to the Landau energy, the terms quadratic in B lead to a diamagnetic shift of the exciton resonances that is approximately quadratic in B.

Numerically evaluating our microscopic theory allows us to compute the linear and nonlinear response to a wide range of excitation conditions. As an example, we show in Fig. 1 the computed linear optical susceptibility of an hBN-encapsulated MoS$_2$ monolayer at zero magnetic field. Here, the hBN encapsulation is modeled by a thin anisotropic dielectric with in-plane and out-of-plane dielectric constants $\epsilon_{\parallel} = 4.91$ and $\epsilon_z = 2.79$, respectively, which is valid at the optical frequency range. Here and in the following, we used a phenomenological dephasing of $\gamma = 2.5\,\text{meV}/\hbar$ for the A-exciton series and $\gamma = 20\,\text{meV}/\hbar$ for the B excitons, respectively, yielding linewidths in the order of experimentally observed values on
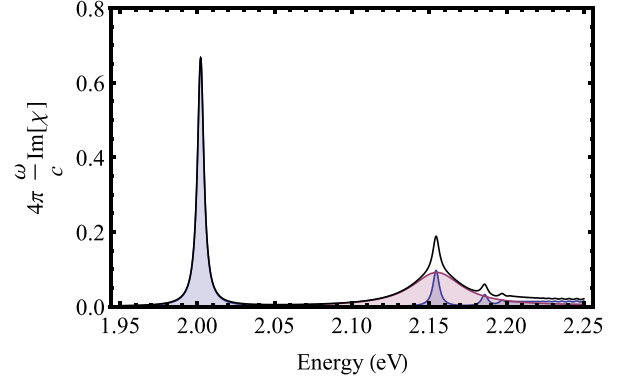

FIG. 1. Imaginary part of the calculated linear optical susceptibility at $B = 0\,\text{T}$ of a hBN-encapsulated MoS$_2$ monolayer on a fused silicon substrate. Blue parts show the contribution of the A-exciton series and red parts of the B-exciton. Spectra have been calculated using a phenomenological decay rate $\gamma = 2.5\,meV/\hbar$ for the A-exciton series and $\gamma = 20\,meV/\hbar$ for the B exciton.

hBN-encapsulated samples. Using *ab-initio* parameters only, we find the renormalized band gap at $E_G = 2.22\,\text{eV}$ and the lowest 1s-exciton resonance at $E_{1s} = 2.00\,\text{eV}$, yielding a binding energy of 220 meV. The calculated 1s-exciton energy is in good agreement with other *ab-initio* values reported in the literature but approximately 50 meV above experimentally reported values. However, the calculated binding energy is in very good agreement with experimental observations [25]. Since our theoretical prediction for the renormalized single-particle gap seems to be slightly too large, we shift the computed spectra in the following by 50 meV for a better quantitative comparison with experiment.

In Fig. 2, we show the magnetic field dependence of the linear transmission spectrum on excitation with σ^+-polarized light for the hBN-encapsulated MoS$_2$ monolayer on a fused silicon substrate. Propagation of the optical field through the sample and the supporting substrate is included into the calculations using the refractive index $n_{\text{SiO}_2} = 1.46$. One clearly recognizes the A_{1s} and B_{1s}—partially overlapped by the A_{2s}—excitons with an extinction of about 10% of the incoming light and a nearly linear B dependency. For stronger magnetic fields, the oscillator strength of the excited states increases, in good agreement with experimental findings [25].

To analyze the dependency on the magnetic field strength, we show the calculated even $(E_{ns}[B] + E_{ns}[-B])/2$ and odd parts $(E_{ns}[B] - E_{ns}[-B])/2$ in Fig. 3. The even part results from the term $\propto B^2\hat{\mathbf{r}}^2$ in the exciton Hamiltonian and contains the diamagnetic shift. As it does not couple to the spin or orbital angular momentum, the diamagnetic shift is equal for both valleys. The odd part results from the Zeeman shift of the underlying atomic orbitals and is of opposite sign in the nonequivalent valleys, leading to a Zeeman valley-splitting twice as large as the shift shown here. Since excitation with circular polarized light of opposite handedness addresses the different valleys, the linear optical spectra under excitation with right- and left-handed circular polarized light are related by changing the direction of the magnetic field, i.e., $T[\sigma^+, B] = T[\sigma^-, -B]$. As can be recognized, the quadratic
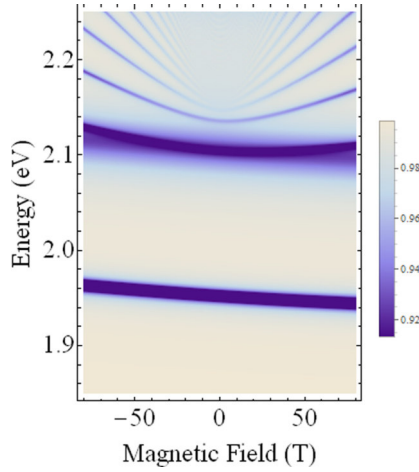
FIG. 2. Calculated transmission spectrum T/T_0 for a hBN-encapsulated MoS$_2$ monolayer on a fused silicon substrate. Spectra have been calculated using a phenomenological decay rate $\gamma = 2.5\,meV/\hbar$ for the A-exciton series and $\gamma = 20\,\text{meV}/\hbar$ for the B excitons and have been shifted by 50 meV to match the experimentally observed gap. Calculations are performed for the $\mathbf{K}^+$ valley that is addressed with right-handed circular polarized light. Results for the $\mathbf{K}^-$ valley (σ^-) are obtained by reversing the sign of the magnetic field.

approximation for the diamagnetic is valid only for a pretty small range of the magnetic field strength. In particular, the shifts of the excited states change their slopes toward a linear dependency in the intermediate field range without

approaching the Landau levels expected in the high field limit. The dots in the left part of Fig. 3 denote experimentally observed values [25]. Although small deviations in the range of few meV exist for the lowest exciton states, the theory/experiment agreement is pretty good in view of the fact that we use only *ab-initio* parameters.

For the Zeeman shift, we find g factors slightly smaller than expected from the atomic orbitals alone. Deviations from the strictly atomic contribution result from the interplay between the gap renormalization and the binding energy. Within a linear approximation in the range $-80\text{T} \leqslant B \leqslant 80\text{T}$, one finds the g factors $g_{1s} = -2.05$, $g_{2s} = -2.10$, $g_{3s} = -2.10$, and $g_{\text{Gap}} = -2.17$, which are all smaller than -2. These results are in good agreement with most experimental findings on similar material systems which observe state-dependent valley g factors $g_{\text{valley}} = 2g$ slightly smaller than -4 [36,37,40,42,58]. However, it should be mentioned that the Zeeman shift is not strictly linear in B; thus, the g factors obtained within a linear approximation depend on the B range used in the fit. Considering $-30\text{T} \leqslant B \leqslant 30\text{T}$, one finds the values $g_{1s} = -2.06$, $g_{2s} = -2.12$, $g_{3s} = -2.13$, and $g_{\text{gap}} = -2.17$, respectively. Furthermore, we note that via Coulomb renormalization effects, the exciton g factors depend on the dielectric environment that screens the monolayer Coulomb potential, though this effect is smaller than the dependency on the considered magnetic field range.

III. LINEAR THZ RESPONSE

To calculate the intra-excitonic absorption, we insert Eqs. (6) and (7) into Eq. (3), yielding

$$\frac{\mathrm{d}}{\mathrm{d}t}\mathbf{j}_{\text{intra}} = \frac{2e}{\hbar m_r}\text{Im}\left[\frac{1}{\mathcal{A}}\sum_{\mathbf{k},\mathbf{Q},\mathbf{q}\neq 0}\hbar\mathbf{k}V_{\mathbf{q}}\langle c^{\dagger}_{\mathbf{k}+\mathbf{Q}_e}v_{\mathbf{k}-\mathbf{Q}_h}v^{\dagger}_{\mathbf{k}-\mathbf{q}-\mathbf{Q}_h}c_{\mathbf{k}-\mathbf{q}+\mathbf{Q}_e}\rangle\right] + \frac{2e^2}{m_0\hbar c}\text{Im}\left[\frac{1}{\mathcal{A}}\sum_{\mathbf{k}}\hbar\mathbf{k}\mathbf{A}\cdot\mathbf{p}_{cv}P^*_{\mathbf{k}}\right] \tag{13}$$

with $\mathbf{Q}_{e/h} = \frac{m_{e/h}}{M}\mathbf{Q}$. The last term on the R.H.S. of Eq. (13) contributes significantly only during the optical pulse and can be neglected for a scenario where a short optical pulse is followed by a THz pulse with a time delay significantly exceeding the pulse duration.

Defining the exciton annihilation operator as

$$B_{\lambda}(\mathbf{Q}) = \sum_{\mathbf{k}}\frac{\psi^*_{\lambda}(\mathbf{k})}{\sqrt{f^v_{\mathbf{k}} - f^c_{\mathbf{k}}}}v^{\dagger}_{\mathbf{k}-\mathbf{Q}_h}c_{\mathbf{k}+\mathbf{Q}_e}, \tag{14}$$

where $\psi_{\lambda}(\mathbf{k})$ is the solution of the Wannier equation (9), one finds for the THz current

$$i\hbar\frac{\mathrm{d}}{\mathrm{d}t}\mathbf{j}_{\text{intra}} = \sum_{\lambda\lambda'}\mathbf{j}_{\lambda\lambda'}(\epsilon_{\lambda'} - \epsilon^*_{\lambda})n_{\lambda\lambda'} - i\hbar\Gamma\mathbf{j}_{\text{THz}}. \tag{15}$$

Here, $\mathbf{j}_{\lambda\lambda'} = \frac{e}{m_r}\sum_{\mathbf{k}}\psi^*_{\lambda}(\mathbf{k})\hbar\mathbf{k}\psi_{\lambda'}(\mathbf{k})$ is the intra-excitonic current matrix element and $n_{\lambda\lambda'} = \frac{1}{\mathcal{A}}\sum_{\mathbf{Q}}\langle B^{\dagger}_{\lambda}(\mathbf{Q})B_{\lambda'}(\mathbf{Q})\rangle$ is the exciton density matrix, respectively. We included a phenomenological dephasing rate Γ.

The equation of motion for the exciton density matrix is

$$i\hbar\frac{\mathrm{d}}{\mathrm{d}t}n_{\lambda\lambda'}(\mathbf{Q}) = (\epsilon_{\lambda'} - \epsilon^*_{\lambda} - i\hbar\gamma)n_{\lambda\lambda'}(\mathbf{Q})$$
$$+ \frac{1}{c}\sum_{\lambda''}(\mathbf{j}_{\lambda\lambda''}n_{\lambda''\lambda'} - n_{\lambda\lambda''}\mathbf{j}_{\lambda'\lambda''})\cdot\mathbf{A}_{\text{THz}}, \tag{16}$$

where we again included a phenomenological dephasing rate γ for the exciton populations. Given an initial exciton density $n_{\lambda\lambda'}$, linearization with respect to the THz field yields

$$\mathbf{j}_{\text{intra}}(\omega) = \frac{1}{c}\sum_{\lambda\lambda'\lambda''}\frac{\epsilon_{\lambda'} - \epsilon^*_{\lambda}}{\epsilon^*_{\lambda} - \epsilon_{\lambda'} - i\hbar\Gamma}$$
$$\times\left[\frac{1}{\hbar\omega + i\hbar(\Gamma + \gamma)} - \frac{1}{\hbar\omega - \epsilon_{\lambda'} + \epsilon^*_{\lambda} + i\hbar\gamma}\right]$$
$$\times\mathbf{j}_{\lambda\lambda'}(\mathbf{j}_{\lambda\lambda''}n_{\lambda''\lambda'} - n_{\lambda\lambda''}\mathbf{j}_{\lambda'\lambda''})\cdot\mathbf{A}_{\text{THz}}, \tag{17}$$

from which the THz-susceptibility can be obtained via

$$\chi_{\text{THz}}(\omega) = \frac{c}{\omega^2}\frac{\delta\mathbf{j}_{\text{intra}}}{\delta\mathbf{A}_{\text{THz}}(\omega)}.$$
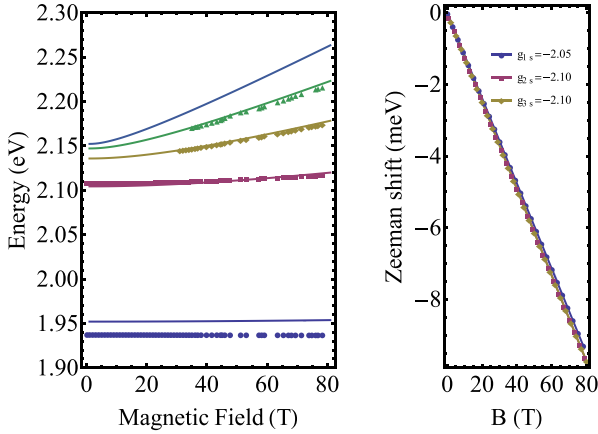
FIG. 3. Even part of the exciton energies containing the diamagnetic shift (left) and Zeeman shift (right) of the optically bright s-type states at the $\mathbf{K}^+$ valley. For the $\mathbf{K}^-$ valley, the Zeeman shift is in opposite direction, leading to a g factor for the valley-splitting twice as large as the g factor here. Dots in the left panel denote experimental values extracted from Ref. [25].

As the intra-excitonic dipole matrix elements are nonvanishing only for $m' = m \pm 1$, the THz-susceptibility displays resonances at the transition energies between s- and p-type states only. In the left panel of Fig. 4, we show the computed spectral position of the dark $p^\pm$ states at the $\mathbf{K}^+$ valley with $m_z = \pm 1$ together with those of the bright s-type states. Results for the $\mathbf{K}^-$ valley are obtained by the relations $E^{K^+}_{np^+}[B] = E^{K^-}_{np^-}[-B]$, $E^{K^+}_{np^-}[B] = E^{K^-}_{np^+}[-B]$. As can be recognized, the $p^\pm$-type states are nondegenerate and energetically below the s-type states with equal main quantum number. In the middle and right panels, we also show the diamagnetic and Zeeman shift of the optically dark p-type states. The p-type states exhibit a diamagnetic shift that is of comparable magnitude for p^+- and p^--type states, but significantly smaller than that

of the s-type excitons. As the diamagnetic shift is a measure for the extension of the exciton wave functions, this is in agreement with the differences in the binding energy. The Zeeman shifts of the p states differ from the Zeeman shift of the s states by $\pm \frac{m_0}{m_r} \mu_B B = \pm 3.83 \, \mu_B B$.

Given an initial exciton density $n_{\lambda\lambda'} = n_\lambda \delta_{\lambda\lambda'}$, transitions to energetically higher excitonic states require the absorption of a THz-photon, where the absorption of a $\sigma^\pm$-polarized THz-photon induces the transition $s \to p^\pm$ with $m' = \pm 1$. Correspondingly, the transitions to energetically lower $p^\pm$ states correspond to the emission of a $\sigma^\mp$-polarized THz-photon, as indicated by the arrows in Figure 4. Hence, a population of the exciton ground state leads to absorptive features in the THz/mid-infrared spectrum only, as shown in the first row of Fig. 5, where we show the mid-infrared absorption $\alpha(\omega) = 4\pi \frac{\omega}{c} \text{Im}[\chi_{\text{THz}}(\omega)]$ of a MoS$_2$ monolayer after resonant optical excitation of the 1s-exciton at the $\mathbf{K}^+$ valley as function of the externally applied magnetic field for different polarizations of the IR/THz-photons. In the low-density regime, the THz absorption increases linearly with the exciton density, and the calculations have been performed for an initial 1s-exciton density of $n_{1s} = 10^{10}$ cm^{-2}. The dominant absorption features around 150 meV result from the $1s \to 2p^\pm$ transition. Clearly observable are also transitions to the 3p and 4p states. With increasing field strength, the oscillator strength to the higher excited states increases, making them more clearly visible. Due to the lifting of the degeneracy of the $p^\pm$ states at $B = 0$, the absorption spectra on σ^+ and σ^- THz probe on the σ^+ pre-excited sample are not related by a sign reversal of the magnetic field. Instead, reversing the sign of the magnetic field B yields the spectra at the $\mathbf{K}^-$ valley. Explicitly, we have the relations for the optical pump-THz-probe spectra $OPTP[\sigma^+\sigma^+, B] = OPTP[\sigma^-\sigma^-, -B]$, $OPTP[\sigma^+\sigma^-, B] = OPTP[\sigma^-\sigma^+, -B]$.

An even more interesting situation arises if an optical pulse predominantly generates excited-state populations. In this case, a population inversion with respect to the energetically lower p states allows the amplification of a subsequent THz probe-pulse as shown in the second row of Fig. 5 for
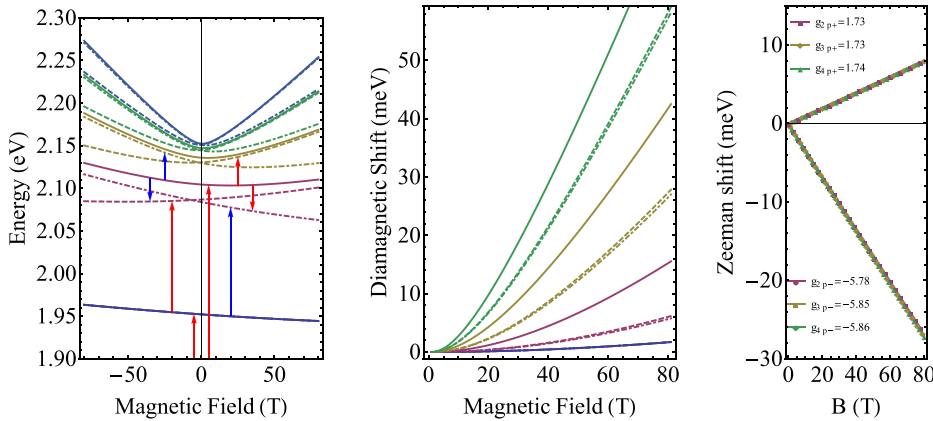

FIG. 4. Left: Spectral position of the bright s-type excitons (solid lines) at the $\mathbf{K}^+$ valley together with those of the dark p^+ (dashed lines) and p^- (dotted-dashed lines) states as function of the magnetic field. The red arrows denote dipole-allowed transitions with right-handed circular polarized light and the blue arrows those for left-handed light. The middle panel shows the diamagnetic shift of the respective states and in the right panel, the Zeeman shift of the optically dark p-type states is visualized.
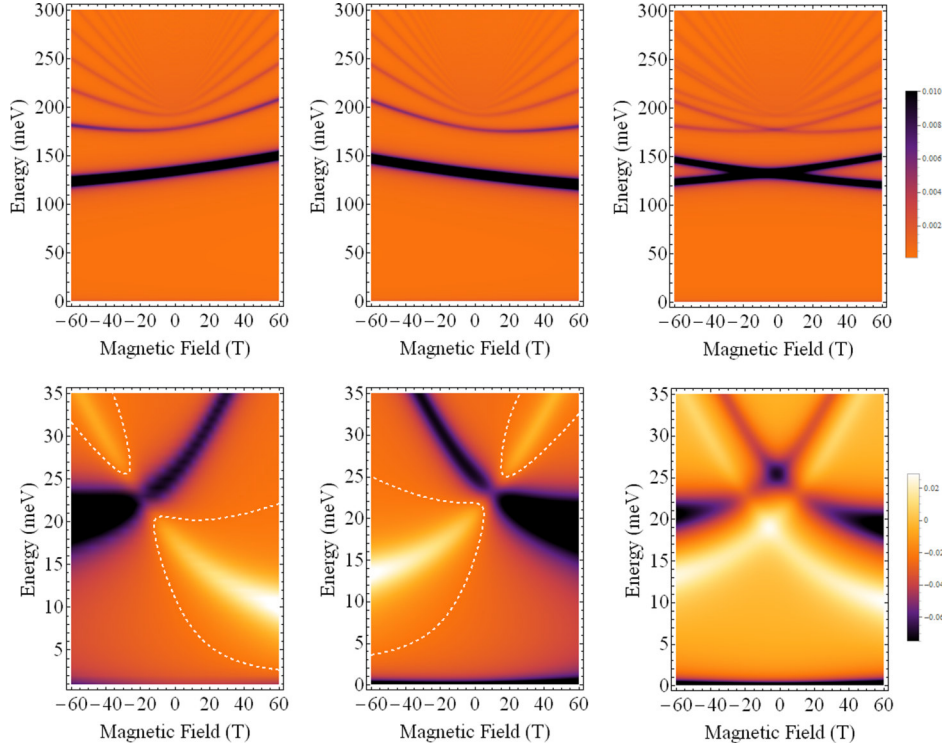
FIG. 5. Mid-IR-absorption as function of a perpendicular magnetic field after resonant optical excitation of the $1s$-exciton resonance (upper part) and THz-gain after resonant optical excitation of the $2s$-exciton resonance (lower part). The left figures show the gain on $\sigma^+\sigma^+$-polarization of the optical and THz-pulses, the middle figures after $\sigma^+\sigma^-$-polarized excitation, and the right figures on $\sigma^+\sigma_x$-excitation. The corresponding spectra on $\sigma^-\sigma^-$- and $\sigma^-\sigma^+$-excitation are obtained by reversing the sign of the magnetic field. The absorption spectra scale linearly with the initial $1s$-exciton density and are shown for $n_{1s/2s} = 10^{10}/\mathrm{cm}^2$ using a phenomenological decay rate $\gamma = 2.5\,\mathrm{meV}/\hbar$ and $\Gamma = 1\,\mathrm{meV}/\hbar$. The white dashed lines separate the regions with positive and negative gain (absorption).

the example of an initial population of the $2s$-exciton after resonant optical excitation and different combination of the pulse polarization. Here, the transition to the $2p$ states induces gain, whereas the transitions to p-type states with $n > 2$ are absorptive. At small magnetic fields, these competing processes lead to a very small net gain of the THz pulse as the absolute energetic distance from the $2p$ and $3p$ states to the $2s$ state are of comparable magnitude. However, as can be recognized from Fig. 5, the Zeeman shift of the $p^\pm$ states leads to a clear separation of absorptive and gain features, leading to clearly recognizable gain in the THz spectra at high magnetic fields. As the Zeemann shift of the p-type states is of opposite sign, the region of gain depends on the polarization sequence of the pulses. For linear polarized light, the net gain even for larger fields is smaller as the processes due to the different p-type states cancel partially.

IV. DISCUSSION

In summary, we investigated the linear optical and the THz response and their dependence on a perpendicular magnetic field of a monolayer TMDC for the example of hBN-encapsulated MoS$_2$ and varying polarization of the pulses. The THz response couples directly to intra-excitonic transitions and thus provides access to otherwise dark p-type

exciton states. Depending on the excitation conditions, we have shown that counteracting processes of absorption and amplification take place. In particular, a net gain in the range of several 10 meV due to the transition from the A_{2s} exciton to the energetically lower $2p$ states is seen. Furthermore, the resonance energies of the intra-excitonic transitions can be tuned with the aid of a perpendicularly applied magnetic field, utilizing the different g factors of the s- and p-type states. The application of a perpendicular magnetic field enables an energetic separation of absorptive and gain features on the one hand, enhancing the THz-amplification, and on the other hand a tuning of the resonance energy that is roughly between 10 and 20 meV for the investigated sample.

APPENDIX A: COMPUTATIONAL DETAILS

For the MDF model Hamiltonian, we use as input spin- and valley-dependent gaps obtained from our DFT calculations.

TABLE I. DFT-based MDF model parameters based used in the calculations.

MoS$_2$	Δ [eV]	m_r [m_0]	$\epsilon_\parallel$	$\epsilon_\perp$	D [Å]	d [Å]	$\sigma^2/2$ [Å^2]
A	1.682	0.261	15.19	6.38	6.18	1.06	3.067
B	1.831	0.284					

The Fermi-velocity v_F is related to the gap and effective exciton reduced mass via $\Delta_{s\tau} = 4m_r v_F^2$ and is obtained by fitting the DFT band structure. Resulting parameters are summarized in Table I. For the Coulomb interaction potential, we use the solution of Poisson's equation within an anisotropic, inhomogeneous dielectric environment as described in Refs. [21,56]. In the strict 2D limit, this yields the screened interaction potential

$$W_{\mathbf{q}} = \frac{2\pi}{\kappa q}(1 + c^{+-} + c^{-+} + c^{--} + c^{--}), \quad (A1)$$

where $\kappa = \sqrt{\epsilon_\parallel \epsilon_\perp}$ contains the in- and out-of-plane dielectric constants of bulk MoS$_2$, $\kappa_{T/B}$ are defined accordingly for the top and bottom dielectric environment,

$$c^{\eta\eta'} = \frac{(\kappa + \eta\kappa_T)(\kappa + \eta'\kappa_B)}{(\kappa + \kappa_T)(\kappa + \kappa_B) - (\kappa - \kappa_T)(\kappa - \kappa_B)e^{-2\tilde{q}_\parallel D}},$$

and D is the interlayer distance in a bulk MoS$_2$ crystal. The required in- and out-of-plane dielectric constants for bulk MoS$_2$ and interlayer distance are also obtained from the DFT calculations. In the strict 2D limit, the electron-hole Coulomb matrix element $W_{\mathbf{k}-\mathbf{k}'}^{cvvc}$ in the exciton equation is given by

$$W_{\mathbf{k}-\mathbf{k}'}^{cvvc} = W_{|\mathbf{k}-\mathbf{k}'|}(u_k^2 u_{k'}^2 + 2u_k v_k u_{k'} v_{k'} e^{\mp i(\theta_{\mathbf{k}}-\theta_{\mathbf{k}'})} + v_k^2 v_{k'}^2 e^{\mp 2i(\theta_{\mathbf{k}}-\theta_{\mathbf{k}'})}),$$
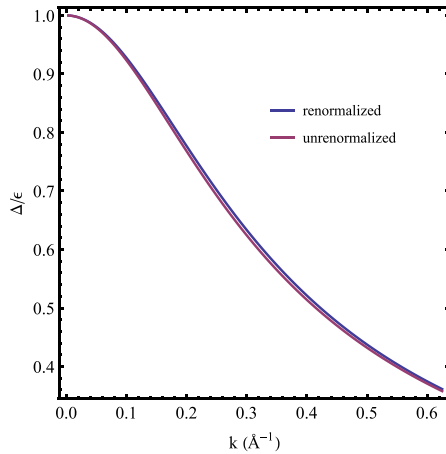
where $u_k^2 = (\epsilon_k + \Delta)/2\epsilon_k = 1 - v_k^2$, $\theta_{\mathbf{k}}$ is the angle of the $\mathbf{k}$-vector and the $\pm$ sign holds for the $\mathbf{K}^\pm$ valley, respectively. To account for the finite extension of the Bloch waves in the z-direction, the strictly 2D Coulomb matrixelements are modified by a form-factor $e^{-q_\parallel d - q_\parallel^2 \sigma^2/2}$ as described in Ref. [56].

Exploiting the rotational symmetry of the gap and Fermi velocity, the gap Eqs. (10) and (11) were integrated inserting the noninteracting values of the gap and Fermi velocity in the integrands. Integrals were performed on an equidistant grid of 200 points spaced by $\Delta k = .025\hbar v_F/\Delta_A = 3.125 \cdot 10^{-3}$ Å with mathematica [59] using standard in-build integration routines. A single shot already yields convergent results, as can be recognized from Fig. 6 showing the ratio $\frac{\tilde{\Delta}_k}{\mathcal{E}_k}$ after 1 iteration of solving the gap equation. If this ratio is unchanged, convergence of the gap equations is achieved.

As the exciton Hamiltonian commutes with the orbital angular momentum $\hat{l}_z$, Eq. (9) was solved for each value m of the angular momentum separately by matrix inversion. To this end, the $\mathbf{k}$ sums in the Coulombic part were converted into integrals according to $\sum_{\mathbf{k}'} \to \frac{A}{(2\pi)^2} \int d^2 k' = \frac{A}{(2\pi)^2} \int d\theta_{\mathbf{k}'} k' dk'$ that were subsequently discretized according to $\int d\theta_{\mathbf{k}'} k' dk' \to \int d\theta_{\mathbf{k}'} \Delta k \sum_j k_j'$. In order to obtain a Hermitian equation, we substituted $\tilde{\psi}(\mathbf{k}) = \sqrt{k}\psi(\mathbf{k})$ and multiplied Eq. (9) with $\sqrt{k}$. Subsequently, the Coulomb interaction for the m states $W_{k,k'}^m = \int d\theta_{\mathbf{k}} \int d\theta_{\mathbf{k}'} e^{-im(\theta_{\mathbf{k}}-\theta_{\mathbf{k}'})} W_{\mathbf{k}-\mathbf{k}'}^{cvvc}$ was evaluated on a 200×200 grid with $\Delta k = 3.125 \cdot 10^{-3}$ Å. Due to the angular dependence of the Coulomb matrix element, states with different angular momentum quantum numbers m are nondegenerate. For the position operator we used $\hat{\mathbf{r}} = i\nabla_{\mathbf{k}}$ and $\nabla_{\mathbf{k}}^2 \psi_{nm}(k) = \frac{1}{\sqrt{k}}\left(\frac{\partial^2}{\partial k^2} + \frac{1-4m^2}{4k^2}\right)\tilde{\psi}_{nm}(k)$. The second-order derivative was discretized according to $\left(\frac{\partial^2}{\partial k^2}\right)_{ij} = \frac{\delta_{i+1,j} - 2\delta_{i,j} + \delta_{i,j+1}}{\Delta k^2}$.
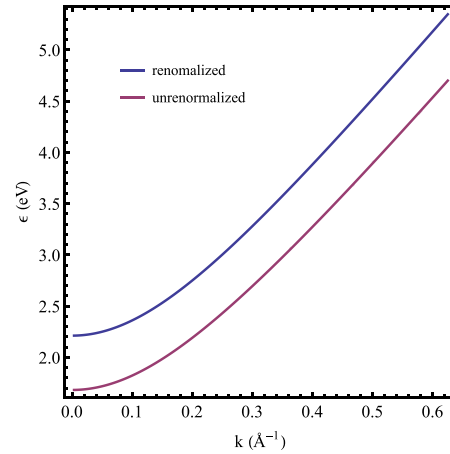

FIG. 6. Left: Ratio of the gap and dispersion before and after renormalization. Right: Quasi-particle dispersion in the vicinity of the K-points before and after renormalization.

[1] K. F. Mak, C. Lee, J. Hone, J. Shan, and T. F. Heinz, Phys. Rev. Lett. **105**, 136805 (2010).

[2] A. Splendiani, L. Sun, Y. Zhang, T. Li, J. Kim, C.-Y. Chim, G. Galli, and F. Wang, Nano Lett. **10**, 1271 (2010).

[3] C. Zhang, H. Wang, W. Chan, C. Manolatou, and F. Rana, Phys. Rev. B **89**, 205436 (2014).

[4] Y. Ding, Y. Wang, J. Ni, L. Shi, S. Shi, and W. Tang, Physica B **406**, 2254 (2011).

[5] D. Y. Qiu, F. H. da Jornada, and S. G. Louie, Phys. Rev. Lett. **111**, 216805 (2013).

[6] K. S. Novoselov, A. Mishchenko, A. Carvalho, and A. H. Castro Neto, Science **353**, 6298 (2016).

[7] T. Cheiwchanchamnangij and W. R. L. Lambrecht, Phys. Rev. B **85**, 205302 (2012).

[8] D. Xiao, G.-B. Liu, W. Feng, X. Xu, and W. Yao, Phys. Rev. Lett. **108**, 196802 (2012).

[9] A. Molina-Sanchez, D. Sangalli, K. Hummer, A. Marini, and L. Wirtz, Phys. Rev. B **88**, 045412 (2013).

[10] J. R. Schaibley, H. Yu, G. Clark, P. Rivera, J. S. Ross, K. L. Seyler, W. Yao, and X. Xu, Nat. Rev. Mater. **1**, 16055 (2016).

[11] M. M. Ugeda, A. J. Bradley, S.-F. Shi, F. H. da Jornada, Y. Zhang, D. Y. Qiu, W. Ruan, S.-K. Mo, Z. Hussain, Z.-X. Shen, F. Wang, S. G. Louie, and M. F. Crommie, Nat. Mater. **13**, 1091 (2014).

[12] A. Chernikov, C. Ruppert, H. M. Hill, A. F. Rigosi, and T. F. Heinz, Nat. Photonics **9**, 466 (2015).

[13] S. Ulstrup, A. G. Cabo, J. A. Miwa, J. M. Riley, S. S. Grønborg, J. C. Johannsen, C. Cacho, O. Alexander, R. T. Chapman, E. Springate, M. Bianchi, M. Dendzik, J. V. Lauritsen, P. D. C. King, and P. Hofmann, ACS Nano **10**, 6315 (2016).

[14] A. Steinhoff, M. Rösner, F. Jahnke, T. O. Wehling, and C. Gies, Nano L **14**, 3743 (2014).

[15] L. Meckbach, T. Stroucken, and S. W. Koch, Appl. Phys. Lett. **112**, 061104 (2018).

[16] L. Meckbach, J. Hader, U. Huttner, J. Neuhaus, J. T. Steiner, T. Stroucken, J. V. Moloney, and S. W. Koch, Phys. Rev. B **101**, 075401 (2020).

[17] A. Chernikov, T. C. Berkelbach, H. M. Hill, A. Rigosi, Y. Li, O. B. Aslan, D. R. Reichman, M. S. Hybertsen, and T. F. Heinz, Phys. Rev. Lett. **113**, 076802 (2014).

[18] K. He, N. Kumar, L. Zhao, Z. Wang, K. F. Mak, H. Zhao, and J. Shan, Phys. Rev. Lett. **113**, 026803 (2014).

[19] Z. Ye, T. Cao, O. K., H. Zhu, X. Yin, Y. Wang, S. G. Louie, and X. Zhang, Nature (London) **513**, 214 (2014).

[20] B. Zhu, X. Chen, and X. Cui, Sci. Rep. **5**, 9218 (2015).

[21] L. Meckbach, T. Stroucken, and S. W. Koch, Phys. Rev. B **97**, 035425 (2018).

[22] G. Wang, A. Chernikov, M. M. Glazov, T. F. Heinz, X. Marie, T. Amand, and B. Urbaszek, Rev. Mod. Phys. **90**, 021001 (2018).

[23] K. F. Mak and J. Shan, Nat. Photonics **10**, 216 (2016).

[24] J. Xiao, M. Zhao, Y. Wang, and X. Zhang, Nanophotonics **6**, 1309 (2017).

[25] M. Goryca, J. Li, A. V. Stier, T. Taniguchi, K. Watanabe, E. Courtade, S. Shree, C. Robert, B. Urbaszek, X. Marie, and S. A. Crooker, Nat. Commun. **10**, 4172 (2019).

[26] S. Brem, M. Selig, G. Berghaeuser, and E. Malic, Sci. Rep. **8**, 8238 (2018).

[27] C. Gies and A. Steinhoff, Laser Photonics Rev. **15**, 2000482 (2021).

[28] C. Poellmann, P. Steinleitner, U. Leierseder, P. Nagler, G. Plechinger, M. Porer, R. Bratschitsch, C. Schüller, T. Korn, and R. Huber, Nat. Mater. **14**, 889 (2015).

[29] S. Cha, J. H. Sung, S. Sim, J. Park, H. Heo, M.-H. Jo, and H. Choi, Nat. Commun. **7**, 10768 (2016).

[30] P. Steinleitner, P. Merkl, P. Nagler, J. Mornhinweg, C. Schüller, T. Korn, A. Chernikov, and R. Huber, Nano Lett. **17**, 1455 (2017).

[31] R. A. Kaindl, M. A. Carnahan, D. Hägele, R. Lövenich, and D. S. Chemla, Nature (London) **423**, 734 (2003).

[32] M. Kira, W. Hoyer, and S. W. Koch, Solid State Commun. **129**, 733 (2004).

[33] S. W. Koch, M. Kira, G. Khitrova, and H. M. Gibbs, Nat. Mater. **5**, 523 (2006).

[34] M. Kira and S. W. Koch, Prog. Quantum Electron. **30**, 155 (2006).

[35] A. V. Stier, K. M. McCreary, B. T. Jonker, J. Kono, and S. A. Crooker, Nat. Commun. **7**, 10643 (2016).

[36] J. Zipfel, J. Holler, A. A. Mitioglu, M. V. Ballottin, P. Nagler, A. V. Stier, T. Taniguchi, K. Watanabe, S. A. Crooker, P. C. M. Christianen, T. Korn, and A. Chernikov, Phys. Rev. B **98**, 075438 (2018).

[37] A. V. Stier, N. P. Wilson, K. A. Velizhanin, J. Kono, X. Xu, and S. A. Crooker, Phys. Rev. Lett. **120**, 057405 (2018).

[38] E. Liu, J. van Baren, T. Taniguchi, K. Watanabe, Y.-C. Chang, and C. H. Lui, Phys. Rev. B **99**, 205420 (2019).

[39] G. Aivazian, Z. Gong, A. M. Jones, R.-L. Chu, J. Yan, D. G. Mandrus, C. Zhang, D. Cobden, W. Yao, and X. Xu, Nat. Phys. **11**, 148 (2015).

[40] A. Srivastava, M. Sidler, A. V. Allain, D. S. Lembke, A. Kis, and A. Imamoğlu, Nat. Phys. **11**, 141 (2015).

[41] A. Spiridonova, Phys. Lett. A **384**, 126850 (2020).

[42] Y. Li, J. Ludwig, T. Low, A. Chernikov, X. Cui, G. Arefe, Y. D. Kim, A. M. van der Zande, A. Rigosi, H. M. Hill, S. H. Kim, J. Hone, Z. Li, D. Smirnov, and T. F. Heinz, Phys. Rev. Lett. **113**, 266804 (2014).

[43] D. MacNeill, C. Heikes, K. F. Mak, Z. Anderson, A. Kormányos, V. Zólyomi, J. Park, and D. C. Ralph, Phys. Rev. Lett. **114**, 037401 (2015).

[44] G. Plechinger, P. Nagler, A. Arora, A. Granados del Águila, M. V. Ballottin, T. Frank, P. Steinleitner, M. Gmitra, J. Fabian, P. C. M. Christianen, R. Bratschitsch, C. Schüller, and T. Korn, Nano Lett. **16**, 7899 (2016).

[45] D. V. Rybkovskiy, I. C. Gerber, and M. V. Durnev, Phys. Rev. B **95**, 155406 (2017).

[46] M. Van der Donck, M. Zarenia, and F. M. Peeters, Phys. Rev. B **97**, 081109(R) (2018).

[47] M. Koperski, M. R. Molas, A. Arora, K. Nogajewski, M. Bartos, J. Wyzula, D. Vaclavkova, P. Kossacki, and M. Potemski, 2D Mater. **6**, 015001 (2018).

[48] F. Xuan and S. Y. Quek, Phys. Rev. Res. **2**, 033256 (2020).

[49] M. Van der Donck, M. Zarenia, and F. M. Peeters, Phys. Rev. B **97**, 195408 (2018).

[50] W. Kohn and L. J. Sham, Phys. Rev. **140**, A1133 (1965).

[51] G. Kresse and J. Hafner, Phys. Rev. B **47**, 558 (1993).

[52] G. Kresse and J. Hafner, Phys. Rev. B **49**, 14251 (1994).

[53] G. Kresse and J. Furthmüller, Comp. Mater. Sci. **6**, 15 (1996).

[54] J. P. Perdew, K. Burke, and M. Ernzerhof, Phys. Rev. Lett. **77**, 3865 (1996).

[55] S. Steiner, S. Khmelevskyi, M. Marsmann, and G. Kresse, Phys. Rev. B **93**, 224425 (2016).

[56] J. Neuhaus, S. C. Liebscher, L. Meckbach, T. Stroucken, and S. W. Koch, J. Phys. Condens. Matter **33**, 035301 (2020).

[57] T. Stroucken and S. W. Koch, in *Optical Properties of Graphene*, edited by R. Binder (World Scientific Publishing, Singapore, 2017), Chap. 2, pp. 43–84.

[58] S.-Y. Chen, Z. Lu, T. Goldstein, J. Tong, A. Chaves, J. Kunstmann, L. S. R. Cavalcante, T. Woźniak, G. Seifert, D. R. Reichman, T. Taniguchi, K. Watanabe, D. Smirnov, and J. Yan, Nano Lett. **19**, 2464 (2019).

[59] Wolfram Research, Inc., Mathematica, Version 12.3.1 (Champaign, IL, 2021).

Paper III

L. Meckbach, J. Hader, U. Huttner, J. Neuhaus, J. T. Steiner, T. Stroucken, J. V. Moloney, and S. W. Koch:

Ultrafast band-gap renormalization and build-up of optical gain in monolayer MoTe$_2$

Abstract: The dynamics of band-gap renormalization and gain build-up in monolayer MoTe$_2$-H is investigated by evaluating the nonequilibrium Dirac-Bloch equations with the incoherent carrier-carrier and carrier-phonon scattering treated via quantum-Boltzmann type scattering equations. For the case where an approximately 300-fs-long high-intensity optical pulse generates charge-carrier densities in the gain regime, the strong Coulomb coupling leads to a relaxation of excited carriers on a few-femtosencond timescale. The pump-pulse generation of excited carriers induces a large band-gap renormalization during the timescale of the pulse. Efficient phonon coupling leads to a subsequent carrier thermalization within a few picoseconds, which defines the timescale for the optical gain build-up energetically close to the low-density exciton resonance.

Ultrafast band-gap renormalization and build-up of optical gain in monolayer MoTe₂

L. Meckbach,[1] J. Hader,[2] U. Huttner,[1] J. Neuhaus,[1] J. T. Steiner,[1] T. Stroucken ⓞ,[1,*] J. V. Moloney,[2] and S. W. Koch[1]

[1]*Department of Physics and Material Sciences Center, Philipps University Marburg, Renthof 5, D-35032 Marburg, Germany*
[2]*Wyant College of Optical Sciences, University of Arizona, 1630 East University Boulevard, Tucson, Arizona 85721, USA*

The dynamics of band-gap renormalization and gain build-up in monolayer MoTe₂-H is investigated by evaluating the nonequilibrium Dirac-Bloch equations with the incoherent carrier-carrier and carrier-phonon scattering treated via quantum-Boltzmann type scattering equations. For the case where an approximately 300-fs-long high-intensity optical pulse generates charge-carrier densities in the gain regime, the strong Coulomb coupling leads to a relaxation of excited carriers on a few-femtosecond timescale. The pump-pulse generation of excited carriers induces a large band-gap renormalization during the timescale of the pulse. Efficient phonon coupling leads to a subsequent carrier thermalization within a few picoseconds, which defines the timescale for the optical gain build-up energetically close to the low-density exciton resonance.

I. INTRODUCTION

Monolayers (MLs) of transition-metal dichalcogenides (TMDCs) hold great promise as active material in next-generation optoelectronic devices. Unlike their bulk counterparts, MLs of many semiconducting TMDCs exhibit a direct gap with transition energies in the visible to near-infrared regime [1–7]. As compared to conventional semiconductors, they provide strong light-matter coupling and many-body effects due to carrier confinement and weak intrinsic screening of the Coulomb interaction. At low excitation levels, the electron-hole attraction leads to the formation of excitons with large binding energies that absorb as much as 10–20% of the incoming light for a single layer [8–11]. Because of this strong light-matter interaction, TMDC-based photonic devices promise high efficiency and have the potential for saturable absorbers, nanoemitters or nanolasers with the smallest possible amount of optically active material. Indeed, room temperature lasing has been reported for different TMDC materials for comparatively low pump intensities and emission frequencies centering around the respective A exciton resonances [12–14].

One of the key properties for operation and design of nanophotonic devices is the quasiparticle or optical band gap. Due to Coulombic renormalizations, the quasiparticle gap is modified by the presence of excited carriers and depends on the precise excitation conditions. In a conventional semiconductor where screening is strong, these band-gap renormalizations are typically in the meV range. In contrast, in TMDCs excitation-induced band-gap shrinkages of several hundred meV have been reported in experimental [15,16] and theoretical [17,18] investigations. The injection of external charge carriers has been proposed as a possibility to dynamically control the optical gap on a femtosecond timescale [15,16]. Furthermore, carrier-carrier and carrier-phonon scattering lead to

excitation-induced dephasing and the build-up of screening, thus dynamically modifying the exciton binding and peak gain positions. In particular, for laser applications precise predictions for the peak gain are desirable to design optical cavities correspondingly.

In this paper, we use the example of MoTe₂-H to perform a microscopic calculation of the carrier dynamics and optical gain development after nonresonant optical excitation. Among semiconducting TMDC materials, MoTe₂-H provides the most favourable conditions to achieve optical plasma gain. Whereas in W-based TMDCs the fundamental gap corresponds to spin-forbidden, dark transitions, in MoTe₂-H, for each spin component, the fundamental gap is undoubtedly direct with a relatively large spin splitting and offset between the side and global minima in the conduction band. Without such an offset substantial amounts of electrons can leak quickly from the K/K′-points to the side valley. This reduces the carrier inversion at the global band minima and reduces or even prevents optical gain.

A well-established scheme to deduce the carrier dynamics and its influence on the optical spectra is to probe the optical response of the system at different delay times after excitation with a strong optical pump pulse. To simulate such a scenario, we extend our recently developed Dirac-Bloch equation (DBE) scheme [18–21] beyond the linear low-excitation and quasiequilibrium regime. In particular, we include incoherent interactions due to electron-electron and electron-phonon scattering to study the carrier dynamics and to determine the dephasing of the optical polarizations and the resulting broadening of optical spectra self-consistently.

II. METHODS

To compute the carrier dynamics and its influence on the optical spectra, we use a hybrid density functional theory (DFT) and equation of motion (EOM) approach. In a first step, we determine the relevant material parameters, i.e.,

*tineke.stroucken@physik.uni-marburg.de

TABLE I. Material parameters for MoTe$_2$-H, i.e., the conduction-band (valence-band) valley minima (maxima) ϵ_K^c and ϵ_Σ^c (ϵ_K^v), effective masses m_K^* and m_Σ^*, dipole-matrix elements $d_K^\pm$, as well as the dielectric constants $\epsilon_\parallel^B$, $\epsilon_\perp$ and out-of-plane lattice constant D ($c/2$), based on our DFT calculations. For the K' and Λ valleys, the spin components are interchanged.

Spin	ϵ_K^c [eV]	ϵ_K^v [eV]	ϵ_Σ^c [eV]	m_K^* [m_0]	m_Σ^* [m_0]	$d_K^\pm$ [eÅ]	$\epsilon_\parallel^B$	$\epsilon_\perp$	D ($c/2$) [Å]
↑	1.017	0.0	1.114	0.607	0.407	3.51			
							20.30	10.90	6.99
↓	1.052	−0.214	1.099	0.728	0.428	2.88			

the band structure, dipole-matrix elements, as well as the dielectric constants of bulk MoTe$_2$-H, via density functional theory. To compute the carrier dynamics and evolution of the optical spectra on a dense **k**-grid, we use an effective four-band Hamiltonian that is based on the single-particle band structure and dipole-matrix elements derived from our DFT calculations to describe the regions of the Brillouin zone that are actually populated. Subsequently, we derive the EOM for interband polarizations that couple directly to the optical field, and the respective occupation probabilities of the involved bands. Since DFT-based band structure calculations usually underestimate the quasiparticle gap, we compute the ground-state band-gap renormalization self-consistently from the gap equations.

A. DFT calculations

The relevant material parameters are calculated via density functional theory (DFT) [22] using the Vienna *ab initio* simulation package (VASP) [23–26] and listed in Table I. All computations employ the generalized-gradient-approximation via the Perdew-Burke-Ernzerhof (PBE) functional [27], including the spin-orbit interaction [28]. The unit cell describing a MoTe$_2$-H ML contains three atoms in total, while a vacuum region of 20 Å around the ML is sufficient to prevent unphysical interactions with its periodic copies. The unit cell of bulk MoTe$_2$-H in the common 2H form, used in the computations of the bulk dielectric constant, consists of two MLs and contains six atoms. The Van-der-Waals interaction between neighboring layers is modeled via Grimme's dispersion correction method (PBE-D3) [29,30]. In both cases, bulk and ML, a full relaxation of atomic positions and the unit cell shape and size is performed until all inter-atomic forces are smaller than 2.5×10^{-3} eV/Å. The reciprocal space is sampled by a $15 \times 15 \times 3$ Monkhorst-Pack [31] k-mesh in the case of the ML and $10 \times 10 \times 10$ in the bulk case. The cutoff energy of the plane wave expansion is set to 750 eV for the structural relaxations and the MLs properties, while a value of 500 eV is used in the bulk case. The self-consistency cycle of the electronic minimization is repeated until an energy convergence criterion of 10^{-8} eV is reached.

The resulting ML band structure is shown in Fig. 1 and exhibits direct gaps at the K and K' points of the Brillouin zone with a noninteracting gap of $\Delta_A = 1.017$ eV and $\Delta_B = 1.266$ eV for the A ($K_\uparrow/K'_\downarrow$) and B ($K_\downarrow/K'_\uparrow$) bands. As in other TMDC materials, the atomic orbitals predominantly contributing to the valence and conduction bands at the K and K' point are the d-type Mo-orbitals with equal parity. Furthermore, the conduction bands display a spin splitting of -35 meV and side valleys at the Σ/Λ points, that are

97 meV ($\Sigma_\uparrow/\Lambda_\downarrow$) and 82 meV ($\Lambda_\uparrow/\Sigma_\downarrow$) above the respective K/K'-valley minima. These values are on the lower end of the range of published values that have been obtained using different functionals for the exchange correlation potential or GW corrections [32–34] and sufficiently large to prevent an excitation-induced transition from a direct to indirect band gap [35,36].

The interband dipole-matrix elements are accessed via the linear optics routine in VASP as described in Ref. [37] and include contributions associated with a geometric phase. Furthermore, we compute the macroscopic static dielectric tensor of bulk MoTe$_2$-H using density functional perturbation theory as described in Refs. [37,38], following Ref. [39].

B. DFT-based model Hamiltonian

To model the DFT band structure presented in the previous section, we include the two spin-split valence and conduction bands to obtain an effective four-band Hamiltonian. As the different valleys are separated by large barriers, intervalley scattering is expected to be significantly slower than intravalley scattering and, on the ultrashort timescale, the valley index can be considered to be approximately conserved. Hence, we
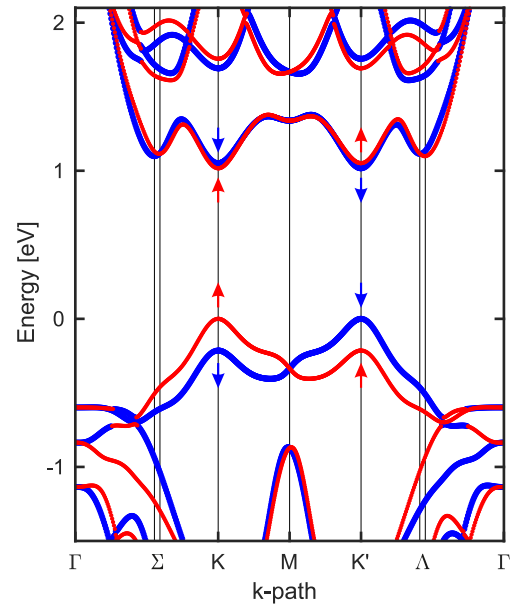

FIG. 1. DFT band structure of a MoTe$_2$-H ML. Bands with spin-up are depicted in red, bands with spin-down in blue.

TABLE II. Resulting MDF model parameters for MoTe$_2$-H.

Band	Δ [eV]	$\hbar v_F$ [eVÅ]	E_F [eV]
A	1.017	2.526	0.509
B	1.266	2.574	0.419

write the single particle part of the Hamiltonian as

$$H_0 = \sum_{\alpha\mathbf{k}} \epsilon_{\alpha\mathbf{k}} c_{\alpha\mathbf{k}}^\dagger c_{\alpha\mathbf{k}},$$

where α combines the spin, valley, and band index. Using the $\mathbf{p} \cdot \mathbf{A}$ gauge, the light matter interaction is given by

$$H_{\mathrm{LM}} = \frac{e}{m_0 c} \sum_{\alpha\alpha'\mathbf{k}} \mathbf{A} \cdot \mathbf{p}_{\alpha\alpha'\mathbf{k}} c_{\alpha\mathbf{k}}^\dagger c_{\alpha'\mathbf{k}},$$

where the interband momentum matrix elements are related to the DFT dipole matrix elements via $\frac{e\hbar}{m_0}\mathbf{p}_{\alpha\alpha'\mathbf{k}} = (\epsilon_{\alpha'\mathbf{k}} - \epsilon_{\alpha\mathbf{k}})\mathbf{d}_{\alpha\alpha'}$. Whereas the side valleys at Σ/Λ are modeled within the effective mass approximation, we treat the K and K' valleys utilizing the widely used massive Dirac-Fermion (MDF) model Hamiltonian [40] to account for the geometric phase contained in the dipole matrix elements. The MDF Hamiltonian has the relativistic dispersion

$$\epsilon_{i\mathbf{k}}^{c/v} = E_{F,i} \pm \frac{1}{2}\sqrt{\Delta_i^2 + (2\hbar v_{F,i} k)^2}, \tag{1}$$

where $i = s\tau$ combines the spin and valley index, Δ_i, $v_{F,i}$, and $E_{F,i}$ are the spin- and valley-dependent gap, Fermi velocity and Fermi level, respectively. Whereas the spin- and valley-dependent band gaps are directly taken from our DFT calculations, the Fermi-velocities of the A and B bands are determined to reproduce the DFT band structure around the K/K' points and listed in Table II. Within the MDF model, the nonvanishing dipole moments at the Dirac points are solely associated with the geometric phase or pseudospin. They are related to the Fermi velocity via $d_i^\pm = e\sqrt{2}\hbar v_{F,i}/\Delta_i$ and agree within less than 5% with the DFT dipole matrix elements. The approximated band structure is shown together with the DFT bands and the equilibrium carrier distributions at the delay time $\tau = 2.5$ ps in Fig. 2.

The Coulomb interaction Hamiltonian

$$H_C = \frac{1}{2}\sum_{\mathbf{q}\neq 0}\sum_{\alpha\alpha'\beta\beta'\mathbf{k}\mathbf{k}'} V_{\mathbf{q};\mathbf{k}';\mathbf{k}}^{\alpha\beta\beta'\alpha'} c_{\alpha\mathbf{k}-\mathbf{q}}^\dagger c_{\beta\mathbf{k}'+\mathbf{q}}^\dagger c_{\beta'\mathbf{k}'} c_{\alpha'\mathbf{k}}$$

contains the quasi-2D Coulomb matrix elements

$$V_{\mathbf{q};\mathbf{k}';\mathbf{k}}^{\alpha\beta\beta'\alpha'} = \int_{ec} d^3 r \int_{ec} d^3 r' \, u_{\alpha\mathbf{k}-\mathbf{q}}^*(\mathbf{r}) u_{\beta\mathbf{k}'+\mathbf{q}}^*(\mathbf{r}')$$
$$\times V_{\mathbf{q}}(z - z') u_{\beta'\mathbf{k}'}(\mathbf{r}') u_{\alpha'\mathbf{k}}(\mathbf{r})$$

that are computed using the DFT wave functions. The Coulomb interaction potential $V_{\mathbf{q}}(z - z')$ for the unexcited ML is determined from Poisson's equation according to Ref. [20]. Here, we use the parameters $\epsilon_\parallel$ and $\epsilon_\perp$ for the in- and out-of-plane dielectric constants based on bulk DFT calculations of MoTe$_2$-H. From the previously stated bulk in-plane dielectric constant $\epsilon_\parallel^B$ we obtained the nonresonant 2D contribution $\epsilon_\parallel = 15.32$ as described in Ref. [20]. The so determined "bare" Coulomb interaction potential contains screening contributions from the dielectric environment and all remote bands,
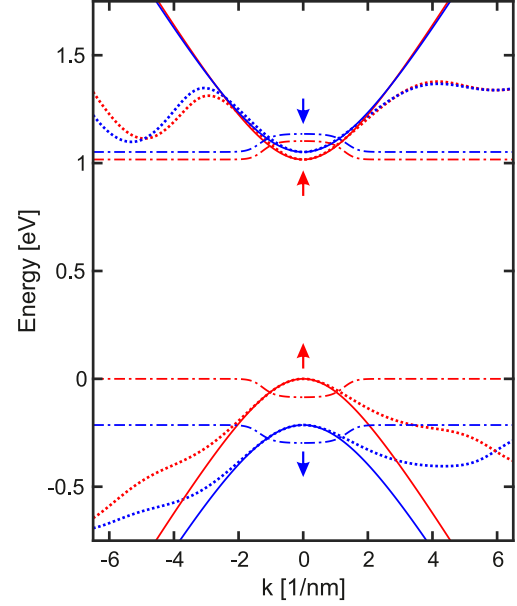

FIG. 2. Comparison of the relevant DFT bands (dotted) with the approximated unrenormalized relativistic band dispersion (solid). Arrows indicate the spin of the correspondingly colored bands. The dashed-dotted lines show the equilibrium carrier distributions (2.5 ps after excitation) for the excitation conditions discussed in the text. For the distributions the baseline is taken to be the edge of the corresponding band and the maximum values are set to be the corresponding chemical potentials.

as well as the ground-state screening contributions from the valence and conduction bands.

The interaction with longitudinal optical (LO) phonons, which has been shown to be the most effective phonon-coupling contribution in monolayer MoTe$_2$-H [41], is contained in the Fröhlich Hamiltonian

$$H_{\mathrm{e-LO}} = \sum_{\alpha\mathbf{k},\mathbf{q}} g_{\mathbf{q}}^0 c_{\alpha,\mathbf{k}+\mathbf{q}}^\dagger c_{\alpha,\mathbf{k}} (b_{\mathbf{q}} + b_{-\mathbf{q}}^\dagger).$$

For the "bare" Fröhlich-interaction matrix element $g_{\mathbf{q}}^0$, we use the explicit expression based on the analytical model of Sohier *et al.* [41] that, similarly to the "bare" Coulomb interaction, already contains background screening contributions from the remote bands and dielectric environment.

C. Dirac-Bloch Equations

To evaluate the material response after optical excitation, we compute the microscopic interband polarizations $P_{i\mathbf{k}} = \langle c_{iv\mathbf{k}}^\dagger c_{ic\mathbf{k}}\rangle$ and occupation probabilities $f_{i\mathbf{k}}^\lambda = \langle c_{i\lambda\mathbf{k}}^\dagger c_{i\lambda\mathbf{k}}\rangle$ ($\lambda = $ c, v) from the Dirac Bloch equations (DBE)

$$i\hbar \frac{d}{dt} P_{i\mathbf{k}} = (\Sigma_{i\mathbf{k}}^c - \Sigma_{i\mathbf{k}}^v) P_{i\mathbf{k}} + (f_{i\mathbf{k}}^v - f_{i\mathbf{k}}^c)\Omega_{i\mathbf{k}}$$
$$+ i\hbar \frac{d}{dt} P_{i\mathbf{k}}\Big|_{\mathrm{corr.}}, \tag{2}$$

$$i\hbar \frac{d}{dt} f_{i\mathbf{k}}^{c/v} = \pm 2i\Im[P_{i\mathbf{k}}\Omega_{i\mathbf{k}}^*] + i\hbar \frac{d}{dt} f_{i\mathbf{k}}^{c/v}\Big|_{\mathrm{corr.}}. \tag{3}$$

Here,

$$\Sigma_{i\mathbf{k}}^{\mathrm{c}} = \epsilon_{i c \mathbf{k}} - \sum_{\mathbf{k}'} \left[V_{\mathbf{k}-\mathbf{k}';\mathbf{k}';\mathbf{k}}^{\mathrm{cccc}} - V_{\mathbf{k}-\mathbf{k}';\mathbf{k}';\mathbf{k}}^{\mathrm{cvcv}} \right] f_{i\mathbf{k}'}^{\mathrm{c}}$$

$$+ \sum_{\mathbf{k}'} \left[V_{\mathbf{k}-\mathbf{k}';\mathbf{k}';\mathbf{k}}^{\mathrm{cvcc}} P_{i\mathbf{k}'} + c.c. \right], \quad (4)$$

$$\Sigma_{i\mathbf{k}}^{\mathrm{v}} = \epsilon_{i v \mathbf{k}} - \sum_{\mathbf{k}'} \left[V_{\mathbf{k}-\mathbf{k}';\mathbf{k}';\mathbf{k}}^{\mathrm{vvvv}} - V_{\mathbf{k}-\mathbf{k}';\mathbf{k}',\mathbf{k}}^{\mathrm{vcvc}} \right] f_{i\mathbf{k}'}^{\mathrm{v}}$$

$$+ \sum_{\mathbf{k}'} \left[V_{\mathbf{k}-\mathbf{k}';\mathbf{k}';\mathbf{k}}^{\mathrm{vvvc}} P_{i\mathbf{k}'} + c.c. \right], \quad (5)$$

$$\Omega_{i\mathbf{k}} = \frac{e}{m_0 c} \mathbf{A} \cdot \mathbf{p}_{icv\mathbf{k}} - \sum_{\mathbf{k}'} V_{\mathbf{k}-\mathbf{k}';\mathbf{k}';\mathbf{k}}^{\mathrm{cvvv}} \left(f_{i\mathbf{k}'}^{\mathrm{v}} - f_{i\mathbf{k}'}^{\mathrm{c}} \right)$$

$$- \sum_{\mathbf{k}'} \left[V_{\mathbf{k}-\mathbf{k}';\mathbf{k}';\mathbf{k}}^{\mathrm{cvvc}} P_{i\mathbf{k}'} + V_{\mathbf{k}-\mathbf{k}';\mathbf{k}';\mathbf{k}}^{\mathrm{ccvv}} P_{i\mathbf{k}'}^{*} \right] \quad (6)$$

contain the Hartree-Fock contributions to the single particle energy renormalizations $\Sigma_{i\mathbf{k}}^{\mathrm{c/v}}$ and the renormalization to the Rabi energy $\Omega_{i\mathbf{k}}$, while all many-body correlations that arise from the two-particle Coulomb interaction and carrier-phonon scattering are contained within $\frac{d}{dt} P_{i\mathbf{k}}|_{\mathrm{corr.}}$ and $\frac{d}{dt} f_{i\mathbf{k}}^{\mathrm{c/v}}|_{\mathrm{corr.}}$, respectively.

The DBE are formally equivalent to the semiconductor Bloch equations (SBE), but the expression for the renormalized Rabi and single particle energies differ by the Coulomb matrix elements of the type $V_{\mathbf{k}-\mathbf{k}';\mathbf{k}';\mathbf{k}}^{\mathrm{cvvv}}$ and $V_{\mathbf{k}-\mathbf{k}';\mathbf{k}';\mathbf{k}}^{\mathrm{ccvv}}$ referring to Auger- and pair creation/annihilation processes, where at least one of the particles changes its band index. Within the MDF model Hamiltonian, these Coulomb matrix elements contain the geometric phase and induce a coupling between a dark static interband polarization and the carrier populations. Consequently, the initial condition $f_{i\mathbf{k}}^{\mathrm{c}} = 1 - f_{i\mathbf{k}}^{\mathrm{v}} = P_{i\mathbf{k}} = 0$ does not correspond to a stationary solution of the DBE in the absence of an external field and hence, does not specify the system's ground state.

To determine the ground-state band renormalization, which is the initial state before the pump pulse arrives, we require a stationary solution of the Dirac-Bloch equations in the absence of an external field as described in Refs. [19,20,42]. This leads to the gap equations

$$\tilde{\Delta}_{i\mathbf{k}} = \Delta_i + \frac{1}{2} \sum_{\mathbf{k}'} V_{|\mathbf{k}-\mathbf{k}'|} \frac{\tilde{\Delta}_{i\mathbf{k}'}}{\tilde{\epsilon}_{i\mathbf{k}'}}, \quad (7)$$

$$\tilde{v}_{i\mathbf{k}} = v_{F,i} + \frac{1}{2} \sum_{\mathbf{k}'} V_{|\mathbf{k}-\mathbf{k}'|} \frac{k'}{k} \frac{\tilde{v}_{i\mathbf{k}'}}{\tilde{\epsilon}_{i\mathbf{k}'}} \cos(\theta_{\mathbf{k}} - \theta_{\mathbf{k}'}), \quad (8)$$

from which the ground-state quasiparticle dispersion is obtained via $\tilde{\epsilon}_{i\mathbf{k}}^{e/h} = \frac{1}{2} \sqrt{\tilde{\Delta}_{i\mathbf{k}}^2 + (2\hbar \tilde{v}_{i\mathbf{k}} k)^2}$. Similar to the Coulomb matrix elements $V_{\mathbf{q};\mathbf{k}';\mathbf{k}}^{\alpha\beta\beta'\alpha'}$, the "bare" quasi-2D Coulomb interaction entering Eqs. (7) and (8) already contains the previously mentioned background and ground-state screening contributions. The solution of the gap equations yields a rigid shift of the single-particle dispersion with an interacting gap $\tilde{\Delta}_{i\mathbf{k}}$ that depends on the dielectric environment. For a suspended ML, we find a ground-state band renormalization of 549 meV for the A band, that shrinks by 70 meV for a SiO$_2$-supported MoTe$_2$-H ML.

In the low density limit, where correlation effects can be neglected, we find the transition energies for the lowest 1s-
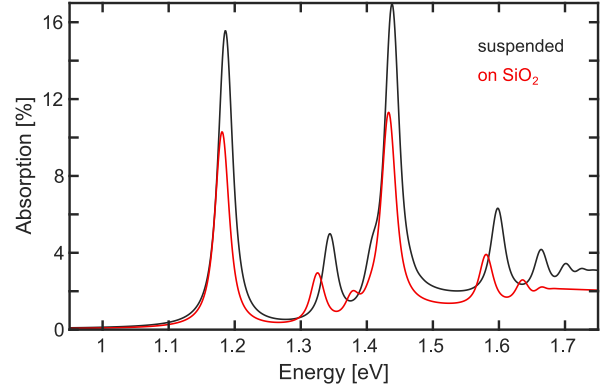

FIG. 3. Linear absorption spectra of a suspended (black) and SiO$_2$-supported (red) ML MoTe$_2$-H. Here, we used a phenomenological dephasing rate of $\hbar\gamma = 10$ meV. To match the experimentally observed data, the spectra have been shifted by -0.044 eV.

exciton resonance at 1.230 and 1.225 eV, for the suspended and SiO$_2$ supported MoTe$_2$-H ML, respectively, which is slightly above the experimentally observed low-temperature resonance energy of about 1.18 eV for the SiO$_2$-supported ML [43]. To allow for a direct comparison between the predicted excitation-induced modifications of the optical spectra with the experiment, we correct the bare DFT computed band gap and shift all spectra by -0.044 eV. The resulting linear absorption spectra for a freely suspended and quartz-supported MoTe$_2$-H ML are shown in Fig. 3 using a phenomenological dephasing rate of $\hbar\gamma = 10$ meV.

D. Many-body correlations

Incoherent processes that lead to the dephasing of the microscopic polarizations and to the carrier relaxation dynamics are contained within $\frac{d}{dt} P_{i\mathbf{k}}|_{\mathrm{corr.}}$ and $\frac{d}{dt} f_{i\mathbf{k}}^{\mathrm{c/v}}|_{\mathrm{corr.}}$, respectively. Using the notation $P_{\mathbf{k}}^{\alpha\alpha'} = \langle c_{\alpha\mathbf{k}}^\dagger c_{\alpha'\mathbf{k}} \rangle$, $f_{\mathbf{k}}^{\alpha} = P_{\mathbf{k}}^{\alpha\alpha}$ for the single-particle expectation values, the Coulomb interaction leads to a contribution

$$i\hbar \frac{d}{dt} P_{\mathbf{k}}^{\alpha\alpha'} \Big|_{\mathrm{corr.}}^{\mathrm{el.}} = \sum_{\mathbf{q}\neq 0} \left[\Delta I_{\mathbf{q};\mathbf{k}}^{\alpha\alpha'} - \left(\Delta I_{\mathbf{q};\mathbf{k}}^{\alpha'\alpha} \right)^* \right], \quad (9)$$

where

$$I_{\mathbf{q};\mathbf{k}}^{\alpha\alpha'} = \sum_{\beta\gamma\gamma'} \sum_{\mathbf{k}'} V_{-\mathbf{q};\mathbf{k}';\mathbf{k}-\mathbf{q}}^{\alpha'\gamma\gamma'\beta} C_{\mathbf{q};\mathbf{k}';\mathbf{k}}^{\alpha\gamma\gamma'\beta}$$

are the density-assisted transition/occupation probabilities that contain the two-particle expectation values $C_{\mathbf{q};\mathbf{k}';\mathbf{k}}^{\alpha\gamma\gamma'\beta} = \langle c_{\alpha\mathbf{k}}^\dagger c_{\gamma\mathbf{k}'-\mathbf{q}}^\dagger c_{\gamma'\mathbf{k}'} c_{\beta\mathbf{k}-\mathbf{q}} \rangle$. In general, the two-particle expectation values can be divided into a Hartree-Fock (singlet) part and a correlated part according to

$$C_{\mathbf{q};\mathbf{k}';\mathbf{k}}^{\alpha\gamma\gamma'\beta} = C_{\mathbf{q};\mathbf{k}';\mathbf{k}}^{\alpha\gamma\gamma'\beta} \Big|_S + \Delta C_{\mathbf{q};\mathbf{k}';\mathbf{k}}^{\alpha\gamma\gamma'\beta},$$

and it is easily verified that the Hartree-Fock contributions to the renormalized single particle energies and Rabi-energy given in Eqs. (4)–(6) correspond to the singlet part $I_{\mathbf{q};\mathbf{k}}^{\alpha\alpha'}|_S$.

Physically, $I_{\mathbf{q};\mathbf{k}}^{\alpha\alpha'}$ describes Coulomb mediated transitions from all initial states $\beta\mathbf{k} - \mathbf{q}$ to the final state $\alpha\mathbf{k}$ via the

intermediate states $\gamma \mathbf{k}' - \mathbf{q}$, $\gamma' \mathbf{k}'$ with the Coulomb matrix elements $V_{-\mathbf{q};\mathbf{k};\mathbf{k}-\mathbf{q}}^{\alpha'\gamma\gamma'\beta}$. As mentioned above, the Coulomb matrix elements with $\beta \neq \alpha'$ and/or $\gamma \neq \gamma'$ correspond to Auger recombinations and pair creation/annihilation processes. Whereas these processes give a small contribution to the static ground-state renormalization of the valence bands contained in the singlet parts, they are strongly nonresonant for the optically induced density dependent modifications contained in the correlated part. As verified numerically, the timescales for Auger recombinations and pair creation/annihilation processes are four to five orders of magnitude longer than those of intraband scattering processes and will be neglected in the following. Additionally neglecting the weak orbital and $\mathbf{k}$, $\mathbf{k}'$-dependence of the Coulomb matrix elements, the expression for the density-assisted transition/occupation probabilities simplifies to

$$I_{\mathbf{q};\mathbf{k}}^{\alpha\alpha'} = \tilde{V}_{\mathbf{q}} \langle c_{\alpha\mathbf{k}}^{\dagger} \rho_{\mathbf{q}} c_{\alpha'\mathbf{k}-\mathbf{q}} \rangle,$$

where $\tilde{V}_{\mathbf{q}}$ is a quasi-2D Coulomb matrix element that again contains ground-state and background screening contributions only and $\rho_{\mathbf{q}} = \sum_{\beta\mathbf{k}'} c_{\beta\mathbf{k}'-\mathbf{q}}^{\dagger} c_{\beta\mathbf{k}'}$ is the density operator.

To derive an approximation for the correlated part of the density-assisted transition amplitudes, we employ a second-order cluster expansion where we derive the EOM for the relevant two-particle correlations and factorize the occurring three-particle expectation values into singlet and doublet contributions [44]. Within this approximation, the singlet factorizations act as source terms for the two-particle correlations, whereas the doublet contributions lead to a renormalization of the single-particle energies, excitonic correlations, biexcitons, and screening of the Coulomb interaction in the Hartree-Fock contributions. Assuming screening to be the dominant correlation effect at elevated densities, we write the EOM for the relevant two-particle correlations as

$$i\hbar \frac{d}{dt} \Delta C_{\mathbf{q};\mathbf{k}';\mathbf{k}}^{\alpha\beta\beta\alpha'} = \left(\Delta \Sigma_{\mathbf{q};\mathbf{k}';\mathbf{k}}^{\alpha\beta\beta\alpha'} - i\hbar\gamma_T \right) \Delta C_{\mathbf{q};\mathbf{k}';\mathbf{k}}^{\alpha\beta\beta\alpha'}$$
$$+ \left(f_{\mathbf{k}'-\mathbf{q}}^{\beta} - f_{\mathbf{k}'}^{\beta} \right) I_{\mathbf{q},\mathbf{k}}^{\alpha\alpha'} + S_{\mathbf{q};\mathbf{k}';\mathbf{k}}^{\alpha\beta\beta\alpha'}$$
$$+ \text{remaining doublets}, \qquad (10)$$

where we explicitly quoted only the doublet correlations that lead to the build-up of screening, $\Delta\Sigma_{\mathbf{q};\mathbf{k}';\mathbf{k}}^{\alpha\beta\beta\alpha'} = \Sigma_{\alpha'\mathbf{k}-\mathbf{q}} + \Sigma_{\beta\mathbf{k}'} - \Sigma_{\beta\mathbf{k}'-\mathbf{q}} - \Sigma_{\alpha\mathbf{k}}$, and included a phenomenological dephasing of the triplets γ_T. Note that in Eq. (10), the density assisted transition probabilities $I_{\mathbf{q},\mathbf{k}}^{\alpha\alpha'}$ contain both the singlet and correlated part and the remaining singlet sources are contained in $S_{\mathbf{q};\mathbf{k}';\mathbf{k}}^{\alpha\beta\beta\alpha'}$. Using the shorthand notation $\bar{f}_{\mathbf{k}}^{\beta} = 1 - f_{\mathbf{k}}^{\beta}$, the singlet sources are explicitly given by

$$S_{\mathbf{q};\mathbf{k}';\mathbf{k}}^{\alpha\beta\beta\alpha'} = \tilde{V}_{\mathbf{q}} \left(P_{\mathbf{k}}^{\alpha\alpha'} f_{\mathbf{k}'-\mathbf{q}}^{\beta} \bar{f}_{\mathbf{k}'}^{\beta} - P_{\mathbf{k}-\mathbf{q}}^{\alpha\alpha'} \bar{f}_{\mathbf{k}'-\mathbf{q}}^{\beta} f_{\mathbf{k}'}^{\beta} \right)$$
$$+ \tilde{V}_{\mathbf{k}-\mathbf{k}'} P_{\mathbf{k}}^{\alpha\beta} \sum_{\gamma} P_{\mathbf{k}'-\mathbf{q}}^{\beta\gamma} \left(P_{\mathbf{k}-\mathbf{q}}^{\gamma\alpha'} - \delta_{\gamma\alpha'} \right)$$
$$- \tilde{V}_{\mathbf{k}-\mathbf{k}'} P_{\mathbf{k}'}^{\alpha\beta} \sum_{\gamma} P_{\mathbf{k}-\mathbf{q}}^{\gamma\alpha'} \left(P_{\mathbf{k}'-\mathbf{q}}^{\beta\gamma} - \delta_{\gamma\beta} \right)$$
$$+ \tilde{V}_{\mathbf{k}-\mathbf{k}'} \left(P_{\mathbf{k}'-\mathbf{q}}^{\beta\alpha'} - P_{\mathbf{k}-\mathbf{q}}^{\beta\alpha'} \right) \sum_{\gamma} P_{\mathbf{k}}^{\alpha\gamma} P_{\mathbf{k}'}^{\gamma\beta} \qquad (11)$$

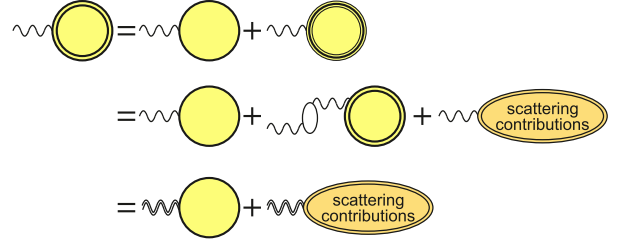and treated on the level of a second Born approximation.

FIG. 4. Diagrammatic representation of the density assisted transition/occupation probabilities. The full density assisted transition amplitudes are represented by twofold contoured circles whereas the singlet and correlated parts are represented by simple and threefold contoured circles, respectively. Similarly, simple and doubly contoured wiggles represent the "bare" and screened Coulomb interaction, respectively. The upper line corresponds to the division into the singlet (Hartree-Fock) and correlated part and the second and third lines represent the first and second line of Eq. (12).

If one assumes quasistatic single-particle distributions $f_{\mathbf{k}}^{\beta}$ and neglects the remaining doublet contributions, then one can analytically solve Eq. (10) in frequency space [44]. A subsequent summation over β and $\mathbf{k}'$ yields the closed expression

$$I_{\mathbf{q};\mathbf{k}}^{\alpha\alpha'}(\omega) = I_{\mathbf{q};\mathbf{k}}^{\alpha\alpha'}(\omega)\big|_S + \tilde{V}_{\mathbf{q}} \Pi_{\mathbf{q};\mathbf{k}}^{\alpha\alpha'}(\omega + i\gamma_T) I_{\mathbf{q},\mathbf{k}}^{\alpha\alpha'}(\omega)$$
$$+ \tilde{V}_{\mathbf{q}} T_{\mathbf{q};\mathbf{k}}^{\alpha\alpha'}(\omega)$$
$$= W_{\mathbf{q};\mathbf{k}}^{\alpha\alpha'}(\omega + i\gamma_T) \sum_{\beta\mathbf{k}'} C_{\mathbf{q};\mathbf{k}';\mathbf{k}}^{\alpha\beta\beta\alpha'}(\omega)\big|_S$$
$$+ W_{\mathbf{q};\mathbf{k}}^{\alpha\alpha'}(\omega + i\gamma_T) T_{\mathbf{q};\mathbf{k}}^{\alpha\alpha'}(\omega), \qquad (12)$$

where the screened Coulomb matrix element $W_{\mathbf{q};\mathbf{k}}^{\alpha\alpha'}$ is given by Dyson's equation

$$W_{\mathbf{q};\mathbf{k}}^{\alpha\alpha'}(\omega) = \tilde{V}_{\mathbf{q}} + \tilde{V}_{\mathbf{q}} \Pi_{\mathbf{q};\mathbf{k}}^{\alpha\alpha'}(\omega) W_{\mathbf{q};\mathbf{k}}^{\alpha\alpha'}(\omega)$$

and

$$\Pi_{\mathbf{q};\mathbf{k}}^{\alpha\alpha'}(\omega) = \Pi_{\mathbf{q}}(\omega + (\Sigma_{\alpha\mathbf{k}} - \Sigma_{\alpha'\mathbf{k}-\mathbf{q}})/\hbar),$$
$$\Pi_{\mathbf{q}}(\omega) = \sum_{\beta\mathbf{k}'} \frac{f_{\mathbf{k}'-\mathbf{q}}^{\beta} - f_{\mathbf{k}'}^{\beta}}{\hbar\omega + \Sigma_{\beta\mathbf{k}'-\mathbf{q}} - \Sigma_{\beta\mathbf{k}'}}$$

is the standard Lindhard polarization function. Furthermore, we define

$$T_{\mathbf{q};\mathbf{k}}^{\alpha\alpha'}(\omega) = \sum_{\beta\mathbf{k}'} \frac{S_{\mathbf{q};\mathbf{k}';\mathbf{k}}^{\alpha\beta\beta\alpha'}(\omega)}{\hbar\omega - \Delta\Sigma_{\mathbf{q};\mathbf{k}';\mathbf{k}}^{\alpha\beta\beta\alpha'} + i\hbar\gamma_T}.$$

Hence, the doublet contributions explicitly written in Eq. (10) lead to screening of the Coulomb potential both in the Hartree-Fock and scattering contributions, as shown schematically in Fig. 4. Note that at this level of approximation, the energy denominators in the scattering integrals and Lindhard polarization function still contain the unscreened Hartree-Fock renormalizations. However, it can be shown that screening in these contributions is introduced by the inclusion of the next level cluster expansion [44] and we will replace all unscreened energy renormalizations $\Sigma_{\mathbf{k}}^{\alpha}$ by their screened counterparts $\tilde{\Sigma}_{\mathbf{k}}^{\alpha}$ in the following.

If one would neglect the remaining scattering integrals contained in $\sum_{\mathbf{q}} W_{\mathbf{q};\mathbf{k}}^{\alpha\alpha'} T_{\mathbf{q};\mathbf{k}}^{\alpha\alpha'}$, then one would thus arrive at the level of the screened Hartree-Fock approximation where all the Coulomb matrix elements in Eqs. (4)–(6) are replaced by their screened counterparts. The remaining scattering contributions predominantly lead to carrier relaxation and excitation-induced dephasing of the coherent interband polarization. They contain only small additional renormalizations of the single-particle dispersion. Hence, the screened Hartree-Fock renormalizations of the single-particle energies provide a useful measure for the band-gap renormalization in the presence of excited carriers. In particular, in a fully incoherent quasistatic equilibrium situation, a steady state solution of the screened DBE equations yields the density-dependent gap equations

$$\tilde{\Delta}_{i\mathbf{k}} = \Delta_i + \frac{1}{2}\sum_{\mathbf{k}'} W_{|\mathbf{k}-\mathbf{k}'|}\frac{\tilde{\Delta}_{i\mathbf{k}'}}{\tilde{\epsilon}_{i\mathbf{k}'}}\big(f_{i\mathbf{k}'}^{\mathrm{v}} - f_{i\mathbf{k}'}^{\mathrm{c}}\big), \qquad (13)$$

$$\tilde{v}_{i\mathbf{k}} = v_{F,i} + \frac{1}{2}\sum_{\mathbf{k}'} W_{|\mathbf{k}-\mathbf{k}'|}\frac{k'}{k}\frac{\tilde{v}_{i\mathbf{k}'}}{\tilde{\epsilon}_{i\mathbf{k}'}}\cos(\theta_{\mathbf{k}} - \theta_{\mathbf{k}'})\big(f_{i\mathbf{k}'}^{\mathrm{v}} - f_{i\mathbf{k}'}^{\mathrm{c}}\big), \qquad (14)$$

where $W_{\mathbf{q}}$ is the statically screened Coulomb interaction.

Equation (12) together with Eq. (11) provides an efficient scheme to compute the Coulomb correlations numerically. As a consequence of the strong Coulomb interaction in TMDCs and the large associated exciton binding, it is important to properly include the full frequency dependence of the screened interband matrix elements $W_{\mathbf{q};\mathbf{k}}^{\mathrm{vc}}$ which enter the scattering contributions of the microscopic polarizations and lead to memory effects beyond the Markov approximation.

In addition to the Coulomb correlations, the inclusion of the Fröhlich Hamiltonian introduces the scattering of excited charge carriers within their bands by the absorption or emission of LO phonons. These are evaluated on the level of quantum-kinetic theory in second Born approximation. Our analysis shows that, similarly as for the Coulombic scattering rates, it is sufficient to treat the phonon scattering rates of the quasistatic carrier distribution functions within the Markov approximation, whereas it is crucial to maintain the full frequency dependency for the polarization-phonon scattering rates. The resulting phononic contributions to the electron and polarization scattering rates are given by

$$\frac{d}{dt}f_{s\mathbf{k}}^{\mathrm{c}}\bigg|_{\mathrm{corr.}}^{\mathrm{ph.}} = \frac{2\pi}{\hbar}\sum_{\mathbf{q}} g_{\mathbf{q}}^0 g_{\mathbf{q};\mathbf{k}+\mathbf{q}}^{\mathrm{cc}}\mathcal{D}_\eta\big(\tilde{\Sigma}_{s\mathbf{k}+\mathbf{q}}^{\mathrm{c}} - \tilde{\Sigma}_{s\mathbf{k}}^{\mathrm{c}} - \hbar\omega_{\mathbf{q}}\big)\big[(n_{\mathbf{q}}+1)f_{s\mathbf{k}+\mathbf{q}}^{\mathrm{c}}\bar{f}_{s\mathbf{k}}^{\mathrm{c}} - n_{\mathbf{q}}f_{s\mathbf{k}}^{\mathrm{c}}\bar{f}_{s\mathbf{k}+\mathbf{q}}^{\mathrm{c}}\big]$$

$$+ \frac{2\pi}{\hbar}\sum_{\mathbf{q}} g_{\mathbf{q}}^0 g_{\mathbf{q};\mathbf{k}}^{\mathrm{cc}}\mathcal{D}_\eta\big(\tilde{\Sigma}_{s\mathbf{k}-\mathbf{q}}^{\mathrm{c}} - \tilde{\Sigma}_{s\mathbf{k}}^{\mathrm{c}} + \hbar\omega_{\mathbf{q}}\big)\big[n_{\mathbf{q}}f_{s\mathbf{k}-\mathbf{q}}^{\mathrm{c}}\bar{f}_{s\mathbf{k}}^{\mathrm{c}} - (1+n_{\mathbf{q}})f_{s\mathbf{k}}^{\mathrm{c}}\bar{f}_{s\mathbf{k}-\mathbf{q}}^{\mathrm{c}}\big], \qquad (15)$$

$$\mathrm{i}\hbar\frac{d}{dt}P_{s\mathbf{k}}\bigg|_{\mathrm{corr.}}^{\mathrm{ph.}} = \mathrm{i}\hbar\frac{d}{dt}P_{s\mathbf{k}}\bigg|_{\mathrm{corr.}}^{\mathrm{c,ph.}} + \mathrm{i}\hbar\frac{d}{dt}P_{s\mathbf{k}}\bigg|_{\mathrm{corr.}}^{\mathrm{v,ph.}}, \qquad (16)$$

$$\mathrm{i}\hbar\frac{d}{dt}P_{s\mathbf{k}}\bigg|_{\mathrm{corr.}}^{\mathrm{c,ph.}} = \mathcal{F}\Bigg[\sum_{\mathbf{q}} g_{\mathbf{q}}^0 g_{\mathbf{q};\mathbf{k}}^{\mathrm{vc}}\left\{\frac{\bar{f}_{s\mathbf{k}-\mathbf{q}}^{\mathrm{c}}n_{\mathbf{q}} + f_{s\mathbf{k}-\mathbf{q}}^{\mathrm{c}}(1+n_{\mathbf{q}})}{\hbar(\omega+\omega_{\mathbf{q}}) + \tilde{\Sigma}_{s\mathbf{k}}^{\mathrm{v}} - \tilde{\Sigma}_{s\mathbf{k}-\mathbf{q}}^{\mathrm{c}} + \mathrm{i}\eta} + \frac{\bar{f}_{s\mathbf{k}-\mathbf{q}}^{\mathrm{c}}(1+n_{\mathbf{q}}) + f_{s\mathbf{k}-\mathbf{q}}^{\mathrm{c}}n_{\mathbf{q}}}{\hbar(\omega-\omega_{\mathbf{q}}) + \tilde{\Sigma}_{s\mathbf{k}}^{\mathrm{v}} - \tilde{\Sigma}_{s\mathbf{k}-\mathbf{q}}^{\mathrm{c}} + \mathrm{i}\eta}\right\}P_{s\mathbf{k}}$$

$$- \sum_{\mathbf{q}} g_{\mathbf{q}}^0 g_{\mathbf{q};\mathbf{k}+\mathbf{q}}^{\mathrm{vc}}\left\{\frac{\bar{f}_{s\mathbf{k}}^{\mathrm{c}}n_{\mathbf{q}} + f_{s\mathbf{k}}^{\mathrm{c}}(1+n_{\mathbf{q}})}{\hbar(\omega+\omega_{\mathbf{q}}) + \tilde{\Sigma}_{s\mathbf{k}+\mathbf{q}}^{\mathrm{v}} - \tilde{\Sigma}_{s\mathbf{k}}^{\mathrm{c}} + \mathrm{i}\eta} + \frac{\bar{f}_{s\mathbf{k}}^{\mathrm{c}}(1+n_{\mathbf{q}}) + f_{s\mathbf{k}}^{\mathrm{c}}n_{\mathbf{q}}}{\hbar(\omega-\omega_{\mathbf{q}}) + \tilde{\Sigma}_{s\mathbf{k}+\mathbf{q}}^{\mathrm{v}} - \tilde{\Sigma}_{s\mathbf{k}}^{\mathrm{c}} + \mathrm{i}\eta}\right\}P_{s\mathbf{k}+\mathbf{q}}\Bigg], \qquad (17)$$

$$\mathrm{i}\hbar\frac{d}{dt}P_{s\mathbf{k}}\bigg|_{\mathrm{corr.}}^{\mathrm{v,ph.}} = \mathcal{F}\Bigg[\sum_{\mathbf{q}} g_{\mathbf{q}}^0 g_{\mathbf{q};\mathbf{k}+\mathbf{q}}^{\mathrm{vc}}\left\{\frac{f_{s\mathbf{k}+\mathbf{q}}^{\mathrm{v}}n_{\mathbf{q}} + \bar{f}_{s\mathbf{k}+\mathbf{q}}^{\mathrm{v}}(1+n_{\mathbf{q}})}{\hbar(\omega+\omega_{\mathbf{q}}) + \tilde{\Sigma}_{s\mathbf{k}+\mathbf{q}}^{\mathrm{v}} - \tilde{\Sigma}_{s\mathbf{k}}^{\mathrm{c}} + \mathrm{i}\eta} + \frac{f_{s\mathbf{k}+\mathbf{q}}^{\mathrm{v}}(1+n_{\mathbf{q}}) + \bar{f}_{s\mathbf{k}+\mathbf{q}}^{\mathrm{v}}n_{\mathbf{q}}}{\hbar(\omega-\omega_{\mathbf{q}}) + \tilde{\Sigma}_{s\mathbf{k}+\mathbf{q}}^{\mathrm{v}} - \tilde{\Sigma}_{s\mathbf{k}}^{\mathrm{c}} + \mathrm{i}\eta}\right\}P_{s\mathbf{k}}$$

$$- \sum_{\mathbf{q}} g_{\mathbf{q}}^0 g_{\mathbf{q};\mathbf{k}}^{\mathrm{vc}}\left\{\frac{f_{s\mathbf{k}}^{\mathrm{v}}n_{\mathbf{q}} + \bar{f}_{s\mathbf{k}}^{\mathrm{v}}(1+n_{\mathbf{q}})}{\hbar(\omega+\omega_{\mathbf{q}}) + \tilde{\Sigma}_{s\mathbf{k}}^{\mathrm{v}} - \tilde{\Sigma}_{s\mathbf{k}-\mathbf{q}}^{\mathrm{c}} + \mathrm{i}\eta} + \frac{f_{s\mathbf{k}}^{\mathrm{v}}(1+n_{\mathbf{q}}) + \bar{f}_{s\mathbf{k}}^{\mathrm{v}}n_{\mathbf{q}}}{\hbar(\omega-\omega_{\mathbf{q}}) + \tilde{\Sigma}_{s\mathbf{k}}^{\mathrm{v}} - \tilde{\Sigma}_{s\mathbf{k}-\mathbf{q}}^{\mathrm{c}} + \mathrm{i}\eta}\right\}P_{s\mathbf{k}-\mathbf{q}}\Bigg], \qquad (18)$$

and a similar equation holds for the valence-band distribution functions. Here, $\pi\mathcal{D}_\eta(x) = \frac{\eta}{x^2+\eta^2}$ denotes the numerical energy-conserving function, $n_{\mathbf{q}}$ is the phonon occupation number, $\hbar\omega_{\mathbf{q}} = 27.72$ meV [41] is the corresponding LO-phonon energy, and $\mathcal{F}[f]$ denotes the Fourier transform of function f. The inclusion of the screened Fröhlich interaction $g_{\mathbf{q},\mathbf{k}}^{\alpha\alpha'}(\omega) = g_{\mathbf{q}}^0 + g_{\mathbf{q}}^0 \Pi_{\mathbf{q},\mathbf{k}}^{\alpha\alpha'}(\omega)g_{\mathbf{q},\mathbf{k}}^{\alpha\alpha'}(\omega)$ accounts for screening contributions arising from the excited charge carriers in addition to the background screening contributions of the remote bands and dielectric environment already included in $g_{\mathbf{q}}^0$. Thus, Coulomb and phonon-coupling matrix elements are treated on the same level of approximation.

III. NUMERICAL RESULTS

In this section, we present the results of our numerical analysis of the excitation dynamics and gain build-up in monolayer MoTe₂-H. As physical conditions, we assume a pump-probe scenario, where we consider a room-temperature ML of MoTe₂-H, which has been placed on a quartz substrate and is excited by a high-intensity linear-polarized optical pump pulse ($E_0 \sim 1.25$ MV/cm). The central pump frequency is chosen to be slightly above the interacting B-band gap and the pump pulse has a full width at half maximum (FWHM) of 333 fs corresponding to a photon density of 1.8×10^{15} cm^{-2}

(a pump fluence of 520 μJ/cm^2). For these excitation conditions, it is ensured that virtually all carriers are created in the K and K' valleys.

For the pump simulations, we solve the Dirac-Bloch Eqs. (2) and (3) in the time domain. The optically induced interband polarizations lead to the generation of excited charge carriers and the subsequent carrier relaxation dynamics is computed from the carrier-carrier and carrier-phonon scattering contributions, Eqs. (9)–(12) for $\alpha = \alpha'$ and Eq. (15), respectively. For the carrier dynamics, the numerically most important effect of the many-body correlations of the interband polarizations is the replacement of the "bare" Coulomb potential by its screened counterpart in the Hartree-Fock contributions, whereas the detailed excitation-induced dephasing of the interband polarizations play only a minor role. As verified numerically, it is sufficient to compute the carrier dynamics within the Markov approximation and the excitation-induced band-gap renormalization is determined from the density dependent gap Eqs. (13) and (14). They yield the renormalized single-particle bands wherein the excited carriers relax on the level of screened Hartree-Fock approximation. We then define the excitation-induced band-gap renormalization as the density-dependent change of the gaps between the spin-split renormalized single-particle bands relative to the respective gaps in the low-density limit.

For the probe pulse and for equilibrium configurations, we solve Eq. (2) in frequency domain via a matrix-inversion scheme, where the carrier distribution functions are quasistatic and we restrict ourselves to the terms linear in $P_{s\mathbf{k}}$ in the singlet sources. However, to predict the correct line shapes of the optical spectra, it turns out to be crucial to include the detailed and fully dynamical many-body correlations of the interband polarizations, Eqs. (9)–(12) for $\alpha/\alpha' = $ v/c and Eq. (16)–(18).

A. Carrier dynamics and band-gap renormalization

In Fig. 5(a), we plot the excitation and subsequent relaxation dynamics of the A-band electron distribution function $f^e_{A,\mathbf{k}}(t) = f^c_{A,\mathbf{k}}(t)$ in the vicinity of the K/K' points. Since conduction and valence bands with the same spin and valley indices have identical effective masses within the MDF model, the evolution of the hole distribution function $f^h_{A,\mathbf{k}}(t) = \bar{f}^v_{A,-\mathbf{k}}(t)$ is identical to that of the electrons. The excitation dynamics of the B-band distribution functions are similar and not shown here.

Due to the strong Coulomb interaction, carrier-carrier scattering is extremely efficient and drives the carrier distributions into hot quasiequilibrium distributions within a few femtoseconds. Here, the carrier temperature reaches $T = 2350$ K 10 fs after the pump maximum has interacted with the sample. This ultrafast carrier-carrier scattering quickly redistributes the pump injected carriers to energies near the band gap and away from the excitation energy, thus almost completely preventing the accumulation of carriers at the excitation energy and effectively removing the associated Pauli-blocking of the absorption during the excitation process. The result is a highly efficient generation of excited charge carriers which is limited only by the absorption coefficient of the unexcited layer. After the pump pulse has passed, we find a total carrier density
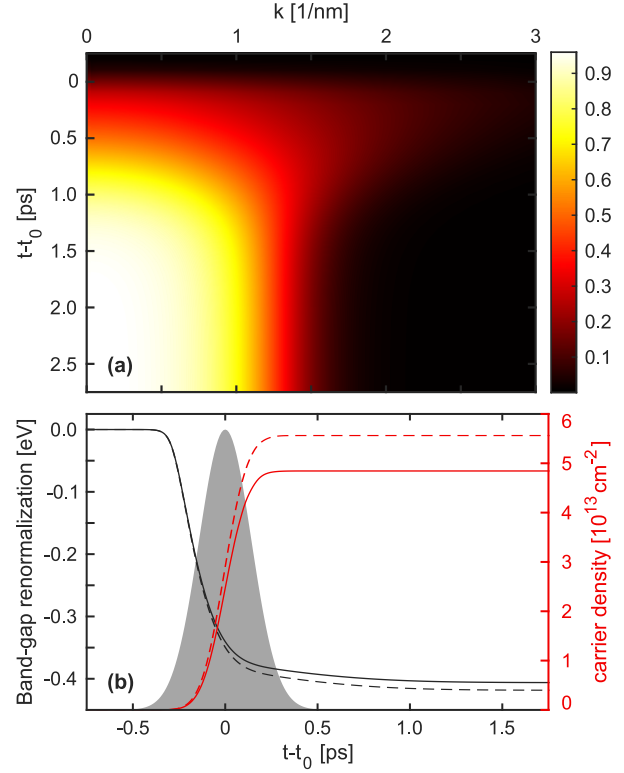
FIG. 5. (a) Dynamics of the A-band electron distribution in the vicinity of the K/K' points after excitation with a 333 fs pump pulse with peak amplitude of 1.25 MV/cm at $t = t_0$. (b) Time evolution of the excitation-induced band-gap renormalization (black) and the density of excited charge carriers (red). The solid lines correspond to the A-band properties, whereas the dashed lines show the B-band properties. The gray shaded area indicates the envelope of the optical pump pulse.

of 1.040×10^{14} cm^{-2}, or equivalently, 5.20×10^{13} cm^{-2} generated electron hole-pairs, corresponding to an absorption of about 2.9% of the incoming photons. Due to the Coulomb enhancement of the above band-edge absorption, this value is slightly larger than the universal low-density continuum absorption of $\pi\alpha = 2.3\%$ for noninteracting Dirac Fermions.

The initial ultrafast relaxation into hot quasiequilibrium distributions is followed by a phonon-induced thermalization that takes about 2.5 ps until a quasiequilibrium at the temperature of the phonon bath (300 K) is reached. At $\tau = 0.1$ ps and $\tau = 1$ ps, we find intermediate temperatures of $T = 2175$ K and $T = 555$ K, respectively. This relaxation time is about twice as fast as in conventional semiconductors and based on the efficient phonon coupling in ML MoTe$_2$-H [41].

The time evolution of the excitation-induced band-gap renormalization (black) and the total carrier density with given spin and valley index $n_i(t) = \frac{1}{A} \sum_{\alpha,\mathbf{k}} f^\alpha_{i\mathbf{k}}(t)$ (red) is shown in Fig. 5(b). With solid lines, we depict the respective A-band properties, whereas the B-band properties are plotted using dashed lines. The gray shaded area shows the envelope of the Gaussian shaped optical pump pulse centered around t_0. Due to the initially nearly resonant excitation with the B-band

gap, the final amount of charge carriers in the B bands ($n_B = 5.56 \times 10^{13}$ cm^{-2}) is slightly higher than in the A bands ($n_A = 4.84 \times 10^{13}$ cm^{-2}). Note that due to the opposite spin, there are no relaxation processes between the B and the A bands on the timescales of interest here.

As can be recognized in Fig. 5(b), the build-up of populations during the excitation process is accompanied by an almost instantaneous large shrinkage of the band gap, followed by a much slower further reduction. The band-edge shrinkage results from combined screening and phase-space-filling effects. As in conventional two-dimensional semiconductors, the screening wave number is proportional to the carrier occupation at $k = 0$. Due to the ultrafast Coulomb scattering, the major contribution to screening develops within the timescale of the pump pulse with a correspondent reduction of the band gap of about 389 meV within the first 0.4 ps. Once the amount of excited charge carriers has saturated, the band edge can only be further reduced by phase-space filling. This leads to an additional reduction of about 17 meV on the timescale of the thermalization, yielding the total excitation-induced band-gap renormalizations of 406 meV (A gap) and 419 meV (B gap), respectively, for the investigated excitation conditions. These results are in good agreement with our previous findings in the equilibrium regime [18] and reported experimental observations [15,16] on similar systems.

B. Evolution of optical spectra and build-up of optical gain

In Fig. 6, we present the time evolution of optical absorption/gain spectra computed as linear response to an ultrashort, low-intensity probe pulse for different delay times $\tau = t - t_0$. To cover the wide relevant energy range of several hundred meV, we choose a temporal width of 10 fs for the probe pulse. The use of such an ultrashort probe pulse also provides the necessary time resolution to study the evolution of the optical response during the excitation process, which is shown in Fig. 6(a). Here, the pump-probe delay increases from $\tau = -0.30$ ps to $\tau = -0.05$ ps in 0.05 ps steps. For comparison, the linear absorption spectrum of the unexcited ML is depicted in black. We notice an initial increase of the excited carrier density leading to dephasing, excitation-induced band-edge shrinkage, and reduction of the exciton binding energy. As a consequence of compensating effects, we observe practically no shift of the exciton resonance position under the given excitation conditions. Excitation-induced dephasing increases the 1-s-exciton linewidth from 2.3 meV at a delay time $\tau = -0.25$ ps to 42.2 meV at $\tau = -0.15$ ps. Note, that we include an additional dephasing constant of 10 meV for the microscopic polarizations to assure convergence in the zero-density limit. At $\tau = -0.05$ ps and a density of about 3.36×10^{13} cm^{-2} the exciton resonance is completely bleached out, marking the Mott-density.

In Fig. 6(b), we show the optical absorption in the thermalization regime. Here, pump-probe delays increase from $\tau = 0.5$ ps to $\tau = 1.5$ ps in 0.2 ps steps. The inset displays snapshots of the corresponding A-band electron distribution functions. In this time regime, no additional excited charge carriers are generated, but thermalization relaxes the existing carriers into quasiequilibrium at the lattice temperature (300 K). As a consequence of the high barriers between
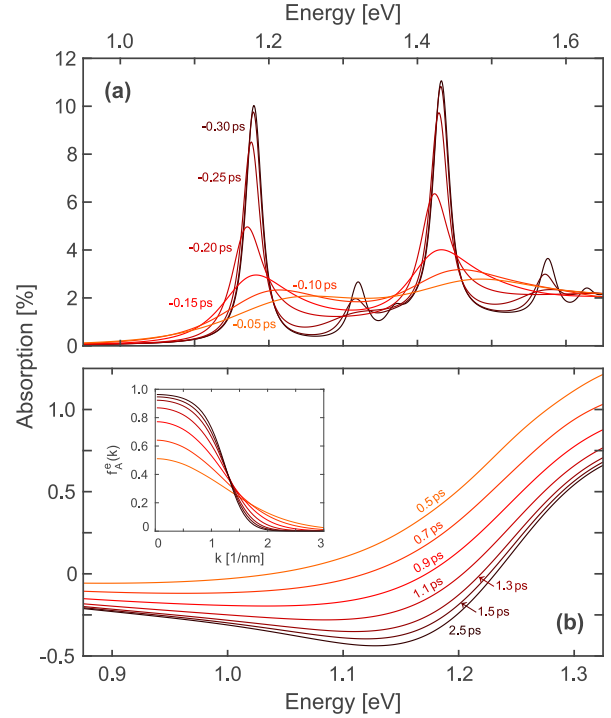

FIG. 6. Optical absorption spectra at distinct pump-probe delays. (a) Excitation regime. Pump-probe delays increase from $\tau = -0.30$ ps to $\tau = -0.05$ ps in 0.05 ps steps. The black solid line represents the low-density limit before the excitation. (b) Thermalization regime. Pump-probe delays increase from $\tau = 0.5$ ps to $\tau = 1.5$ ps in 0.2 ps steps. The absorption spectrum in the quasiequilibrium limit ($\tau \geq 2.5$ ps) is shown in black. The corresponding A-band distribution functions are depicted in the inset.

the K/K' and Σ/Λ valleys, no significant percentage of the excited carriers can reach the side valleys on the fast carrier relaxation timescale. Therefore, the total carrier densities in the K/K' valleys is practically conserved. The absorption spectrum for quasiequilibrium conditions is depicted in black in Fig. 6(b). With decreasing temperature of the quasiequilibrium distributions, the occupation probabilities near the band-gap increase. About 0.5 ps after the pump pulse, inversion with $(1 - f_{i\mathbf{k}}^e - f_{i\mathbf{k}}^h) < 0$ is reached and optical gain (negative absorption) appears in the spectrum. Inversion and gain increase with increasing cooling of the carriers. After about 2.5 ps thermal equilibrium is reached, where we observe broad A-band optical gain with a peak energy of 1.13 eV, slightly below the low density A-exciton resonance. Note that while the inclusion of the carrier-phonon scattering is crucial for the thermalization of the carriers, linewidths and energy renormalizations within the optical spectra are dominated by polarization-carrier rather than polarization-phonon scattering contributions. The maximum gain approaches a value of 0.5% amplification of the incoming light, which is clearly below the theoretical upper limit of $\pi\alpha/2 = 1.15\%$ for the free carrier, single-band case. Therefore, continuum absorption of the A band overcompensates the gain of the B band at higher
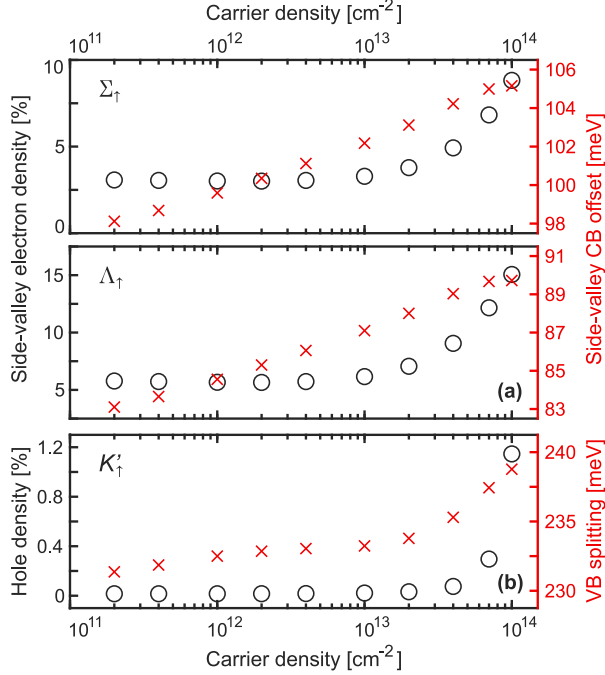
FIG. 7. (a) $\Sigma_\uparrow$ (top) and $\Lambda_\uparrow$ (bottom) side-valley electron densities (left axis, black circles) and $\Sigma_\uparrow$ (top) and $\Lambda_\uparrow$ (bottom) conduction-band offsets (right axis, red crosses) in dependence of the total amount of excited charge carriers. (b) Similarly, charge-carrier dependence of the $K'_\uparrow$ hole density (left axis, black circles) and $K_\uparrow/K'_\uparrow$ valence-band splitting (right axis, red crosses). The respective spin-up electron (hole) densities are stated as fraction of the total spin-up electron (hole) density.

energies yielding a net absorption in the frequency range of the B exciton.

C. Influence of the side valleys

The full DFT band structure displays six side minima in the conduction band located at the Σ/Λ points of the Brillioun zone. For the previously considered excitation conditions, carrier equilibration leads to a net electron drain from the K/K' to the Σ/Λ valleys as well as a hole drift between the K and K' valleys. To compute this side-valley drain and hole drift and its influence on the optical gain spectra, we consider an equilibrium situation where all electrons and holes have relaxed to a common chemical potentials. The side valleys are treated within the effective mass approximation and the influence of their populations is considered self-consistently including their contribution to screening and excitation-induced renormalizations.

The electron drain to the side valleys critically depends on the offset between the side valleys and the conduction band minima at the K/K' points, which in turn are modified by the carrier occupations in each valley. In Fig. 7(a), we depict the $\Sigma_\uparrow$ (top) and $\Lambda_\uparrow$ (bottom) side-valley electron densities (black circles) as well as the corresponding conduction-band offsets (red crosses) in dependence of the total density of excited charge carriers. Increasing the total carrier density
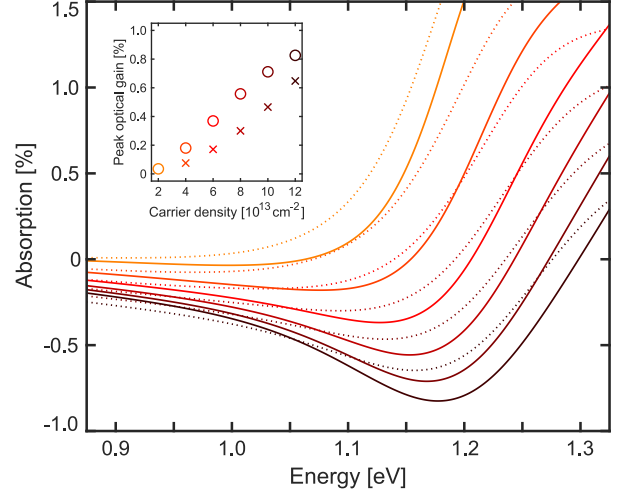
FIG. 8. Optical absorption spectra before and after equilibration of the carriers between the different valleys. The solid lines show the optical spectra after equilibration, the dotted lines before equilibration, where all carriers are located in the K and K' valleys. The inset shows the peak optical gain for the corresponding charge-carrier densities after (before) equilibration in circles (crosses).

from 2×10^{11} cm^{-2} to 10^{14} cm^{-2}, the $\Sigma_\uparrow$ ($\Lambda_\uparrow$) conduction-band offset increases by 7.0 meV (6.6 meV), while the fraction of $\Sigma_\uparrow$ ($\Lambda_\uparrow$) electrons increases from about 3.1% (5.8%) in the low-density regime to about 8.8% (15.1%) in the regime investigated by the pump-probe simulations. The larger electron drain towards the $\Lambda_\uparrow$ valleys arises from the smaller side-valley offset, that increases from 82 meV (DFT value) to 89.7 meV for the highest investigated carrier density. For the $\Sigma_\uparrow$ valleys, the band offset increases from 97 meV (DFT value) to 105.2 meV.

In addition to the electron drain, intervalley scattering leads to a drift of the hole density between the K and K' valleys. In our calculations, the influence of this is taken into account in a similar manner as the side-valley drain, i.e., by considering an equilibrium situation with a common chemical potential for the holes in different valleys. In Fig. 7(b), we plot the charge-carrier dependence of the fractional $K'_\uparrow$ hole density (black circles) and the corresponding $K_\uparrow/K'_\uparrow$ valence-band splitting (red crosses). Because of the large valence-band splitting in the low-density limit, almost all the holes from the $K'_\uparrow$ valley have drifted to the energetically favorable $K_\uparrow$ valley after equilibration. Only for carrier densities as high as 10^{14} cm^{-2}, the $K'_\uparrow$ valley is occupied with at least 1% of the spin-up holes. Thus, the increasing valence-band splitting with increasing carrier density is exclusively introduced by the dominant occupation of holes in the $K_\uparrow$ valley. For the shown carrier densities, the valence-band splitting increases by 7.4 meV from 231.4 to 238.8 meV.

Finally, we present the resulting optical absorption spectra after equilibration within the entire Brillioun zone for elevated charge-carrier densities in Fig. 8. The carrier densities increase from orange (2.0×10^{13} cm^{-2}) to black (1.2×10^{14} cm^{-2}). The solid (dotted) lines show the optical spectra after (before) equilibration. The inset depicts the peak optical

gain for the corresponding charge-carrier densities. Prior to equilibration, all carriers are assumed to be located in the K and K' valleys. As pointed out before, equilibration not only leads to electron drain to the side valleys, but also to hole drift between the K and K' valleys. Both processes have counteracting effects on the optical spectra. While the electron drain to the side-valleys leads to a loss of optically recombining electrons, the hole drift between the K and K' valleys increases the amount of optically recombining holes. Because of the large $K_\uparrow/K'_\uparrow$ ($K'_\downarrow/K_\downarrow$) valence-band splitting about 99% of the holes contribute to A-band population inversion after equilibration, compared to the nearly 50% before equilibration. This overcompensates the effect of electron drain—between 10.8% and 26.9% of the electrons for the stated carrier densities—to the side valleys. Consequently, enhanced peak optical gain is observed in equilibrium. In particular, for carrier densities of $0.8/1.0/1.2 \times 10^{14}\,\mathrm{cm}^{-2}$ peak optical gain increases by 86/53/28% due to equilibration. For a carrier density as high as $1.2 \times 10^{14}\,\mathrm{cm}^{-2}$, we observe peak optical gain occurring slightly below the low-density A-exciton resonance with a magnitude of 0.83% of the incoming light. Normalized to the layer thickness of $D = 6.99$ Å (see Table I), this corresponds to a peak gain of about $10^5\,\mathrm{cm}^{-1}$, which should be compared to the gain maximum of $5000\,\mathrm{cm}^{-1}$ in typical III/V semiconductors under realistic excitation conditions [45].

IV. DISCUSSION

In summary, we investigated the carrier dynamics in ML MoTe$_2$-H after excitation with a strong optical pump pulse slightly above the interacting B-band gap. Our investigations cover two distinct time regimes. In the excitation regime, i.e., during the optical pulse, generation of photo-induced charge carriers is accompanied by an almost instantaneous band-gap renormalization of about 410 meV in our case, that exceeds the exciton binding energy of the unexcited crystal. In the low-density regime, the band-gap renormalization is almost exactly canceled by the weakening of the excitonic

binding such that the exciton resonance displays a negligible spectral shift. The initial fast carrier relaxation is followed by a much slower thermalization of the hot carriers. Due to efficient phonon coupling, the thermalization occurs within a few picoseconds, whereas it is typically of the order of tens of picoseconds in conventional III–V quantum well systems. For the chosen pump-pulse intensity, thermalization finally leads to population inversion. Here, we observe the transition from plasma absorption to broadband optical gain. The maximum of the A-band optical gain occurs slightly below the low-density A-exciton resonance and its magnitude approaches 0.5% of the incoming light.

On the longer timescale, equilibration of the excited carriers among different valleys is expected with a simultaneous electron drain from the K/K' to the side valleys at the Σ/Λ points of the Brillioun zone. Although the electron drain leads to an efficiency drop of several percent in the gain regime, there is no evidence for an excitation-dependent roll-over from a direct to an indirect band gap, as has been predicted theoretically for similar material systems [35,36]. Instead, we find that the drop due to the electron drain is overcompensated by a hole drift between the K and K' valleys, leading to a net increase of the optical gain up to several 10%.

Our results are in general agreement with experimentally observed excitation-induced band-gap shrinkage of similar TMDC systems [15,16] and confirms the possibility of ultrafast band-gap modulation by the injection of carriers. Furthermore, our results identify conditions for achieving plasma gain in ML MoTe$_2$-H and the short relaxation times enable high repetition rates for possible applications in pulsed laser operation.

[1] K. F. Mak, C. Lee, J. Hone, J. Shan, and T. F. Heinz, Phys. Rev. Lett. **105**, 136805 (2010).

[2] A. Splendiani, L. Sun, Y. Zhang, T. Li, J. Kim, C. Y. Chim, G. Galli, and F. Wang, Nano Lett. **10**, 1271 (2010).

[3] C. Zhang, H. Wang, W. Chan, C. Manolatou, and F. Rana, Phys. Rev. B **89**, 205436 (2014).

[4] Y. Ding, Y. Wang, J. Ni, L. Shi, S. Shi, and W. Tang, Physica B: Phys. Condens. Matter **406**, 2254 (2011).

[5] D. Y. Qiu, F. H. da Jornada, and S. G. Louie, Phys. Rev. Lett. **111**, 216805 (2013).

[6] K. S. Novoselov, A. Mishchenko, A. Carvalho, and A. H. Castro Neto, Science **353**, aac9439 (2016).

[7] T. Cheiwchanchamnangij and W. R. L. Lambrecht, Phys. Rev. B **85**, 205302 (2012).

[8] A. Chernikov, T. C. Berkelbach, H. M. Hill, A. Rigosi, Y. Li, O. B. Aslan, D. R. Reichman, M. S. Hybertsen, and T. F. Heinz, Phys. Rev. Lett. **113**, 076802 (2014).

[9] K. He, N. Kumar, L. Zhao, Z. Wang, K. F. Mak, H. Zhao, and J. Shan, Phys. Rev. Lett. **113**, 026803 (2014).

[10] Z. Ye, T. Cao, O. K., H. Zhu, X. Yin, Y. Wang, S. G. Louie, and X. Zhang, Nature **513**, 214 (2014).

[11] B. Zhu, X. Chen, and X. Cui, Sci. Rep. **5**, 9218 (2015).

[12] O. Salehzadeh, M. Djavid, N. H. Tran, I. Shih, and Z. Mi, Nano Lett. **15**, 5302 (2015).

[13] Y. Ye, Z. J. Wong, X. Lu, X. Ni, H. Zhu, X. Chen, Y. Wang, and X. Zhang, Nat. Photon. **9**, 733 (2015).

[14] Y. Li, J. Zhang, D. Huang, H. Sun, F. Fan, J. Feng, Z. Wang, and C. Z. Ning, Nat. Nanotech. **12**, 987 (2017).

[15] A. Chernikov, C. Ruppert, H. M. Hill, A. F. Rigosi, and T. F. Heinz, Nat. Photon. **9**, 466 (2015).

[16] S. Ulstrup, A. G. Čabo, J. A. Miwa, J. M. Riley, S. S. Grønborg, J. C. Johannsen, C. Cacho, O. Alexander, R. T. Chapman, E. Springate, M. Bianchi, M. Dendzik, J. V. Lauritsen, P. D. C. King, and P. Hofmann, ACS Nano **10**, 6315 (2016).

[17] A. Steinhoff, M. Rösner, F. Jahnke, T. O. Wehling, and C. Gies, Nano Lett. **14**, 3743 (2014).

[18] L. Meckbach, T. Stroucken, and S. W. Koch, Appl. Phys. Lett. **112**, 061104 (2018).

[19] T. Stroucken and S. W. Koch, in *Optical Properties of Graphene*, edited by R. Binder (World Scientific Publishing, Singapore, 2017), Chap. 2, pp. 43–84.

[20] L. Meckbach, T. Stroucken, and S. W. Koch, Phys. Rev. B **97**, 035425 (2018).

[21] L. Meckbach, U. Huttner, L. Bannow, T. Stroucken, and S. W. Koch, J. Phys.: Condens. Matter **30**, 374002 (2018).

[22] W. Kohn and L. J. Sham, Phys. Rev. **140**, A1133 (1965).

[23] G. Kresse and J. Hafner, Phys. Rev. B **47**, 558 (1993).

[24] G. Kresse and J. Hafner, Phys. Rev. B **49**, 14251 (1994).

[25] G. Kresse and J. Furthmüller, Phys. Rev. B **54**, 11169 (1996).

[26] G. Kresse and J. Furthmüller, Comp. Mater. Sci. **6**, 15 (1996).

[27] J. P. Perdew, K. Burke, and M. Ernzerhof, Phys. Rev. Lett. **77**, 3865 (1996).

[28] S. Steiner, S. Khmelevskyi, M. Marsmann, and G. Kresse, Phys. Rev. B **93**, 224425 (2016).

[29] S. Grimme, J. Antony, S. Ehrlich, and H. Krieg, J. Chem. Phys. **132**, 154104 (2010).

[30] S. Grimme, S. Ehrlich, and L. Goerigk, J. Comput. Chem. **32**, 1456 (2011).

[31] H. J. Monkhorst and J. D. Pack, Phys. Rev. B **13**, 5188 (1976).

[32] A. Molina-Sánchez, K. Hummer, and L. Wirtz, Surf. Sci. Rep. **70**, 554 (2015).

[33] A. Kormányos, G. Burkard, M. Gmitra, J. Fabian, V. Zólyomi, N. D. Drummond, and V. Fal'ko, 2D Materials **2**, 022001 (2015).

[34] D. Novko, arXiv:1907.04766 [cond-mat.mtrl-sci].

[35] D. Erben, A. Steinhoff, C. Gies, G. Schönhoff, T. O. Wehling, and F. Jahnke, Phys. Rev. B **98**, 035434 (2018).

[36] F. Lohof, A. Steinhoff, M. Florian, M. Lorke, D. Erben, F. Jahnke, and C. Gies, Nano Lett. **19**, 210 (2019).

[37] M. Gajdoš, K. Hummer, G. Kresse, J. Furthmüller, and F. Bechstedt, Phys. Rev. B **73**, 045112 (2006).

[38] S. Baroni and R. Resta, Phys. Rev. B **33**, 7017 (1986).

[39] A. Laturia, M. L. Van de Put, and W. G. Vandenberghe, npj 2D Mater. Appl. **2**, 6 (2018).

[40] D. Xiao, G.-B. Liu, W. Feng, X. Xu, and W. Yao, Phys. Rev. Lett. **108**, 196802 (2012).

[41] T. Sohier, M. Calandra, and F. Mauri, Phys. Rev. B **94**, 085415 (2016).

[42] T. Stroucken, J. H. Grönqvist, and S. W. Koch, Phys. Rev. B **84**, 205445 (2011).

[43] C. Robert, R. Picard, D. Lagarde, G. Wang, J. P. Echeverry, F. Cadiz, P. Renucci, A. Högele, T. Amand, X. Marie, I. C. Gerber, and B. Urbaszek, Phys. Rev. B **94**, 155425 (2016).

[44] M. Kira and S.W. Koch, Progr. Quant. Electron. **30**, 155 (2006).

[45] See http://www.nlcstr.com/publications.htm and http://www.nlcstr.com/examples0.htm for examples.

Paper IV

J. Hader, J. Neuhaus, J. V. Moloney, and S. W. Koch:

On the importance of electron-electron and electron-phonon scatterings and energy renormalization during carrier relaxation in monolayer transition metal dichalcogenides

Abstract: An *ab initio* based fully microscopic many-body approach is used to study the carrier relaxation dynamics in monolayer transition-metal dichalcogenides. Bandstructures and wavefunctions as well as phonon energies and coupling matrix elements are calculated using density functional theory. The resulting dipole and Coulomb matrix elements are implemented in the Dirac-Bloch equations to calculate carrier-carrier and carrier-phonon scatterings throughout the whole Brillouin zone (BZ). It is shown that carrier scatterings lead to a relaxation into hot quasi-Fermi distributions on a single femtosecond timescale. Carrier cool down and inter-valley transitions are mediated by phonon scatterings on a picosecond timescale. Strong, density-dependent energy renormalizations are shown to be valley-dependent. For $MoTe_2$, $MoSe_2$ and MoS_2 the change of energies with occupation is found to be about 50% stronger in the Σ and Λ side valleys than in the K and K' valleys. However, for realistic carrier densities, the materials always maintain their direct bandgap at the K points of the Brillouin zone.

On the importance of electron–electron and electron–phonon scatterings and energy renormalizations during carrier relaxation in monolayer transition-metal dichalcogenides

Jörg Hader[1,*] ⓘ **, Josefine Neuhaus**[2] ⓘ **, Jerome V Moloney**[1] ⓘ
and Stephan W Koch[2] ⓘ

[1] Wyant College of Optical Sciences, University of Arizona, 1630 E. University Blvd., Tucson, Arizona 85721, United States of America
[2] Department of Physics and Material Sciences Center, Philipps-University Marburg, Renthof 5, 35032 Marburg, Germany

E-mail: jhader@acms.arizona.edu

CrossMark

Abstract

An *ab initio* based fully microscopic many-body approach is used to study the carrier relaxation dynamics in monolayer transition-metal dichalcogenides. Bandstructures and wavefunctions as well as phonon energies and coupling matrix elements are calculated using density functional theory. The resulting dipole and Coulomb matrix elements are implemented in the Dirac–Bloch equations to calculate carrier–carrier and carrier–phonon scatterings throughout the whole Brillouin zone (BZ). It is shown that carrier scatterings lead to a relaxation into hot quasi-Fermi distributions on a single femtosecond timescale. Carrier cool down and inter-valley transitions are mediated by phonon scatterings on a picosecond timescale. Strong, density-dependent energy renormalizations are shown to be valley-dependent. For $MoTe_2$, $MoSe_2$ and MoS_2 the change of energies with occupation is found to be about 50% stronger in the Σ and Λ side valleys than in the K and K' valleys. However, for realistic carrier densities, the materials always maintain their direct bandgap at the K points of the BZ.

(Some figures may appear in colour only in the online journal)

1. Introduction

Monolayer transition-metal dichalcogenides (TMDCs) have a variety of properties that make them very interesting for applications in opto-electronic devices. Two of the most important

characteristics are their direct bandgap and the exceptionally strong Coulomb interaction due to inefficient screening outside the monolayer plane. The highly efficient optical coupling leads to a near-bandgap absorption of up to 10%–20% from a single layer [1, 2] which makes the material attractive for applications like photo-detectors [3–5] or solar cells [6, 7]. The prominent optical coupling also leads to strong luminescence

1
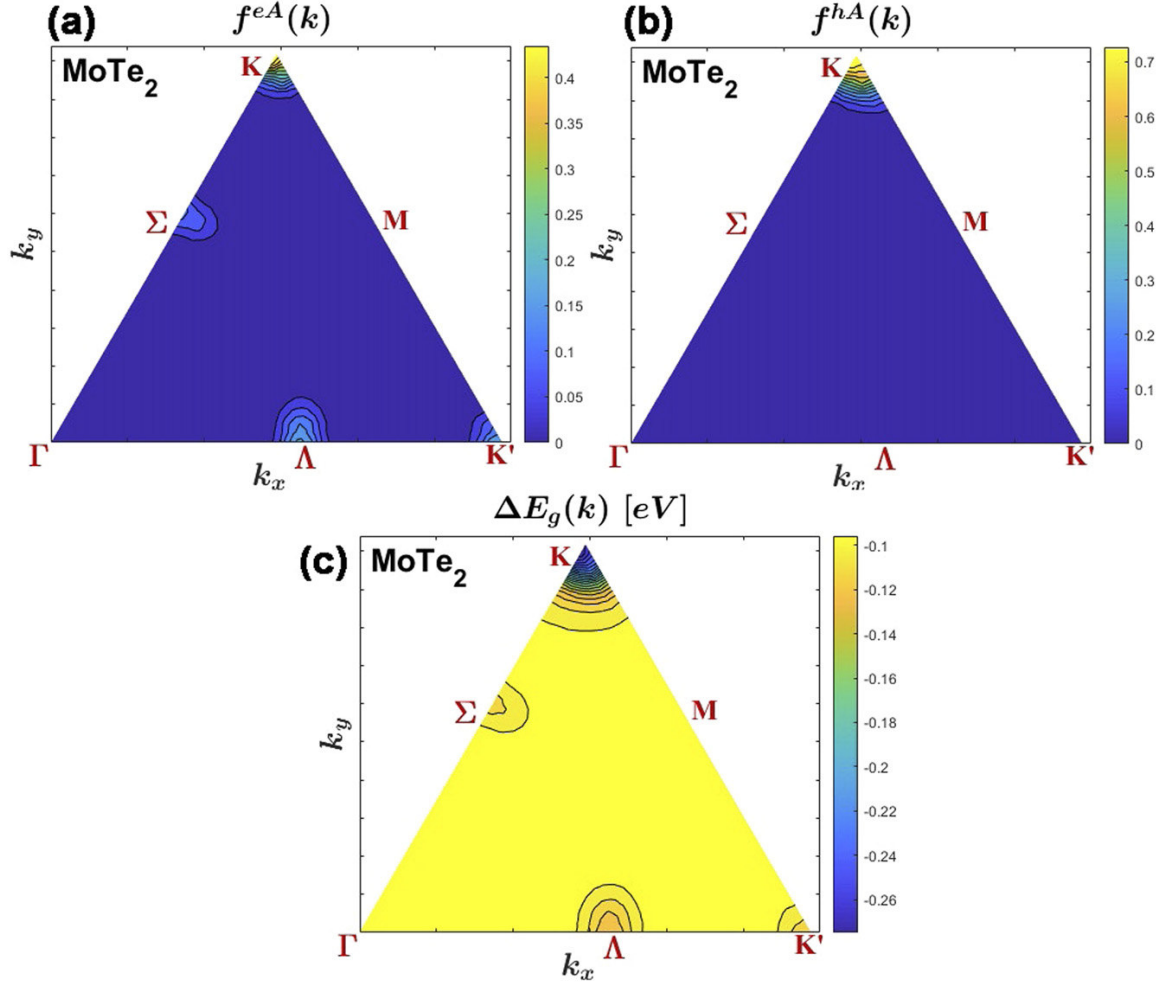
Figure 1. (a)/(b) Electron/hole occupations of the A-band for a total electron/hole density of 12.5×10^{12} cm^2 in a monolayer MoTe$_2$. Carriers are assumed to be in thermal equilibrium Fermi distributions at 300 K. (c) Renormalization of the A-bandgap in the presence of the carriers.

and, consequently, promising performance as light-emitting diodes [8–10]. Monolayer TMDCs have also been shown to be able to provide strong optical gain [11, 12] which enables them to be used as active material in lasers [13–15].

The strong Coulomb interaction also enables the possibility to tune the bandgap over a wide spectral range. Injecting carriers into the system leads to energy renormalizations on the order of the exciton binding energy which in these materials is of the order of hundreds of meV [16–19]. Figure 1 gives an example for the energy renormalizations in a monolayer of MoTe$_2$. Here, equal electron and hole densities of 12.5×10^{12} cm^2 were placed in Fermi distributions at 300 K. Figures 1(a) and (b) show the carrier distributions in the band that is energetically closest to the bandgap at the K-point (A-band). Mirroring these results along the Γ–M line gives the results for the B-band which has the opposite spin and the same gap at K' as the A-band at K. As can be seen from figure 1(c), the presence of the quasi-equilibrium carriers

reduces the bandgap by about 100 meV throughout the whole Brillouin zone (BZ). The renormalization is strongly enhanced in the vicinity of high carrier occupations, reaching over 260 meV at the K-point.

The strong energy renormalizations open the interesting possibility to tune the operating wavelength through controlled carrier injection. Also, the energetic order of the valleys could potentially be changed, e.g., by exciting resonantly with a specific valley transition and/or using polarized, spin-valley sensitive excitation [20, 21]. However, valley specific renormalizations require non-thermal carrier distributions. Once pump injected carriers have thermalized into Fermi distributions with a global Fermi level throughout the BZ, the energies of individual valleys will only be determined by the total carrier density. A potential drawback of the density dependent renormalizations was pointed out in references [11, 22]. If the energies of a side valley of the electron A-band renormalize faster with increasing carrier density than the energy at the direct bandgap

at K, it could potentially happen that the side valley is lowered below the K-valley and the material becomes optically indirect. In this case, the pump injected electrons would predominantly occupy the side valley, and, since the hole bandstructure does not have side valleys, electrons in them are not available to recombine optically. This will degrade the material's performance for applications like light emitting diodes or lasers. As we will show here, whether such a transition will occur strongly depends on details of the bandstructure.

Valley- and excitation-dependent renormalizations for carriers in static thermal equilibrium distributions were discussed in reference [22] using similar first principles based microscopic models as we employ here. In reference [23] a similar model was extended in order to be able to study the nonequilibrium carrier relaxation due to electron–electron scatterings. However, inter-valley carrier transitions involve large momentum transfer which is predominantly mediated by scatterings involving optical and acoustical phonons. These were not included in reference [23]. The influence of phonon-assisted inter- and intra-valley scatterings were investigated in references [24–26], but only for carriers in equilibrium distributions. In reference [12] electron–electron and electron–phonon scatterings were included to study nonequilibrium carrier relaxation. However, that investigation was limited to intra-valley dynamics using a simplified one-dimensional bandstructure model.

Here, we employ a fully microscopic many-body model that includes electron–electron and electron–phonon scatterings throughout the full BZ. The model is based on input from first principle density functional theory (DFT) for bandstructures, electron wavefunctions and phonon energies and coupling matrix elements. The model is used to determine timescales for the relaxation of carriers that are excited above the bandgap. It also yields times for inter-valley and intra-valley scatterings that lead to global quasi equilibrium distributions as well as for the subsequent cool-down to the ambient temperature by removal of excess energy via phonon emission.

Details of the model are outlined in section 2 where we will also show results of the DFT calculations. Results of the many-body model are discussed in section 3 for monolayer MoTe$_2$, MoSe$_2$ and MoS$_2$. In section 3.1 we present numerical results assuming an artificial static carrier distribution to initialize the system in order to be able to clearly distinguish between the excitation related dynamics and the subsequent carrier relaxation. Carrier scattering processes are turned on after the initialization. In section 3.1.1 we examine the case of an initial distribution that is energetically located above the barriers separating different bandstructure valleys. We determine the characteristic carrier relaxation times and show the influence of electron–electron scatterings versus electron–phonon scatterings due to optical and acoustical phonons at various stages of the relaxation process. In section 3.1.2 we present results where we assume excitation at the bandgap in the K-valley and investigate the subsequent carrier transfer to the K', Σ and Λ valleys. After that, in section 3.2, we simulate the situation where the system is excited dynamically using a 50 fs optical pulse which allows us to identify characteristic details of the relaxation dynamics might be observable in the experiment.

Finally, in section 3.3, we investigate the energy renormalizations after full carrier thermalisation for various excitation levels in order to see if a transition from direct to indirect bandgap occurs. We summarize our results in section 4.

2. Theoretical models

The theoretical approach used here is based on the Dirac–Bloch equations (DBE) as described in reference [12] and references therein. The DBE are the equations of motions for the microscopic polarizations, $p_{\mathbf{k}i}$, and the occupation probabilities for electrons/holes, $f_{\mathbf{k}i}^{\mathrm{e/h}}$:

$$i\hbar \frac{\mathrm{d}}{\mathrm{d}t} p_{\mathbf{k}i} = \left(\varepsilon_{\mathbf{k}i}^{\mathrm{e}} - \varepsilon_{\mathbf{k}i}^{\mathrm{h}} \right) p_{\mathbf{k}i} - \left(1 - f_{\mathbf{k}i}^{\mathrm{e}} - f_{\mathbf{k}i}^{\mathrm{h}} \right) \Omega_{\mathbf{k}i} + i\hbar \frac{\mathrm{d}}{\mathrm{d}t} p_{\mathbf{k}i} \Big|_{\mathrm{corr}}, \tag{1}$$

$$\frac{\mathrm{d}}{\mathrm{d}t} f_{\mathbf{k}i}^{\mathrm{e/h}} = -\frac{2}{\hbar} \mathrm{Im} \left(\Omega_{\mathbf{k}i} p_{\mathbf{k}i}^* \right) + \frac{\mathrm{d}}{\mathrm{d}t} f_{\mathbf{k}i}^{\mathrm{e/h}} \Big|_{\mathrm{corr}}. \tag{2}$$

Here, Ω are the renormalized Rabi frequencies

$$\Omega_{\mathbf{k}i} = \frac{e}{m_0 c} \mathbf{A} \cdot \boldsymbol{\mu}_{\mathbf{k}i} - \sum_{\mathbf{k}'} V_{\mathbf{k}-\mathbf{k}';k';k}^{\mathrm{ehhh}} (f_{\mathbf{k}'i}^{\mathrm{e}} - f_{\mathbf{k}'i}^{\mathrm{h}})$$
$$- \sum_{\mathbf{k}'} \left[V_{\mathbf{k}-\mathbf{k}';k';k}^{\mathrm{ehhe}} p_{\mathbf{k}'i} + V_{\mathbf{k}-\mathbf{k}';k';k}^{\mathrm{eehh}} p_{\mathbf{k}'i}^* \right], \tag{3}$$

where $\boldsymbol{\mu}_{\mathbf{k}i}$ are the dipole matrix elements between the electron and hole bands with band index i and momentum $\mathbf{k}$, and ε are the renormalized energies:

$$\varepsilon_{\mathbf{k}i}^{\mathrm{e/h}} = \epsilon_{\mathbf{k}i}^{\mathrm{e/h}} - \sum_{\mathbf{k}'} \left[V_{\mathbf{k}-\mathbf{k}';k';k}^{\mathrm{eeee/hhhh}} - V_{\mathbf{k}-\mathbf{k}';k';k}^{\mathrm{eheh/hehe}} \right] f_{\mathbf{k}'i}^{\mathrm{e/h}}$$
$$+ \sum_{\mathbf{k}'} \left[V_{\mathbf{k}-\mathbf{k}';k';k}^{\mathrm{ehee/hhhe}} p_{\mathbf{k}'i} + \mathrm{c.c.} \right]. \tag{4}$$

Coulomb matrix elements of the type V^{ehhh} in equation (3) and $V^{\mathrm{ehee/hhhe}}$ in equation (4) mediate Auger-like processes. Coulomb terms of the type V^{eehh} in equation (3) and $V^{\mathrm{eheh/hehe}}$ in equation (4) represent pair creation and annihilation processes. Whereas these processes can be neglected in systems with weaker Coulomb interaction, like III–V semiconductors, they are important in TMDCs. Here, they lead to a non-trivial ground state deviating from the case of zero occupations and polarizations. The dominant influence of these terms is to contribute to a renormalisation of the hole bands which we take into account by calculating the so-called Coulomb hole. We have tested that these Auger- and pair-processes have a negligible impact on the carrier dynamics and can be neglected there.

The term involving V^{ehhe} in equation (3) represents the renormalisation of the optical coupling as known from the classical semiconductor Bloch equations (SBE). It leads to the generation of bound excitonic states below the bandgap and to the Coulomb-enhancement of the continuum absorption. As in the SBE, the term involving $V^{\mathrm{eeee/hhhh}}$ in equation (4) leads

to the exitation dependent energy renormalisation that we will investigate in detail here.

The terms marked $|_{corr}$ summarize many-body correlations beyond the Hartree–Fock level. They contain carrier scatterings due to electron–electron and electron–phonon interactions. The higher order correlations are also responsible for the plasma-screening of the Coulomb interaction. In monolayer TMDCs, the correct inclusion of these higher order terms is of particular importance due to the exceptional strength of the Coulomb interaction. We treat these terms and the resulting screening as outlined in reference [12].

For the calculations as shown here, scatterings are only taken into account explicitly for the carrier distributions. Polarizations are only included for the optical excitation of carriers. Since our focus is on the subsequent incoherent dynamics of the distributions and not details of the excitation, we approximate the scatterings that lead to the dephasing of the polarisations by a simple dephasing rate.

The electron–electron scattering equations solved here are outlined in reference [12]. Whereas in that reference only one branch of dispersionless optical phonons was taken into account for the electron–phonon scattering, here, we include all optical and acoustical phonon branches. The generalized electron–phonon scattering equations take the form:

$$\frac{\mathrm{d}}{\mathrm{d}t} f_{\mathbf{k}i} \bigg|_{\text{corr.}}^{\text{ph.}} = \frac{2\pi}{\hbar} \sum_{\mathbf{q},m} g_{\mathbf{k};\mathbf{q}}^{i,m} \tilde{g}_{\mathbf{k};\mathbf{q};\mathbf{k}+\mathbf{q}}^{i,m} \mathcal{D}\left(\tilde{\varepsilon}_{\mathbf{k}+\mathbf{q}i} - \tilde{\varepsilon}_{\mathbf{k}i} - \hbar\omega_{\mathbf{q}}^m\right)$$
$$\times \left[(n_{\mathbf{q}}^m + 1) f_{\mathbf{k}+\mathbf{q}i} \bar{f}_{\mathbf{k}i} - n_{\mathbf{q}}^m f_{\mathbf{k}i} \bar{f}_{\mathbf{k}+\mathbf{q}i} \right]$$
$$+ \frac{2\pi}{\hbar} \sum_{\mathbf{q},m} g_{\mathbf{k};\mathbf{q}}^{i,m} \tilde{g}_{\mathbf{k};\mathbf{q};\mathbf{k}}^{i,m} \mathcal{D}\left(\tilde{\varepsilon}_{\mathbf{k}-\mathbf{q}i} - \tilde{\varepsilon}_{\mathbf{k}i} - \hbar\omega_{\mathbf{q}}^m\right)$$
$$\times \left[n_{\mathbf{q}}^m f_{\mathbf{k}-\mathbf{q}i} \bar{f}_{\mathbf{k}i} - (1 + n_{\mathbf{q}}^m) f_{\mathbf{k}i} \bar{f}_{\mathbf{k}-\mathbf{q}i} \right], \quad (5)$$

where we use the abbreviation $\bar{f}$ for $(1 - f)$ and combined the band indices i with the electron/hole index e/h. $\pi\mathcal{D}(x) = \frac{\eta}{x^2 + \eta^2}$ denotes the numerical energy-conserving function, where we include a phenomenological broadening of $\eta = 50$ meV. Numerical tests showed that the exact value of this broadening was insignificant for the final results. The renormalized transition energies $\tilde{\varepsilon}$ are calculated as in equation (4) but with Coulomb matrix elements which include plasma-screening due to excited carriers in addition to the screening from the dielectric environment which is already included in the matrix elements V. The index m labels the nine phonon branches [39, 40], all of which are taken into account in our numerical evaluations. The phonon energies are denoted by $\hbar\omega_{\mathbf{q}}^m$. $n_{\mathbf{q}}^m$ are the phonon occupation numbers. The quantities g and $\tilde{g}$ are the unscreened and screened phonon coupling matrix elements, respectively. The additional $\mathbf{k}$-index on the phonon coupling matrix elements arises from the fact that the momentum dependence of the electron wavefunctions is included explicitly here while the studies in reference [12] exclusively focused on the K-valley and used the electron wavefunctions at this point only.

In equation (5), the first term of the second line corresponds to scattering of carriers into the state $\mathbf{k}, i$ via phonon emission and the second term represents out-scattering via phonon absorption. The first term of the fourth line represents in-scattering via phonon absorption and the last term out-scattering via phonon emission. For all processes the initial state has to be occupied, i.e. the occupation f has to be non-zero, and the final state has to be at least partially empty, $(1 - f) > 0$. Energy has to be conserved and the scattering probability is given by the phonon coupling matrix elements g.

The unrenormalized single-particle energies, ϵ, are calculated via DFT using the Vienna *ab initio* simulation package [27–31]. Details of these calculations are described in reference [12] for MoTe$_2$ and executed analogously for the other materials. Besides the bandstructures, we also extract the dipole matrix elements and the wavefunctions needed to evaluate the Coulomb matrix elements from these calculations. The full k-dependence throughout the BZ is taken into account in all calculations for the single particle energies and dipole matrix elements. Unlike in reference [12], no simplification in terms of a massive Dirac fermion model with fitted bands is used. For the Coulomb matrix elements we evaluate the wavefunction-dependent form factors only in the vicinity of the K and Σ point and assume the same factors for the K' and Λ valleys. In regions away from these points the form factor of the nearest valley is used.

For all materials investigated here, the bandstructure has the same basic features. As representative example, figure 2 shows the calculated unrenormalized electron and hole bands for the case of a monolayer of MoTe$_2$. The lowest two electron bands and highest two hole bands are related through time reversal symmetry. Spin–orbit splitting lifts the degeneracy of the bands with opposite spin at K and K'. The electron band with the lowest energy at K and the hole band with the highest energy at K are referred to as the A-bands. Carriers in the so-called B-band have the opposite spin from those in the A-band. Energies of the B-band can be derived from those of the A-band by mirroring perpendicular to the Γ-M line. For excitation with linear polarized light the physics within the A-band at K is the same as that within the B-band at K'. Thus, we reduce our presentations to the the A-band in the following.

There are three additional minima in the electron A-band structure at K', Σ and Λ. The hole A-band has maxima at the K- and K'-points and, additionally, a local maximum at the Γ-point. The energies of the unrenormalized electron A-bands at critical points of the BZ are listed for all materials investigated here in table 1. Hole energies in the A-band are listed in table 2.

It should be noted that the exact valley energies are very sensitive to details of the DFT calculation. In turn, the excitation dependent energy renormalizations that will be studied in section 3.3 are strongly influenced by the exact separations between main and side valleys. One major aspect concerning the offset between the different valleys is the lattice constant. Already differences of one percent in the lattice constant change the calculated DFT bandgap in the range of 100 meV and may result in the transition from a direct to an indirect semiconductor [32–35]. In order to be as precise as
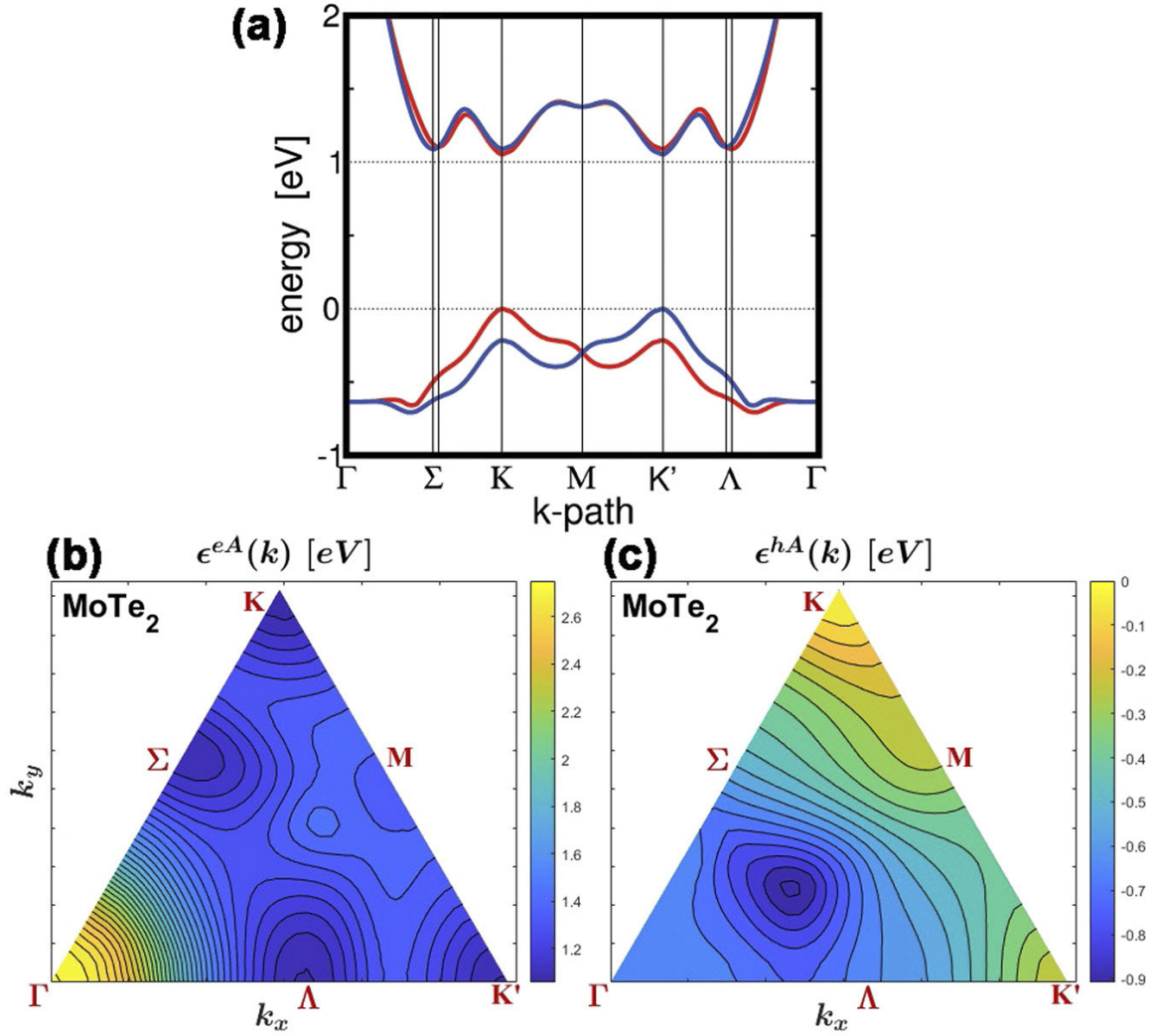
Figure 2. (a) Lowest two electron and highest two hole bands in a monolayer of MoTe$_2$ along a one-dimensional path through the BZ. Red/blue: bands for carriers with spin up/down (A/B-band). Bottom: energy of the electron (b) and hole (c) A-bands in the irreducible sector of the BZ. Spacing between contour lines is 50 meV.

Table 1. Calculated unrenormalized energies in the electron A-band at critical points of the BZ and at energy maxima, $m_{P;P'}$, between points P and P'. Energies in (eV).

	K	K'	Λ	Σ	$m_{K;\Sigma}$	$m_{K';\Lambda}$	$m_{K;K'}$
MoTe$_2$	1.058	1.093	1.091	1.108	1.323	1.363	1.410
MoSe$_2$	1.446	1.468	1.496	1.474	1.769	1.784	1.900
MoS$_2$	1.708	1.711	1.821	1.892	2.156	2.160	2.309

possible, we included van-der-Waals interaction via Grimme's dispersion correction, resulting in relaxed in-plane lattice constants of 3.50 Å for MoTe$_2$, 3.28 Å for MoSe$_2$, and 3.15 Å for MoS$_2$, which is comparable to experimental findings [38]. Based on these parameters, we find a direct bandgap at K for all materials investigated here and a separation from the side valleys at Σ and Λ that exceeds the room temperature thermal energy of about 26 meV.

Phonon energies and coupling matrix elements are calculated using the DFT software Quantum Espresso [36, 37]. For the non-collinear Kohn–Sham wavefunctions with spin–orbit coupling, the plane-wave basis set with a 49 Rydberg energy cut-off, Perdew–Burke–Ernzerhof type generalized gradient approximated exchange–correlation functional, and projector augmented wave method with full-relativistic potentials were used. The resulting phonon dispersions were found

Table 2. Calculated unrenormalized energies in the hole A-band at K, K' and Γ and at energy minima, $m_{P,P'}$, between points P and P'. Energies in (eV).

	K	K'	Γ	$m_{K;K'}$	$m_{K;\Gamma}$	$m_{K';\Gamma}$
MoTe$_2$	0.000	−0.214	−0.393	−0.633	−0.656	−0.705
MoSe$_2$	0.000	−0.183	−0.670	−0.435	−0.777	−0.853
MoS$_2$	0.000	−0.146	−0.153	−0.706	−0.838	−0.919

in good agreement with the literature (see e.g. references [39, 40]). The full **k**- and **q**-dependence of the phonon dispersions and coupling matrix elements are taken into account in all calculations.

3. Results

In the following we examine results for monolayers of MoTe$_2$, MoSe$_2$ and MoS$_2$ suspended on a SiO$_2$ substrate and at a temperature of 300 K. In all studies of the dynamics only the lowest two electron and highest two hole bands—A and B—are included. Excitation with linear polarized light is assumed which creates equal amounts of carriers at the K and K' points in bands of opposite spin.

3.1. Artificial excitation

Here, we initialize the carrier distributions with an artificial, static distribution that allows to clearly determine timescales in the subsequent relaxation as well as the importance of various scattering processes within it. The initial distributions are given by the formula:

$$f_{\mathbf{k}i} = \frac{f_0 \mu_{\mathbf{k}i}^2}{\mu_{\max}^2} \exp\left(-\frac{1}{2}\left(\frac{\epsilon_{\mathbf{k}i}^e - \epsilon_{\mathbf{k}i}^h - \hbar\omega_L}{\Delta}\right)^2\right), \quad (6)$$

where **k** is the two-dimensional momentum vector, i is the band index and $\epsilon^{e/h}$ are the unrenormalized electron/hole energies. These distributions approximate a case where carriers are optically excited at an energy $\hbar\omega_L$ and form a Gaussian distribution of width Δ. The occupation probabilities are weighted with the square of the dipole matrix element $\mu_{\mathbf{k}i}$ between the ith electron and hole band assuming a vanishing optical coupling between states with unequal spin. $\mu_{\max}$ is the largest dipole matrix element between any states. For all cases studied here, a broadening $\Delta = 66$ meV is used.

3.1.1. Above bandgap excitation.
Figure 3(a) shows the distributions created in the electron A-band using equation (6) for an excitation energy $\hbar\omega_L$ 800 meV above the unrenormalized bandgap. Here, a scaling $f_0 = 1.28$ was used which leads to a total electron sheet carrier density of about 1×10^{14} cm^2. Figures 3(b)–(d) show the distributions after 1 fs, 10 fs, and 500 fs of relaxation, respectively. As can be seen in figure 3(b), carrier scatterings broaden the distribution dramatically on a single femtosecond timescale. The excitation high above the bandgap is ideal for fast relaxation. Initial states are highly occupied and final states at lower energies are mostly empty which eliminates slow down of the relaxation due to phase space filling in this initial phase. Also, carriers

located in rather narrow momentum regions at high energies screen the Coulomb interaction far less efficiently than if the same amount of carriers are relaxed and distributed throughout wide regions of the BZ.

After only 10 fs the carriers have relaxed to the bottom of the band and assume Fermi-like distributions with maximum occupation at minimum energy (see figure 3(c)). The excess energy from the excitation leads to very hot distributions. Using Fermi distributions for the same electron density we find a very good match to the distribution after 10 fs assuming a carrier temperature of 8500 K (see figure 3(e)). The carriers subsequently cool down due to phonon emission. As can be seen from figures 3(d) and (f), after 500 fs the distribution can be matched assuming a carrier temperature of 1900 K. Subsequently, the carriers cool down further toward the lattice temperature of 300 K on a picosecond timescale.

Figure 4 shows the individual contributions of electron–electron scatterings and of electron–phonon scatterings to the carrier relaxation at the start of the relaxation and after 10 and 500 fs of relaxation. Initially, the relaxation is dominated by electron–electron scattering which broadens the localized distributions according to a hot plasma temperature on a single femtosecond timescale. During this initial phase, the dynamic due to electron–phonon scatterings is about two orders of magnitude slower and, thus, irrelevant at that time. Once the carriers have relaxed into hot quasi-Fermi distributions after about 10 fs, the overall dynamic slows down by two to three orders of magnitude (see the change of units in figure 4 from [1 fs] to [1 ps]). Here, electron–electron scattering and electron–phonon scattering become equally important. The scatterings slow further down by roughly another order of magnitude once the distributions cool down near room temperature after a few picoseconds. In- and out-scatterings due to electron–electron and electron–phonon scatterings lead eventually to the detailed balance that defines equilibrium Fermi distributions.

As can be seen in figure 5, during the first few femtoseconds of relaxation the phonon scatterings involving acoustic phonons are of similar importance as scatterings on optical phonons. Here, the phonon scattering rates including all phonon contributions are about twice as high as when acoustical phonons are omitted. For the broadening of the initial distribution scatterings involving large momentum transfers are of particular importance. While acoustical phonons have rather limited coupling strength for small momentum transfers as they are typically involved in intra-valley relaxation, their coupling strength and energy increases with increasing momentum transfer which increase their importance for intervalley scatterings. Without the acoustic phonons there are only
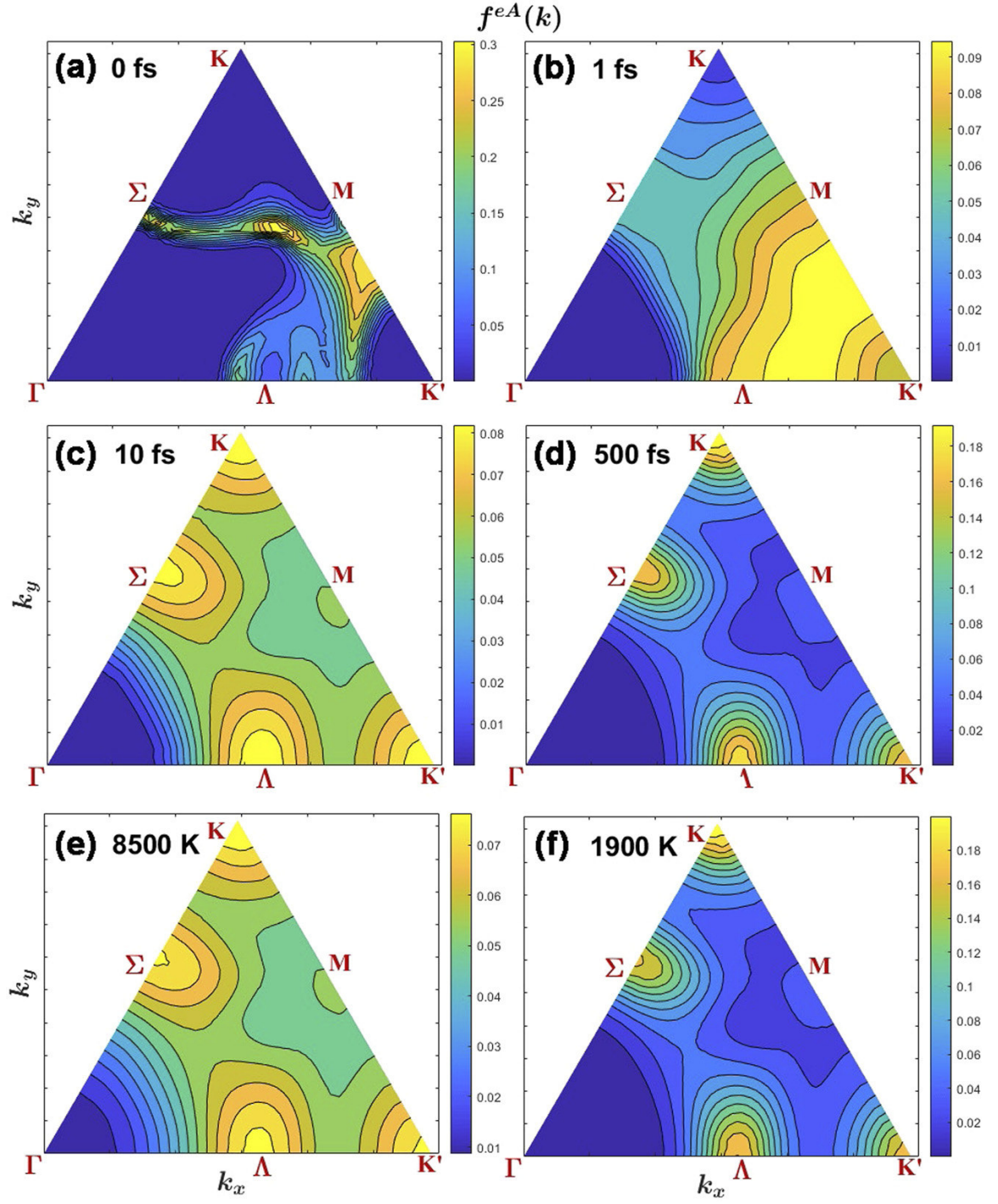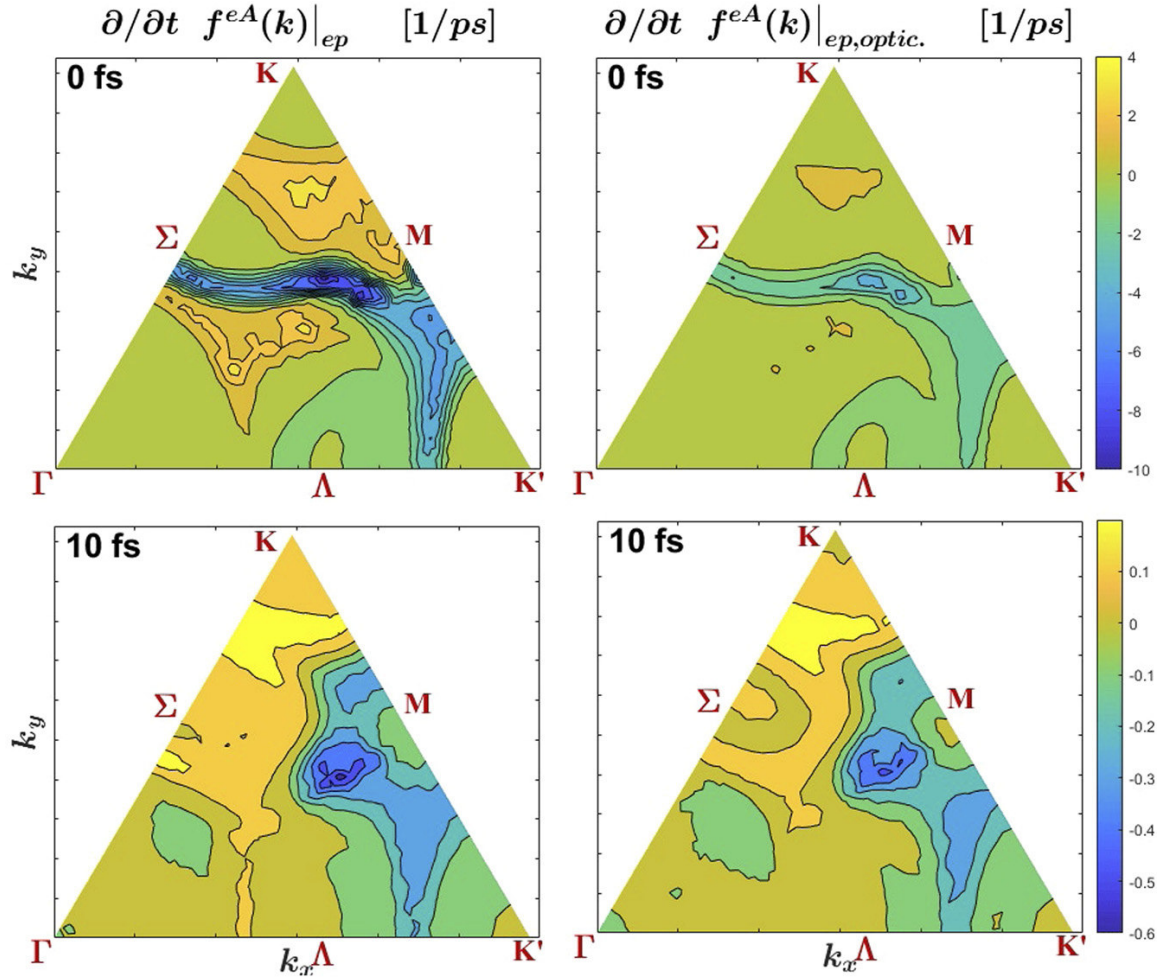
Figure 3. (a)–(d) Occupations of the electron A-band in a monolayer MoTe$_2$ at various times after initialisation according to equation (6) with $f_0 = 1.28$. Labels give the time after the start of relaxation. (e) and (f) Occupation of the electron A-band for the same total electron density as in (a)–(d), but using Fermi distributions with carrier temperatures of 8500 K and 1900 K, respectively.
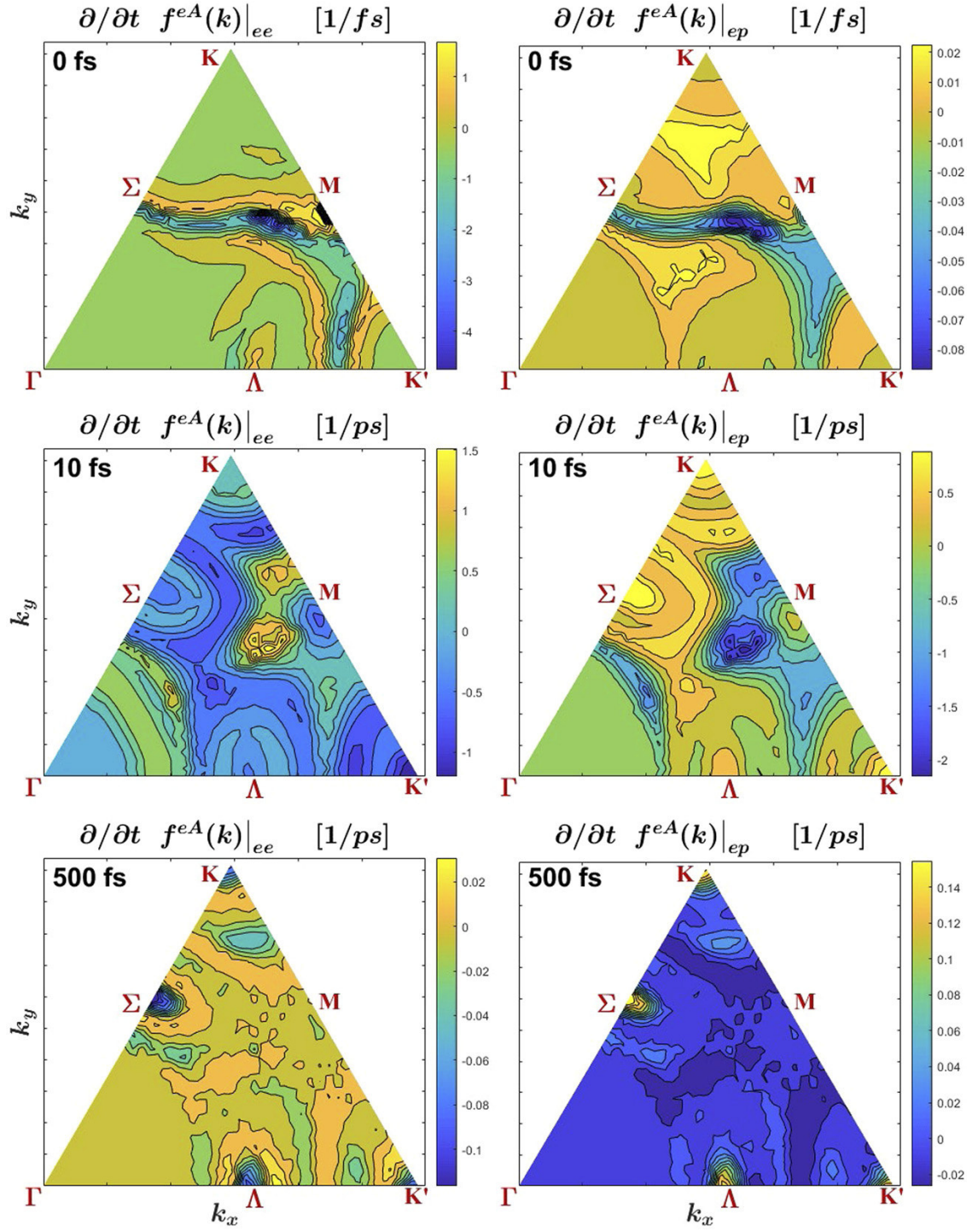
Figure 4. Change of occupations of the electron A-band in a monolayer MoTe₂ at various times after initialisation as for figure 3. Left: change due to electron–electron scattering. Right: change due to electron–phonon scattering. Units for the top two (bottom four) panels are [1 fs] ([1 ps]).

Figure 5. Change of occupations of the electron A-band in a monolayer MoTe$_2$ due to phonon scatterings only. Top: at the beginning of carrier relaxation. Bottom: after 10 fs of relaxation. Initialisation as for figure 3 but with $f_0 = 0.16$. Left: change due to all electron–phonon scatterings. Right: change only due to optical phonons.

very few scatterings far from the initial distribution, like into the area between Σ, K, and M or between Σ, Λ and Γ. After the carriers have assumed a hot quasi-Fermi distribution after about 10 fs, the carrier relaxation becomes dominated by intra-valley scatterings. Here, scatterings involving optical phonons dominate the total electron–phonon interaction and the total phonon rates are almost identical to those in the absence of processes involving acoustical phonons.

For the comparison of phonon scattering contributions in figure 5 we assumed an eight-times weaker excitation than for the results in figures 3 and 4. Electron–electron scattering roughly scales with the density squared, while electron–phonon scattering scales about linearly with it. Thus, for this lower excitation, phonon scatterings are overall more relevant than in the earlier study. Also, it has been observed that for strong excitations the limited phonon density of states in the two-dimensional system leads to a hot phonon bottleneck [41–44]. Here, a build-up of a nonequilibrium distribution

for optical phonons can strongly limit their cooling power which, in turn, increases the relative importance of acoustical phonons. This hot phonon effect is not included in our current model.

3.1.2. Resonant excitation. In order to study the inter-valley carrier transfer we place an artificial initial distribution almost exclusively in the K-valley of the A-band (and K'-valley of the B-band) and then calculate the scattering related carrier generation in the other valleys. Figure 6 shows the occupations of the electron A-band in MoTe$_2$ 2 fs after initialisation with equation (6) resonantly at the bandgap, i.e. with $\hbar\omega_L = (\epsilon^{\mathrm{e}}_{K,A} - \epsilon^{\mathrm{h}}_{K,A})$, and $f_0 = 1.28$. This initialisation creates an occupation of about 0.75 at K. After the initial 2 fs of dynamics, scatterings have created electron occupations of about 0.0014 at K, 0.0003 at Σ and 0.0007 at Λ.

Electron–electron scattering leads to a very fast initial relaxation within the K-valley to establish a Fermi-like
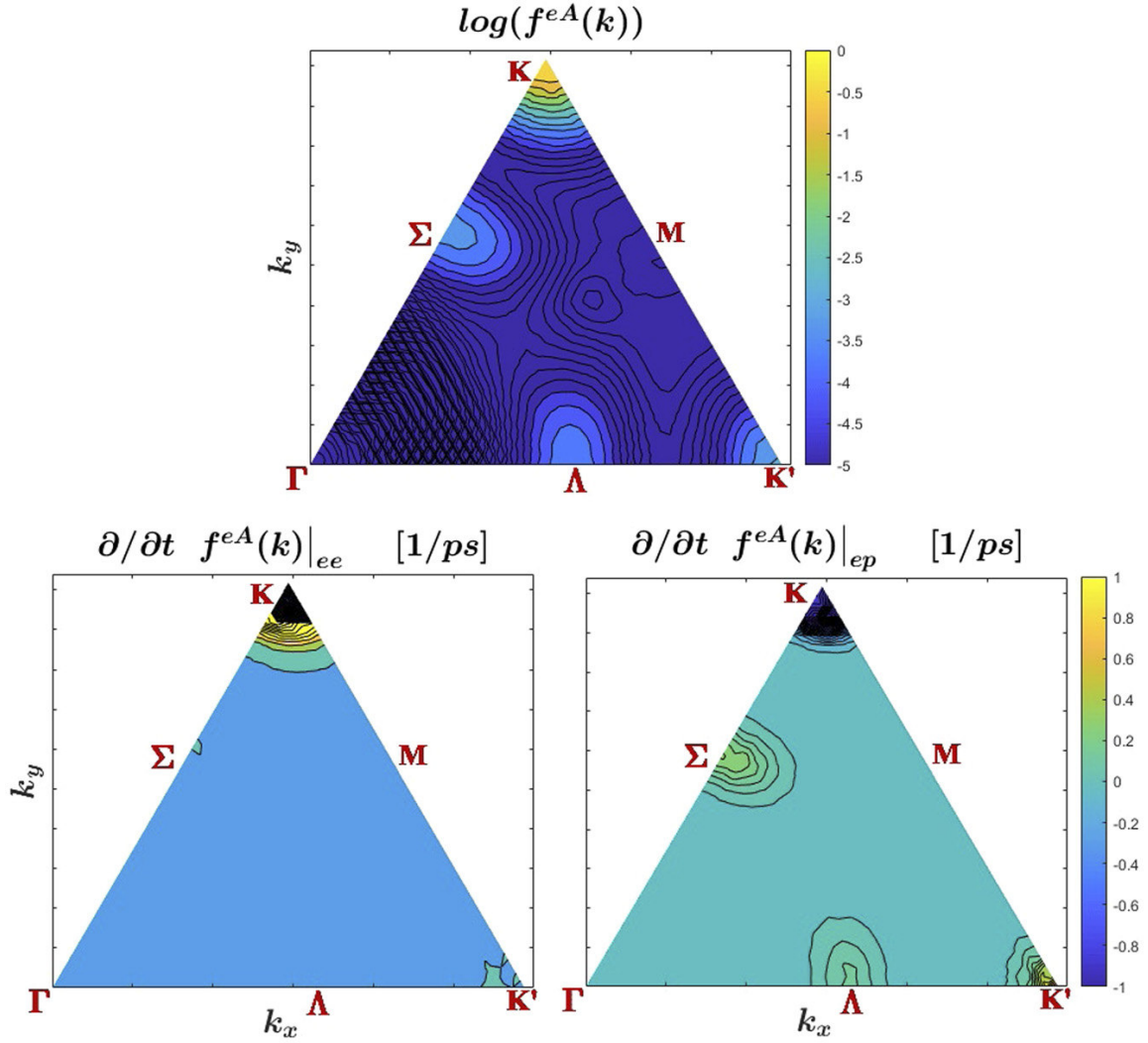
Figure 6. Top: logarithm of the occupation of the electron A-band in a monolayer MoTe$_2$ 2 fs after initialisation with equation (6) resonantly at the bandgap with $f_0 = 1.28$. Bottom left: change in occupations within the electron A-band due to electron–electron scattering. Bottom right: change due to electron–phonon scattering. Grid-line spacing is 0.05 ps in the lower two figures. Please note that the solid black areas near K in the lower two graphs are due to steep slopes resulting in overlapping contour lines and not data exceeding the color bar scale.

distribution there on a femtosecond timescale. However, it does not lead to significant inter-valley scattering due to the large involved momentum transfer. The rate is only about 0.1 ps for electron–electron scattering from K to K' and even less for transitions to Σ and Λ. Inter-valley transfer is dominated by electron–phonon scattering which during this initial phase creates carrier at a rate of about 0.8 ps in the K'-valley, 0.2 ps in the Λ-valley, and 0.3 ps in the Σ-valley.

Due to the much larger energy separation between the K and K' valley for holes than for electrons, the carrier transfer is significantly slower for these. We find a carrier generation rate at K' for holes within the A-band of only 0.004 ps for electron–electron scattering and 0.0006 ps for electron–phonon scattering,

3.2. Optical excitation

After having used artificial occupations in section 3.1 in order to determine carrier relaxation timescales and the importance of underlying mechanisms, we investigate here signatures of carrier relaxation under more realistic optical excitation conditions. We excite the system with a Gaussian pulse with an envelope of $E_0 \exp\left(-(t - t_0)^2/\Delta_t^2\right)$, with a width Δ_t of 50 fs. Since we are not concerned with details of the polarisation dynamics we do not evaluate the pertinent microscopic scattering processes but use a simple phenomenological dephasing rate $\hbar\gamma = 30$ meV. The central frequency of the pulse is 800 meV above the unrenormalized bandgap. While the pulse is present, carriers created by it lead to a dynamic renormalization of the bandgap [12]. As we have shown in section 3.1, these renormalizations can be comparable to the
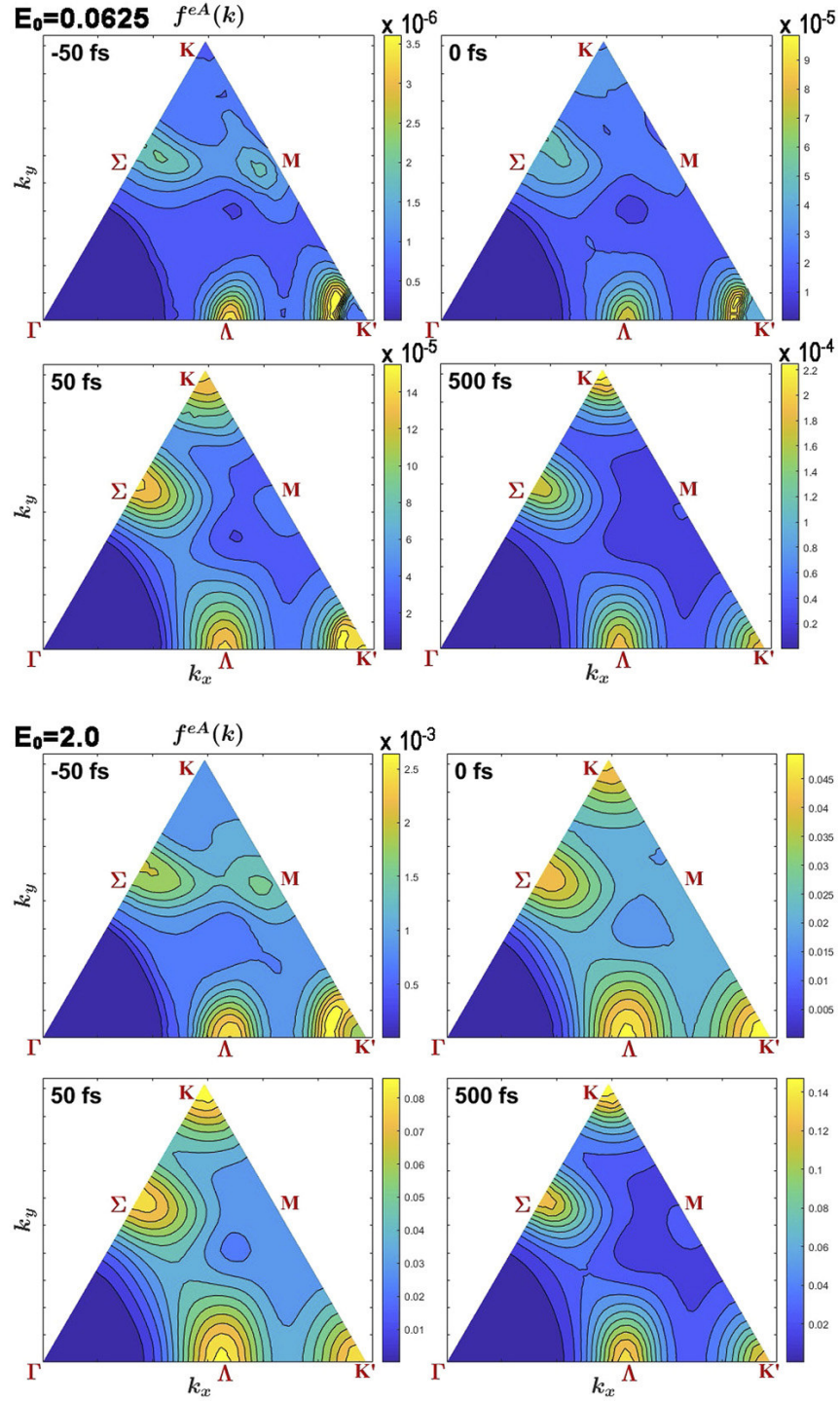
Figure 7. Occupation of the electron A-band at various times during optical excitation with a 50 fs long Gaussian pulse. The pulse maximum is at 0 fs and the excitation energy is 800 meV above the renormalized bandgap. Top (bottom): for an optical field $E_0 = 0.0625$ MV cm^{-1} ($E_0 = 2.00$ MV cm^{-1}).
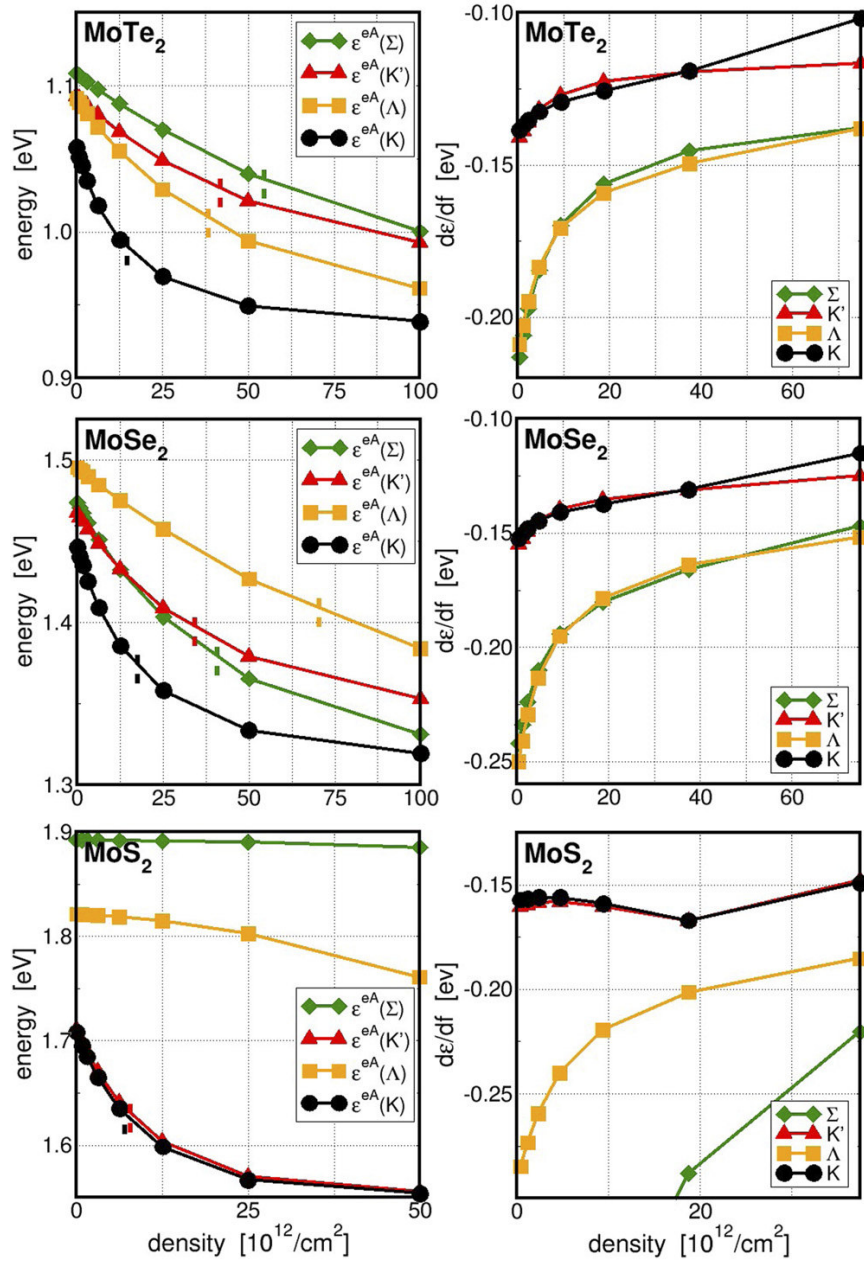
Figure 8. Left: renormalized energies of the electron A-band at critical points in the BZ as function of the electron density for monolayers of $MoTe_2$, $MoSe_2$ and MoS_2. Short dashed vertical lines mark the density at which the occupations are 50%. Right: change of energies with increase of occupation.

spectral width of the 50 fs pulse. Thus, the detuning between central frequency of the pulse and the renormalized bandgap changes during the pulse which leads to an excitation that is spectrally broader than the one created by the artificial instantaneous excitation.

Figure 7 shows the occupations in the electron A-band of a monolayer of $MoTe_2$ at various times during the excitation and for two optical field strength, $E_0 = 0.0625$ MV cm^{-1} and $E_0 = 2.00$ MV cm^{-1}. These pulses create electron densities of

about 1×10^{11} cm^2 and 8×10^{13} cm^2, respectively. For low excitation the carrier occupations stay below one percent at all times and smaller than 10^{-4} until after the center of the pulse passed. For these low occupations electron–electron scattering is very weak. Carriers remain near the original excitation until after the pulse maximum has passed and relax into the side valleys on a 10 fs timescale rather than the single femtosecond scale seen for higher excitation levels in section 3.1. Some deviations from the strictly monotone energy dependence of

the quasi Fermi distributions can still be seen 50 fs after the pulse maximum at the K' point.

For the strong excitation carriers relax into hot quasi-Fermi distributions already during the pulse. At the pulse maximum carriers are already predominantly relaxed to the bottom of all valleys and the only non-thermal signature is the fact that occupations at the individual valleys are not increasing with decreasing valley energy and are, e.g. higher at Λ and K' than at K. The subsequent cooling down of the carriers happens on a similar timescale as for lower excitation.

3.3. Energy renormalizations

In the next step, we evaluate the density dependence of the energy renormalizations for monolayers of MoTe$_2$, MoSe$_2$ and MoS$_2$ with carriers in global thermal equilibrium in order to check whether a transition from direct gap to indirect gap occurs. Figure 8 shows the computed renormalizations at the points K, K', Σ and Λ for these materials. At the highest densities considered here, the occupations at the K-point of the electron A-band reach reach values above 90%. For MoTe$_2$ the occupation at the highest density of 10^{14} cm^2 is about 95%, for MoSe$_2$ it is about 93%, and for MoS$_2$ the occupation at the highest density of 0.55×10^{14} cm^2 is about 97%. We use these high percentages in order to test the extreme limits of the renormalizations, well knowing that realistic densities for technical applications such as lasers create electron occupations of only about 50% which is sufficient to generate inversion in the gain regime since the hole occupation at the K-point are usually larger due to the lack of side valleys in the hole bandstructure. To provide benchmark, we therefore mark in figure 8 the densities at which the occupations reach the 50% level.

All together, we never observe a transition to an indirect bandstructure for any of the materials investigated here. For all realistic densities, the lowest electron energy always remains at the K-point. For all materials, the change in energy with change in occupation is stronger in the Σ and Λ side valleys than at the K and K' points (see the right-hand side panels of figure 8). This difference in renormalizations is caused in part by the valley dependence of the Coulomb interaction strength due to its dependence on the local wavefunction overlaps. It is also a consequence of the local bandstructure dispersion. In valleys with lower effective mass and, thus, lower density of states the occupations change stronger for a given change in the overall excitation level. However, since the side valleys are energetically significantly above the K-valley energies, their occupations in thermal equilibrium are low such that the local energy renormalizations are not strong enough to catch up to or even go below the K-point energy. Only in the hypothetical case where the energy separations in the unexcited ystems were smaller, the occupations in all valleys would be of similar order and a transition from direct to indirect would be possible.

The DFT determined energetic differences between the side- and the main-valley used in our work are considerably larger than those assumed in reference [22] where, e.g., the valley splitting at zero density in MoS$_2$ was assumed to be less than 15 meV while our calculations yield a separation of 113 meV (see table 1). For MoSe$_2$, we find a direct gap with a minimum valley separation of about 30 meV while reference [22] assumes an indirect bandgap for that material. Our determination of a direct bandgap for MoSe$_2$ agrees with most of the literature (see e.g. references [45, 46] and references therein). Alltogether, the larger energy separations are the main reason why our calculations do not predict any transition to an indirect band configuration in contrast to the findings of reference [22].

4. Summary and outlook

We combine first principle DFT calculations with fully microscopic many-body models based on the semiconductor DBEs in order to study the carrier dynamics and excitation induced energy renormalizations in monolayer TMDCs. Quantum Boltzmann type scattering equations for the electron–electron and electron–phonon scattering are solved taking into account the full BZ in order to resolve the detailed inter- and intra-valley relaxation processes.

For excitation high above the bandgap, we find that the carriers relax into hot quasi-Fermi distributions at the valley minima within less than 10 fs. This initial relaxation is dominated by electron–electron scatterings. For the subsequent intra-valley relaxation, electron–electron and electron–phonon scatterings turn out to be of comparable importance. The subsequent cooling of the hot plasma is mediated by phonon emission on a picosecond timescale. For resonant excitation at the K-gap, the subsequent transfer of carriers to other valleys is found to be dominated by phonon scatterings on a single picosecond timescale.

We find that non-equilibrium signatures in the electron distribution as caused by a spectrally narrow optical excitation are only observable in the low excitation regime. Electron–electron scattering processes on the same timescale of typical femtosecond pulses hide details of the excitation at higher excitation levels.

Finally, we show that for monolayer TMDCs with a direct bandgap at zero excitation and an energetic separation between the main valley and side valleys on the order of the thermal energy or more, like MoTe$_2$, MoSe$_2$ and MoS$_2$, the valley dependent energy renormalizations do not lead to a transition from direct to indirect bandgap. While the energy renormalization with increasing density can be stronger in the side valleys, at realistic densities it is not sufficient to shift the side-valley energetically below the K-point energy for any of the materials investigated here.

An investigation of further mono- and multi-layer TMDC materials and their heterostructures is required in order to see whether one of them allows for such a transition from direct

to indirect due to smaller valley separations, and/or a significantly valley-dependent Coulomb strength and/or density of states (effective mass). For example, an excitation induced transition from an indirect to a direct gap configuration might be possible in TMDC bi-layer systems.

Acknowledgments

Data availability statement

All data that support the findings of this study are included within the article (and any supplementary files).

ORCID iDs

Jörg Hader https://orcid.org/0000-0003-1760-3652
Josefine Neuhaus https://orcid.org/0000-0003-1440-1588
Jerome V Moloney https://orcid.org/0000-0001-8866-0326
Stephan W Koch https://orcid.org/0000-0001-5473-0170

References

[1] Chernikov A, Berkelbach T C, Hill H M, Rigosi A, Li Y, Aslan O B, Reichman D R, Hybertsen M S and Heinz T F 2014 Exciton binding energy and nonhydrogenic Rydberg series in monolayer WS$_2$ *Phys. Rev. Lett.* **113** 076802

[2] He K, Kumar N, Zhao L, Wang Z, Mak K F, Zhao H and Shan J 2014 Tightly bound excitons in monolayer WSe$_2$ *Phys. Rev. Lett.* **113** 026803

[3] Lopez-Sanchez O, Lembke D, Kayci M, Radenovic A and Kis A 2013 Ultrasensitive photodetectors based on monolayer MoS$_2$ *Nat. Nanotechnol.* **8** 497–501

[4] Zhang W, Huang J-K, Chen C-H, Chang Y-H, Cheng Y-J and Li L-J 2013 High-gain phototransistors based on a CVD MoS$_2$ monolayer *Adv. Mater.* **25** 3456–61

[5] Kufer D and Konstantatos G 2015 Highly sensitive, encapsulated MoS$_2$ photodetector with gate controllable gain and speed *Nano Lett.* **15** 7307–13

[6] Pospischil A, Furchi M M and Mueller T 2014 Solar-energy conversion and light emission in an atomic monolayer p–n diode *Nat. Nanotechnol.* **9** 257–61

[7] Sumesh C K 2019 Towards efficient photon management in nanostructured solar cells: role of 2D layered transition metal dichalcogenide semiconductors *Sol. Energy Mater. Sol. Cells* **192** 16–23

[8] Sundaram R S, Engel M, Lombardo A, Krupke R, Ferrari A C, Avouris P and Steiner M 2013 Electroluminescence in single layer MoS$_2$ *Nano Lett.* **13** 1416–21

[9] Ross J S *et al* 2014 Electrically tunable excitonic light-emitting diodes based on monolayer WSe$_2$ p–n junctions *Nat. Nanotechnol.* **9** 268–72

[10] Baugher B W H, Churchill H O H, Yang Y and Jarillo-Herrero P 2014 Optoelectronic devices based on electrically tunable p–n diodes in a monolayer dichalcogenide *Nat. Nanotechnol.* **9** 262–7

[11] Lohof F, Steinhoff A, Florian M, Lorke M, Erben D, Jahnke F and Gies C 2019 Prospects and limitations of transition metal dichalcogenide laser gain materials *Nano Lett.* **19** 210–7

[12] Meckbach L, Hader J, Huttner U, Neuhaus J, Steiner J T, Stroucken T, Moloney J V and Koch S W 2020 Ultrafast band-gap renormalization and build-up of optical gain in monolayer MoTe$_2$ *Phys. Rev.* B **101** 075401

[13] Wu S *et al* 2015 Monolayer semiconductor nanocavity lasers with ultralow thresholds *Nature* **520** 69–72

[14] Li Y, Zhang J, Huang D, Sun H, Fan F, Feng J, Wang Z and Ning C Z 2017 Room-temperature continuous-wave lasing from monolayer molybdenum ditelluride integrated with a silicon nanobeam cavity *Nat. Nanotechnol.* **12** 987–92

[15] Shang J *et al* 2017 Room-temperature 2D semiconductor activated vertical-cavity surface-emitting lasers *Nat. Commun.* **8** 543

[16] Chernikov A, Ruppert C, Hill H M, Rigosi A F and Heinz T F 2015 Population inversion and giant bandgap renormalization in atomically thin WS$_2$ layers *Nat. Photon.* **9** 466–70

[17] Steinhoff A, Rösner M, Jahnke F, Wehling T O and Gies C 2014 Influence of excited carriers on the optical and electronic properties of MoS$_2$ *Nano Lett.* **14** 3743–8

[18] Gao S and Yang L 2017 Renormalization of the quasiparticle band gap in doped two-dimensional materials from many-body calculations *Phys. Rev.* B **96** 155410

[19] Meckbach L, Stroucken T and Koch S W 2018 Giant excitation induced bandgap renormalization in TMDC monolayers *Appl. Phys. Lett.* **112** 061104

[20] Zeng H, Dai J, Yao W, Xiao D and Cui X 2012 Valley polarization in MoS$_2$ monolayers by optical pumping *Nat. Nanotechnol.* **7** 490–3

[21] Mak K F, He K, Shan J and Heinz T F 2012 Control of valley polarization in monolayer MoS$_2$ by optical helicity *Nat. Nanotechnol.* **7** 494–8

[22] Erben D, Steinhoff A, Gies C, Schönhoff G, Wehling T O and Jahnke F 2018 Excitation-induced transition to indirect bandgaps in atomically thin transition-metal dichalcogenide semiconductors *Phys. Rev.* B **98** 035434

[23] Steinhoff A, Florian M, Rösner M, Lorke M, Wehling T O, Gies C and Jahnke F 2016 Nonequilibrium carrier dynamics in transition metal dichalcogenide semiconductors *2D Mater.* **3** 031006

[24] Kaasbjerg K, Thygesen K S and Jacobsen K W 2012 Phonon-limited mobility in n-type single-layer MoS$_2$ from first principles *Phys. Rev.* B **85** 115317

[25] Selig M *et al* 2016 Excitonic linewidth and coherence lifetime in monolayer transition metal dichalcogenides *Nat. Commun.* **7** 13279

[26] Helmrich S *et al* 2021 Phonon-assisted Intervalley scattering determines ultrafast exciton dynamics in MoSe$_2$ bilayers *Phys. Rev. Lett.* **127** 157403

[27] Kohn W and Sham L J 1965 Self-consistent equations including exchange and correlation effects *Phys. Rev.* **140** A1133–8

[28] Kresse G and Hafner J 1993 *Ab initio* molecular dynamics for liquid metals *Phys. Rev.* B **47** R558–61

[29] Kresse G and Hafner J 1994 *Ab initio* molecular-dynamics simulation of the liquid–metal amorphous-semiconductor transition in germanium *Phys. Rev.* B **49** 1425–69

[30] Kresse G and Furthmüller J 1996 Efficient iterative schemes for *ab initio* total-energy calculations using a plane-wave basis set *Phys. Rev.* B **54** 11169–86

[31] Kresse G and Furthmüller J 1996 Efficiency of *ab initio* total energy calculations for metals and semiconductors using a plane-wave basis set *Comput. Mater. Sci.* **6** 15–50

[32] Rasmussen F A and Thygesen K S 2015 Computational 2D materials database: electronic structure of transition-metal dichalcogenides and oxides *J. Phys. Chem.* C **119** 13169–83

[33] Korkmaz Y A, Bulutay C and Sevik C 2021 $k \cdot p$ parameterizaion and linear and circular dichroism in strained monolayer (Janus) transition metal dichalcogenides from first-principles *J. Phys. Chem.* C **125** 7439–50

[34] Blundo E *et al* 2020 Evidence of the direct-to-indirect band gap transition in strained two-dimensional WS_2, MoS_2, and WSe_2 *Phys. Rev. Res.* **2** 012024

[35] Zhang C, Chen Y, Johnson A, Li M-Y, Li L-J, Mende P C, Feenstra R M and Shih C-K 2015 Probing critical point energies of transition metal dichalcogenides: surprising indirect gap of single layer WSe_2 *Nano Lett.* **15** 6494–500

[36] Giannozzi P *et al* 2009 QUANTUM ESPRESSO: a modular and open-source software project for quantum simulations of materials *J. Phys.: Condens. Matter* **21** 395502

[37] Giannozzi P *et al* 2017 Advanced capabilities for materials modelling with QUANTUM ESPRESSO *J. Phys.: Condens. Matter* **29** 465901

[38] Kormányos A, Burkard G, Gmitra M, Fabian J, Zólyomi V, Drummond N D and Fal'ko V 2015 $k \cdot p$ theory for two-dimensional transition metal dichalcogenide semiconductors *2D Mater.* **2** 022001

[39] Shafique A and Shin Y-H 2017 Strain engineering of phonon thermal transport properties in monolayer $2H\text{-}MoTe_2$ *Phys. Chem. Chem. Phys.* **19** 32072–8

[40] Zulfiqar M, Zhao Y, Li G, Li Z and Ni J 2019 Intrinsic thermal conductivities of monolayer transition metal dichalcogenides MX_2 (M = Mo, W; X = S, Se, Te) *Sci. Rep.* **9** 4571

[41] Kaasbjerg K, Bhargavi K S and Kubakaddi S S 2014 Hot-electron cooling by acoustic and optical phonons in monolayers of MoS_2 and other transition-metal dichalcogenides *Phys. Rev.* B **90** 165436

[42] Nie Z, Long R, Teguh J S, Huang C-C, Hewak D W, Yeow E K L, Shen Z, Prezhdo O V and Loh Z-H 2015 Ultrafast electron and hole relaxation pathways in few-layer MoS_2 *J. Phys. Chem.* C **119** 20698–708

[43] Shah J, Pinczuk A, Gossard A C and Wiegmann W 1985 Energy-loss rates for hot electrons and holes in GaAs quantum wells *Phys. Rev. Lett.* **54** 2045–8

[44] Breusing M *et al* 2011 Ultrafast nonequilibrium carrier dynamics in a single graphene layer *Phys. Rev.* B **83** 153410

[45] Pandey S K, Das R and Mahadevan P 2020 Layer-dependent electronic structure changes in transition metal dichalcogenides: the microscopic origin *ACS Omega* **5** 15169–76

[46] Silva-Guillén J, San-Jose P and Roldán R 2016 Electronic band structure of transition metal dichalcogenides from *ab initio* and Slater–Koster tight-binding model *Appl. Sci.* **6** 284

Paper V

J. Neuhaus,T. Stroucken, and S. W. Koch:

Electron-hole Plasma-Induced Dephasing in Transition Metal Dichalcogenides

Abstract: The electron-hole-plasma induced dephasing and its influence on the excitonic absorption and the degenerate four-wave mixing spectra in monolayer transition metal dichalcogenides is investigated. A systematic microscopic theory is presented that combines density functional calculations for the linear material properties with a many-body equation of motion approach for the optical response. Numerical results are obtained for the example of an hBN encapsulated layer of MoS_2. It is shown that the influence of the excitation induced dephasing depends only weakly on the exact shape of the carrier distribution for small densities whereas distribution details become more important with increasing density.

Check for updates

Electron–Hole Plasma-Induced Dephasing in Transition Metal Dichalcogenides

Josefine Neuhaus,* Tineke Stroucken, and Stephan W. Koch*

Electron–hole plasma-induced dephasing and its influence on the excitonic absorption and the degenerate four-wave mixing spectra in monolayer transition metal dichalcogenides are investigated. A systematic microscopic theory is presented that combines density functional calculations for the linear material properties with a many-body equation of motion approach for the optical response. Numerical results are obtained for the example of an hBN-encapsulated layer of MoS_2. It is shown that the influence of the excitation-induced dephasing depends only weakly on the exact shape of the carrier distribution for small densities, whereas distribution details become more important with increasing density.

1. Introduction

Since the first successful studies on graphite and its single and few-layer configurations, the research on van der Waals bonded materials, including the class of semiconducting transition metal dichalcogenides (TMDCs), has become increasingly topical. While several aspects of bulk TMDCs were already investigated in the 1960s and 1970s,[1–3] it was the ability to systematically reduce the thickness down to a monolayer that revealed the transition from an indirect to a direct bandgap in these materials.[4] This feature, in combination with the strong light–matter interaction and the additional degrees of freedom such as the valley index resulting from the quasi-2D hexagonal symmetry, stimulated vivid and manifold research on these systems and makes TMDCs interesting even for technological applications.

Generally, the TMDC thickness reduction down to a monolayer not only leads to a direct bandgap but also to strong Coulomb interactions and reduced intrinsic screening, yielding excitonic binding energies of several hundred meV.[5–8] Many aspects of the resulting pronounced excitonic properties and related interaction effects in semiconducting TMDC materials have been investigated and

discussed in the past years.[4,5,9–11] As one of the consequences of the reduced intrinsic screening in monolayer TMDCs, one experiences a strong dependence of near-bandgap optical properties on details of the dielectric environment and the excitation conditions. With regard to the excitonic linewidth, a drastic narrowing was seen in experiments when monolayers were encapsulated in hBN. Even though this feature is not yet completely understood, it was interpreted as a suppression of inhomogeneities due to reduced sample imperfections.[12]

As an intrinsic feature, the excitonic resonance broadening due to temperature changes or the additional occupation of different excitonic states has been analyzed both experimentally and theoretically.[13–19] For example, in four-wave mixing experiments, exciton population changes have been induced by varying the spectrally selective excitation power of the first pulse.[20] It was shown that the details of the excitonic scattering processes are influenced by the different energetic structures in molybdenum and tungsten-based materials.[16]

To extend these studies into the range of unbound electron–hole plasma excitations, we theoretically investigate in this work the homogeneous linewidth changes and the four-wave mixing decay in the presence of the above-bandgap-excited TMDCs. As a representative example, we evaluate a fully microscopic theory to determine the impact of prepulse-generated incoherent carrier populations for parameters corresponding to an hBN-encapsulated monolayer of MoS_2. In particular, we analyze the excitation-induced dephasing (EID) dependence on details of the carrier distributions in different parts of the bandstructure and at different electronic temperatures.

2. Theory

In our calculations, we use a systematic approach where density functional theory (DFT)[21,22] is utilized to extract the fundamental material properties such as its bandstructure, as well as the Coulomb and optical dipole matrix elements. These quantities serve as inputs for our many-body equation of motion (EOM) approach, which is then numerically evaluated to gain insight into the dynamical and optical properties of the system under investigation. For the studies presented in this work, we map our full DFT bandstructure onto an effective four-band Hamiltonian. In particular, we include the spin-split conduction and valence bands as these are dominant for the optical response of the system and take the bandstructure around the direct bandgap (K/K') and side (Σ/Λ) valley into account.

J. Neuhaus, T. Stroucken, S. W. Koch
Department of Physics and Material Sciences Center
Philipps University Marburg
Renthof 5, D-35032 Marburg, Germany
E-mail: josefine.neuhaus@physik.uni-marburg.de;
stephan.w.koch@physik.uni-marburg.de

The ORCID identification number(s) for the author(s) of this article can be found under https://doi.org/10.1002/pssr.202100391.

ADVANCED SCIENCE NEWS
www.advancedsciencenews.com

pss rrl
physica status solidi
www.pss-rapid.com

We use the massive Dirac–Fermion (MDF) model[23] to describe the single-particle dispersion around the K/K' valley, yielding a noninteracting relativistic single-particle dispersion of $\varepsilon^{c,v}_{\sigma\tau\mathbf{k}} = \pm\frac{1}{2}\sqrt{\Delta^2_{\sigma\tau} + 4\hbar^2 v^2_{\mathrm{F},\sigma\tau}k^2}$, with spin ($\sigma$)- and valley ($\tau$)-dependent gap $\Delta_{\sigma\tau}$ and Fermi velocity $v_{\mathrm{F},\sigma\tau}$, and treat the dispersion at the side valley in effective mass approximation. Here, the necessary input parameters are obtained by fitting the DFT bandstructure that is calculated using the Perdew–Burke–Ernzerhof (PBE)[24] functional as implemented in the Vienna Ab initio Simulation Package (VASP).[25–27] Due to the finite thickness of monolayer TMDCs, the dielectric environment as well as the finite extension play a crucial role for the Coulomb interaction in these materials. The screening contributions resulting from remote bands and the dielectric environment are modeled within an analytic approach by solving Poisson's equation for the layered system[28] and the Coulomb matrix elements are calculated exploiting the DFT wave functions.[29]

In this work, we are interested in the electron–hole plasma-induced dephasing of the interband polarization $P^{vc}_{\mathbf{k}} = \langle c^\dagger_{\mathbf{k}} \nu_{\mathbf{k}}\rangle$ and its manifestation in the linear and the four-wave mixing (FWM) spectrum. We assume a scenario where an initial quasi-static carrier distribution $f^0_{\mathbf{k}}$ is generated by a pulse that precedes any later probe or FWM pulses such that the prepulse-induced polarization $P^{vc,0}_{\mathbf{k}}$ already decays. For this case, the dynamics of the interband polarization caused by additional pulses can be described via the screened Dirac–Bloch equation.

$$i\hbar\frac{d}{dt}P^{vc}_{\mathbf{k}} = (2\tilde{\Sigma}^{[0]}_{\mathbf{k}} - i\gamma)P^{vc}_{\mathbf{k}} - (1 - 2f^0_{\mathbf{k}})\tilde{\Omega}^{vc}_{\mathbf{k}} + \Gamma^{vc}_{\mathbf{k}}[f^0_{\mathbf{k}}]$$
$$- 2\left(\sum_{\mathbf{k}'}(W^{vvvv}_{\mathbf{k}-\mathbf{k}';\mathbf{k};\mathbf{k}'} - W^{cvvc}_{\mathbf{k}-\mathbf{k}';\mathbf{k};\mathbf{k}'})\Delta f_{\mathbf{k}'} - \Delta f_{\mathbf{k}}\tilde{\Omega}^{vc}_{\mathbf{k}}\right) \quad (1)$$

where $\Delta f_{\mathbf{k}}$ denotes the changes in the carrier distribution arising from the later pulses. In Equation (1), the first line represents the linear part and the second line contains the nonlinear sources. Furthermore, $\tilde{\Sigma}^{[0]}_{\mathbf{k}}$ describes the renormalized single-particle energy, $\tilde{\Omega}^{vc}_{\mathbf{k}}$ the renormalized Rabi energy including the interband momentum matrix element p_{cv} with $p_{cv,K^{(')}} = m_0 v_{\mathrm{F}}$ for linear polarized light, and γ is a phenomenological dephasing rate

$$2\tilde{\Sigma}^{[0]}_{\mathbf{k}} = 2\varepsilon_{\mathbf{k}} + \sum_{\mathbf{k}'}(W^{vvvv}_{\mathbf{k}-\mathbf{k}';\mathbf{k};\mathbf{k}'} - W^{cvvc}_{\mathbf{k}-\mathbf{k}';\mathbf{k};\mathbf{k}'})(1 - 2f^0_{\mathbf{k}'})$$
$$\tilde{\Omega}^{vc}_{\mathbf{k}} = \frac{e}{m_0 c}p_{cv}\cdot A - \sum_{\mathbf{k}'}W^{ccvv}_{\mathbf{k}-\mathbf{k}';\mathbf{k};\mathbf{k}'}P^{vc}_{\mathbf{k}'} \quad (2)$$

The contribution $\Gamma^{vc}_{\mathbf{k}}[f^0_{\mathbf{k}}]$ represents the linearized scattering due to the initial carrier densities from polarization-carrier interaction in second-order Born approximation. Beyond that, correlation effects enter the calculations through screening of the Coulomb interaction

$$W^{\alpha,\beta,\beta',\alpha'}_{\mathbf{q},\mathbf{k},\mathbf{k}'} = W_{\mathbf{q}}(\omega)\langle\alpha\mathbf{k} - \mathbf{q}|\alpha'\mathbf{k}\rangle\langle\beta\mathbf{k}' + \mathbf{q}|\beta'\mathbf{k}'\rangle$$
$$W_{\mathbf{q}}(\omega) = V_{\mathbf{q}} + V_{\mathbf{q}}\Pi_{\mathbf{q}}(\omega)W_{\mathbf{q}}(\omega)$$
$$\Pi_{\mathbf{q}}(\omega) = \sum_{\alpha,\mathbf{p}}\frac{f^{0,\alpha}_{\mathbf{p}-\mathbf{q}} - f^{0,\alpha}_{\mathbf{p}}}{\hbar\omega - \tilde{\Sigma}^\alpha_{\mathbf{p}-\mathbf{q}} + \tilde{\Sigma}^\alpha_{\mathbf{p}} + i\hbar\gamma_T} \quad (3)$$

where $V_{\mathbf{q}}$ is the Coulomb potential that includes contributions from ground state and environmental screening. In the Lindhard polarization function, $\Pi_{\mathbf{q}}$, the sum is evaluated for all spin, valley, and band indices subsumed in α. Here, the screened renormalized energies enter the denominator and we include a phenomenological background dephasing γ_T to account for all the processes not treated explicitly in our theory. In our numerical evaluations, we use a value of 300 meV to match the experimentally determined slope of the excitation-induced bandgap renormalization.[30]

With all those ingredients, the scattering contributions are

$$\Gamma^{vc}_{\mathbf{k}}[f_{\mathbf{k}}](\omega)\big|_{\mathrm{el}} = \sum_{\mathbf{q}\neq 0}[I^{vc}_{\mathbf{q};\mathbf{k}}(\omega) - I^{vc}_{\mathbf{q};\mathbf{k}+\mathbf{q}}(\omega)] \quad (4)$$

$$I^{vc}_{\mathbf{q};\mathbf{k}}(\omega) = \sum_{\alpha\mathbf{k}'}V_{\mathbf{q}}W_{\mathbf{q}}(\omega)\frac{\left(\overline{f}^c_{\mathbf{k}-\mathbf{q}}f^\alpha_{\mathbf{k}'}\overline{f}^\alpha_{\mathbf{k}'+\mathbf{q}}\right)_\Sigma P_{\mathbf{k}} - \left(f^v_{\mathbf{k}}f^\alpha_{\mathbf{k}'}\overline{f}^\alpha_{\mathbf{k}'+\mathbf{q}}\right)_\Sigma P_{\mathbf{k}-\mathbf{q}}}{\hbar\omega - \tilde{\Sigma}^c_{\mathbf{k}-\mathbf{q}} + \tilde{\Sigma}^v_{\mathbf{k}} - \tilde{\Sigma}^\alpha_{\mathbf{k}'+\mathbf{q}} + \tilde{\Sigma}^\alpha_{\mathbf{k}'} + i\hbar\gamma_T}$$
$$(5)$$

where we used the shorthand notation $(f^\alpha_{\mathbf{k}_1}f^\beta_{\mathbf{k}_2}\overline{f}^\gamma_{\mathbf{k}_3})_\Sigma = f^\alpha_{\mathbf{k}_1}f^\beta_{\mathbf{k}_2}(1 - f^\gamma_{\mathbf{k}_3}) + (1 - f^\alpha_{\mathbf{k}_1})(1 - f^\beta_{\mathbf{k}_2})f^\gamma_{\mathbf{k}_3}$.

3. Numerical Results

We numerically evaluate our coupled set of equations for parameters corresponding to an hBN-encapsulated monolayer of MoS$_2$. As shown in **Figure 1**, the unrenormalized band dispersion $\varepsilon_{\alpha,\mathbf{k}}$ in the vicinity of the main (K/K') and side (Σ/Λ) valleys is approximated on the basis of the DFT bandstructure. The resulting non-interacting bandgap at the K/K' point is $\Delta_{\mathrm{A}} = 1.682$ eV and $\Delta_{\mathrm{B}} = 1.831$ eV for the A ($K_\uparrow/K'_\downarrow$) and B ($K_\downarrow/K'_\uparrow$) bands, respectively. The valence band maxima are split by 146 meV. The local conduction band minima marking the side valley (Σ/Λ) are $\lambda_{c,\mathrm{A}} = 133$ meV, respectively, and $\lambda_{c,\mathrm{B}} = 200$ meV above the minima at the K/K' point with the corresponding spin. The local band curvature is described in good approximation by a relativistic dispersion with Fermi velocity $\hbar v_{\mathrm{F,A}} = 3.532$ eVÅ and $\hbar v_{\mathrm{F,B}} = 3.467$ eVÅ for the main and by an effective mass approach with $m^*_\mathrm{A} = 0.611 m_0$ and $m^*_\mathrm{B} = 0.705 m_0$ for the side valley, respectively. Comparable
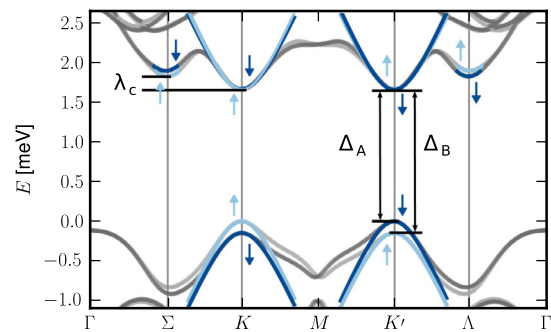
Figure 1. DFT bandstructure of a MoS$_2$ monolayer (gray scale) and approximated unrenormalized band dispersion (blue scale) around the main and side valleys. The spin of the bands is indicated by the corresponding colored arrows.

results were reported in different DFT studies.[31,32] Furthermore, to model the background screening, we carried out DFT calculations for the bulk structure of MoS_2, yielding in-plane and out-of-plane dielectric constants of $\varepsilon_\parallel^B = 15.19$ and $\varepsilon_\perp = 6.38$ and an interlayer distance of $D = 6.18$ Å, respectively. To model the influence of the encapsulating hBN, we use $\kappa = \sqrt{\varepsilon_\parallel \varepsilon_\perp} = 4.2$.

3.1. Excitation-Induced Absorption Changes

Generally, after the short-pulse excitation of a TMDC monolayer well above the bandgap, strong Coulomb scattering leads to relaxation into hot quasiequilibrium distributions within the first tens of femtoseconds. Thereafter, the carriers equilibrate with the lattice via carrier–phonon interactions on the timescale of few picoseconds.[30] To analyze the consequences of the pre-excited carrier populations, we evaluate the excitation-induced broadening of the 1s-exciton absorption linewidth for different distributions. As relevant examples, we show in **Figure 2** results for the case where we have an equal amount of carriers in the A- and B-band and compare it with the situation of thermal equilibrium, where the holes experience a drain between the K and K' valley due to the large energy offset between the valleys. In all calculations we assume that the carriers can be described via Fermi distributions $f_{\alpha \mathbf{k}}(\mu_\alpha, T) = (1 + e^{(\Sigma_{\mathbf{k}}^{[0]} - \mu_\alpha)\beta})^{-1}$ with the chemical potential μ_α that is determined iteratively with the renormalized single-particle dispersion and the screened Coulomb matrix elements.

Figure 2a shows the impact of the excited electron–hole plasma on the excitation-induced broadening of the linear

Figure 2. a) Dependency of the excitation-dependent linewidth of the E_{1s} exciton resonance on the carrier distribution in the sample. The carriers are either distributed equally to the A- and B-bands in the different K-valleys (light blue) or a common chemical potential is assumed (dark blue), resembling the situation of thermal equilibrium, where a drain of holes between the K valleys is observed. The carrier distribution in the b) conduction and c) valence band and the different bands (A: dashed, B: solid) at the K-valley are shown exemplarily for $n_0 = 2.0 \times 10^{12}$ cm^{-2}.

spectra. As a dominant effect, we notice a nearly linear increase of the 1s-exciton linewidth with the carrier density by evaluating the first line of Equation (1) in the frequency domain. To investigate the dependence on details of the electron–hole distributions, we carry out calculations for different equilibration conditions and an electronic temperature of $T = 300$ K.
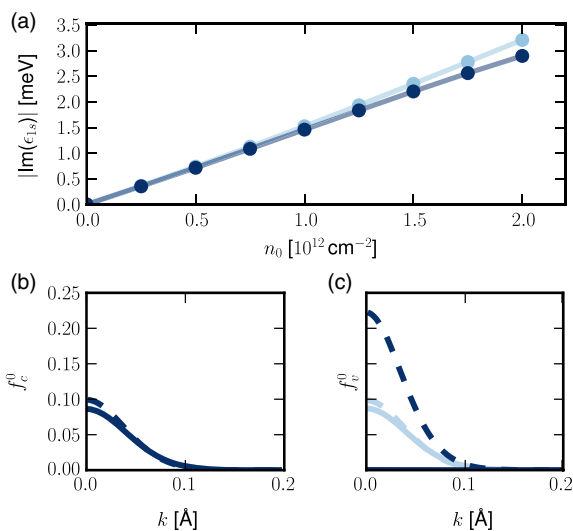
As a representative example, Figure 2b shows for the density $n_0 = 2 \times 10^{12}$ cm^{-2} that the carrier distribution in the conduction band is only weakly affected by the overall carrier equilibration within the bandstructure. However, due to the large valence band splitting, there is a significant drift of holes between the valleys, as depicted in Figure 2c. This leads to a higher occupation of the lowest-lying band and further increases the valence band offset by 27 meV for the illustrated density.

Comparing the different results in Figure 2a, we see that the dependence of the linewidth increase on the details of the carrier distributions is marginal for low densities, whereas it becomes somewhat more pronounced in the regime of elevated electron–hole pair populations. Moreover, we notice that the unequal hole distribution in different valence bands, respectively, the different valleys, leads to a somewhat reduced broadening of the lowest excitonic state.

The different distributions selected for Figure 2 are motivated by the fact that generally, in addition to the redistribution of the holes between the K valleys, an electron drift toward the side valleys takes place. However, as the offset between the valleys is considerably large—133 meV in MoS_2 without initial carriers—in the regimes considered in this work, only a small amount of carriers is located in the side valley. Hence, the influence of the side valley in MoS_2 in the low-density regime is negligible if only scattering processes with incoherent carriers are considered. This scenario differs from that in a tungsten-based sample, where EID effects were studied depending on the exciton density, and a crucial importance of the intervalley scattering with the side valley was reported.[13,16] These observations demonstrate the importance of the different energetic structures in tungsten- and molybdenum-based materials on the one hand and the dependence of EID effects on the particular nature of the investigated scattering processes on the other hand.
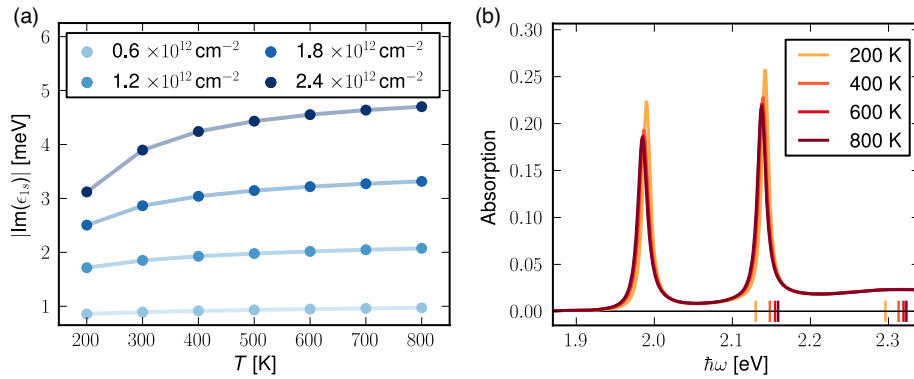
To get some insight into the importance of carrier temperature on the excitation-induced modifications of the optical response, we show in **Figure 3** the changes in the linear absorption spectra and the excitonic linewidth. In Figure 3a, we see that resonance broadening increases with increasing temperature for all densities investigated. The changes become more pronounced for elevated densities and reach a plateau for higher temperatures. While the increase in the linewidth for $n_0 = 0.6 \times 10^{12}$ cm^{-2} is in the range of 0.1 meV, the overall broadening for $n_0 = 2.4 \times 10^{12}$ cm^{-2} increases by 1.58 meV between a carrier temperature of $T = 200$ K and $T = 800$ K, which can be seen even in the linear absorption spectrum (Figure 3b).

Generally, an increasing carrier temperature leads to a spreading of the Fermi distributions and less occupation close to the main valley. As is indicated on the energy axis of Figure 3b, this distribution broadening goes along with a smaller bandgap renormalization. The microscopic origin of this reduction can be found in both the influence of the screening, that is approximately described by the screening wave number, which in turn is

**ADVANCED
SCIENCE NEWS**

www.advancedsciencenews.com

pss rrl
physica status solidi

www.pss-rapid.com

Figure 3. a) Dependency of the excitation-dependent 1s-exciton linewidth on the carrier temperature for different carrier densities distributed equally in the bands. The dephasing increases with elevated temperatures and reaches a density-dependent plateau for high temperatures. b) The linear absorption spectrum for the carrier density $n_0 = 2.4 \times 10^{12}$ cm^{-2} and the carrier temperatures of 200, 400, 600, and 800 K. The respective renormalized A and B bandgaps are marked by the vertical bars on the energy axis.

proportional to the carrier occupation at $k = K$, and the influence of phase-space filling that decreases due to the distribution broadening effects. In addition to the carrier temperature-dependent bandgap reduction, a shift of the excitonic resonance on the order of few meV can be noticed in Figure 3b.

3.2. EID Signatures in Four-Wave Mixing Spectroscopy

Experimentally, homogeneous and inhomogeneous broadening effects cannot be separated in a linear absorption spectrum. However, the influence of homogeneous broadening can be identified using nonlinear spectroscopic techniques such as degenerate four-wave mixing (DFWM) spectroscopy. In DFWM, two laser pulses with wave vectors $\mathbf{k}_1$ and $\mathbf{k}_2$, varying time delay τ, and low intensities are used, and the scattered signal $P^{[3]}$, resulting from the interaction of the second pulse with the grating induced by the interaction of the polarization $P^{[1]}$ generated by the first pulse and the second pulse, in direction $2\mathbf{k}_2 - \mathbf{k}_1$, is measured.

Assuming low-intensity pulses and complete decay of the prepulse-induced coherent polarization, changes in the

population due to the four-wave mixing pulses in the presence of initial incoherent carriers can be approximated by $\Delta f_{\mathbf{k}} \approx \frac{|P^{vc}_{\mathbf{k}}|^2}{1-2f^0_{\mathbf{k}}} \equiv |\tilde{P}^{vc}_{\mathbf{k}}|^2$. The resulting equation for the polarization $\tilde{P}^{vc}_{\mathbf{k}}$ is solved iteratively in the eigenbasis of

$$H^{[0]} = 2\tilde{\Sigma}^{[0]}_{\mathbf{k}}\delta_{\mathbf{k},\mathbf{k}'} - \sqrt{1-2f^0_{\mathbf{k}}}\, W^{ccvv}_{\mathbf{k};\mathbf{k}'}\sqrt{1-2f^0_{\mathbf{k}'}} + \frac{\sqrt{1-2f^0_{\mathbf{k}}}}{\sqrt{1-2f^0_{\mathbf{k}'}}}\Gamma_{\mathbf{k},\mathbf{k}'}$$
(6)

with the left and right eigenstates $\phi^{\mathrm{L}}_\lambda(k)$ and $\phi^{\mathrm{R}}_\lambda(k)$ for eigenvalues $\varepsilon_\lambda = \hbar\omega_\lambda$. Here, the Coulomb matrix elements are evaluated for the dominating frequency $\omega = \omega_{1s}$. The polarization of nth order in the optical field is then given by $P^{[n]}_\lambda(t) = \frac{1}{i\hbar}\int^t_{-\infty}dt' e^{-i(\omega_\lambda - i\gamma)(t-t')}Q^{[n]}_\lambda(t')$, with the linear source $Q^{[1]}_\lambda = \frac{e}{m_0 c}\sum_k \sqrt{1-2f^0_k}\,\mathbf{p}_{vc}\cdot\mathbf{A}[\phi^{\mathrm{L}}_\lambda(k)]^*$ and the relevant parts of the cubic source, that is, the parts that are $\propto A^*_1 A^2_2$.

$$Q^{[3,\mathrm{FWM}]}_\lambda/2 = \frac{e}{m_0 c}\sum_k \sum_{\lambda_1,\lambda_2}\frac{\mathbf{p}_{vc}\cdot\mathbf{A}_2}{\sqrt{1-2f^0_k}}[\phi^{\mathrm{L}}_\lambda(k)]^*[\phi^{\mathrm{R}}_{\lambda_1}(k)]^*\phi^{\mathrm{R}}_{\lambda_2}(k)P^*_{1,\lambda_1}P_{2,\lambda_2}$$

$$+ \sum_{k,k'}\sum_{\lambda_1,\lambda_2,\lambda_3}[\phi^{\mathrm{L}}_\lambda(k)]^*[\phi^{\mathrm{R}}_{\lambda_1}(k)]^*\phi^{\mathrm{R}}_{\lambda_2}(k)\phi^{\mathrm{R}}_{\lambda_3}(k')W^{ccvv}_{k,k'}\frac{\sqrt{1-2f^0_{k'}}}{\sqrt{1-2f^0_k}}P^*_{1,\lambda_1}P_{2,\lambda_2}P_{2,\lambda_3}$$
(7)

$$+ \sum_{k,k'}\sum_{\lambda_1,\lambda_2,\lambda_3}[\phi^{\mathrm{L}}_\lambda(k)]^*[\phi^{\mathrm{R}}_{\lambda_1}(k')]^*\phi^{\mathrm{R}}_{\lambda_2}(k)\phi^{\mathrm{R}}_{\lambda_3}(k')(W^{vvvv}_{k,k'} - W^{cvvc}_{k,k'})P^*_{1,\lambda_1}P_{2,\lambda_2}P_{2,\lambda_3}$$

The intensity of the FWM signal is proportional to the sum over the contributions from the different eigenstates, $|\mathbf{P}(t,\tau)|^2 = \left|\frac{e}{2\pi m_0}\mathbf{p}_{vc}\sum_\lambda P^{[3,\mathrm{FWM}]}_\lambda(t,\tau)\gamma_\lambda\right|^2$ with $\gamma_\lambda = \sum_k \sqrt{1-2f^0_k}\phi_\lambda(k)$.

As an example of our results, we show in **Figure 4** the computed dependence of the time-resolved DFWM signal on the initial carrier density for the case of zero delay between

the pulses ($\tau = 0$ ps). Here, we assumed excitation pulses resonant to the lowest exciton having a temporal width of 150 fs. Due to the carrier-induced increase in dephasing, we notice a significantly faster decay of the DFWM signal with increasing density.

Figure 5 shows the integrated FWM signal for different initial carrier densities. The pulses have a temporal width of 150 fs and their central frequency is adjusted to the 1s excitonic resonance.
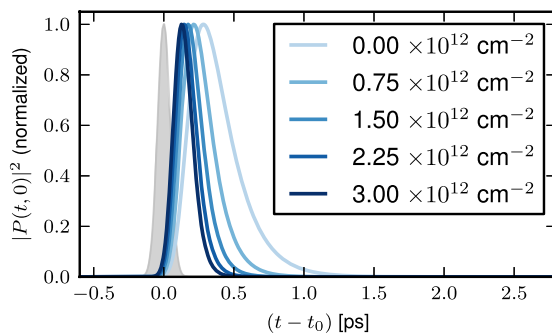
Figure 4. Time-resolved DFWM signal for $\tau = 0$ ps and different initial carrier densities n_0 distributed equally in the A- and B-band. The self-correlated signal of the pulses with central frequency matching the exciton resonance energy $\omega_t = \omega_p = \omega_{1s}$, maximum at $t = t_0$, and width $t_{width} = 150$ fs is marked as the gray area.
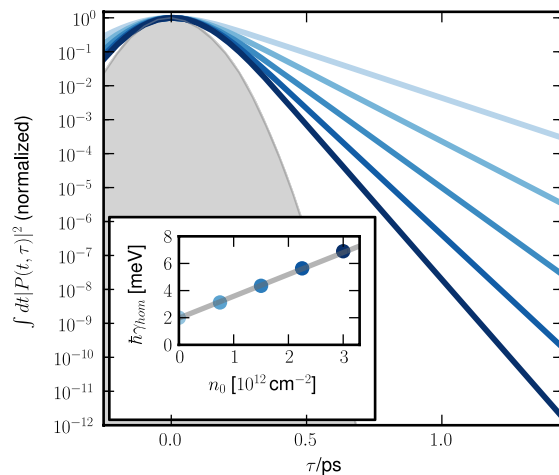
Figure 5. Integrated DFWM signal for different initial carrier densities n_0 distributed equally in the A- and B-band. The self-correlated signal of the pulses with central frequency matching the exciton resonance energy $\omega_t = \omega_p = \omega_{1s}$ and width $t_{width} = 150$ fs is marked as the gray area. The integrated signal decreases for larger τ proportional to $\exp(-2\gamma_{hom}\tau)$, the fitted values for γ_{hom} are depicted in the inset.

For positive delay times, the signal decreases proportional to $2\gamma_{hom}$, where γ_{hom} is composed of the inserted phenomenological background dephasing $\hbar\gamma = 2$ meV and the EID of the lowest-lying exciton resonance. Due to the density-dependent increase in EID, the slope of the integrated signal gets steeper with increasing carrier densities, approaching the self-correlated signal of the pulses depicted as gray areas in the figure.

4. Summary and Conclusion

Using a fully microscopic approach combined with DFT calculations of the linear material properties, we investigated EID effects caused by incoherent electron–hole excitations.

We evaluated the theory for different carrier distributions for the example of hBN-encapsulated MoS_2 and computed the excitation-dependent linewidth of the energetically lowest exciton resonance as well as the decay of the DFWM signal. As relevant examples, we analyzed the influence of different static carrier distributions within the bands and the consequences of an increased carrier temperature. For small densities, our results show that the EID depends only weakly on the exact carrier distribution, whereas distribution details become more important with increasing density. The unequal occupation of the valence bands resulting from the hole drain between the K and K' valley leads to a reduced dephasing. Furthermore, an increase in carrier temperature results in an EID increase, reaching a plateau for high temperatures. These effects should manifest themselves, for example, in time-dependent measurements of the excitonic linewidth and in DFWM spectroscopy. In particular, the EID after incoherent carrier generation is expected to decrease with increasing time as both the cooling of hot carrier distributions on a short timescale as well as the drain of the holes due to inter-valley scattering on a longer timescale result in an EID decrease.

Conflict of Interest

The authors declare no conflict of interest.

Data Availability Statement

The data that support the findings of this study are available from the corresponding author upon reasonable request.

[1] J. A. Wilson, A. D. Yoffe, *Adv. Phys.* **1969**, *18*, 193.
[2] A. J. Grant, J. A. Wilson, A. D. Yoffe, *Philos. Mag.: J. Theor. Exp. Appl. Phys.* **1972**, *25*, 625.
[3] A. R. Beal, J. C. Knights, W. Y. Liang, *J. Phys. C: Solid State Phys.* **1972**, *5*, 3540.
[4] K. F. Mak, C. Lee, J. Hone, J. Shan, T. F. Heinz, *Phys. Rev. Lett.* **2010**, *105*, 136805.
[5] A. Chernikov, T. C. Berkelbach, H. M. Hill, A. Rigosi, Y. Li, O. B. Aslan, D. R. Reichman, M. S. Hybertsen, T. F. Heinz, *Phys. Rev. Lett.* **2014**, *113*, 076802.

[6] S. Park, N. Mutz, T. Schultz, S. Blumstengel, A. Han, A. Aljarb, L.-J. Li, E. J. W. List-Kratochvil, P. Amsalem, N. Koch, *2D Mater.* **2018**, *5*, 025003.

[7] K. He, N. Kumar, L. Zhao, Z. Wang, K. F. Mak, H. Zhao, J. Shan, *Phys. Rev. Lett.* **2014**, *113*, 026803.

[8] B. Zhu, X. Chen, X. Cui, *Sci. Rep.* **2015**, *5*, 9218.

[9] F. Katsch, M. Selig, A. Carmele, A. Knorr, *Phys. Status Solidi B* **2018**, *255*, 1800185.

[10] H. M. Hill, A. F. Rigosi, C. Roquelet, A. Chernikov, T. C. Berkelbach, D. R. Reichman, M. S. Hybertsen, L. E. Brus, T. F. Heinz, *Nano Lett.* **2015**, *15*, 2992.

[11] D. Y. Qiu, F. H. da Jornada, S. G. Louie, *Phys. Rev. Lett.* **2013**, *111*, 216805.

[12] C. Robert, M. A. Semina, F. Cadiz, M. Manca, E. Courtade, T. Taniguchi, K. Watanabe, H. Cai, S. Tongay, B. Lassagne, P. Renucci, T. Amand, X. Marie, M. M. Glazov, B. Urbaszek, *Phys. Rev. Mater.* **2018**, *2*, 011001.

[13] D. Erkensten, S. Brem, E. Malic, *Phys. Rev. B* **2021**, *103*, 045426.

[14] G. Moody, C. Kavir Dass, K. Hao, C.-H. Chen, L.-J. Li, A. Singh, K. Tran, G. Clark, X. Xu, G. Berghäuser, E. Malic, A. Knorr, X. Li, *Nat. Commun.* **2015**, *6*, 8315.

[15] M. R. Carbone, M. Z. Mayers, D. R. Reichman, *J. Chem. Phys.* **2020**, *152*, 194705.

[16] M. Selig, G. Berghäuser, A. Raja, P. Nagler, C. Schüller, T. F. Heinz, T. Korn, A. Chernikov, E. Malic, A. Knorr, *Nat. Commun.* **2016**, *7*, 13279.

[17] T. Jakubczyk, G. Nayak, L. Scarpelli, W.-L. Liu, S. Dubey, N. Bendiab, L. Marty, T. Taniguchi, K. Watanabe, F. Masia, G. Nogues, J. Coraux, W. Langbein, J. Renard, V. Bouchiat, J. Kasprzak, *ACS Nano* **2019**, *13*, 3500.

[18] T. Jakubczyk, M. Bartos, L. Scarpelli, K. Nogajewski, W. Langbein, M. Potemski, J. Kasprzak, *Proc. SPIE* **2020**, *11278*, 112781C.

[19] P. Dey, J. Paul, Z. Wang, C. Stevens, C. Liu, A. Romero, J. Shan, D. Hilton, D. Karaiskaj, *Phys. Rev. Lett.* **2016**, *116*, 127402.

[20] C. Boule, D. Vaclavkova, M. Bartos, K. Nogajewski, L. Zdražil, T. Taniguchi, K. Watanabe, M. Potemski, J. Kasprzak, *Phys. Rev. Mater.* **2020**, *4*, 034001.

[21] P. Hohenberg, W. Kohn, *Phys. Rev.* **1964**, *136*, B864.

[22] W. Kohn, L. J. Sham, *Phys. Rev.* **1965**, *140*, A1133.

[23] D. Xiao, G.-B. Liu, W. Feng, X. Xu, W. Yao, *Phys. Rev. Lett.* **2012**, *108*, 196802.

[24] J. P. Perdew, K. Burke, M. Ernzerhof, *Phys. Rev. Lett.* **1996**, *77*, 3865.

[25] G. Kresse, J. Furthmüller, *Phys. Rev. B* **1996**, *54*, 11169.

[26] G. Kresse, J. Hafner, *Phys. Rev. B* **1994**, *49*, 14251.

[27] G. Kresse, J. Hafner, *Phys. Rev. B* **1993**, *47*, 558.

[28] L. Meckbach, T. Stroucken, S. W. Koch, *Phys. Rev. B* **2018**, *97*, 035425.

[29] J. Neuhaus, S. C. Liebscher, L. Meckbach, T. Stroucken, S. W. Koch, *J. Phys.: Condens. Matter* **2020**, *33*, 035301.

[30] L. Meckbach, J. Hader, U. Huttner, J. Neuhaus, J. T. Steiner, T. Stroucken, J. V. Moloney, S. W. Koch, *Phys. Rev. B* **2020**, *101*, 075401.

[31] A. Kormányos, G. Burkard, M. Gmitra, J. Fabian, V. Zólyomi, N. D. Drummond, V. Fal'ko, *2D Mater.* **2015**, *2*, 022001.

[32] A. Molina-Sánchez, K. Hummer, L. Wirtz, *Surf. Sci. Rep.* **2015**, *70*, 554.

Lebenslauf

Der Lebenslauf ist aufgrund der enthaltenen persönlichen Daten nicht Bestandteil der Online-Veröffentlichung.